Towards a more realistic discrete element model of solid-state sintering : grain growth and non-spherical particles

Brayan Marcelo Paredes Goyes

THÈSE

Pour obtenir le grade de

DOCTEUR DE L'UNIVERSITÉ GRENOBLE ALPES

École doctorale : I-MEP2 - Ingénierie - Matériaux, Mécanique, Environnement, Energétique, Procédés, Production
Spécialité : 2MGE : Matériaux, Mécanique, Génie civil, Electrochimie
Unité de recherche : Science et Ingénierie des Matériaux et Procédés

Modélisation par éléments discrets du frittage à l'état solide : prise en compte du grossissement des grains et de particules non sphériques

Towards a more realistic discrete element model of solid-state sintering: grain growth and non-spherical particles

Présentée par :

Brayan Marcelo PAREDES GOYES

Direction de thèse :

Christophe MARTIN DIRECTEUR DE RECHERCHE, Université Grenoble Alpes	Directeur de thèse
David JAUFFRES MAITRE DE CONFERENCES, Université Grenoble Alpes	Co-encadrant de thèse

Rapporteurs :

Marc BERNACKI
PROFESSEUR, MINES ParisTech
Guillaume BERNARD-GRANGER
DIRECTEUR DE RECHERCHE, CEA centre de Marcoule
Rajendra BORDIA
PROFESSEUR, Clemson University, South Carolina

Thèse soutenue publiquement le **2 décembre 2022**, devant le jury composé de :

Christophe MARTIN DIRECTEUR DE RECHERCHE, CNRS délégation Alpes	Directeur de thèse
Marc BERNACKI PROFESSEUR, MINES ParisTech	Rapporteur
Guillaume BERNARD-GRANGER DIRECTEUR DE RECHERCHE, CEA centre de Marcoule	Rapporteur
Rajendra BORDIA PROFESSEUR, Clemson University, South Carolina	Rapporteur
Jérôme DURIEZ CHARGE DE RECHERCHE, INRAE centre Procence-Alpes-Côte d'Azur	Examinateur
Helen REVERON DIRECTRICE DE RECHERCHE, CNRS délégation Rhône Auvergne	Présidente
Bruno CHAREYRE MAITRE DE CONFERENCES HDR, Université Grenoble Alpes	Examinateur

Invités :

David Jauffrès
MAITRE DE CONFERENCE, UGA

Abstract

Solid state sintering is a widely used powder processing technique for ceramics and metals. The treatment is carried out at high temperatures, below the melting point. Consolidation, densification, and grain growth occur during sintering. The discrete element method (DEM) has been effectively applied for modeling densification and consolidation at the mesoscale for spherical particles. Nevertheless, grain growth affects sintering during the intermediate and final stages. It is not considered by actual DEM simulations. Here, a realistic grain growth model is developed. The mechanisms considered are surface diffusion and grain boundary migration. The standard densification model, based on grain boundary diffusion and surface diffusion, is refined to take into account large particle size ratios. Both models are coupled for studying the microstructural evolution during sintering until the relative density approaches 0.90. The densification and grain growth kinetics, the sintering trajectories, and the evolution of the particle size distribution are analyzed for an initial packing with realistic size distribution. The results are in good agreement with grain growth experimental data from the literature for conventional sintering of alumina. Grain growth is particularly problematic and difficult to avoid for nano-powders. A possible approach to mitigate grain growth is two-step sintering, which uses a combination of high and low temperatures during the sintering thermal cycle. DEM simulations are employed to explore the mechanisms that can explain the success of two-step sintering. Another means to improve the realism of DEM sintering models is to consider actual particle shapes instead of spheres. This is particularly relevant for sintering since the driving force is the local curvature. The real shape of particles can be captured using the level set discrete element method (LS-DEM). An optimization-based contact detection algorithm is proposed to reduce computational cost. The proposed LS-DEM implementation is a proof of concept of its potential effectiveness for sintering. For illustration, simulations of ellipsoidal particle packings with elastic and sintering interactions are shown. Sintering simulations allow to analyze the influence of the particle aspect ratio on shrinkage.

Keywords: sintering, discrete element method, grain growth, nano-powders, two-step sintering, non-spherical particles, Level-Sets

Résumé

Le frittage à l'état solide est un procédé de mise en œuvre des poudres largement utilisée pour les céramiques et les métaux. Le traitement s'effectue à des températures élevées, inférieures au point de fusion. Consolidation, densification et croissance des grains se produisent au cours du frittage. La méthode des éléments discrets (DEM) a été appliquée efficacement pour modéliser la densification et la consolidation à l'échelle mésoscopique pour des particules sphériques. Néanmoins, la croissance des grains affecte le frittage pendant les étapes intermédiaires et finales. Elle n'est pas prise en compte par les simulations DEM actuelles. Dans ce travail, un modèle réaliste de croissance des grains est développé. Les mécanismes considérés sont la diffusion de surface et la migration des joints de grain. Le modèle de densification standard, basé sur la diffusion aux joints de grain et la diffusion de surface, est raffiné pour prendre en compte les grands rapports de taille des particules. Les deux modèles sont couplés pour étudier l'évolution microstructurale pendant le frittage jusqu'à des densités relatives proches de 0,90. La cinétique de densification et de croissance des grains, les trajectoires de frittage et l'évolution de la distribution de taille des particules sont analysées pour un empilement initial avec une distribution de taille réaliste. Les résultats sont en bon accord avec les données expérimentales de la littérature sur la croissance des grains pour le frittage conventionnel de l'alumine. La croissance des grains est particulièrement problématique et difficile à éviter pour les nanopoudres. Une approche possible pour limiter la croissance des grains est le frittage en deux étapes, qui utilise une combinaison de températures élevées et basses pendant le cycle thermique de frittage. Les simulations DEM sont utilisées pour explorer les mécanismes qui peuvent expliquer le succès du frittage en deux étapes. Un autre moyen d'améliorer le réalisme des modèles de frittage DEM est de considérer les formes réelles des particules plutôt que des sphères. Ceci est particulièrement pertinent pour le frittage puisque la force motrice est la courbure locale. La forme réelle des particules peut être capturée à l'aide de la méthode des éléments discrets Level-Sets (LS-DEM). Un algorithme de détection des contacts basé sur l'optimisation est proposé pour réduire le temps de calcul. La mise en œuvre proposée de la LS-DEM est une preuve de concept de son efficacité potentielle pour le frittage. À titre d'illustration, des simulations d'empilement de particules ellipsoïdales avec des interactions élastiques et de frittage sont présentées. Les simulations de frittage permettent d'analyser l'influence du rapport d'aspect des particules sur le retrait.

Mots-clés : frittage, méthode des éléments discrets, croissance des grains, nanopoudres, frittage en deux étapes, particules non sphériques, Level-Sets

Acknowledgements

The PhD was a great journey that helped me to confirm that what I want and what I am passionate about doing professionally is teaching and researching. But that was only a part of it, because all the people and experiences that I lived in these 3 years shaped this stage.

I remember that I was afraid before starting the PhD, because of the delay I had in the master and because I thought I was not prepared for the PhD, that in my head I should already know everything. But from the beginning Christophe and David taught me so much technically and with a lot of patience, showing me that the research career is a long process and that one of the objectives of the PhD was to learn. And they inspire me by their simplicity and humility as human beings.

I thank Jean-Michel Missiaen and Didier Bouvard for their availability and kindness to teach me so much about sintering, which was a very important basis of this thesis. To Marc Fivel for his frequent and willing help in everything related to the calculating machines. And to all the interns, PhD students, professors, technicians, administrative and financial staff of SIMaP.

I would also like to thank Helen Reveron and Bruno Chareyre for all their time and advice since my first CSI in 2020 until now being part of the jury. To Guillaume Bernard-Granger, Marc Bernacki and Raj Bordia for their time and valuable contributions as rapporteurs, which certainly improved the quality of the thesis. And to Jerome Duriez for his availability to be part of the jury and his LS-DEM advices.

Of course, my thanks to the European Union for funding my PhD through Mathegram. To Charley Wu and all Mathegram members for the support during the whole program.

This journey would have been incomplete and bitter without the support of my great friends. To Aatreya, Oguz, Gilmar and Sara for having been a source of joy and rest throughout this time in Grenoble, which I strongly wish to continue in the future. To Edgar, Joffre, Raquel and Carla, for always showing their concern and love despite the distance, as their friendship gives me peace. To Renato for his friendship, and his guidance and loving care that he has for us, especially in those moments that we have felt a little lost, outside of Brazil. And to Caluga, Dani, Glauco, Thayse, Luis, Norallys, Alex and Claudia for taking care of us from a distance during this period of the PhD. I also thank Prof. Leonel for his teachings and patience that although he could not see its fruits in the master's degree, now there certainly are.

To my Pepita (Palloma) for being my unconditional partner, friend, wife, my safe harbor. For being with me in this adventure from the beginning, in spite of so many uncertainties. For supporting me every day and for being that solid base, without which I would not have had the emotional health to do and finish my doctorate. And I was able to achieve this dream of doing my doctorate thanks to the efforts of many people from many years ago. To my mommy Lucy, who encouraged me to study since I was 4 years old. For her extraordinary effort of more than 12 hours of work per day for so many years that she made so that I could study. For her love that made everything so peaceful even though the conditions were not. Likewise to grandma Tere, for her sacrifices and her unconditional incentive to study, even though it is something far from her reality. To Davicho, Gabuchitas, for all the time we grew up together and then for your love as brothers so strong despite the distance, without you I would be incomplete. And to nana Andrea, nano Gandy, Luis and tia Anita for taking care of me and helping me in so many ways and in times when I had no energy.

To God for his unconditional love, for giving me all the physical, emotional and spiritual conditions to be able to do my PhD. And for showing me every day in science the beauties of his creation.

Contents

Introduction générale

Ce doctorat s'inscrit dans le cadre du projet MATHEGRAM, un programme de la communauté Européenne ITN (Integrated Training Network). L'objectif de MATHEGRAM est d'étudier le comportement thermomécanique des matériaux granulaires à travers 15 thèses basées sur la modélisation et l'expérimentation. Le présent travail concerne la modélisation du frittage à l'échelle de la particule avec la méthode des éléments discrets (Discrete Element Method, DEM). Ce sujet est lié au thème d'un autre doctorant de MATHEGRAM (Aatreya Venkatesh, également à SIMaP), qui se concentre sur l'analyse nanotomographique in-situ du frittage.

Le frittage est utilisé par l'humanité depuis des milliers d'années. Une des caractéristiques originales du frittage est qu'en fournissant simplement de l'énergie thermique à un milieu particulaire poreux (sans aucune force mécanique externe), le système évolue naturellement vers un état plus dense. La réduction de l'énergie libre de surface s'effectue par transport de masse, et l'augmentation de la température ne déclenche dans la plupart des cas aucune réaction chimique, mais est seulement utilisée pour augmenter la cinétique de la densification.

Bien que de nombreuses nouvelles technologies soient apparues à l'époque moderne, le frittage continue d'être largement utilisé pour le traitement des poudres céramiques, métalliques, polymères et composites. Les techniques de frittage, qu'elles soient conventionnelles ou plus novatrices, sont étudiées pour mieux comprendre les mécanismes, améliorer l'efficacité des procédés et trouver de nouvelles applications. En complément de l'approche expérimentale, la modélisation a été utilisée pour atteindre ces objectifs. La grande variété des méthodes employées comprend : les modèles analytiques, les techniques de différences finies, les éléments finis, les éléments discrets, les techniques de champs de phase, la méthode de Monte-Carlo cinétique, les méthodes de minimisation d'énergie de surface, et les level sets, entre autres. Ces modélisations ont été réalisées à l'échelle de l'atome, du grain ou du composant. Dans certains cas, elles ont également tenté de coupler plusieurs échelles. Les méthodes citées diffèrent dans l'échelle de longueur considérée, le niveau de description physique et l'étape de frittage considérée. La méthode des éléments discrets (DEM) a la particularité de représenter chaque particule de la poudre, avec une forme constante tout au long du processus, ce qui permet de simuler plusieurs centaines de milliers de particules en un temps raisonnable. La méthode a été utilisée pour modéliser la densification de céramiques polycristallines et de métaux pendant les étapes initiales et intermédiaires du frittage. Des questions

d'intérêt pratique pour le processus de frittage ont été couvertes par la modélisation DEM telles que : le réarrangement des particules, la densification anisotrope, la propagation des défauts, l'effet des inclusions, le frittage sous contrainte et le frittage des composites.

Cependant, il existe encore plusieurs améliorations cruciales qui peuvent conduire les modèles de frittage DEM vers une description plus réaliste du processus. La première est la prise en compte du grossissement des grains, qui n'a pas été incluse de manière réaliste jusqu'à présent. Le grossissement des grains est pertinent car il entre en compétition avec la densification et a un impact sur l'évolution microstructurale et la cinétique de densification. Dans la plupart des cas, la croissance des grains n'est pas souhaitée car elle a un effet négatif sur les propriétés, en particulier mécaniques, du matériau final. Par exemple, les céramiques suivent une relation de type Hall-Petch, qui prédit une diminution de la contrainte à rupture avec l'augmentation de la taille des grains. Comme le grossissement des grains se produit naturellement pendant le frittage, il doit être inclus dans les simulations discrètes.

Un autre aspect qui doit être amélioré dans la modélisation DEM du frittage est la forme des particules. Les modèles actuels considèrent les particules comme des sphères. Ceci est dû au fait qu'en DEM, une étape cruciale consiste à rechercher les contacts entre les particules. Cette recherche est relativement facile pour les sphères car elle n'implique que la comparaison entre deux distances. Mais elle devient beaucoup plus difficile lorsque la forme s'éloigne de la sphère. Ainsi, les simulations de très grands empilements avec des millions de particules ont été réalisées avec des sphères mais sont encore rares pour les particules non sphériques. À ce jour, nous n'avons connaissance d'aucun travail pour simuler le frittage avec des particules non sphériques en DEM.

Et cependant la plupart des poudres céramiques ne présentent pas de particules parfaitement sphériques. Cela peut être critique dans le frittage car il s'agit d'un processus gouverné par la courbure locale. Par conséquent, les deux axes de cette thèse de doctorat sont :

- Le développement d'un modèle DEM de grossissement des grains pour le frittage. Il doit être basé sur des mécanismes réalistes de transfert de masse. Le modèle doit être couplé avec les modèles de densification, ce qui permettra d'étudier l'évolution microstructurale d'empilements réels pendant le frittage.

- La mise en œuvre d'un cadre pour étudier le frittage de particules non sphériques dans le contexte de la DEM. La méthodologie choisie est la méthode des éléments discrets level set (LS-DEM).

Le projet est centré sur le frittage à l'état solide de poudres polycristallines poreuses.

Du point de vue des matériaux, le champ d'application des modèles développés sera dirigé vers les poudres métalliques et principalement céramiques. Les résultats sont présentés pour l'alumine, une poudre largement utilisée dans le frittage pour laquelle de nombreuses données expérimentales et de propriétés sont disponibles.

Les principaux modèles et résultats du projet sont discutés dans trois articles scientifiques. Deux d'entre eux ont été acceptés et le dernier sera soumis prochainement. Le chapitre 2 décrit les principaux concepts du frittage conventionnel à l'état solide qui seront utiles tout au long de ce travail. Une revue critique des différentes méthodologies existantes dans la littérature pour la modélisation du frittage à différentes échelles est proposée. L'accent est mis sur l'état de l'art des modèles de frittage en DEM. Dans la deuxième section de ce chapitre, les principes fondamentaux de la DEM et de la LS-DEM sont détaillés.

Le modèle de croissance des grains est basé sur deux mécanismes de transport de masse : la diffusion de surface et la migration aux joints de grains. La description détaillée des modèles de grossissement et de densification des grains est présentée dans un premier article (chapitre 3), qui a été accepté dans *Acta Materialia* en 2021 [1]. Les résultats de la simulation sont comparés aux données expérimentales de frittage pour les poudres d'alumine microniques. Le bon accord entre la simulation et les expériences sur l'évolution microstructurale de grands empilements pour un frittage conventionnel rend possible la simulation de processus de frittage plus complexes. Dans le deuxième article (chapitre 4), qui a été accepté dans *Journal of the European Ceramic Society* en 2022 [2], des simulations du frittage en deux étapes de nanopoudres d'alumine sont réalisées. Le but du frittage en deux étapes est de limiter le grossissement des grains, mais les mécanismes sous-jacents qui peuvent expliquer l'arrêt de la croissance des grains ne sont pas encore clarifiés. En particulier, le modèle explore l'hypothèse de la littérature selon laquelle le succès du frittage en deux étapes est dû à une forte augmentation de l'énergie d'activation de la mobilité des joints de grain à basse température. Toutes les simulations sont effectuées dans des conditions non isothermes pour différents vitesses de montée en température.

Ayant atteint le premier objectif du projet, nous procédons au développement d'une preuve de concept d'un modèle de frittage LS-DEM pour des particules de forme arbitraire. Contrairement à la méthodologie LS-DEM originale, nous mettons en œuvre un schéma basé sur l'optimisation pour la détection des contacts. Ce schéma particulier devrait être plus efficace pour détecter les petits contacts, qui sont particulièrement pertinents pour le frittage. Ce développement et des simulations d'empilements de particules ellipsoïdales en frittage sont décrits dans le troisième article (chapitre 5), qui sera soumis prochainement.

Le chapitre 6 résume les principales conclusions de ce travail et propose quelques perspectives pour la modélisation du grossissement des grains et des particules non sphériques en frittage dans le cadre de la DEM.

References

[1] B. Paredes-goyes, D. Jauffres, J.-m. Missiaen, and C. L. Martin, "Grain growth in sintering : A discrete element model on large packings," *Acta Materialia*, vol. 218, p. 117 182, 2021, ISSN: 1359-6454. DOI: 10.1016/j.actamat.2021.117182.

[2] B. Paredes-Goyes, A. M. Venkatesh, D. Jauffres, and C. L. Martin, "Two-step sintering of alumina nano-powders: A discrete element study," *Journal of the European Ceramic Society*, 2023, ISSN: 0955-2219. DOI: https://doi.org/10.1016/j.jeurceramsoc.2022.10.001.

Chapter 1

General introduction

This PhD is part of the MATHEGRAM, project, a European ITN (Integrated Training Network) program. The aim of MATHEGRAM is to study the thermomechanical behavior of granular materials through 15 PhD projects based on modeling and experiments. The present work concerns the modeling of sintering at the particle scale with the Discrete Element Method (DEM). This topic is linked with the subject of another PhD in MATHEGRAM (Aatreya Venkatesh, also at SIMaP), which focuses on the in-situ nanotomography analysis of sintering.

Sintering has been used by humanity for thousands of years. A great feature of sintering is that by simply supplying thermal energy to a porous particulate medium (without any external mechanical force), the system naturally evolves towards a denser state. The reduction of surface free energy takes place by mass transport, and increasing temperature does not in many cases trigger any chemical reaction, but is simply used to increase the kinetics of densification.

Despite the appearance of many new technologies in modern times, sintering continues to be widely used in the processing of ceramic, metallic, polymeric and composite powders. Conventional and new sintering techniques are being studied to better understand the mechanisms, improve process efficiency and find new applications. Complementary to the experimental approach, modeling has been used to achieve these goals. The wide variety of employed methods include: analytical models, finite differences, finite elements, discrete elements, phase-field, kinetic Monte-Carlo, surface evolver, level sets, among others. The modeling has been performed at the atomistic, grain, or component length scales. It has also in some cases attempted to couple various scales. The cited methods differ in the length scale considered, the level of physical description and the sintering stage considered. The Discrete Element Method (DEM) has the particularity of representing each particle of the powder, with a constant shape throughout the process, allowing the simulation of up to hundreds of thousands of particles in a reasonable time. The method has been used to model the densification of porous polycrystalline ceramics and metals during the initial and intermediate stages of sintering. Questions of practical interest for the sintering process have been covered by DEM modeling such as: particle rearrangement, anisotropic densification, defect propagation, the effect of inclusions, constrained sintering and sintering of composites.

However, there are still some crucial improvements that can lead DEM sintering

models towards a more realistic description of the process. The first is the consideration of grain growth, which to date has not been realistically included. Grain growth is relevant since it competes with densification and impacts the microstructural evolution and densification kinetics. In most cases, grain growth is not desired because it has a detrimental bearing on the properties, in particular mechanical, of the final material. For example, oxide ceramics follow a Hall–Petch relationship, which predicts a decrease in strength with increasing grain size. However, grain growth naturally arises during sintering and thus should be included in discrete simulations.

Another aspect that needs improvement in DEM modeling of sintering is the particle shape. Current models consider particles as spheres. This is because in DEM, a crucial step consists in searching for contacts between particles. This is relatively easy for spheres as it only involves the comparison between two distances. But it becomes much more challenging as the shape departs from the sphere. Thus, the simulation of very large packings with millions of particles have been carried out with spheres but are still rare for non-spherical particles. To date, we are not aware of any effort to simulate sintering with non-spherical particles in DEM.

Nevertheless, most ceramics powders do not have perfect spherical particles. This can be critical in sintering as it is a curvature-driven process. Therefore, the two axes of this PhD thesis are:

- The development of a grain growth DEM model for sintering. It should be based on realistic mass transfer mechanisms. The model is to be coupled with the densification models, that will allow to study the microstructural evolution of real packings during sintering.

- The implementation of a framework to study the sintering of non-spherical particles in the DEM context. The selected methodology is the Level Set Discrete Element Method (LS-DEM).

The interest of the project is on solid-state sintering of porous polycrystalline powders. The scope of the developed models is to represent a variety of metallic and mainly ceramic powders. Results are presented for alumina, a powder widely used in sintering for which extensive experimental and material property data are available.

The main models and results of the project are discussed through three scientific articles. Two of them accepted and one will be submitted in the near future. Chapter 2 describes the main concepts of conventional solid-state sintering that will be useful all along this work. A critical review of the various existing methodologies in the literature for modeling sintering at different scales is proposed. Emphasis is placed on

the state of the art of DEM sintering models. In the second section of this chapter, the fundamentals of DEM and LS-DEM are detailed.

The grain growth model is based on two mass transport mechanisms: surface diffusion and grain boundary migration. The detailed description of the grain growth and densification models is reported in a first paper (chapter 3), which was accepted in *Acta Materialia* in 2021 [1]. The simulation results are compared against sintering experimental data for alumina micronic powders. The good agreement between simulation and experiments on the microstructural evolution of large packings for standard sintering makes it possible to simulate more challenging sintering processes. In the second article (chapter 4), which has been accepted in *Journal of the European Ceramic Society* in 2022 [2], simulations of two-step sintering of alumina nano-powders are carried out. The goal of two-step sintering is to limit grain growth, but the underlying mechanisms that may explain the arrest of grain growth are not yet clarified. In particular, the model explores the literature hypothesis stating that the success of two-step sintering is due to a large increase in the activation energy of the grain boundary mobility at low temperatures. All the simulations are performed in nonisothermal conditions for different heating rates.

Having reached the first project goal, we proceed to the development of a proof of concept of a LS-DEM sintering model for particles of arbitrary shape. Unlike the original LS-DEM methodology, we implement an optimization-based scheme for contact detection. This particular scheme should be efficient to capture small contacts, that are particularly relevant for sintering. This development and the simulations of packings of ellipsoidal particles in sintering are described in the third article (chapter 5), which will be submitted in the near future.

Chapter 6 summarizes the main conclusions of this work and proposes some perspectives for modeling grain growth and non-spherical particles in sintering in the DEM framework.

References

[1] B. Paredes-goyes, D. Jauffres, J.-m. Missiaen, and C. L. Martin, "Grain growth in sintering : A discrete element model on large packings," *Acta Materialia*, vol. 218, p. 117 182, 2021, ISSN: 1359-6454. DOI: 10.1016/j.actamat.2021.117182.

[2] B. Paredes-Goyes, A. M. Venkatesh, D. Jauffres, and C. L. Martin, "Two-step sintering of alumina nano-powders: A discrete element study," *Journal of the*

European Ceramic Society, 2023, ISSN: 0955-2219. DOI: https://doi.org/10.1016/j.jeurceramsoc.2022.10.001.

Chapter 2
Literature review and Methods

2.1 Solid-state sintering

This section is dedicated to single phase solid-state sintering with conventional heating source. Free sintering condition is considered, i.e., no external pressure is applied. The focus is on porous polycrystalline structures. The aim of this section is to review the main ideas that have been developed to model solid-state sintering. These models have been proposed in the last 60 years and are extremely useful to build analytical or numerical solutions for sintering. We will use some important concepts in these models to develop our own in the chapters devoted to the Discrete Element simulation of sintering.

2.1.1 Fundamentals

Sintering is a high temperature process, below the melting point, for consolidating ceramic or metallic powders. The driving force is the decrease of the total interfacial energy E_{int}, given by [1]:

$$E_{int} = \gamma_S A_S + \gamma_{GB} A_{GB} \tag{2.1}$$

where γ is the specific interfacial energy, A the area, S is for solid-gas interfaces (pore surfaces) and GB for solid-solid interfaces (grain boundaries). The decrease of solid-gas area is reached by consolidation and the decrease of solid-solid area by grain growth [1]. Fig. 2.1 shows a schematic of these two competitive processes during sintering. For any pair of adjacent grains, the grain boundary and the pore surfaces intersect forming a junction surface. At equilibrium, the forces on both sides of the junction are balanced. The balance can be reached at one point of the junction on a perpendicular plane to the grain boundary. Forces can be calculated from the specific interfacial energies, leading to the following equilibrium balance [2]:

$$\gamma_{GB} = 2\gamma_S cos\left(\frac{\Psi_{eq}}{2}\right) \tag{2.2}$$

where Ψ_{eq} is the equilibrium dihedral angle.

Consolidation and grain growth are carried out by mass transport. It is feasible only if a gradient of chemical potential exists. In the absence of external pressure and

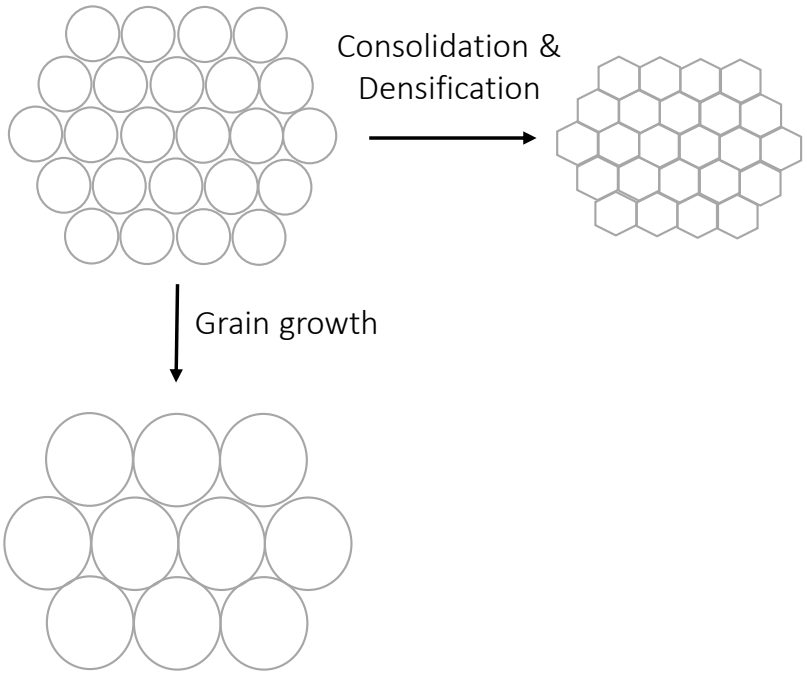

Figure 2.1: Main processes during sintering.

chemical reaction, and electric potential, the chemical potential gradient is generated by the pressure difference of a curved surface, i.e., the Laplace pressure. In sintering of polycrystals, both pores and grain boundaries have a curved surface.

2.1.1.1 Consolidation and densification

A comprehensive list of sintering mechanisms was first proposed by Ashby [3]. All mechanisms involve diffusive transport of matter driven by the curvature gradient and leading to consolidation, i.e., neck growth. The mechanisms differ from each other by the type of diffusion and the source of matter. Some mechanisms lead to center-to-center approach, that is a densification at the macroscopic scale (shown in blue in Fig. 2.2). Non-densifying mechanisms are shown in gray and have the surface as source of matter. On the other hand, densifying mechanisms have the internal body and the grain boundary as sources.

Generally, for oxide ceramics surface diffusion is the dominant mechanism at the beginning of sintering and grain boundary diffusion is the dominant mechanism for densification. In contrast, vapor transport only appears if the material has a high vapor pressure [4], meanwhile, the diffusion from dislocations (plastic flow) is more common in sintering of metal powders [2].

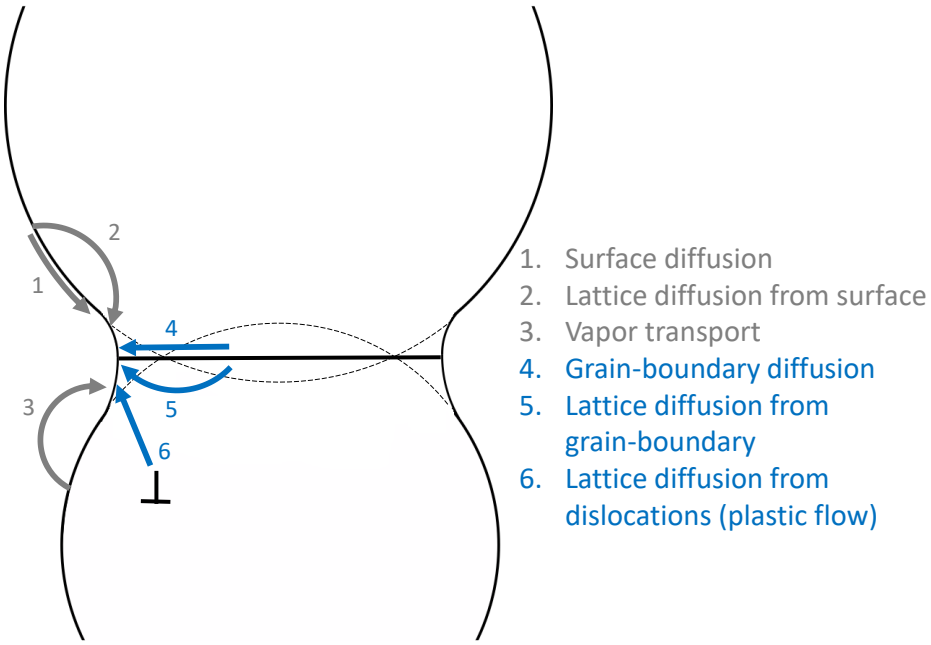

Figure 2.2: Densifying (blue) and nondensifying (gray) sintering mechanisms.

2.1.1.2 Grain growth

Our interest is to study grain growth in porous systems. As mentioned above, grain growth is an unavoidable process driven by the decrease of the total solid-solid area. In general terms, large grains grow at the expense of small ones by diffusion mechanisms. The mean grain size increases because of the continuous disappearance of smaller grains.

Fig. 2.3 shows a simplified sketch of diffusion-controlled grain growth. The external transport refers to transport via vapor or liquid phases in the pores. Grain boundary migration can be understood as a mass transfer across the grain boundary, instead of parallel as in the consolidation mechanism. Grain boundary migration is the main mechanism for grain growth but it can encounter energy barrier depending on the local curvature. In order to overcome this barrier, grain growth first occurs by other diffusion mechanisms, like surface diffusion or vapor transport. [5].

Grain growth is affected both by process variables (sintering temperature, heating rate, initial green density and time) and by grain properties (specific interfacial energies, diffusivities, crystal orientation and secondary phases) [4]. The effect of the temperature on grain growth depends strongly on the densification material properties. Assuming that the material has a higher densification activation energy than its grain growth activation energy, both a higher temperature and a higher heating rate will retard grain growth. This is the case of alumina as investigated in chapter 4. A

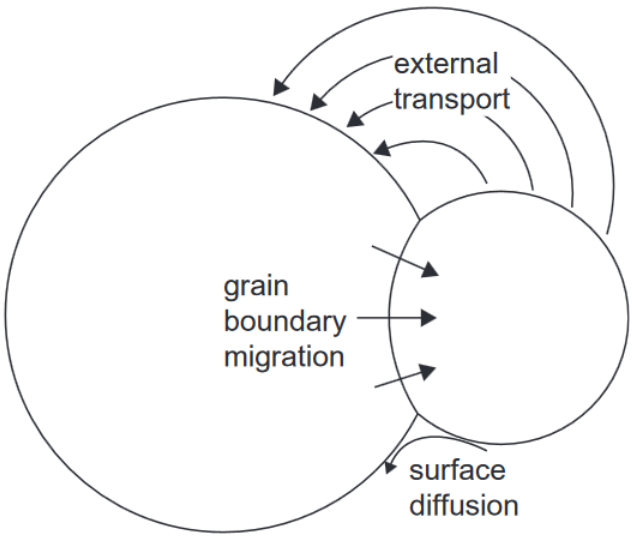

Figure 2.3: Diffusion controlled grain growth. [4]

higher green density also hinders grain growth [6]. Regarding grain properties, higher specific interfacial energies or higher diffusivities increase grain growth. Moreover, two grains in contact with low crystallographic misorientation are more likely to boost grain growth by coalescence (removal of the grain boundary) [4]. The effect of the secondary phase depends on its solubility [7], for instance MgO inhibits while FeO enhance grain growth in pure alumina [8]. Therefore, in real conditions more complex scenarios than those shown in Fig. 2.3 can appear modifying the grain growth mechanism or its rate. They include: pore drag, pore separation, solute drag, pore growth and complexion transitions [9].

During sintering, for a wide variety of conditions and powders, it is observed that grain size distribution is self-similar. It means that the grain size distribution normalized by the grain size is not significantly modified along time. When this self-similar behavior is observed, it is denominated normal grain growth [10]. On the other hand, abnormal grain growth arises when a few grains grow significantly at the expense of others. Usually, abnormal grain growth is caused by a non-uniformity of the microstructure, for instance: anisotropic grain boundary energy or mobility, impurity segregation or the existence of few large grains at the onset of sintering [7].

It is important to note that the analysis described for consolidation/densification and grain growth assumes that the diffusion of atoms is the rate-limiting step. But as pointed by Bordia et al. [11], recent works show that in some cases, kinetics can be governed by the interface reaction (detachment from the source) of transport atoms instead of the diffusion.

The mechanisms and models of grain growth will be explored in more details in

Chapter 3.

2.1.1.3 The different stages of sintering

As discussed above, consolidation, densification and grain growth have different driving forces and mechanisms, thus sintering proceeds in several stages. Generally, the sintering process can be divided in three main stages according to pore geometry. Fig. 2.4 shows the three stages for the sintering of initially spherical grains.

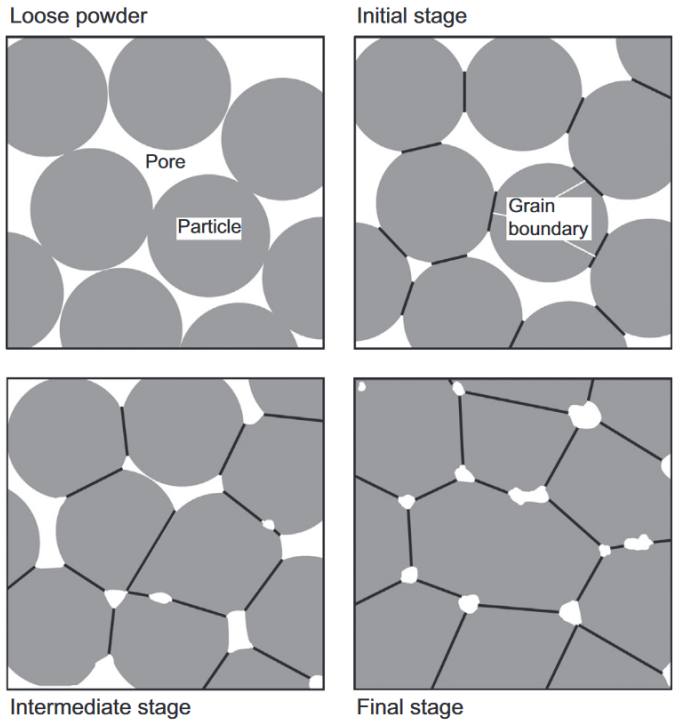

Figure 2.4: Schematic of the four sintering stages of initially spherical grains. [4]

In the initial stage, necks are formed between adjacent grains. They grow (consolidation) rapidly, decreasing the curvature gradient. This stage ends when the curvature between two adjacent grain boundaries is almost uniform [1] and the pores become nearly cylindrical. The densification is limited, up to a relative density of about 66%, and grain growth is negligible [4].

At this point, there is a network of interconnected pores, i.e., open porosity. During the intermediate stage, the open porosity will be gradually eliminated, resulting in a considerable densification (up to about 90%) and closed porosity. The neck growth of a contact stops when the decrease in surface energy is lower than the increase of grain boundary energy [5]. This initiates the growth of the grain, which emerges slowly in this intermediate stage.

Finally, the closed pores are eliminated by diffusion from grain-boundaries and from the core of the grain. Here the grain growth is considerable. The evolution at this final

stage is controlled by the interaction between pore and grain boundary [11].

2.1.2 Models

For clarity, we classify sintering models according to a characteristic length scale: atomistic, grain and component (continuum). Grain-scale models are discussed in more detail as they are central to this thesis.

2.1.2.1 Atomistic scale

The most detailed description of sintering can be obtained when modeling at the atomistic scale. Molecular dynamics (MD) is the most common method for this task. By simulating hundreds or thousands of atoms per grain, it allows to elucidate the sintering mechanisms at play. For example, surface diffusion, grain boundary migration and viscous flow mechanisms were detected by calculating the mean square displacement of atoms and analyzing their displacement vector for nickel particles [12]. For iron grains, the following mechanisms have been identified: surface and grain boundary diffusion, viscous flow and plastic deformation [13].

In MD, the interaction between a pair of atoms is defined by a potential. For illustration, a basic 2D Lennard-Jones potential U for a distance r between two atoms is [14]:

$$U(r) = 4\epsilon \left[\left(\frac{\sigma}{r} \right)^{12} - \left(\frac{\sigma}{r} \right)^{6} \right] \tag{2.3}$$

where ϵ is the depth of the potential in energy units and σ is the length range. In the literature, more accurate potentials have been proposed. For instance, Roy et al. [15] compare several atomic potentials for alumina, which, as an oxide material, requires the inclusion of long-range effects. Most of the MD models for sintering are dedicated to metals, however some works also focuses on ceramics [15]–[19].

Molecular dynamics allows to study the influence of the orientation of the crystal structure [20]–[22]. Arcidiacono et al. [23] observed that misoriented grains have a smaller neck size at the beginning of sintering, but later it can be slightly larger than well oriented grains. Moreover, the misaligned grains can rotate and remove the grain boundary [14]. These authors performed simulations for three grains (Fig. 2.5), reporting on grain growth as compared to those obtained at the particle scale (see Chapter 4).

The effect of the sintering temperature has also been analyzed. Jiang et al. [24] obtained a linear dependence between the grain size and the temperature at which the neck starts to form. Liu et al. [25] studied the effect of the heating rate. Also

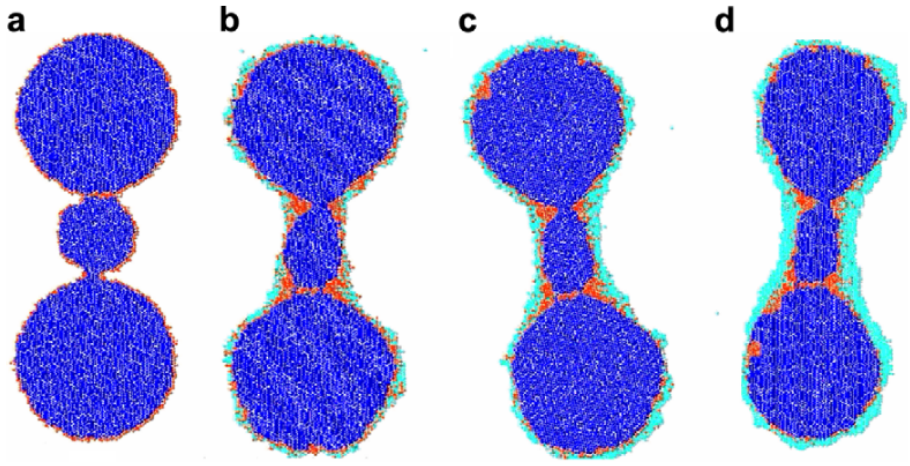

Figure 2.5: Evolution three nanograins simulated by MD. [14]

they found by MD simulations that some organic coating can delay the sintering of aluminum nanoparticles.

Due to their high computational cost, MD simulations are normally carried out for two nanoparticles. For the first time, four particles and periodic boundary conditions has been included in [26]. Another general limitation of MD simulations is that the timescale is of the order of picoseconds or nanoseconds of real time.

2.1.2.2 Grain scale

Analytical

Historically the analytical methods at the grain scale were the first class of methods to be proposed for sintering. The basic idea was to represent grains with a simplified geometry and limit the study to the interaction between two equal-sized grains. It was assumed that those two grains represent in average the whole packing. The main developments were proposed by Kuczynski [27], Herring [28], Kingery and Berg [29], Coble [30], [31], Johnson [32], Ashby [3], [33] and Coblenz [34]. Because of the differences commented above along sintering, different models are proposed for each stage of sintering.

For the initial stage, Coble proposed a two-sphere approximation of the grains for both densifying and non-densifying mechanisms as shown in Fig. 2.6. This geometrical assumption results in the well-known relation between the indentation h and the neck radius a for densifying mechanisms:

$$a^2 = 2Rh. \tag{2.4}$$

where R is the particle radius.

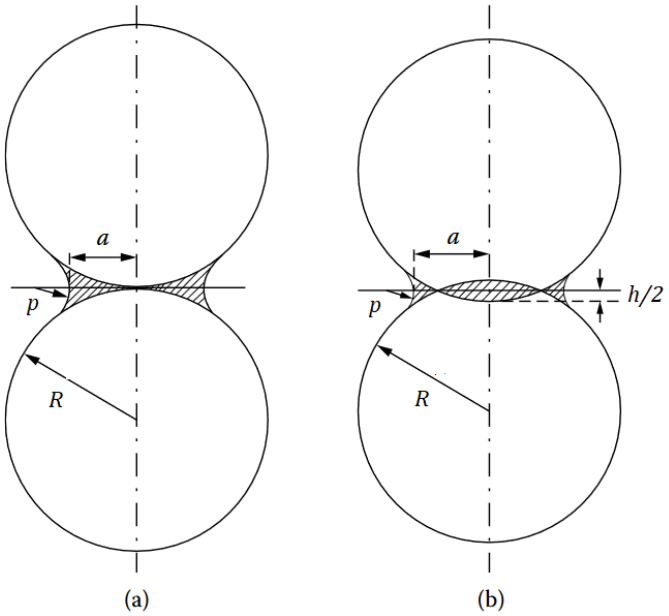

Figure 2.6: Assumed geometry for initial stage of sintering. (a) For nondensifying mechanisms and (b) for densifying mechanisms [2].

Applying diffusive fluxes between the two grains, kinetic equations are developed both for the neck size and the indentation. Here, the expressions developed by Coblenz: [34], as a correction of the original Coble results, are presented. These equations are obtained when grain boundary diffusion is the controlling mechanism:

$$\left(\frac{a}{R}\right)^6 = 192\frac{t}{\tau_g} \tag{2.5}$$

$$\left(\frac{h}{R}\right)^3 = 3\frac{t}{\tau_g} \tag{2.6}$$

where $\tau_g = \frac{k_b T R^4}{\delta_{GB} D_{GB} \Omega \gamma_S}$ is an important characteristic time that introduces the Boltzmann constant k_b, the temperature T, the grain boundary thickness δ_{GB}, the grain boundary diffusivity D_{GB}, the atomic volume Ω and the surface energy γ_S.

As summed up by Rahaman [2], a general expression for consolidation and shrinkage during the first stage can be written as:

$$\left(\frac{a}{R}\right)^n = \frac{K}{R^{n-m}}t \tag{2.7}$$

$$\left(\frac{h}{R}\right)^{n/2} = -\frac{K}{2^n R^{n-m}}t \tag{2.8}$$

where m and n depend on the sintering mechanism and K is a function of the geometrical and material parameters of the powder and of the sintering temperature. The

above equations simply point to some basic aspects of sintering: the importance of temperature (via the diffusivity), and of grain size in the kinetics of sintering.

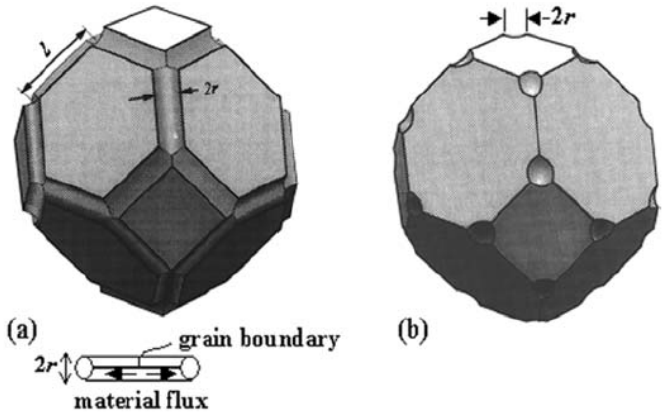

Figure 2.7: Coble's geometry for (a) intermediate stage and (b) for final stage [35].

For intermediate stage, Coble [31] proposed a tetrakaidecahedral shape to emulate the consolidated grains and cylinders on its edges. This is to account for the open porosity as shown in the Fig. 2.7a. While for the final stage, the closed porosity is represented as spheres on the corners of the tetrakaidecahedral (Fig. 2.7b). The rate of porosity change can be calculated and consequently the relative density rate ($\mathrm{d}D/\mathrm{d}t$). Eq. (2.9) shows a general density rate expression [35]:

$$\frac{1}{D}\frac{\mathrm{d}D}{\mathrm{d}t} = K_1 \frac{(1-D)^k}{G^m D} \tag{2.9}$$

where K_1 depends on the material parameters and G is the grain size. The densification rate depends on the grain size and hence is influenced by grain growth.

Regarding grain growth, the first theoretical analyses were developed in the absence of pores by Mullins [36] and Hillert [10]. Later, several studies deduced expressions for different mechanisms of grain growth from the consideration of pores (see for instance Riedel and Svoboda [37]). A more recent study [38] proposes new analytical equations for mechanisms present in the solid-state sintering of ceramics. Eq. (2.10) shows a general grain growth rate at final stage sintering [35]:

$$\frac{1}{G}\frac{\mathrm{d}G}{\mathrm{d}t} = K_2 \frac{1}{G^n (1-D)^l} \tag{2.10}$$

where K_2 depends on the material parameters and l is an exponent dependent on the grain growth mechanism. This equation is valid when pores and grains are uniformly distributed and when there is no separation of pores from the grain boundary [11]. A more comprehensive review of analytical models can be found in [39].

Finite Difference Method

Instead of solving analytically the diffusive fluxes in fixed simple geometries, another solution is to use numerical tools in order to track the evolution of grain shape. One of the tools is the Finite Difference Method (FDM). Starting more than 50 years ago, researchers have used FDM to study the sintering between two initially spherical particles [40]–[45]. These particles change their curvature depending on the diffusive fluxes.

Bouvard and McMeeking [43] developed a FDM model for the deformation of the particle neck by grain boundary diffusion, surface diffusion and an additional stress (tensile or compressive) acting on the junction. They analyzed the influence of the dihedral angle and of the diffusivities ratio $\xi = \delta_{GB}D_{GB}/\delta_S D_S$, where δ_{GB} is the grain boundary thickness and δ_S the thickness of the surface diffusion layer. The numerical results were fitted to an expression that takes the form of the Coblenz Eqs. (2.5) and (2.6). The resulting formula relates the shrinkage rate with the neck size and the neck stress:

$$\frac{\mathrm{d}h}{\mathrm{d}t} = \frac{\alpha\Delta_{GB}}{a^4}R\gamma_S - \frac{\beta\Delta_{GB}}{a^2}\sigma \tag{2.11}$$

where $\Delta_{GB} = \frac{\Omega}{k_b T}D_{GB}\delta_{GB}$, σ the average stress on the neck and α, and β are parameters of the model. $\beta = 4$ while $\alpha = 4.5$ for $\xi = 2$, $\alpha = 3$ for $\xi = 0.2$ and $\alpha = 2.5$ for $\xi = 0.02$.

Later, Pan et al. [45] developed a FDM approach similar to the Bouvard and McMeeking, but generalizing the problem to particles of different sizes. Likewise, they fitted their results with the following equation:

$$\frac{\mathrm{d}h}{\mathrm{d}t} = 0.5\left(1 + \frac{r_s}{r_l}\right)\left(\frac{\alpha\Delta_{GB}}{a^4}r_l\gamma_S - \frac{\beta\Delta_{GB}}{a^2}\sigma\right) \tag{2.12}$$

where r_s and r_l are the radii of the small and large particles, respectively. Eqs. (2.11) and (2.12) are relevant as they give important information on the sintering between two particles for a large range of shrinkage. This information will be used in DEM (see Chapter 3). In particular, we will see that the introduction of an additional stress term σ (on top of the free sintering term), allows for the derivation of a normal force expression that is necessary in DEM simulations. The study of Pan et al. [45] also presents a fitted expression for geometrically relating the indentation h and the neck size a:

$$a^2 = \kappa\left[0.5\left(1 + \frac{r_s}{r_l}\right)\right]^{\zeta} r_l h \tag{2.13}$$

where $\kappa = 2.4$ and $\zeta = 1.5$ are fitted values. Unlike Coble equation (Eq. (2.4)), Eq. (2.13)) is valid for particles of different sizes. In many studies, Coble expression has been generalized to $a^2 = 4R_{eq}h$ using the equivalent radius $R_{eq} = r_s r_l/(r_s + r_l)$. However, adapted Coble equation underestimates a for the same h, this effect is higher

as the particle size ratio increases.

Finally, in a very recent FDM work, Weiner et al. [46] use non-spherical particles as starting geometry, that are defined by a first-order wave function. The considered mechanisms are grain boundary diffusion and surface diffusion. The simulations are carried out for two particles. In a subsequent study [47], the same authors use their model to compare results for spherical and non-spherical initial grains. They observed clear differences on the neck size but minor ones on the shrinkage.

Discrete Element Method

Two-particle systems are somewhat limited to account for the behaviors observed in real sintering packings. This is why, numerical methods able to work with packing of particles were employed to model sintering. One of these methods is the Discrete Element Method (DEM) initially developed by Cundall and Strack [48] to model the mechanical behavior of granular materials (geomaterials). An advantage of DEM is that it naturally accounts for the rearrangement of particles during sintering. Particle rearrangement is an important feature that characterizes particulate systems. It was observed experimentally by Petzow and Exner [49] on sintering copper particles arranged on a planar substrate. Since the end of the 90's, DEM has been used to study sintering at the particle scale for a large number of particles. The interaction among particles is transmitted by normal and tangent forces. A detailed description of DEM methodology is given in section 2.2.1. Here, we will limit the description of DEM to the sintering force laws that are used in the simulations.

The model of Parhami and McMeeking [50] is, to the best of our knowledge, the first DEM approach to study sintering by grain boundary and surface diffusion. However, for historical interest it is also worth noting the paper of Soppe et al. from Netherlands [51] who devised a program in 1994 for simulating dynamically the sintering of a 3D random packing of 450 particles that integrates grain boundary diffusion and lattice diffusion.

Unlike Cundall and Strack, the resolution of the mechanical equilibrium in [50] is carried out with an implicit static numerical approach. The model was used for a 3D simulation of 266 copper spheres. The expression for the magnitude of the normal force was derived from the work of Bouvard and McMeeking [43] using Coble's geometry [30]:

$$N = \frac{\pi a^4}{8\Delta_{GB}} \frac{\mathrm{d}h}{\mathrm{d}t} - \pi\gamma_S \left[4R \left(1 - \cos\frac{\psi}{2} \right) + a \sin\frac{\psi}{2} \right] \tag{2.14}$$

where ψ is the dihedral angle. The first term on the RHS is a viscous resistance to the particle relative motion, while the second term is the sintering attractive force.

Later, Martin et al. [52] used Eq. (2.14) in their DEM model but allowing new contacts or the loss of contacts thanks to an explicit numerical scheme. The DEM employed here is more similar to the classical Cundall and Strack method. The simulations were carried out for the first time for a large packing of 40 000 micronic copper particles during free sintering. The results were compared with experimental data. Almost in parallel, Henrich et al. [53] developed a DEM model for free and pressure-assisted sintering. They used an expression for normal force from [54] and [55] that is similar in its form to (2.14):

$$N = \frac{\pi a^4}{8\Delta_{GB}} \frac{\mathrm{d}h}{\mathrm{d}t} + \frac{\pi^{2/3} R \gamma_S}{3^{1/6} (1-\epsilon)^{2/3}} Y(\epsilon, \psi) \tag{2.15}$$

where $Y(\epsilon, \psi)$ is a polynomial function of the porosity ϵ and the dihedral angle ψ. They also analyzed the influence of mass upscaling; this concept is discussed in section 2.2.1.1. Another similar function for the normal force can be deduced directly from the Bouvard and McMeeking eq. (2.11):

$$N = \frac{\pi a^4}{8\Delta_{GB}} \frac{\mathrm{d}h}{\mathrm{d}t} - \frac{\alpha}{4} \pi R \gamma_S \tag{2.16}$$

The parameter α allows a direct influence of the surface diffusion mechanism.

While normal force accounts for consolidation and densification, Henrich et al. [53] and Martin et al. [56] attempted to elucidate the importance of a tangential force that opposes shear at the contact between particles. They observed that the tangential force impacts directly the rearrangement of particles and thus the densification rate and the propagation of cracks. A common expression for the magnitude of the tangential force during sintering is [54], [57]:

$$T = -\mu_v \frac{\pi a^2 R^2}{8\Delta_{GB}} \frac{\mathrm{d}\delta_t}{\mathrm{d}t} \tag{2.17}$$

where μ_v is a dimensionless viscous parameter. The tangential force is a viscous force that opposes the tangential component of the relative velocity at the contact $\frac{\mathrm{d}\delta_t}{\mathrm{d}t}$. The choice of the value of the dimensionless viscosity is not trivial, recently $\mu_v = 0.1$ [58] reported a good agreement with experiments for a simulation of densification and grain growth of alumina. But other studies [53], [56] have used different values (from 0.01 to 0.5).

The models of Martin et al. [52] and Henrich et al. [53] were the basis for most of the DEM subsequent studies. Eqs. (2.14), (2.15) or (2.16) or some generalizations have been widely used in the DEM literature [59]–[67]. A slight modification was proposed by Nosewicz et al. [63]. They added a viscoelastic component to the model (instead of the purely viscous model of [52], [53]) for the first term of the normal force. This

allows the possibility of using larger time steps. A very different approach is using Non-Smooth Discrete Element Method as in S. Martin et al. [68]. It introduces an implicit time integration and indentation among particles is not allowed. The authors reported a more accurate rearrangement calculation when comparing with smooth/traditional DEM owing to the fact that no mass upscaling is required with their approach.

Using DEM sintering models, the influence on sintering of the initial microstructure has been analyzed by studying the initial size distribution [60],[69], green density [70] and coordination number [71]. The microstructure evolution was studied in the presence of inclusions [72] [70], agglomerates [73] [70] and pore formers [70]. Likewise, the anisotropy observed during some sintering processes was investigated [59], [74], [75]. Pressure-assisted sintering has been also considered [53], [63]. The constrained sintering case was considered in some works [61], [76], [77]. The defect formation and evolution were also evaluated extensively [53], [56], [70], [77]–[79]. For example, Fig. 2.8 [77] shows a good agreement of the crack propagation between experiments and DEM simulations for the sintering of thin films with cylindrical cavity. DEM allowed to conclude that micro fractures existing before sintering can be the cause for the formation of macroscopic cracks, that evolve from the cavity during sintering. The sintering of composite powders was also modeled [72], [80]–[83]. Tomographic images were used to validate the results [80], [84] and to use as initial microstructure in DEM [74], [85]. DEM can also be used to calculate the mechanical properties of partially sintered bodies [86]–[89].

Generally, the sintering models are performed at isothermal conditions, Teixeira et al. [90] considered the heating ramp and also heat transfer among the particles. A model of thermal conductance for DEM was proposed recently [91]. A quite new interesting study [92] coupled DEM and FDM in the modelling of initial stage sintering. The idea was to solve the issue that the empirical eq. (2.11) was originally fitted for a fixed ratio ξ. But the ratio can change with temperature, so this new model can allow to perform more accurate DEM simulations of non-isothermal sintering.

Grain growth has not been well studied with DEM. Simple models with no realistic driven force was proposed in [52] and in [59]. A new realistic DEM grain growth model is proposed in Chapter 3. In addition, to the best of my knowledge, all the reviewed DEM models consider always sphere particles. A model for sintering of particles with initially arbitrary shape is proposed in chapter 5.

Phase-Field

Another class of models at the grain scale is the phase-field approach. This method has been widely used in literature for modeling sintering [93]–[110] of porous and poly-

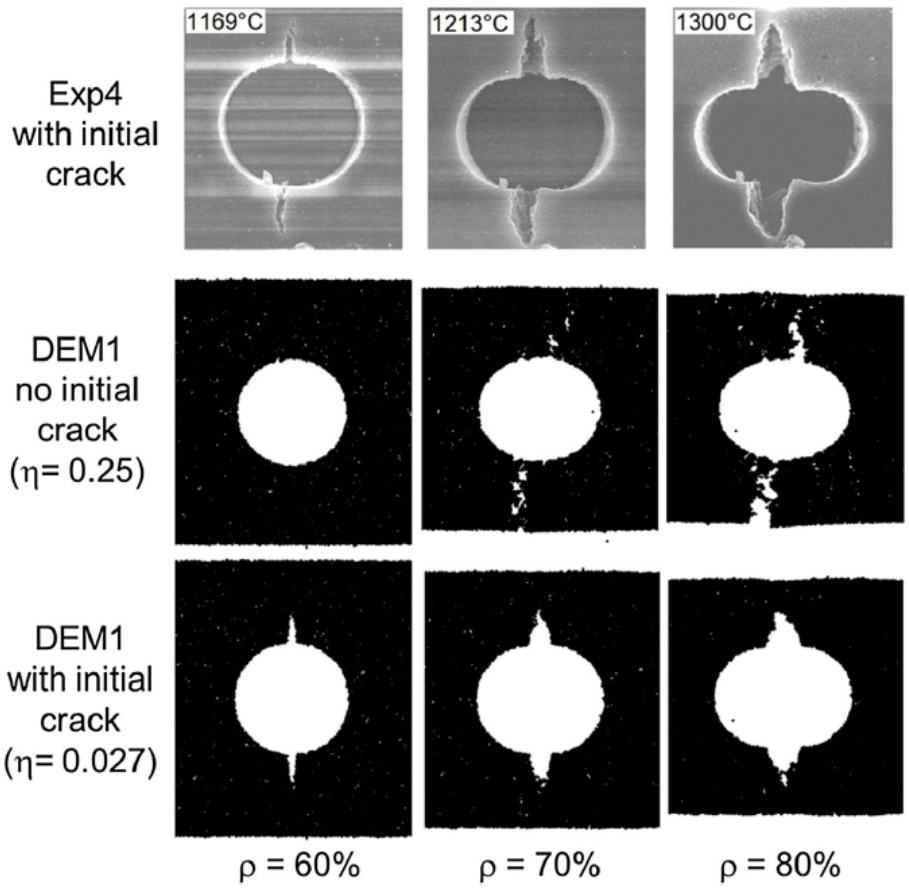

Figure 2.8: Crack propagation in experiments (top), DEM without initial crack (middle) and DEM with initial crack [77].

crystalline systems.

The method allows the motion of grain interfaces by reducing the total free energy driven by diffusion and structural relaxation [107]. In other words, the grains shape is not constrained to remain the same along time. Instead of re-meshing as in other methods, the phase-field uses fixed grid points and track implicitly the moving interfaces [106]. In order to account for the rigid-body motion, some authors include an advection term in the evolution equations. Also, there is a model that couples phase-field with DEM [111]. Some works also treat grain growth [100], [104], [106]. As the geometry evolution is very accurate, the computational time for phase-field is high. Therefore, many models were developed for a limited number of particles and restricted to 2D. Recently, Termuhlen et al. [106] developed a 3D phase-field simulation including rigid-body motion and grain growth. Using large computational resources, they were able to simulate up to 3 000 particles. Fig. 2.9 shows the microstructural evolution and shape change of a packing of particles (initially spherical). Recently, phase-field formulations for pressure-assisted sintering have also been proposed [104], [109]. For this end, the latter uses a fully coupled mechano-diffusional phase-field model.

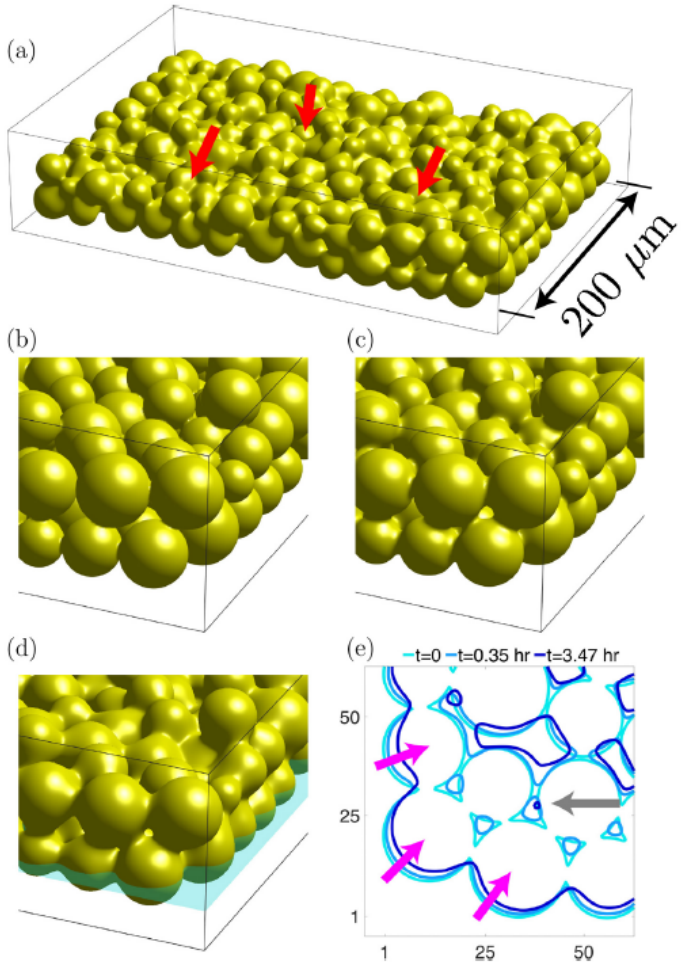

Figure 2.9: Sintering structure evolution from a phase-field simulation. [106]

Kinetic Monte Carlo

Kinetic Monte Carlo (kMC) is another common method for modeling sintering [112]–[124]. The microstructure is represented in a voxel grid, where each voxel can represent solid or void. As in other methods, the objective is to minimize the total interfacial free energy. It is calculated straightforwardly by the number of distinct neighbors for a given voxel. The microstructure evolution is dictated by a series of kMC processes. Each kMC process represents a physical process, such as: grain and pore growth, pore migration and vacancy annihilation and formation. Each process is randomly chosen in a random voxel. If the energy decreases, the process is directly accepted else the process is accepted with a given probability [123]. This description allows a complex variation of grains and pores shape. The simulations are performed in a non-dimensional framework. In order to obtain real values, it is necessary to find scale factors, for instance for: the time, grain growth and temperature [115]. There is one study on constrained sintering [119], while we did not find any kMC treating pressure assisted sintering.

Surface Evolver

Wakai and his colleagues have extensively used the surface evolver approach to simulate sintering [125]–[132]. Here, the particles are meshed and the velocity of the vertex depends on its curvature. The surface evolver can be classified as a Front Tracking Method with discretization. These authors have considered several mechanisms of diffusion: grain boundary, surface and evaporation-condensation. Grain growth [126] and recently rigid-body motion have been implemented [132]. The same method was also used for the simulation of nanoparticles [133]. The description of the diffusion processes is very accurate. Nevertheless, the high computational cost limits the simulations to only a few particles. Finally at the grain scale, Bruchon et al. [134] used the finite element method to study sintering by surface and lattice diffusion in 2D up to 82 grains.

Differences have been found when comparing models at the atomistic scale and at the grain scale. One cause can be the faceted nature of the nanocrystals against the smooth crystals assumed by analytical sintering theories [21]. In addition, Ding et al. [14] compared MD results with finite element simulations at the particle scale for two nanograins. They concluded that nano-powders can behave in many different scenarios that the FEM cannot detect. The first observation was that at the beginning of sintering, one particle can reorient causing the elimination of the grain boundary with a particle, while the grain boundary with another particle is preserved. This results in different rates and mechanisms for the growth of different necks. Another interesting scenario observed is the switch of the sintering mechanism along the process for a given neck.

2.1.2.3 Component scale

The methods discussed in previous sections are crucial for understanding the mechanisms of sintering. Nevertheless, it is useful for practical and industrial applications to have models at the scale of the real sintered parts. Commonly, the finite element method (FEM) is used for this task. An example is given in Fig. 2.10 [4] for the sintering of an inverted T part. The initial height was 30cm and after sintering the part was 19cm high. The predicted part is reasonable when comparing with the real sintered part.

This type of modeling is based on continuum mechanics and allows to study the influence of macroscopic factors on sintering. Basically, it calculates the response of a sintering part to a given general state of stress. The sintering body is modeled as a visco-plastic material [11]. A constitutive law relates the stress and the strain rate.

The continuum theory of sintering had its origin in the early 1970s. The idea was

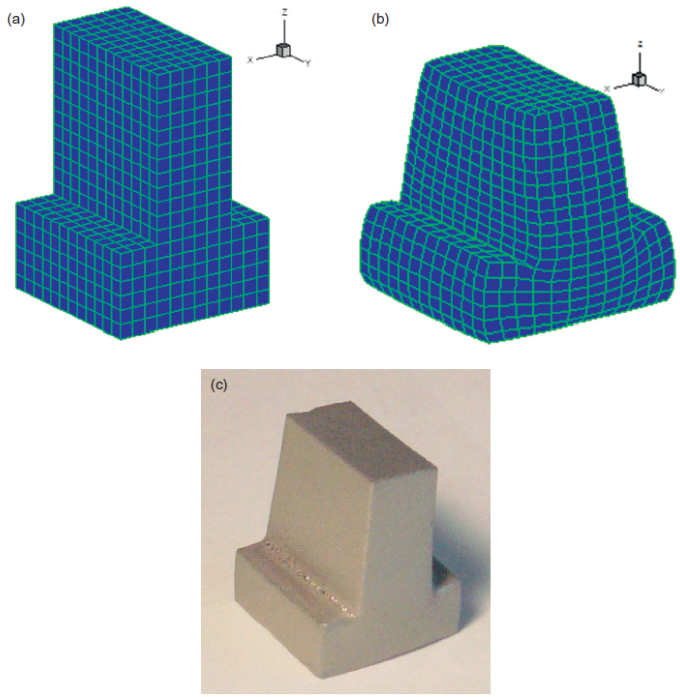

Figure 2.10: Finite element simulation of the sintering of an inverted T part. [4]

to treat the diffusion process in sintering as a creep process [135]. As reviewed by Bordia et al. [11], the most well-known model of continuum sintering was developed by Olevsky [136]. The isotropic constitutive law for linear viscous materials in the principal coordinate system is given by [11]:

$$\dot{\epsilon}_i = \dot{\epsilon}_f + \left(\frac{1}{E_p}\right)(\sigma_i - \nu_p\,(\sigma_j + \sigma_k)) \tag{2.18}$$

where the strain rate $\dot{\epsilon}_i$ is a function of the principal stresses $\sigma_i, \sigma_j, \sigma_k$. The free sintering rate $\dot{\epsilon}_f$ and the two constitutive parameters, i.e., the uniaxial viscosity E_p and the viscous Poisson's ratio ν_p, are needed. Depending on the complexity of the model, these parameters may be written as functions of the local relative density, of the grain size, pore size, size distributions, etc...

More recently, anisotropic laws were proposed [137], [138] to investigate the anisotropic shrinkage observed during the sintering of powders pre-compacted with uniaxial loading. They concluded that the pre-sintering cold compaction is the main cause for the anisotropy. The continuum theory of sintering has been applied to free sintering [139], [140], pressure-assisted sintering [141]–[143], constrained sintering [144], [145], composites [146]–[148], multilayers [149], [150] and reaction sintering [151]. One of the main challenges of this approach is to estimate the constitutive parameters. For isotropic conditions, these parameters can be obtained experimentally. For example, by using stairway heating cycles with samples of different green densities [140]. On

the other hand, this approach is challenging for estimating the anisotropic constitutive parameters. A prominent solution to this is the multi-scale simulation [11].

2.1.2.4 Multiscale

A more complete understanding of the sintering phenomena might be reached with a multiscale modeling. Two approaches are possible [11]: determine the parameters at a small scale for use in a simulation at a larger scale, or the large-scale simulation itself composed of small-scale simulators.

Regarding the first approach, Olevsky et al. [152] used a 2D kinetic Monte Carlo method to determine the constitutive parameters to be used in a 3D macroscopic finite element model of sintering. Their kMC simulations calculated the sintering stress and the bulk viscosity. Using a similar approach, Nosewicz and his team [153], [154] proposed a multiscale method with three levels. These authors used a Molecular Dynamics model to calculate the grain boundary diffusivity, that will be used in the discrete element method. Then, the DEM model was used to find the values of the viscous moduli, that is used in the continuum model.

Concerning the second approach, Maximenko et al. [155] and Molla et al. [156] proposed a finite element method composed of kMC mesoscale simulators. Fig. 2.11a) shows the schematic of how both scales are coupled. The microstructural evolution of the sintering of a bi-layer part is shown in Fig. 2.11b). Fig.2.11c) shows the stress on the final distorsed system. For future works, DEM could be used to calculated the anisotropic constitutive parameters that are needed for the continuum model. [11]

2.2 Discrete element methods

2.2.1 Classic discrete element method (DEM)

By classic discrete element method, we mean the discrete element method that uses spheres as discrete elements. This is in contrast with the level-sets method that can be used in conjunction with DEM and that will be described in section 2.2.2. Also, in the following sections, we will describe the DEM by describing general techniques from the literature. However, we often specialize this description to techniques used in the in-house code `dp3D` that will be involved in this work.

2.2.1.1 General description

The discrete or distinct element method (DEM) studies the dynamic interaction of individual particles. Cundall and Strack [48] proposed this method using the so-called

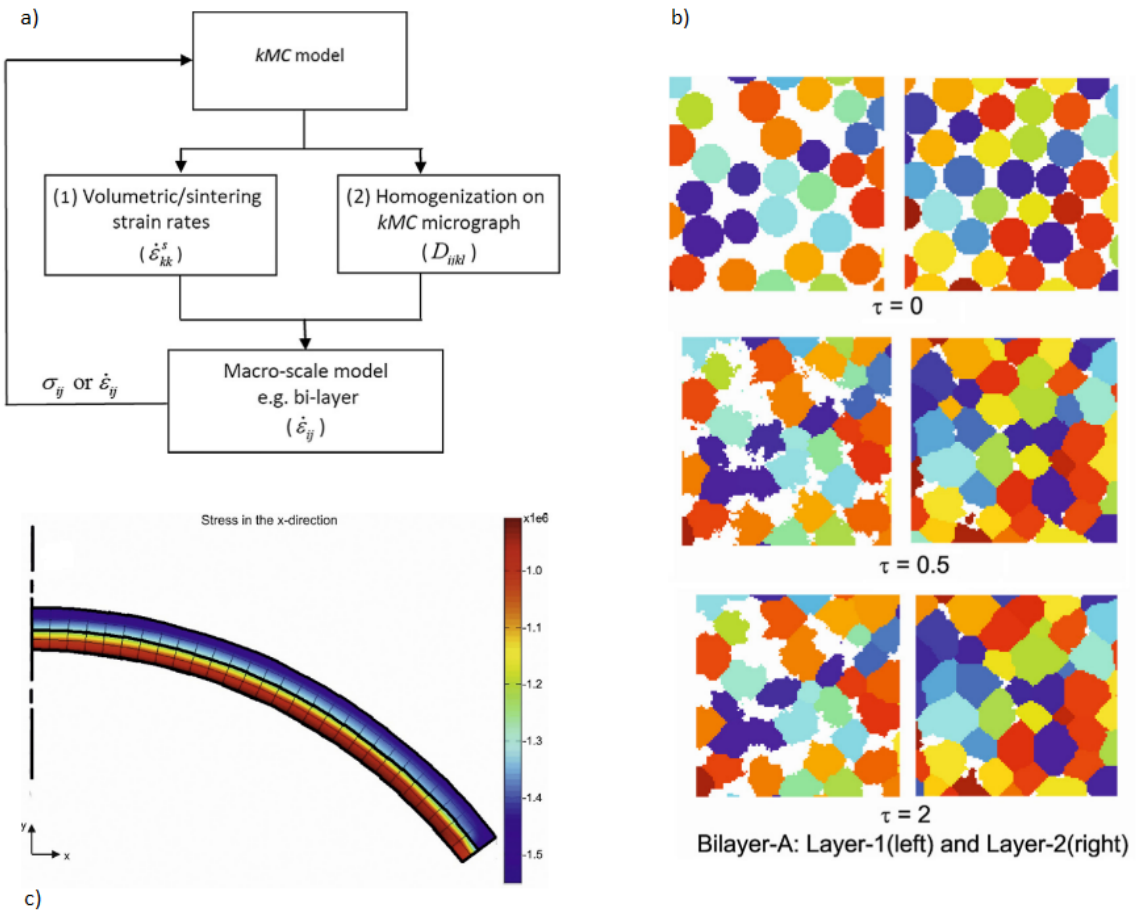

Figure 2.11: Multiscale simulation of the sintering of a bi-layer porous structure. [156]

soft-sphere approach [157]. In this approach, the particles are geometrical objects invariant in shape but that are allowed to overlap. This overlap models a possible deformation and it will determine the force magnitude. The translation and rotation of each particle is given by Newton's second law of motion. For simplicity, spherical particles are generally considered. The contact force is calculated for a pair of particles in contact and generally is considered independent of the presence of other neighboring contacts (pair interactions). The force between two particles i and j is decomposed in a tangential and normal components:

$$\vec{F_{ij}} = \vec{N_{ij}} + \vec{T_{ij}} \tag{2.19}$$

A sketch of two particles i and j in DEM is shown in Fig. 2.12. $\vec{l_{ij}}$ is the branch vector connecting the two particle centers $\vec{x_i}$ and $\vec{x_i}$, while h is the indentation.

The general expressions for the position $\vec{x_i}$ and the angular displacement $\vec{\theta_i}$ of any particle i with contact forces $\vec{F_{ij}}$ and external body force $\vec{F_{b,i}}$ (gravity, magnetic field,

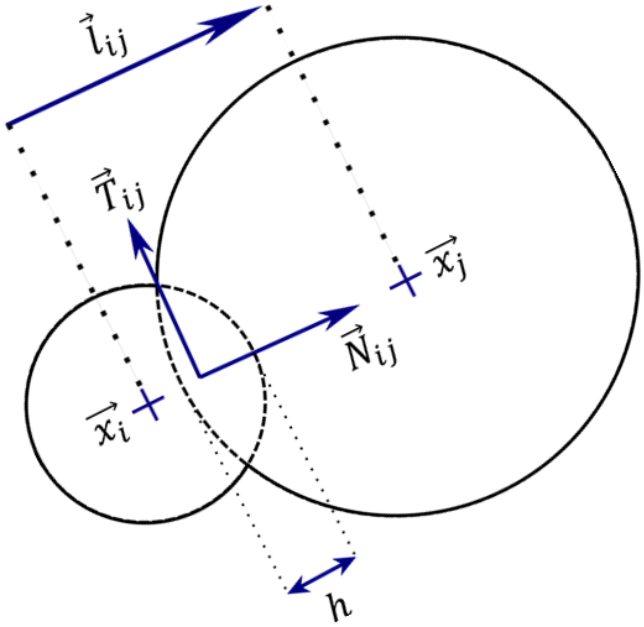

Figure 2.12: A general pair of particles in DEM.

etc.) are given by:

$$m_i \ddot{\vec{x}}_i = \sum \vec{F}_{ij} + \vec{F}_{b,i} \tag{2.20}$$

$$I_i \ddot{\vec{\theta}}_i = \sum \vec{M}_{ij} \tag{2.21}$$

where m_i and I_i are the particle mass and moment of inertia and $\vec{M}_{ij}$ the torque between two particles. The rotation equation takes this simple expression for 2D analysis or for spherical particles in 3D [158]. The simplicity of the equations allows to model millions of particles in many applications. From an initial state, the packing of particles will evolve iteratively depending on the phenomena described by the laws of the normal and tangent forces. At each time step, a sequence of operations is performed as showing in Fig. 2.13. The main steps are explained in the next sections.

2.2.1.2 Contact detection

One of the main tasks of a DEM code is to determine the list of contacts that need to be treated in Eq. (2.20). The detection is simply carried out by comparing the center-to-center distance to the sum of radii: the contact exists if $||\vec{x_i} - \vec{x_j}|| < r_i + r_j$, where $\vec{x}$ and r are the center position and the radius of a particle, respectively. The easiest implementation is to apply it at every time step for all the particle pairs. However, this crude implementation would result in a waste of CPU time.

It is possible to filter the pairs in order to search contacts only within nearby particles. Those form the so-called list of potential contacts or Verlet list. Because the

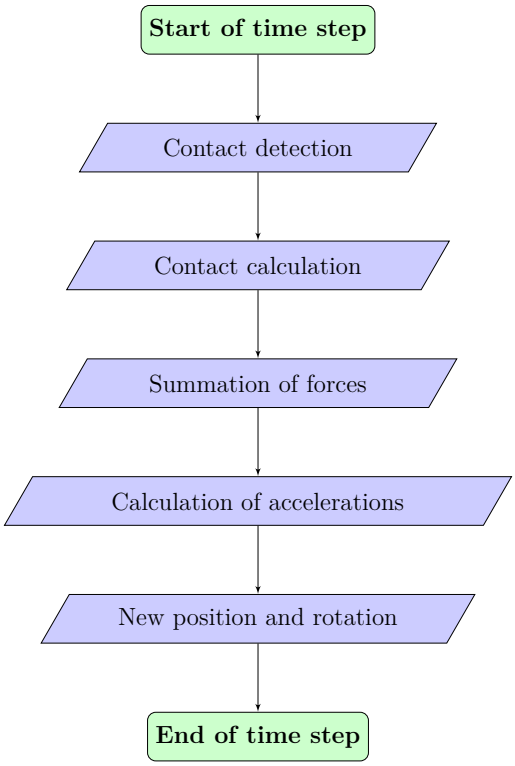

Figure 2.13: DEM main steps during one time iteration.

list includes potential contacts, it does not need to be actualized at each time step, thus saving CPU time. To include a contact in the list, the basic idea is to use the geometrical relation above, with the addition of a "radius" s. The condition is given by the following relation [159]:

$$||\vec{x_i} - \vec{x_j}|| < r_i + r_j + s \tag{2.22}$$

where s is called the Verlet parameter. It may also take an alternative but similar form:

$$||\vec{x_i} - \vec{x_j}|| < \alpha\,(r_i + r_j) \tag{2.23}$$

where $\alpha > 1$. The number of time steps for which the Verlet list remains valid (N_{verlet}) can be estimated conservatively based on the Verlet parameter s and assuming a constant time step and a maximum particle velocity v_{max} [159]:

$$N_{verlet} = \frac{s}{2v_{max}\Delta t} \tag{2.24}$$

or if using Eq. 2.23:

$$N_{verlet} = (\alpha - 1)\,\frac{2r_{min}}{v_{max}\Delta t} \tag{2.25}$$

where r_{min} is the minimum particle radius in the packing.

The above method can be complemented by the linked-cell method [160] to build the list of potential contacts. The method creates a uniform grid with a cell size equal to the diameter of the largest particle in the packing. The list is built by considering only the discrete objects in the same cell and in the surrounding cells.

The linked-cell method is not effective for packings with a large size distribution, which is the case of our sintering powders. Building a hierarchical grid with different cell sizes is a class of methods to address spheres with dispersed size. Ogarko and Luding [161] proposed a fast hierarchical contact detection method. The algorithm has two stages: a mapping phase followed by a contact detection phase. In the first stage, L uniform grids are created, each one with independent different cell size. The levels are ordered from the smallest to the largest cell size. For every particle, the lower level that has a cell size equal or greater than the particles size is called its level of insertion. An advantage of this algorithm is that the authors proposed an optimal way for estimating the number of levels L and the cell size of each level depending on the size distribution of the packing. The main idea is to keep constant the number of particles per cell for all the levels. A detailed explanation can be found in [162].

In the second stage, there are two main steps. First, the contact detection is performed for particles in the same level, where the linked-cell method can be used. Then, the search is performed between different levels (cross-level search) as sketched in Fig. 2.14. The figure shows a bimodal packing with two grid levels, each one with cell size equal to the size of its corresponding particle. The cross-level search is performed between a given particle and lower levels. In the example, a search for potential contacts among the large particle B and the small particles A is carried out. Based on the size of the particle B and on the cell size of its level of insertion, a search region is built around it (gray box in Fig.2.14). Finally, the contact is tested among the particle B and particles A that have their centers inside the search region. Those particles A are shown in green.

2.2.1.3 Contact calculation

Once the contacts have been detected, the total force at each contact is calculated. The nature of the force law depends on the physics of the contact. Some possibilities are: elasticity, plasticity, elasticity with adhesion, bonding, fracture, sintering, where the latter is the focus of this work. The force at each contact has a normal and a tangential component (Eq. (2.19)). The normal component $\vec{N}_{ij}$ direction is given by the vector $\frac{\vec{x_i}-\vec{x_j}}{||\vec{x_i}-\vec{x_j}||}$. The amplitude of the normal component depends mainly on the indentation that is calculated in the contact detection stage.

The tangential component that represents frictional forces can simply be modeled

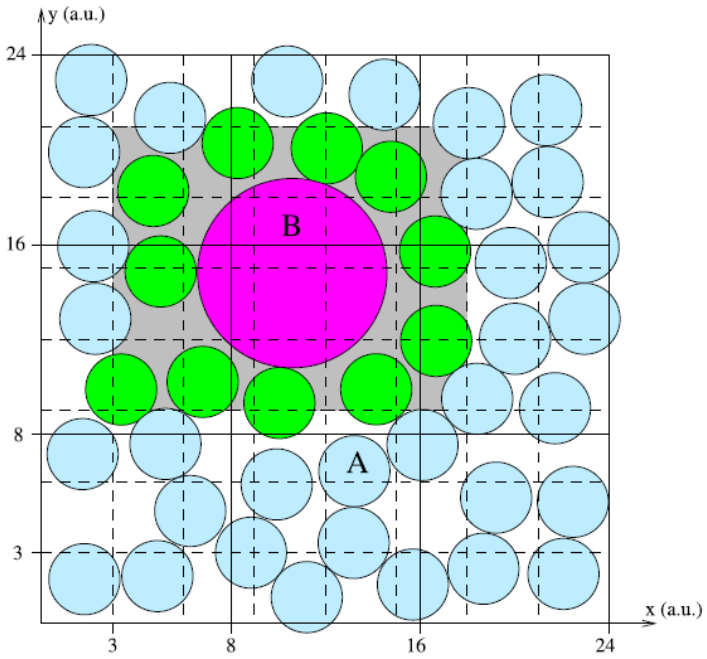

Figure 2.14: Multilevel contact detection. [161]

through a Coulomb law. Its direction may oppose the relative shear velocity of the two particles or may depend on the total displacement integrated from the initial contact [163], [164].

2.2.1.4 Time integration

In order to know the new position and rotation of each particle, it is necessary to integrate equations (2.20)-(2.21) with respect to time. The integration in the DEM soft-sphere approach is performed numerically using an explicit scheme. Mainly three classes of numerical schemes are used: one-step, multi-step and predictor-corrector. The velocity Verlet algorithm described hereafter is a one-step algorithm commonly used in DEM. A description and comparison of the different integration schemes can be found in [165].

The velocity Verlet algorithm is a central difference scheme that has been used since the proposition of DEM by Cundall and Strack [48]. A common implementation of this method is detailed below for a particle i at each time step:

1. The velocity is calculated at the half step:
   $\vec{x_i}\left(t+\frac{1}{2}\Delta t\right) = \vec{x_i}(t) + \frac{1}{2}\vec{\ddot{x}_i}(t)\,\Delta t$

2. The new position is calculated using the velocity calculated in step 1:
   $\vec{x_i}(t+\Delta t) = \vec{x_i}(t) + \vec{x_i}\left(t+\frac{1}{2}\Delta t\right)\Delta t$

3. The new acceleration $\vec{\ddot{x}_i}(t+\Delta t)$ is calculated using the second law of Newton

4. The new velocity is calculated using the new acceleration and the velocity at the half-step:
$\vec{\dot{x}_i}\left(t+\Delta t\right)=\vec{\dot{x}_i}\left(t+\frac{1}{2}\Delta t\right)+\frac{1}{2}\vec{\ddot{x}_i}\left(t+\Delta t\right)\Delta t.$

2.2.1.5 Quasi-static analysis and time step calculation

A special case of dynamic systems is the quasi-static regime, that occurs when the system evolves as a series of equilibrium states. The inertia number I_N is a very useful parameter to identify if the system is quasi-static and is given by [166]:

$$I_N=\dot{\epsilon}\sqrt{\frac{m}{PG}} \tag{2.26}$$

where $\dot{\epsilon}$ is a characteristic strain rate, m the mass of the particle, P the confinement pressure and G the particle size. This dimensionless number represents the ratio of two time scales: the inertial time over the shear time. In a quasi-static system, the inertial effects can be neglected, that is, when the inertial number is small. This definition is quite important in the DEM context as the timestep in quasi-static simulations can be significantly increased. To give an example, let's consider a two-mass spring system, the critical time step to ensure numerical stability is [63]:

$$\Delta t_c=\sqrt{2}\sqrt{\frac{m}{k_n}} \tag{2.27}$$

where k_n is the contact stiffness. In practice, for a DEM simulation a safety factor f_t of the order of 0.01 to 0.1 is used to determine the timestep: $\Delta t=f_t\sqrt{\frac{m}{k_n}}$. In quasi-static simulations, the time step can be increased (gain in CPU time) by increasing artificially the mass (the so-called mass upscaling) without consequences in the result if I_N is small enough (typically $I_N<10^{-3}$).

An alternative to the inertia number, which is useful when the macroscopic pressure P is very small (typically the case of sintering) is the normalized kinetic energy, defined as [167]:

$$\tilde{E}_c=\frac{E_c}{n\max\left(NR\right)} \tag{2.28}$$

where E_c is the kinetic energy of the packing (taking into account translation and rotation), $\max\left(NR\right)$ is the maximum of the product of contact force and particle radius in the packing, and n is the number of particles in the packing. Agnolin and Roux propose that $\tilde{E}_c=1.E^{-08}-1.E^{-07}$ is a good range of values for ensuring quasi-static conditions.

2.2.1.6 Boundary conditions

The most direct representation of boundary conditions in the simulation domain is to include the walls or free surfaces present in the real experiment. On the other hand, in most cases, it is not computationally feasible to run the same number of particles as in the experiment. In those cases, it is more effective to use a representative volume of particles with periodic boundary conditions as sketched in Fig. 2.15 for a periodic box of length L.

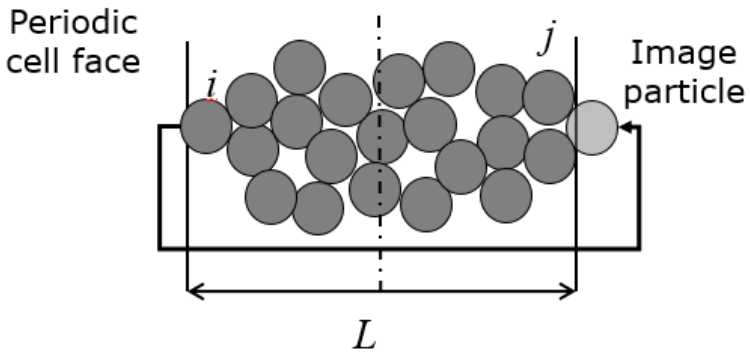

Figure 2.15: Periodic conditions. Particle i is in contact with particle j through the periodicity.

2.2.1.7 Stress calculation

The macroscopic stress tensor on the packing Σ_{pq} can be calculated using the Love's formula (originally derived by Dantu) [168], [169]:

$$\Sigma_{pq} = \frac{1}{V} \sum_{1}^{contacts} (N n_p + T t_p)\, l_{ij,q} \tag{2.29}$$

where V is the volume of the periodic simulation box (or of the volume of consideration for the contact summation), n_p and t_p the p^{th} component of the normal and the tangential vector and $l_{ij,q}$ is the q^{th} component of the branch vector between particles i and j.

2.2.1.8 DEM simulation of sintering in `dp3D`

The above sections have briefly described the main necessary ingredients of a DEM simulation. In this section, we describe the special features of DEM simulations for sintering. In particular, we describe the methodology employed for sintering in the in-house code `dp3D`, which is used all along this work. Sintering can be considered as a quasi-static process, with negligible inertia effects.

For free sintering, the macroscopic stress on the packing of particles should be close to zero. A characteristic stress in sintering is the so-called sintering stress: $\frac{\gamma_s}{R}$, where γ_s is the surface energy ($\mathrm{J.m^{-2}}$), and R is a characteristic length (the radius of the spherical particles). In `dp3D`, a very small compressive macroscopic pressure is sought for to ensure numerical stability. This compressive macroscopic pressure is set to $P_0 = 0.004 \times \frac{\gamma_s}{R}$. At each timestep, the three principal stresses computed by Eq. (2.29) are compared to P_0. Using a scheme similar to the one proposed in [53], the error between the sought stress and the actual stress is used to compute the macroscopic strain-rate $\dot{\epsilon}_{pp}$ to be applied to the periodic box at the next time step in the direction p:

$$\dot{\epsilon}_{pp}\left(t+\Delta t\right) = \dot{\epsilon}_{pp}\left(t\right) + \frac{\Sigma_{pp} - P_0}{P_0}\frac{\Delta t}{\eta} \tag{2.30}$$

where η is an empirical numerical constant. With this scheme, the pressure P_0 is obtained after a few thousand time steps.

Following the methodology proposed by Thornton and Antony [170], the centers of all spheres in the periodic box move at the start of the timestep according to the macroscopic strain-rate calculated from Eq. (2.30). This is the so-called affine solution as though they are points in a continuum:

$$\Delta x_p = \dot{\epsilon}_{pp} x_p \Delta t \tag{2.31}$$

Once this affine displacement is imposed, contacts are sought for, and the Verlet algorithm is applied to obtain an additional Δx_p for all particles to approach the quasi-static equilibrium (Fig. 2.13).

The time step for sintering is not obtained as in elasticity through Eq. (2.27). Instead, it is simply given by:

$$\Delta t = \frac{\epsilon_{max}}{\max\left(\dot{\epsilon}_i\right)} \tag{2.32}$$

where ϵ_{max} is the maximum characteristic indentation (set to 10^{-5}) that is permitted during a time step to ensure stability in the velocity Verlet algorithm. With this scheme, the time step may gradually increase as the densification rate decreases upon sintering. This time step may be reduced if the error $\frac{\Sigma_{ii} - P_0}{P_0}$ becomes too large.

2.2.2 Level-set discrete element method (LS-DEM)

Here the original LS-DEM method proposed by Kawamoto et al. [171] is described. Some improvements proposed in this work or by other authors in the literature are detailed in Chapter 5. The general methodology originally proposed by the team of Prof. Andrade (in collaboration with laboratory 3SR at Univ. Grenoble Alpes) has

been used to study triaxial tests with an initial packing configuration that originates from X-ray tomography images [171], predicting shear banding [172], investigating the effect of brittle breakage of particles [173], and the effect of particle bonding [174]. All these studies focused on granular materials for geomechanics applications.

2.2.2.1 General description

The LS-DEM combines the dynamic behavior of particles of the classical DEM and the shape description using the Level-Set method. The shape of particles can be arbitrary, but remains constant along the simulation. The level-set is a scalar function that computes the signed distance of a point to an interface. In our context, the interface is the particle surface. The level-set is zero for any point on the particle surface, negative inside the particle and positive outside the particle. More detailed information on the concepts of Level-Sets and its use in other domains can be found in [175], [176].

A Cartesian local uniform grid is built around each particle with grid size Δl in all direction. The first step is to assess the level-set values at the grid points as shown in Fig. 2.16a. The level-set can be computed analytically from the equation of a 3D shape or obtained from tomography images of a packing of particles. The latter is one of the main advantages of LS-DEM, as it allows to use real arbitrary particle shapes. In that case, it only needs a distance field in order to describe the shape of particles.

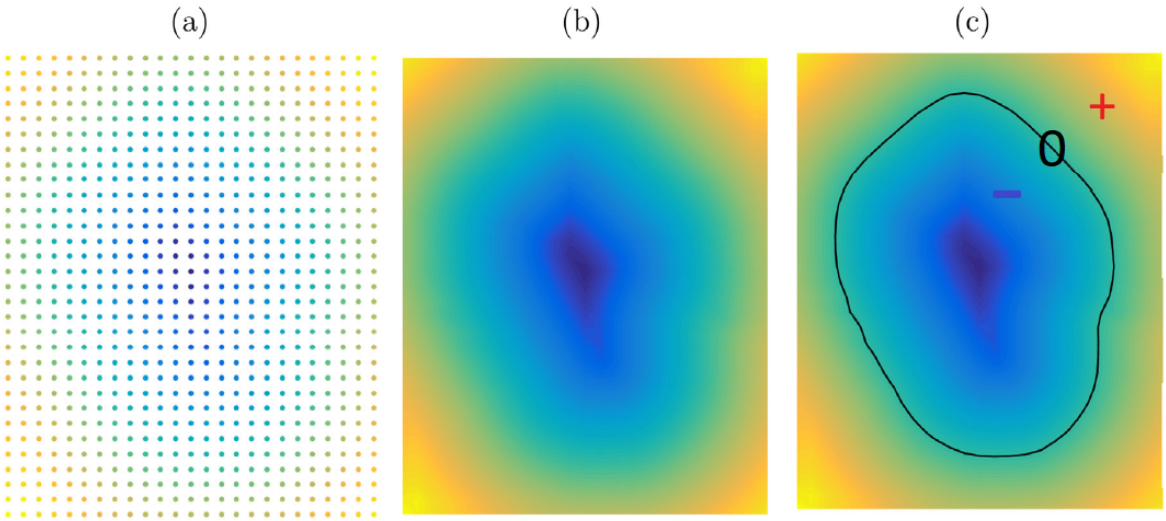

Figure 2.16: Level-set calculation. Adapted from [171].

It is necessary to know the level-set value $\phi(p)$ at any point $p\,(x, y, z)$ inside or around the particle. A trilinear interpolation is used based on the known level-set

values ϕ_{abc} of grid points around the point p:

$$\phi(p) = \sum_{a=0}^{1}\sum_{b=0}^{1}\sum_{c=0}^{1} \phi_{abc}\left[(1-a)(1-x)+ax\right]\left[(1-b)(1-y)+by\right]\left[(1-c)(1-z)+cz\right] \tag{2.33}$$

The parameters a, b, c can be 0 or 1, where the combination represents the 8 grid points around any point p. The interpolation allows to have the level-set values at any point around the particle (Fig. 2.16b). In practice, just a few points p are evaluated on-demand by the contact detection algorithm (see next section 2.2.2.2). If desired, the particle surface can be reconstructed by determining the points that fulfill the condition $\phi = 0$ (Fig. 2.16c). By differentiating Eq. (2.33), an expression for the gradient of the level-set $\nabla\phi(p)$ is obtained. It will be used in the contact detection stage as well.

As already commented, LS-DEM follows the same dynamic approach of DEM, which means that the DEM main stages showed in Fig. 2.13 are also applied here. Nevertheless, non-spherical particles make that different approaches are adopted mainly in the contact detection and contact calculation stages. This is shown in the next sections, as well as the calculation of inertial properties that must be adapted for arbitrary particle shapes.

2.2.2.2 Contact detection

The contact detection of arbitrary shape particles is more challenging and with higher computational cost than the one for spheres. The basic idea in LS-DEM is to create boundary nodes on the particle surface and check if any node is inside the other particle. Fig. 2.17 shows a general case of two particles that may or may not be in contact.

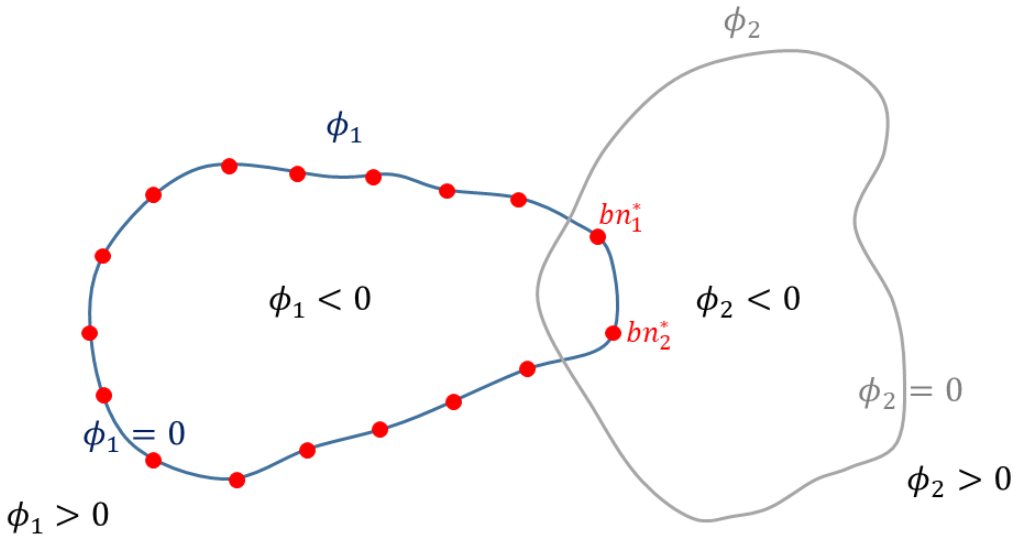

Figure 2.17: Contact detection in LS-DEM. Particle 1 is the master particle. It carries nodes that are used to check contact with slave particle 2.

The level-set values of each particle ϕ_1, ϕ_2 are already known inside the particle and in its surroundings. Uniform nodes (red dots in Fig. 2.17) are created on the surface of the so-called master particle (particle 1). The level set of the slave particle (2) is calculated at each boundary node of particle 1. If at least one of these nodes has a $\phi_2 < 0$ value, it means that the node of particle 1 is inside particle 2, i.e., there is contact. In figure 2.17, a contact is detected at two nodes (bn_1^*, bn_2^*) on particle 1 as they fulfill the condition $\phi_2 < 0$. For a pair of particles with a detected contact, the parameters of the contact are calculated as detailed in the next section.

2.2.2.3 Contact calculation

Unlike spheres in classical DEM, LS-DEM allows to have more than one contact point between a contact pair ij. The number of contact points depends on the number cp of boundary nodes of particle i inside the particle j. The indentation and the normal at the contact are calculated at each contact point. LS-DEM adopts a node-to-surface approach, i.e., the contact properties of the boundary nodes in i are calculated in relation to the surface of particle j. The indentation and the unit normal vector at a contact point (bn_i^p) on particle i are given respectively by:

$$h_{j,i}^p = \phi_j \left(bn_i^p\right) \tag{2.34}$$

$$\vec{n}_{j,i}^p = \frac{\nabla \phi_j \left(bn_i^p\right)}{||\nabla \phi_j \left(bn_i^p\right)||} \tag{2.35}$$

The contact calculation is thus relatively fast as it only requires the computation of level-set and gradient values.

The normal and tangential forces are calculated at each contact point with the same expressions as those used in classic DEM. Then the total force at the contact ij is obtained by summing the forces at every contact point between the two particles:

$$\vec{F_{ij}} = \sum_{p=1}^{cp} \left(\vec{N_{ij}^p} + \vec{T_{ij}^p}\right) \tag{2.36}$$

Different ways of computing this total force at the contact, such as taking the average or maximum indentation, are discussed and compared in [177].

2.2.2.4 Calculation of inertial properties

In order to calculate the new positions and rotations in DEM, the inertial particle properties (mass, moment of inertia and center of mass) are needed. The same applies for LS-DEM, however the calculation of these properties for arbitrary shape particles

is not as trivial and needs the local grid of each particle. All points of the grid are defined by a negative (inside the particle) or positive (outside) level-set function ϕ. A smoothed Heaviside function $H(\phi)$ of the level-set value may be defined as:

$$H(\phi) = \begin{cases} 0 & \text{if } \phi < -\epsilon_H \\ \frac{1}{2}\left(1 + \frac{\phi}{\epsilon_H} + \frac{sin\left(\frac{\pi\phi}{\epsilon_H}\right)}{\pi}\right) & \text{if } -\epsilon_H < \phi < \epsilon_H \\ 1 & \text{if } \phi > \epsilon_H \end{cases} \tag{2.37}$$

where ϵ_H is the Heaviside parameter that smooths the function near the surface of the particle. The Heaviside function $H(-\phi)$ may be seen as a weight function that equals 1 inside the particle and vanishes rapidly outside. The summation of this function for each point of the grid (x_i, y_j, z_k) is used for calculating all the necessary inertial properties. The particle mass is given by:

$$m = \rho\Delta l^3 \sum_{i=1}^{I}\sum_{j=1}^{J}\sum_{k=1}^{K} H(-\phi(x_i, y_j, z_k)) \tag{2.38}$$

where I,J,K are the number of grid points in each direction. Eq. (2.38) shows that m is proportional to the mass of a grid cell $\rho\Delta l^3$, where ρ is the particle density. Similarly, the center of mass is estimated by:

$$\begin{aligned} c_x &= \frac{\rho\Delta l^3}{m} \sum_{i=1}^{I}\sum_{j=1}^{J}\sum_{k=1}^{K} H(-\phi(x_i, y_j, z_k))x_i \\ c_y &= \frac{\rho\Delta l^3}{m} \sum_{i=1}^{I}\sum_{j=1}^{J}\sum_{k=1}^{K} H(-\phi(x_i, y_j, z_k))y_j \\ c_z &= \frac{\rho\Delta l^3}{m} \sum_{i=1}^{I}\sum_{j=1}^{J}\sum_{k=1}^{K} H(-\phi(x_i, y_j, z_k))z_k \end{aligned} \tag{2.39}$$

And the moment of inertia tensor is given by:

$$
\begin{aligned}
I_{11} &= \rho\Delta l^3 \sum_{i=1}^{I}\sum_{j=1}^{J}\sum_{k=1}^{K} H(-\phi(x_i, y_j, z_k)) \left[(y_j - c_y)^2 + (z_k - c_z)^2\right] \\
I_{22} &= \rho\Delta l^3 \sum_{i=1}^{I}\sum_{j=1}^{J}\sum_{k=1}^{K} H(-\phi(x_i, y_j, z_k)) \left[(x_i - c_x)^2 + (z_k - c_z)^2\right] \\
I_{33} &= \rho\Delta l^3 \sum_{i=1}^{I}\sum_{j=1}^{J}\sum_{k=1}^{K} H(-\phi(x_i, y_j, z_k)) \left[(x_i - c_x)^2 + (y_j - c_y)^2\right] \\
I_{12} &= I_{21} = -\rho\Delta l^3 \sum_{i=1}^{I}\sum_{j=1}^{J}\sum_{k=1}^{K} H(-\phi(x_i, y_j, z_k)) \left[(x_i - c_x)(y_j - c_y)\right] \\
I_{13} &= I_{31} = -\rho\Delta l^3 \sum_{i=1}^{I}\sum_{j=1}^{J}\sum_{k=1}^{K} H(-\phi(x_i, y_j, z_k)) \left[(x_i - c_x)(z_k - c_z)\right] \\
I_{23} &= I_{32} = -\rho\Delta l^3 \sum_{i=1}^{I}\sum_{j=1}^{J}\sum_{k=1}^{K} H(-\phi(x_i, y_j, z_k)) \left[(y_j - c_y)(z_k - c_z)\right]
\end{aligned}
\tag{2.40}
$$

2.3 Conclusion

Sintering is a high temperature manufacturing process, where consolidation, densification and grain growth interact. The investigation from the atomistic sintering mechanisms to the full sintered component is a multi-scale task. Efforts have been undertaken with a variety of numerical methods at different scales for modeling sintering. Among them, the discrete element method represents particles in a straightforward form, which allows the study of packings with large number of particles. It has been applied to investigate different sintering conditions. However, a realistic description of grain growth is lacking. A new realistic DEM model of sintering is presented in the next chapter (chapter 3). This will expand the grain growth scenarios that can be examined for large packings and that are difficult to tackle with theoretical models. Some of them are the influence of the size distribution, non-isothermal conditions, sintering of composites and constrained sintering. Another aspect that can be improved in DEM models is the description of the particle shape, which until now is spherical for sintering simulations. Mainly phase-field, surface evolver and finite difference methods have been used to describe in detail the evolution of particle shape during sintering. Kinetic Monte Carlo also stands out for the ability of allowing shape evolution considering different microstructural aspects. However, here the aim is to remain in the DEM framework to be able to simulate large packings and in a dimensional domain unlike kMC. The LS-DEM approach seems a prominent method as it captures arbitrary shape particles preserving the general methodology of DEM. Chapter 5 presents a LS-DEM model for sintering with an alternative contact detection scheme as compared to the original LS-DEM reviewed in the present chapter. Chapter 5 also reviews the context of LS-DEM and other methods in DEM for modeling non-spherical particles.

References

[1] J.-M. Missiaen, "Le frittage naturel," in *Métallurgie des poudres*, D. Bouvard, Ed., Paris: Hermes Science Publications, 2002, ch. 4, pp. 177–238.

[2] M. Rahaman, *Ceramic processing and sintering, second edition*. CRC Press, Jan. 2003, pp. 1–875. DOI: 10.1201/9781315274126.

[3] M. F. Ashby, "A first report on sintering diagrams," *Acta Metallurgica*, vol. 22, no. 3, pp. 275–289, 1974, ISSN: 00016160. DOI: 10.1016/0001-6160(74)90167-9.

[4] R. M. German, *Sintering: from Empirical Observations to Scientific Principles*. Boston: Butterworth-Heinemann, 2014, ISBN: 978-0-12-401682-8.

[5] F. F. Lange and B. J. Kellett, "Thermodynamics of Densification: II, Grain Growth in Porous Compacts and Relation to Densification," *Journal of the American Ceramic Society*, vol. 72, no. 5, pp. 735–741, 1989, ISSN: 15512916. DOI: 10.1111/j.1151-2916.1989.tb06209.x.

[6] Z. Z. Fang, H. Wang, and V. Kumar, "Coarsening, densification, and grain growth during sintering of nano-sized powders—A perspective," *International Journal of Refractory Metals and Hard Materials*, vol. 62, pp. 110–117, 2017, ISSN: 22133917. DOI: 10.1016/j.ijrmhm.2016.09.004.

[7] R. M. German, "Coarsening in sintering: Grain shape distribution, grain size distribution, and grain growth kinetics in solid-pore systems," *Critical Reviews in Solid State and Materials Sciences*, vol. 35, no. 4, pp. 263–305, 2010, ISSN: 10408436. DOI: 10.1080/10408436.2010.525197.

[8] J. Zhao and M. P. Harmer, "Sintering of Ultra-High-Purity Alumina Doped Simultaneously with MgO and FeO," *Journal of the American Ceramic Society*, vol. 70, no. 12, pp. 860–866, 1987, ISSN: 15512916. DOI: 10.1111/j.1151-2916.1987.tb04906.x.

[9] S. J. Dillon and M. P. Harmer, "Relating grain-boundary complexion to grain-boundary kinetics II: Silica-doped alumina," *Journal of the American Ceramic Society*, vol. 91, no. 7, pp. 2314–2320, 2008, ISSN: 00027820. DOI: 10.1111/j.1551-2916.2008.02432.x.

[10] M. Hillert, "On the theory of normal and abnormal grain growth," *Acta Metallurgica*, vol. 13, no. 3, pp. 227–238, 1965, ISSN: 00016160. DOI: 10.1016/0001-6160(65)90200-2.

[11] R. K. Bordia, S. J. L. Kang, and E. A. Olevsky, "Current understanding and future research directions at the onset of the next century of sintering science and technology," *Journal of the American Ceramic Society*, vol. 100, no. 6, pp. 2314–2352, 2017, ISSN: 15512916. DOI: 10.1111/jace.14919.

[12] Z. J. Liu, Q. Cheng, Y. Wang, Y. Li, and J. Zhang, "Sintering neck growth mechanism of Fe nanoparticles: A molecular dynamics simulation," *Chemical Engineering Science*, vol. 218, p. 115 583, 2020, ISSN: 00092509. DOI: 10.1016/j.ces.2020.115583.

[13] P. Song and D. Wen, "Molecular dynamics simulation of the sintering of metallic nanoparticles," *Journal of Nanoparticle Research*, vol. 12, no. 3, pp. 823–829, 2010, ISSN: 13880764. DOI: 10.1007/s11051-009-9718-7.

[14] L. Ding, R. L. Davidchack, and J. Pan, "A molecular dynamics study of sintering between nanoparticles," *Computational Materials Science*, vol. 45, no. 2, pp. 247–256, 2009, ISSN: 09270256. DOI: 10.1016/j.commatsci.2008.09.021.

[15] S. Roy, A. Prakash, and S. Sandfeld, "Sintering of Alumina Nanoparticles: Comparison of Interatomic Potentials, Molecular Dynamics Simulations, and Data Analysis," 2022.

[16] K. Tsuruta, A. Omeltchenko, R. K. Kalia, and P. Vashishta, "Early stages of sintering of silicon nitride nanoclusters: A molecular-dynamics study on parallel machines," *Europhysics Letters*, vol. 33, no. 6, pp. 441–446, 1996, ISSN: 02955075. DOI: 10.1209/epl/i1996-00359-2.

[17] S. Ogata, H. Iyetomi, K. Tsuruta, F. Shimojo, A. Nakano, R. K. Kalia, and P. Vashishta, "Role of atomic charge transfer on sintering of TiO2 nanoparticles: Variable-charge molecular dynamics," *Journal of Applied Physics*, vol. 88, no. 10, pp. 6011–6015, 2000, ISSN: 00218979. DOI: 10.1063/1.1321785.

[18] V. N. Koparde and P. T. Cummings, "Molecular dynamics simulation of titanium dioxide nanoparticle sintering," *Journal of Physical Chemistry B*, vol. 109, no. 51, pp. 24 280–24 287, 2005, ISSN: 15206106. DOI: 10.1021/jp054667p.

[19] B. Buesser, A. J. Grhn, and S. E. Pratsinis, "Sintering rate and mechanism of TiO2 nanoparticles by molecular dynamics," *Computational Molecular Science and Engineering Forum - Core Programming Topic at the 2011 AIChE Annual Meeting*, pp. 173–175, 2011.

[20] H. Zhu and R. S. Averback, "Sintering processes of two nanoparticles: A study by molecular dynamics simulations," *Philosophical Magazine Letters*, vol. 73, no. 1, pp. 27–33, 1996, ISSN: 13623036. DOI: 10.1080/095008396181073.

[21] L. J. Lewis, P. Jensen, and J. L. Barrat, "Melting, freezing, and coalescence of gold nanoclusters," *Physical Review B - Condensed Matter and Materials Physics*, vol. 56, no. 4, pp. 2248–2257, 1997, ISSN: 1550235X. DOI: 10.1103/PhysRevB.56.2248.

[22] E. Goudeli and S. E. Pratsinis, "Crystallinity Dynamics of Gold Nanoparticles During Sintering or Coalescence," *AIChE Journal*, vol. 62, no. 2, pp. 589–598, 2016, ISSN: 12350621. DOI: 10.1002/aic.

[23] S. Arcidiacono, N. R. Bieri, D. Poulikakos, and C. P. Grigoropoulos, "On the coalescence of gold nanoparticles," *International Journal of Multiphase Flow*, vol. 30, no. 7-8 SPEC. ISS. Pp. 979–994, 2004, ISSN: 03019322. DOI: 10.1016/j.ijmultiphaseflow.2004.03.006.

[24] J. Jiang, P. Chen, and W. Sun, "Monitoring micro-structural evolution during aluminum sintering and understanding the sintering mechanism of aluminum nanoparticles: A molecular dynamics study," *Journal of Materials Science and Technology*, vol. 57, pp. 92–100, 2020, ISSN: 10050302. DOI: 10.1016/j.jmst.2020.03.068.

[25] J. Liu, M. Wang, P. Liu, R. Sun, Y. Yang, and G. Zou, "Molecular dynamics study of sintering of Al nanoparticles with/without organic coatings," *Computational Materials Science*, vol. 190, no. December 2020, p. 110 265, 2021, ISSN: 09270256. DOI: 10.1016/j.commatsci.2020.110265.

[26] B. Cheng and A. H. Ngan, "The sintering and densification behaviour of many copper nanoparticles: A molecular dynamics study," *Computational Materials Science*, vol. 74, pp. 1–11, 2013, ISSN: 09270256. DOI: 10.1016/j.commatsci.2013.03.014.

[27] G. C. Kuczynski, "Study of the sintering of glass," *Journal of Applied Physics*, vol. 20, no. 12, pp. 1160–1163, 1949, ISSN: 00218979. DOI: 10.1063/1.1698291.

[28] C. Herring, "Diffusional viscosity of a polycrystalline solid," *Journal of Applied Physics*, vol. 21, no. 5, pp. 437–445, 1950, ISSN: 00218979. DOI: 10.1063/1.1699681.

[29] W. D. Kingery and M. Berg, "Study of the initial stages of sintering solids by viscous flow, evaporation-condensation, and self-diffusion," *Journal of Applied Physics*, vol. 26, no. 10, pp. 1205–1212, 1955, ISSN: 00218979. DOI: 10.1063/1.1721874.

[30] R. L. Coble, "Initial Sintering of Alumina and Hematite," *Journal of the American Ceramic Society*, vol. 41, no. 2, pp. 55–62, 1958.

[31] R. L. Coble, "Sintering crystalline solids. I. intermediate and final state diffusion models," *Journal of Applied Physics*, vol. 32, no. 5, pp. 787–792, 1961, ISSN: 00218979. DOI: 10.1063/1.1736107.

[32] D. L. Johnson, "New method of obtaining volume, grain-boundary, and surface diffusion coefficients from sintering data," *Journal of Applied Physics*, vol. 40, no. 1, pp. 192–200, 1969, ISSN: 00218979. DOI: 10.1063/1.1657030.

[33] F. B. Swinkels and M. F. Ashby, "A second report on sintering diagrams," *Acta Metallurgica*, vol. 29, no. 2, pp. 259–281, 1981, ISSN: 00016160. DOI: 10.1016/0001-6160(81)90154-1.

[34] R. Coblenz William; Coble, "Iniitial stage solid state sintering models. A critical analysis and assesment," *Sintering Processes*, vol. 13, no. January 1980, pp. 141–157, 1980. DOI: 10.1007/978-1-4899-5301-8.

[35] S.-J. L. Kang, *Sintering Densification, Grain Growth, and Microstructure*. Oxford: Butterworth-Heinemann, 2005, pp. xi –xii, ISBN: 978-0-7506-6385-4. DOI: https://doi.org/10.1016/B978-075066385-4/50000-5.

[36] W. W. Mullins, "Two-dimensional motion of idealized grain boundaries," *Journal of Applied Physics*, vol. 27, no. 8, pp. 900–904, 1956, ISSN: 00218979. DOI: 10.1063/1.1722511.

[37] H. Riedel and J. Svoboda, "A theoretical study of grain growth in porous solids during sintering," *Acta Metallurgica Et Materialia*, vol. 41, no. 6, pp. 1929–1936, 1993, ISSN: 09567151. DOI: 10.1016/0956-7151(93)90212-B.

[38] G. Bernard-Granger and C. Guizard, "New relationships between relative density and grain size during solid-state sintering of ceramic powders," *Acta Materialia*, vol. 56, no. 20, pp. 6273–6282, 2008, ISSN: 13596454. DOI: 10.1016/j.actamat.2008.08.054.

[39] J.-M. Missiaen, "Modelling of sintering : recent developments and perspectives," *Revue de Métallurgie*, vol. 99, no. 12, pp. 1009–1019, 2002, ISSN: 0035-1563. DOI: 10.1051/metal:2002149.

[40] F. A. Nichols and W. W. Mullins, "Morphological changes of a surface of revolution due to capillarity-induced surface diffusion," *Journal of Applied Physics*, vol. 36, no. 6, pp. 1826–1835, 1965, ISSN: 00218979. DOI: 10.1063/1.1714360.

[41] P Bross and H. Exner, "Computer simulation of sintering processes," *Acta Metallurgica*, vol. 27, no. 6, pp. 1013–1020, 1979.

[42] J. Svoboda and H. Riedel, "New solutions describing the formation of interparticle necks in solid-state sintering," *Acta Metallurgica Et Materialia*, vol. 43, no. 1, pp. 1–10, 1995, ISSN: 09567151. DOI: 10.1016/0956-7151(95)90255-4.

[43] D. Bouvard and R. M. McMeeking, *Deformation of Interparticle Necks by Diffusion-Controlled Creep*, 1996. DOI: 10.1111/j.1151-2916.1996.tb07927.x.

[44] W. Zhang and I. Gladwell, "Sintering of two particles by surface and grain boundary diffusion - A three-dimensional model and a numerical study," *Computational Materials Science*, vol. 12, no. 2, pp. 84–104, 1998, ISSN: 09270256. DOI: 10.1016/s0927-0256(98)00035-4.

[45] J. Pan, H. Le, S. Kucherenko, and J. A. Yeomans, "A model for the sintering of spherical particles of different sizes by solid state diffusion," *Acta Materialia*, vol. 46, no. 13, pp. 4671–4690, 1998, ISSN: 13596454. DOI: 10.1016/S1359-6454(98)00144-X.

[46] M. Weiner, M. Schmidtchen, and U. Prahl, "A New Approach for Sintering Simulation of Irregularly Shaped Powder Particles—Part I: Model Development and Case Studies," *Advanced Engineering Materials*, vol. 2101513, 2022, ISSN: 15272648. DOI: 10.1002/adem.202101513.

[47] M. Weiner, T. Zienert, M. Schmidtchen, J. Hubálková, C. G. Aneziris, and U. Prahl, "A New Approach for Sintering Simulation of Irregularly Shaped Powder Particles—Part II: Statistical Powder Modeling," *Advanced Engineering Materials*, no. June, p. 2 200 443, 2022, ISSN: 1438-1656. DOI: 10.1002/adem.202200443.

[48] P. Cundall and O. Strack, "A discrete numerical model for granular assemblies," *Géotechnique*, pp. 47–65, 1979, ISSN: 01489062. DOI: 10.1016/0148-9062(79)91211-7.

[49] G. Petzow and H. E. Exner, *Particle Rearrangement in Solid State Sintering.* 1976. DOI: 10.1515/ijmr-1976-670906.

[50] F. Parhami and R. M. McMeeking, "A network model for initial stage sintering," *Mechanics of Materials*, vol. 27, no. 2, pp. 111–124, 1998, ISSN: 01676636. DOI: 10.1016/S0167-6636(97)00034-3.

[51] W. J. Soppe, G. J. M. Janssen, B. C. Bonekamp, L. A. Correia, and H. J. Veringa, "A computer-simulation method for sintering in 3-dimensional powder compacts," *J. Mater. Sci.*, vol. 29, pp. 754–761, 1994.

[52] C. L. Martin, L. C. Schneider, L. Olmos, and D. Bouvard, "Discrete element modeling of metallic powder sintering," *Scripta Materialia*, vol. 55, no. 5, pp. 425–428, 2006, ISSN: 13596462. DOI: 10.1016/j.scriptamat.2006.05.017.

[53] B. Henrich, A. Wonisch, T. Kraft, M. Moseler, and H. Riedel, "Simulations of the influence of rearrangement during sintering," *Acta Materialia*, vol. 55, no. 2, pp. 753–762, 2007, ISSN: 13596454. DOI: 10.1016/j.actamat.2006.09.005.

[54] H. Riedel, H. Zipse, and J. Svoboda, "Equilibrium pore surfaces, sintering stresses and constitutive equations for the intermediate and late stages of sintering-II. Diffusional densification and creep," *Acta Metallurgica Et Materialia*, vol. 42, no. 2, pp. 445–452, 1994, ISSN: 09567151. DOI: 10.1016/0956-7151(94)90499-5.

[55] J. Svoboda, H. Riedel, and H. Zipse, "Equilibrium pore surfaces, sintering stresses and constitutive equations for the intermediate and late stages of sintering-I. computation of equilibrium surfaces," *Acta Metallurgica Et Materialia*, vol. 42, no. 2, pp. 435–443, 1994, ISSN: 09567151. DOI: 10.1016/0956-7151(94)90498-7.

[56] C. L. Martin, H. Camacho-Montes, L. Olmos, D. Bouvard, and R. K. Bordia, "Evolution of defects during sintering: Discrete element simulations," *Journal of the American Ceramic Society*, vol. 92, no. 7, pp. 1435–1441, 2009, ISSN: 00027820. DOI: 10.1111/j.1551-2916.2009.03014.x.

[57] R. Raj and M. F. Ashby, "On grain boundary sliding and diffusional creep," *Metallurgical Transactions*, vol. 2, no. 4, pp. 1113–1127, 1971, ISSN: 03602133. DOI: 10.1007/BF02664244.

[58] B. Paredes-goyes, D. Jauffres, J.-m. Missiaen, and C. L. Martin, "Grain growth in sintering : A discrete element model on large packings," *Acta Materialia*, vol. 218, p. 117 182, 2021, ISSN: 1359-6454. DOI: 10.1016/j.actamat.2021.117182.

[59] A. Wonisch, O. Guillon, T. Kraft, M. Moseler, H. Riedel, and J. Rödel, "Stress-induced anisotropy of sintering alumina: Discrete element modelling and experiments," *Acta Materialia*, vol. 55, no. 15, pp. 5187–5199, 2007, ISSN: 13596454. DOI: 10.1016/j.actamat.2007.05.038.

[60] A. Wonisch, T. Kraft, M. Moseler, and H. Riedel, "Effect of different particle size distributions on solid-state sintering: A microscopic simulation approach," *Journal of the American Ceramic Society*, vol. 92, no. 7, pp. 1428–1434, 2009, ISSN: 00027820. DOI: 10.1111/j.1551-2916.2009.03012.x.

[61] C. L. Martin and R. K. Bordia, "The effect of a substrate on the sintering of constrained films," *Acta Materialia*, vol. 57, no. 2, pp. 549–558, 2009, ISSN: 13596454. DOI: 10.1016/j.actamat.2008.09.041.

[62] J Rojek, K Pietrzak, M Chmielewski, D Kali\'nski, and S Nosewicz, "Discrete element simulation of powder sintering," *Comput. METHODS Mater. Sci.*, vol. 11, no. 1, pp. 68–73, 2011.

[63] S. Nosewicz, J. Rojek, K. Pietrzak, and M. Chmielewski, "Viscoelastic discrete element model of powder sintering," *Powder Technology*, vol. 246, pp. 157–168, 2013, ISSN: 00325910. DOI: 10.1016/j.powtec.2013.05.020.

[64] C Wang and S Chen, "Application of the complex network method in solid-state sintering," *Comput. Mater. Sci.*, vol. 69, pp. 14–21, 2013, ISSN: 0927-0256. DOI: 10.1016/j.commatsci.2012.11.020.

[65] R. Besler, M. Rossetti Da Silva, J. J. Do Rosario, M. Dosta, S. Heinrich, and R. Janssen, "Sintering Simulation of Periodic Macro Porous Alumina," *Journal of the American Ceramic Society*, vol. 98, no. 11, pp. 3496–3502, 2015, ISSN: 15512916. DOI: 10.1111/jace.13684.

[66] H. Xin, W. C. Sun, and J. Fish, "Discrete element simulations of powder-bed sintering-based additive manufacturing," *Int. J. Mech. Sci.*, vol. 149, no. November 2017, pp. 373–392, 2018, ISSN: 00207403. DOI: 10.1016/j.ijmecsci.2017.11.028.

[67] S. Nosewicz, J. Rojek, M. Chmielewski, and K. Pietrzak, "Discrete element modeling of intermetallic matrix composite manufacturing by powder metallurgy," *Materials (Basel).*, vol. 12, no. 2, pp. 1–18, 2019, ISSN: 19961944. DOI: 10.3390/ma12020281.

[68] S. Martin, M. Guessasma, J. Léchelle, J. Fortin, K. Saleh, and F. Adenot, "Simulation of sintering using a Non Smooth Discrete Element Method. Application to the study of rearrangement," *Computational Materials Science*, vol. 84, pp. 31–39, 2014, ISSN: 09270256. DOI: 10.1016/j.commatsci.2013.11.050.

[69] S. Martin, R. Parekh, M. Guessasma, J. Léchelle, J. Fortin, and K. Saleh, "Study of the sintering kinetics of bimodal powders. A parametric DEM study," *Powder Technology*, vol. 270, no. PB, pp. 637–645, 2015, ISSN: 1873328X. DOI: 10.1016/j.powtec.2014.03.057.

[70] C. L. Martin, Z. Yan, D. Jauffres, D. Bouvard, and R. K. Bordia, "Sintered ceramics with controlled microstructures: Numerical investigations with the Discrete Element Method," *Journal of the Ceramic Society of Japan*, vol. 124, no. 4, pp. 340–345, 2016, ISSN: 13486535. DOI: 10.2109/jcersj2.15269.

[71] T. Rasp, T. Kraft, and H. Riedel, "Discrete element study on the influence of initial coordination numbers on sintering behaviour," *Scripta Materialia*, vol. 69, no. 11-12, pp. 805–808, 2013, ISSN: 13596462. DOI: 10.1016/j.scriptamat.2013.09.003.

[72] Z. Yan, C. L. Martin, O. Guillon, and D. Bouvard, "Effect of size and homogeneity of rigid inclusions on the sintering of composites," *Scripta Materialia*, vol. 69, no. 4, pp. 327–330, 2013, ISSN: 13596462. DOI: 10.1016/j.scriptamat.2013.05.013.

[73] C. Wang and S. H. Chen, "The influence of agglomerates on the densification and microstructural evolution in sintering of a multi-particle system," *Science China: Physics, Mechanics and Astronomy*, vol. 55, no. 6, pp. 1051–1058, 2012, ISSN: 16747348. DOI: 10.1007/s11433-012-4743-4.

[74] A. Lichtner, D. Roussel, D. Röhrens, D. Jauffres, J. Villanova, C. L. Martin, and R. K. Bordia, "Anisotropic sintering behavior of freeze-cast ceramics by optical dilatometry and discrete-element simulations," *Acta Materialia*, vol. 155, pp. 343–349, 2018, ISSN: 13596454. DOI: 10.1016/j.actamat.2018.06.001.

[75] B. Hugonnet, J. M. Missiaen, C. L. Martin, and C. Rado, "Effect of contact alignment on shrinkage anisotropy during sintering: Stereological model, discrete element model and experiments on NdFeB compacts.," *Materials and Design*, vol. 191, p. 108 575, 2020, ISSN: 18734197. DOI: 10.1016/j.matdes.2020.108575.

[76] T. Rasp, C. Jamin, A. Wonisch, T. Kraft, and O. Guillon, "Shape distortion and delamination during constrained sintering of ceramic stripes: Discrete element simulations and experiments," *Journal of the American Ceramic Society*, vol. 95, no. 2, pp. 586–592, 2012, ISSN: 00027820. DOI: 10.1111/j.1551-2916.2011.04939.x.

[77] T. Rasp, C. Jamin, O. Guillon, and T. Kraft, "Cracking and shape deformation of cylindrical cavities during constrained sintering," *Journal of the European Ceramic Society*, vol. 37, no. 8, pp. 2907–2917, 2017, ISSN: 1873619X. DOI: 10.1016/j.jeurceramsoc.2017.03.013.

[78] J. R. Carazzone, C. L. Martin, and Z. C. Cordero, "Crack initiation, propagation, and arrest in sintering powder aggregates," *Journal of the American Ceramic Society*, vol. 103, no. 9, pp. 4754–4773, 2020, ISSN: 15512916. DOI: 10.1111/jace.17170.

[79] M. Dosta, K. P. Furlan, V. Skorych, S. Heinrich, and R. Janssen, "Influence of pores arrangement on stability of photonic structures during sintering," *Journal of the European Ceramic Society*, vol. 40, no. 13, pp. 4562–4571, 2020, ISSN: 1873619X. DOI: 10.1016/j.jeurceramsoc.2020.04.019.

[80] L. Olmos, C. L. Martin, D. Bouvard, D. Bellet, and M. Di Michiel, "Investigation of the sintering of heterogeneous powder systems by synchrotron microtomography and discrete element simulation," *Journal of the American Ceramic Society*, vol. 92, no. 7, pp. 1492–1499, 2009, ISSN: 00027820. DOI: 10.1111/j.1551-2916.2009.03037.x.

[81] Z. Yan, C. L. Martin, O. Guillon, D. Bouvard, and C. S. Lee, "Microstructure evolution during the co-sintering of Ni/BaTiO3 multilayer ceramic capacitors modeled by discrete element simulations," *Journal of the European Ceramic Society*, vol. 34, no. 13, pp. 3167–3179, 2014, ISSN: 09552219. DOI: 10.1016/j.jeurceramsoc.2014.04.013.

[82] R. Besler, M. R. d. Silva, M. Dosta, S. Heinrich, and R. Janssen, "Discrete element simulation of metal ceramic composite materials with varying metal content," *Journal of the European Ceramic Society*, vol. 36, no. 9, pp. 2245–2253, 2016, ISSN: 1873619X. DOI: 10.1016/j.jeurceramsoc.2015.12.051.

[83] S. Nosewicz, J. Rojek, and M. Chmielewski, "Discrete Element Framework for Determination of Sintering and Postsintering Residual Stresses of," *Materials*, vol. 13, no. 4015, pp. 1–21, 2020. DOI: 10.3390/ma13184015.

[84] S. Martin, S. Navarro, H. Palancher, A. Bonnin, J. Léchelle, M. Guessasma, J. Fortin, and K. Saleh, "Validation of DEM modeling of sintering using an in situ X-ray microtomography analysis of the sintering of NaCl powder," *Computational Particle Mechanics*, vol. 3, no. 4, pp. 525–532, 2016, ISSN: 21964386. DOI: 10.1007/s40571-015-0062-7.

[85] D. Roussel, A. Lichtner, D. Jauffrès, J. Villanova, R. K. Bordia, and C. L. Martin, "Strength of hierarchically porous ceramics: Discrete simulations on X-ray nanotomography images," *Scripta Materialia*, vol. 113, pp. 250–253, 2016, ISSN: 13596462. DOI: 10.1016/j.scriptamat.2015.11.015.

[86] D. Jauffrès, C. L. Martin, A. Lichtner, and R. K. Bordia, "Simulation of the elastic properties of porous ceramics with realistic microstructure," *Modelling and Simulation in Materials Science and Engineering*, vol. 20, no. 4, pp. 1–18, 2012, ISSN: 09650393. DOI: 10.1088/0965-0393/20/4/045009.

[87] D. Jauffrès, C. L. Martin, A. Lichtner, and R. K. Bordia, "Simulation of the toughness of partially sintered ceramics with realistic microstructures," *Acta Materialia*, vol. 60, no. 12, pp. 4685–4694, 2012, ISSN: 13596454. DOI: 10.1016/j.actamat.2012.05.024.

[88] M. Dosta, R. Besler, C. Ziehdorn, R. Janßen, and S. Heinrich, "Approximation of mechanical properties of sintered materials with discrete element method," *EPJ Web of Conferences*, vol. 140, 2017, ISSN: 2100014X. DOI: 10.1051/epjconf/201714015022.

[89] D. Jauffrès, C. L. Martin, and R. K. Bordia, "Design of strain tolerant porous microstructures – A case for controlled imperfection," *Acta Materialia*, vol. 148, pp. 193–201, 2018, ISSN: 13596454. DOI: 10.1016/j.actamat.2017.12.039.

[90] M. H. P. Teixeira, V. Skorych, R. Janssen, S. Y. G. González, A. De Noni, J. B. Rodrigues Neto, D. Hotza, and M. Dosta, "High heating rate sintering and microstructural evolution assessment using the discrete element method," *Open Ceramics*, vol. 8, no. September, 2021, ISSN: 26665395. DOI: 10.1016/j.oceram.2021.100182.

[91] J Rojek, R Kasztelan, and R Tharmaraj, "Discrete element thermal conductance model for sintered particles," *Powder Technology*, vol. 405, p. 117 521, 2022, ISSN: 0032-5910. DOI: 10.1016/j.powtec.2022.117521.

[92] T. Matsuda, "Development of a DEM taking account of neck increments caused by surface diffusion for sintering and application to analysis of the initial stage of sintering," *Computational Materials Science*, vol. 196, no. April, p. 110 525, 2021, ISSN: 0927-0256. DOI: 10.1016/j.commatsci.2021.110525.

[93] A. Kazaryan, Y. Wang, S. A. Dregia, and B. R. Patton, "Grain growth in systems with anisotropic boundary mobility: Analytical model and computer simulation," *Physical Review B - Condensed Matter and Materials Physics*, vol. 63, no. 18, pp. 1–11, 2001, ISSN: 1550235X. DOI: 10.1103/PhysRevB.63.184102.

[94] K. Asp and J. Ågren, "Phase-field simulation of sintering and related phenomena - A vacancy diffusion approach," *Acta Materialia*, vol. 54, no. 5, pp. 1241–1248, 2006, ISSN: 13596454. DOI: 10.1016/j.actamat.2005.11.005.

[95] Y. U. Wang, "Computer modeling and simulation of solid-state sintering: A phase field approach," *Acta Materialia*, vol. 54, no. 4, pp. 953–961, 2006, ISSN: 13596454. DOI: 10.1016/j.actamat.2005.10.032.

[96] V. Kumar, Z. Z. Fang, and P. C. Fife, "Phase field simulations of grain growth during sintering of two unequal-sized particles," *Materials Science and Engineering A*, vol. 528, no. 1, pp. 254–259, 2010, ISSN: 09215093. DOI: 10.1016/j.msea.2010.08.061.

[97] K. Ahmed, C. A. Yablinsky, A. Schulte, T. Allen, and A. El-Azab, "Phase field modeling of the effect of porosity on grain growth kinetics in polycrystalline ceramics," *Modelling and Simulation in Materials Science and Engineering*, vol. 21, no. 6, 2013, ISSN: 09650393. DOI: 10.1088/0965-0393/21/6/065005.

[98] K. Ahmed, J. Pakarinen, T. Allen, and A. El-Azab, "Phase field simulation of grain growth in porous uranium dioxide," *Journal of Nuclear Materials*, vol. 446, no. 1-3, pp. 90–99, 2014, ISSN: 00223115. DOI: 10.1016/j.jnucmat.2013.11.036.

[99] K. Ahmed, T. Allen, and A. El-Azab, "Phase field modeling for grain growth in porous solids," *Journal of Materials Science*, vol. 51, no. 3, pp. 1261–1277, 2016, ISSN: 15734803. DOI: 10.1007/s10853-015-9107-9.

[100] S. Biswas, D. Schwen, J. Singh, and V. Tomar, "A study of the evolution of microstructure and consolidation kinetics during sintering using a phase field modeling based approach," *Extreme Mechanics Letters*, vol. 7, pp. 78–89, 2016, ISSN: 23524316. DOI: 10.1016/j.eml.2016.02.017.

[101] V. Rehn, J. Hötzer, W. Rheinheimer, M. Seiz, C. Serr, and B. Nestler, "Phase-field study of grain growth in porous polycrystals," *Acta Materialia*, vol. 174, pp. 439–449, Aug. 2019, ISSN: 13596454. DOI: 10.1016/j.actamat.2019.05.059.

[102] Y. Liu, M. Militzer, and M. Perez, "Phase field modelling of abnormal grain growth," *Materials*, vol. 12, no. 24, 2019, ISSN: 19961944. DOI: 10.3390/MA12244048.

[103] J. Hötzer, M. Seiz, M. Kellner, W. Rheinheimer, and B. Nestler, "Phase-field simulation of solid state sintering," *Acta Materialia*, vol. 164, pp. 184–195, 2019, ISSN: 13596454. DOI: 10.1016/j.actamat.2018.10.021.

[104] B. Dzepina, D. Balint, and D. Dini, "A phase field model of pressure-assisted sintering," *Journal of the European Ceramic Society*, vol. 39, no. 2-3, pp. 173–182, 2019, ISSN: 1873619X. DOI: 10.1016/j.jeurceramsoc.2018.09.014.

[105] Y. Zhang and L. Liu, "Phase field simulation of abnormal grain growth mediated by initial particle size distribution," *Advanced Powder Technology*, no. xxxx, 2021, ISSN: 09218831. DOI: 10.1016/j.apt.2021.07.025.

[106] R. Termuhlen, X. Chatzistavrou, J. D. Nicholas, and H. C. Yu, "Three-dimensional phase field sintering simulations accounting for the rigid-body motion of individual grains," *Computational Materials Science*, vol. 186, no. June 2020, p. 109 963, 2021, ISSN: 09270256. DOI: 10.1016/j.commatsci.2020.109963.

[107] R. Shi, M. Wood, T. W. Heo, B. C. Wood, and J. Ye, "Towards understanding particle rigid-body motion during solid-state sintering," *Journal of the European Ceramic Society*, no. April, 2021, ISSN: 09552219. DOI: 10.1016/j.jeurceramsoc.2021.09.039.

[108] V. Ivannikov, F. Thomsen, T. Ebel, and R. Willumeit-Römer, "Capturing shrinkage and neck growth with phase field simulations of the solid state sintering," *Modelling and Simulation in Materials Science and Engineering*, vol. 29, no. 7, 2021, ISSN: 1361651X. DOI: 10.1088/1361-651X/ac1f87.

[109] Z. Zhao, X. Zhang, H. Zhang, H. Tang, and Y. Liang, "Numerical investigation into pressure-assisted sintering using fully coupled mechano-diffusional phase-field model," *International Journal of Solids and Structures*, vol. 234-235, no. April 2021, p. 111 253, 2022, ISSN: 00207683. DOI: 10.1016/j.ijsolstr.2021.111253.

[110] A. Ishii, A. Yamanaka, E. Miyoshi, and A. Yamamoto, "Efficient estimation of material parameters using DMC-BO: Application to phase-field simulation of solid-state sintering," *Materials Today Communications*, vol. 30, no. July 2021, p. 103 089, 2022, ISSN: 23524928. DOI: 10.1016/j.mtcomm.2021.103089.

[111] K. Shinagawa, "Simulation of grain growth and sintering process by combined phase-field/discrete-element method," *Acta Materialia*, vol. 66, pp. 360–369, 2014, ISSN: 13596454. DOI: 10.1016/j.actamat.2013.11.023.

[112] D. Zhang, A. Weng, S. Gong, and D. Zhou, "Computer simulation of grain growth of intermediate*/ and final-stage sintering and Ostwald ripening of BaTiO 3-based PTCR ceramics," *Materials Science and Engineering: B*, vol. 99, pp. 428–432, 2003. DOI: 10.1016/S0921-5107(02)00449-X.

[113] M. Braginsky, V. Tikare, and E. Olevsky, "Numerical simulation of solid state sintering," *International Journal of Solids and Structures*, vol. 42, no. 2, pp. 621–636, 2005, ISSN: 00207683. DOI: 10.1016/j.ijsolstr.2004.06.022.

[114] H. Itahara, T. Tani, H. Nomura, and H. Matsubara, "Computational design for grain-oriented microstructure of functional ceramics prepared by templated grain growth," *Journal of the American Ceramic Society*, vol. 89, no. 5, pp. 1557–1562, 2006, ISSN: 00027820. DOI: 10.1111/j.1551-2916.2006.00954.x.

[115] M. W. Reiterer and K. G. Ewsuk, "An analysis of four different approaches to predict and control sintering," *Journal of the American Ceramic Society*, vol. 92, no. 7, pp. 1419–1427, Jul. 2009, ISSN: 00027820. DOI: 10.1111/j.1551-2916.2009.03009.x.

[116] V. Tikare, M. Braginsky, D. Bouvard, and A. Vagnon, "Numerical simulation of microstructural evolution during sintering at the mesoscale in a 3D powder compact," *Computational Materials Science*, vol. 48, no. 2, pp. 317–325, 2010, ISSN: 09270256. DOI: 10.1016/j.commatsci.2010.01.013.

[117] R. Bjork, V. Tikare, H. L. Frandsen, and N. Pryds, "The sintering behavior of close-packed spheres," *Scripta Materialia*, vol. 67, no. 1, pp. 81–84, 2012, ISSN: 13596462. DOI: 10.1016/j.scriptamat.2012.03.024.

[118] R. Bjørk, V. Tikare, H. L. Frandsen, and N. Pryds, "The effect of particle size distributions on the microstructural evolution during sintering," *Journal of the American Ceramic Society*, vol. 96, no. 1, pp. 103–110, 2013, ISSN: 00027820. DOI: 10.1111/jace.12100.

[119] R. Bjørk, H. L. Frandsen, and N. Pryds, "Modeling the Microstructural Evolution during Constrained Sintering," *Journal of the American Ceramic Society*, vol. 98, no. 11, pp. 3490–3495, 2015, ISSN: 15512916. DOI: 10.1111/jace.13701.

[120] S. Hara, A. Ohi, and N. Shikazono, "Sintering analysis of sub-micron-sized nickel powders: Kinetic Monte Carlo simulation verified by FIB-SEM reconstruction," *Journal of Power Sources*, vol. 276, pp. 105–112, Feb. 2015, ISSN: 03787753. DOI: 10.1016/j.jpowsour.2014.11.110.

[121] Z. Yan, S. Hara, and N. Shikazono, "Effect of powder morphology on the microstructural characteristics of La0.6Sr0.4Co0.2Fe0.8O3 cathode: A Kinetic Monte Carlo investigation," *International Journal of Hydrogen Energy*, vol. 42, no. 17, pp. 12 601–12 614, 2017, ISSN: 03603199. DOI: 10.1016/j.ijhydene.2017.03.136.

[122] Z. Yan, S. Hara, and N. Shikazono, "Towards a realistic prediction of sintering of solid oxide fuel cell electrodes: From tomography to discrete element and kinetic Monte Carlo simulations," *Scripta Materialia*, vol. 146, pp. 31–35, 2018, ISSN: 13596462. DOI: 10.1016/j.scriptamat.2017.10.035.

[123] R. Bjørk, "The sintering behavior of ellipsoidal particles," *Journal of the American Ceramic Society*, no. May, pp. 1–10, 2022, ISSN: 0002-7820. DOI: 10.1111/jace.18580.

[124] T. Matsuda, "Distortion prediction during sintering using Monte Carlo method implemented with virtual springs," *International Journal of Ceramic Engineering & Science*, no. May, pp. 1–11, 2022, ISSN: 2578-3270. DOI: 10.1002/ces2.10135.

[125] F. Wakai and F. Aldinger, "Equilibrium configuration of particles in sintering under constraint," *Acta Materialia*, vol. 51, no. 3, pp. 641–652, 2003, ISSN: 13596454. DOI: 10.1016/S1359-6454(02)00443-3.

[126] F. Wakai, M. Yoshida, Y. Shinoda, and T. Akatsu, "Coarsening and grain growth in sintering of two particles of different sizes," *Acta Materialia*, vol. 53, no. 5, pp. 1361–1371, 2005, ISSN: 13596454. DOI: 10.1016/j.actamat.2004.11.029.

[127] F. Wakai, "Modeling and simulation of elementary processes in ideal sintering," *Journal of the American Ceramic Society*, vol. 89, no. 5, pp. 1471–1484, 2006, ISSN: 00027820. DOI: 10.1111/j.1551-2916.2006.01001.x.

[128] F. Wakai and K. A. Brakke, "Mechanics of sintering for coupled grain boundary and surface diffusion," *Acta Materialia*, vol. 59, no. 14, pp. 5379–5387, 2011, ISSN: 13596454. DOI: 10.1016/j.actamat.2011.05.006.

[129] F. Wakai and K. A. Brakke, "Tensor virial equation of evolving surfaces in sintering of aggregates of particles by diffusion," *Acta Materialia*, vol. 61, no. 11, pp. 4103–4112, 2013, ISSN: 13596454. DOI: 10.1016/j.actamat.2013.03.035.

[130] F. Wakai, O. Guillon, G. Okuma, and N. Nishiyama, "Sintering forces acting among particles during sintering by grain-boundary/surface diffusion," *Journal of the American Ceramic Society*, vol. 102, no. 2, pp. 38–43, 2018, ISSN: 15512916. DOI: 10.1111/jace.15716.

[131] F. Wakai, G. Okuma, N. Nishiyama, and O. Guillon, "Micromechanics of formation and shrinkage of a closed pore in sintering by coupled grain boundary/surface diffusion," *Journal of the European Ceramic Society*, vol. 39, no. 9, pp. 2952–2959, 2019, ISSN: 1873619X. DOI: 10.1016/j.jeurceramsoc.2019.03.022.

[132] F. Wakai and G. Okuma, "Rigid Body Motion of Multiple Particles in Solid-State Sintering," *SSRN Electronic Journal*, vol. 235, p. 118 092, 2022, ISSN: 1359-6454. DOI: 10.2139/ssrn.4073477.

[133] L Benabou and X Wang, "International Journal for Computational Methods in Simulation of silver nanoparticles sintering at high temperatures based on theoretical evaluations of surface and grain boundary mobilities," *International Journal for Computational Methods in Engineering Science and Mechanics*, vol. 0, no. 0, pp. 1–12, 2020. DOI: 10.1080/15502287.2020.1841334.

[134] J. Bruchon, D. Pino-Muñoz, F. Valdivieso, and S. Drapier, "Finite element simulation of mass transport during sintering of a granular packing. Part I. Surface and lattice diffusions," *Journal of the American Ceramic Society*, vol. 95, no. 8, pp. 2398–2405, 2012, ISSN: 00027820. DOI: 10.1111/j.1551-2916.2012.05073.x.

[135] D. J. Green, O. Guillon, and J. Rödel, "Constrained sintering: A delicate balance of scales," *Journal of the European Ceramic Society*, vol. 28, no. 7, pp. 1451–1466, 2008, ISSN: 09552219. DOI: 10.1016/j.jeurceramsoc.2007.12.012.

[136] E. A. Olevsky, "Theory of sintering: From discrete to continuum," *Materials Science and Engineering R: Reports*, vol. 23, no. 2, pp. 41–100, 1998, ISSN: 0927796X. DOI: 10.1016/S0927-796X(98)00009-6.

[137] E. A. Olevsky, B. Kushnarev, A. Maximenko, V. Tikare, and M. Braginsky, "Modelling of anisotropic sintering in crystalline ceramics," *Philosophical Magazine*, vol. 85, no. 19, pp. 2123–2146, 2005, ISSN: 14786435. DOI: 10.1080/14786430412331331989.

[138] E. Torresani, D. Giuntini, C. Zhu, T. Harrington, K. S. Vecchio, A. Molinari, R. K. Bordia, and E. A. Olevsky, "Anisotropy of Mass Transfer During Sintering of Powder Materials with Pore–Particle Structure Orientation," *Metallurgical and Materials Transactions A: Physical Metallurgy and Materials Science*, vol. 50, no. 2, pp. 1033–1049, 2019, ISSN: 10735623. DOI: 10.1007/s11661-018-5037-x.

[139] C. R. Reid, "Numerical simulation of free shrinkage using a continuum theory for sintering," *Powder Technology*, vol. 81, no. 3, pp. 287–291, 1994, ISSN: 00325910. DOI: 10.1016/0032-5910(94)02887-7.

[140] H. G. Kim, O. Gillia, and D. Bouvard, "A phenomenological constitutive model for the sintering of alumina powder," *Journal of the European Ceramic Society*, vol. 23, no. 10, pp. 1675–1685, 2003, ISSN: 09552219. DOI: 10.1016/S0955-2219(02)00411-9.

[141] M. Reiterer, T. Kraft, U. Janosovits, and H. Riedel, "Finite element simulation of cold isostatic pressing and sintering of SiC components," *Ceramics International*, vol. 30, no. 2, pp. 177–183, 2004, ISSN: 02728842. DOI: 10.1016/S0272-8842(03)00086-5.

[142] E. Olevsky and A. Molinari, "Kinetics and stability in compressive and tensile loading of porous bodies," *Mechanics of Materials*, vol. 38, no. 4, pp. 340–366, 2006, ISSN: 01676636. DOI: 10.1016/j.mechmat.2005.11.002.

[143] H. Camacho-Montes, P. E. García-Casillas, R. Rodríguez-Ramos, M. E. Fuentes-Montero, and L. E. Fuentes-Cobas, "Simulation of the stress-assisted densification behavior of a powder compact: Effect of constitutive laws," *Journal of the American Ceramic Society*, vol. 91, no. 3, pp. 836–845, 2008, ISSN: 00027820. DOI: 10.1111/j.1551-2916.2007.02219.x.

[144] R. K. Bordia and R. Raj, "Sintering Behavior of Ceramic Films Constrained by a Rigid Substrate," *Journal of the American Ceramic Society*, vol. 68, no. 6, pp. 287–292, 1985, ISSN: 15512916. DOI: 10.1111/j.1151-2916.1985.tb15227.x.

[145] C. Hsueh, "Sintering of a ceramic film on a rigid substrate," *Scripta Metallurgica*, vol. 19, no. 10, pp. 1213–1217, 1985, ISSN: 0036-9748. DOI: https://doi.org/10.1016/0036-9748(85)90240-6.

[146] R. Raj and R. K. Bordia, "Sintering behavior of bi-modal powder compacts," *Acta Metallurgica*, vol. 32, no. 7, pp. 1003–1019, 1984, ISSN: 00016160. DOI: 10.1016/0001-6160(84)90003-8.

[147] C. H. Hsueh, A. G. Evans, R. M. Cannon, and R. J. Brook, "Viscoelastic stresses and sintering damage in heterogeneous powder compacts," *Acta Metallurgica*, vol. 34, no. 5, pp. 927–936, 1986, ISSN: 00016160. DOI: 10.1016/0001-6160(86)90066-0.

[148] R. K. Bordia and G. W. Scherer, "On constrained sintering-III. Rigid inclusions," *Acta Metallurgica*, vol. 36, no. 9, pp. 2411–2416, 1988, ISSN: 00016160. DOI: 10.1016/0001-6160(88)90191-5.

[149] G. Largiller, L. Dong, D. Bouvard, C. P. Carry, and A. Gabriel, "Deformation and cracking during sintering of bimaterial components processed from ceramic and metal powder mixes. Part II: Numerical simulation," *Mechanics of Materials*, vol. 53, pp. 132–141, 2012, ISSN: 01676636. DOI: 10.1016/j.mechmat.2012.05.012.

[150] E. Olevsky, T. T. Molla, H. L. Frandsen, R. Bjørk, V. Esposito, D. W. Ni, A. Ilyina, and N. Pryds, "Sintering of multilayered porous structures: Part I-constitutive models," *Journal of the American Ceramic Society*, vol. 96, no. 8, pp. 2657–2665, 2013, ISSN: 00027820. DOI: 10.1111/jace.12375.

[151] G. Largiller, L. Dong, D. Bouvard, C. P. Carry, and A. Gabriel, "Constitutive modeling of the behaviour of cermet compacts during reaction sintering," *Powder Technology*, vol. 208, no. 2, pp. 496–502, 2011, ISSN: 00325910. DOI: 10.1016/j.powtec.2010.08.049.

[152] E. A. Olevsky, V. Tikare, and T. Garino, "Multi-scale study of sintering: A review," *Journal of the American Ceramic Society*, vol. 89, no. 6, pp. 1914–1922, 2006, ISSN: 00027820. DOI: 10.1111/j.1551-2916.2006.01054.x.

[153] S. Nosewicz, J. Rojek, K. Wawrzyk, P. Kowalczyk, G. Maciejewski, and M. Maździarz, "Multiscale modeling of pressure-assisted sintering," *Computational Materials Science*, vol. 156, no. May 2018, pp. 385–395, 2019, ISSN: 09270256. DOI: 10.1016/j.commatsci.2018.10.001.

[154] J. Rojek, S. Nosewicz, M. Maździarz, P. Kowalczyk, K. Wawrzyk, and D. Lumelskyj, "Modeling of a Sintering Process at Various Scales," *Procedia Engineering*, vol. 177, pp. 263–270, 2017, ISSN: 18777058. DOI: 10.1016/j.proeng.2017.02.210.

[155] A. Maximenko, A. Kuzmov, E. Grigoryev, and E. Olevsky, "Direct multi-scale modeling of sintering," *Journal of the American Ceramic Society*, vol. 95, no. 8, pp. 2383–2388, 2012, ISSN: 00027820. DOI: 10.1111/j.1551-2916.2012.05083.x.

[156] T. T. Molla, R. Bjørk, E. Olevsky, N. Pryds, and H. L. Frandsen, "Multi-scale modeling of shape distortions during sintering of bi-layers," *Computational Materials Science*, vol. 88, pp. 28–36, 2014, ISSN: 09270256. DOI: 10.1016/j.commatsci.2014.02.041.

[157] H. P. Zhu, Z. Y. Zhou, R. Y. Yang, and A. B. Yu, "Discrete particle simulation of particulate systems: Theoretical developments," *Chemical Engineering Science*, vol. 62, no. 13, pp. 3378–3396, 2007, ISSN: 00092509. DOI: 10.1016/j.ces.2006.12.089.

[158] A. Wachs, L. Girolami, G. Vinay, and G. Ferrer, "Grains3D, a flexible DEM approach for particles of arbitrary convex shape - Part I: Numerical model and validations," *Powder Technology*, vol. 224, pp. 374–389, 2012, ISSN: 00325910. DOI: 10.1016/j.powtec.2012.03.023.

[159] C. Kloss, C. Goniva, A. Hager, S. Amberger, and S. Pirker, "Models, algorithms and validation for opensource DEM and CFD-DEM," *Progress in Computational Fluid Dynamics*, vol. 12, no. 2-3, pp. 140–152, 2012, ISSN: 17415233. DOI: 10.1504/PCFD.2012.047457.

[160] S. Plimpton, "Fast parallel algorithms for short-range molecular dynamics," *Journal of Computational Physics*, vol. 117, no. 1, pp. 1–19, 1995, ISSN: 0021-9991. DOI: https://doi.org/10.1006/jcph.1995.1039.

[161] V. Ogarko and S. Luding, "A fast multilevel algorithm for contact detection of arbitrarily polydisperse objects," *Computer Physics Communications*, vol. 183, no. 4, pp. 931–936, 2012, ISSN: 00104655. DOI: 10.1016/j.cpc.2011.12.019.

[162] D. Krijgsman, V. Ogarko, and S. Luding, "Optimal parameters for a hierarchical grid data structure for contact detection in arbitrarily polydisperse particle systems," *Computational Particle Mechanics*, vol. 1, no. 3, pp. 357–372, 2014, ISSN: 21964386. DOI: 10.1007/s40571-014-0020-9.

[163] L Vu-Quoc and X. Zhang, "An accurate and efficient tangential force–displacement model for elastic frictional contact in particle-flow simulations," *Mech. Mater.*, vol. 31, pp. 235–269, 1999.

[164] F. A. Gilabert, J.-N. Roux, and A Castellanos, "Computer simulation of model cohesive powders: Influence of assembling procedure and contact laws on low consolidation states," *Phys. Rev. E*, vol. 75, p. 11 303, 2007.

[165] H. Kruggel-Emden, M. Sturm, S. Wirtz, and V. Scherer, "Selection of an appropriate time integration scheme for the discrete element method (DEM)," *Computers and Chemical Engineering*, vol. 32, no. 10, pp. 2263–2279, 2008, ISSN: 00981354. DOI: 10.1016/j.compchemeng.2007.11.002.

[166] F. Radjai and F. Dubois, *Discrete-element modeling of granular materials*. Wiley-Iste, 2011, 425 p.

[167] I Agnolin and J.-N. Roux, "Internal states of model isotropic granular packings. I. Assembling process, geometry, and contact networks," *Phys. Rev. E*, vol. 76, p. 61 302, 2007.

[168] P Dantu, "Etude statistique des forces intergranulaires dans un milieu pulv{é}rulent," *G{é}otechnique*, vol. 18, pp. 50–55, 1968.

[169] J. Christoffersen, M. M. Mehrabadi, and S. Nemat-Nasser, "A Micromechanical Description of Granular Material Behavior.," vol. 48, no. June, p. 67, 1981.

[170] C. Thornton and Z. Ning, "A theoretical model for the stick/bounce behaviour of adhesive, elastic- plastic spheres," *Powder Technology*, vol. 99, no. 2, pp. 154–162, 1998, ISSN: 00325910. DOI: 10.1016/S0032-5910(98)00099-0.

[171] R. Kawamoto, E. Andò, G. Viggiani, and J. E. Andrade, "Level set discrete element method for three-dimensional computations with triaxial case study," *Journal of the Mechanics and Physics of Solids*, vol. 91, pp. 1–13, 2016, ISSN: 00225096. DOI: 10.1016/j.jmps.2016.02.021.

[172] R. Kawamoto, J. Andrade, and T. Matsushima, "A 3-D mechanics-based particle shape index for granular materials," *Mechanics Research Communications*, vol. 92, pp. 67–73, 2018, ISSN: 00936413. DOI: 10.1016/j.mechrescom.2018.07.002.

[173] J. M. Harmon, D. Arthur, and J. E. Andrade, "Level set splitting in DEM for modeling breakage mechanics," *Computer Methods in Applied Mechanics and Engineering*, vol. 365, p. 112 961, 2020, ISSN: 00457825. DOI: 10.1016/j.cma.2020.112961.

[174] J. M. Harmon, K. Karapiperis, L. Li, and S. Moreland, "Particle bonding within the level set discrete element method," *Computer Methods in Applied Mechanics and Engineering*, vol. 373, p. 113 486, 2021, ISSN: 0045-7825. DOI: 10.1016/j.cma.2020.113486.

[175] S. Osher and R. P. Fedkiw, "Level Set Methods: An Overview and Some Recent Results," *Journal of Computational Physics*, vol. 169, no. 2, pp. 463–502, 2001, ISSN: 00219991. DOI: 10.1006/jcph.2000.6636.

[176] F. Gibou, R. Fedkiw, and S. Osher, "A review of level-set methods and some recent applications," *Journal of Computational Physics*, vol. 353, pp. 82–109, 2018, ISSN: 10902716. DOI: 10.1016/j.jcp.2017.10.006.

[177] L. Li, E. Marteau, and J. E. Andrade, "Capturing the inter-particle force distribution in granular material using LS-DEM," *Granular Matter*, vol. 21, no. 3, pp. 1–16, 2019, ISSN: 14347636. DOI: 10.1007/s10035-019-0893-7.

Chapter 3

Grain growth model

This chapter introduces the grain growth model developed within the DEM code `dp3D`. The validation of the model and its application to the isothermal sintering of a micronic alumina powder is discussed. This is presented as a scientific article entitled *Grain growth in sintering: A discrete element model on large packings* published in *Acta Materialia* in July 2021 [1]. The article is reported as published, with Supplementary Information (SI) included in Appendix A and supplementary videos in v1 and v2.

Chapter 2 discussed the relevance of grain growth in sintering and the competition with densification. However as also examined, realistic grain growth DEM models lack in the literature. From this arose the first objective of this PhD thesis concerning the development of a grain growth model within a discrete element framework. The model must be simple enough to allow for large-scale computations and clear interpretation of the results. The model must nevertheless be able to take into account the main ingredients of grain growth. The model is based on two mass transport mechanisms valid for a variety of ceramics and metals: surface diffusion and grain boundary migration.

The previous chapter reviewed different formulas for the normal force and the neck size evolution to model densification with DEM. These formulas, originally developed for equal-size particles, were extended for non-monomodal packings by introducing the equivalent radius concept. Due to the transfer of matter among particles arising during grain growth, contacts between particles with very large size ratio may appear. In that case, simply replacing the radius in equations by twice the equivalent radius ($R_{eq} = \frac{r_i r_j}{r_i + r_j}$) of two particles with radii r_i and r_j is not anymore valid. More accurate formulas, available in the literature, are used here for this type of contacts. Many particles will disappear during grain growth, making it necessary to use a large number of particles for the initial packing. The simple methodology of DEM explained in chapter 2 allows to start here with very large packings of up to 400 000 particles.

A couple of models reviewed in chapter 2, such as the phase field model and the surface evolution model, which have a more detailed description of the physics of sintering, are used to validate the grain growth model for a two-particle system. The simulation of the sintering of large packings are compared with experimental data. The model shows the ability of studying the microstructural evolution caused by densification and grain growth during conventional sintering. The application of the model in more complex sintering scenarios will be investigated in chapter 4.

Abstract

Sintering is a high temperature process used for ceramic or metallic powder consolidation that consists of concurrent densification and grain growth. This work presents a coupled solid-state sintering and grain growth model capable of studying large packings of particles within the Discrete Element Method (DEM) framework. The approach uses a refinement for large particle size ratios of previously established contact laws to model shrinkage. In addition, mass transfer between neighboring particles is implemented to model grain growth by surface diffusion and grain boundary migration. The model assumptions are valid for initial and intermediate stage sintering. The model is validated on a two-particle system by comparing neck and particle size evolutions with those obtained by phase-field and meshed-based methods. Simulations on large packings (up to 400 000 particles) with particle size distributions originating from experiments are performed. The results of these simulations using physical data from the literature are compared to experimental data with good accordance of the key features of the microstructure evolution (densification kinetics, grain size-density trajectory, evolution of the mean grain size and of the size distribution). The simulations show that even at an early stage of sintering, hardly detectable grain growth actually affects the sintering kinetics to a non-negligible extent and that the realism of DEM simulations of sintering is improved when grain growth is considered. Taking advantage of the possibility to simulate large packings, the model elucidates the influence of the initial particle size distribution on the grain growth kinetics.

Keywords: sintering, grain growth, grain boundary migration, grain size distribution, discrete element method

3.1 Introduction

The sintering of metallic or ceramic powders is a high temperature process occurring below the melting temperature. It leads to the consolidation of the powder by growing necks between particles while generally decreasing the porosity of the packing [2]. The fundamental driving force for sintering is the reduction of the interfacial energy of the system, which, in addition to the reduction of the free surface, can result in grain growth [3], [4]. For relatively dense powder compact (green density 0.5-0.6), grain growth is mostly observed in the intermediate and final stages of sintering (typically for relative density $D > 0.8$) and is driven by grain boundary migration, leading to the coarsening of larger grains at the expense of the smaller ones and to an increase of the average grain size $\bar{G}$. Grain growth kinetics is classically described by a power

law of the type $\bar{G}^n - \bar{G}_0^n \propto t$ with $\bar{G}_0$ the initial grain size. Under the assumption of grain growth by grain boundary (GB) migration the theoretical value of the exponent n is 2 for a dense body [5] while for a body with closed porosity the growth is slower due to the pinning of the grain boundaries by closed pores leading theoretically to $n = 3$ for volume diffusion and $n = 4$ for surface diffusion [6]. Experimental data on sintering confirms an exponential type law but with n generally close to 3 [4], [7]. Lange and Kellet [3] have described grain growth during sintering of porous compacts with a broad particle size distribution by inter-particle mass transport followed by GB migration. For a wide variety of ceramics and metals, surface diffusion is the most relevant mechanisms of inter-particle mass transport [8], [9]. Lange and Kellet scenario is in line with experimental observation: a linear grain size evolution with fractional porosity at lower densities, followed by a non-linear evolution in the late stages of sintering [4]. On the other hand, Bernard-Granger et al. have shown that a wide range of experimental data on alumina is correctly described by a theoretical relationship between $\bar{G}$ and the relative density D derived under the assumption of grain growth by GB migration ($1/\bar{G}^2 - 1/\bar{G}_0^2 \propto D$) in solid-state sintering, which tends to demonstrate that GB migration is the dominant mechanism [10], [11].

The control of grain growth during sintering is an important topic as coarse microstructures are generally detrimental for material performance, in particular for mechanical properties. When the grain size distribution maintains the self-similarity predicted theoretically [5] the grain growth is referred to as normal but under specific conditions a few large grains can exhibit very fast growth, giving rise to so-called abnormal grain growth, characterized by a significant broadening of the grain size distribution. An explanation often provided is that large GB mobility appears locally because of a non-uniform distribution of impurities or secondary phase [9]. Indeed, the presence of secondary phase at a GB can influence positively or negatively its mobility, a phenomenon that can also be advantageously used to limit grain growth [4], [12], [13]. Recently, numerical modeling of sintering coupled with grain growth have been proposed through finite difference method [14], Monte Carlo (MC) model [15]–[19], phase field approach [20]–[25], finite element or meshed-based methods [26], [27], Discrete Element Method (DEM) [28] or a combination of methods [29], [30]. Due to the complexity of the representation of the shape and of the physics of sintering, these approaches are, with the exception of DEM, generally computationally limited to a few particles, rarely a few hundreds, and often in 2D. Still, simulations with relatively large number of particles have been performed using a Monte Carlo model [15]–[19]. The advantage of such simulations is their capability to describe the evolution of realistic microstructures with all the necessary kinetic processes that come

with solid-state sintering. This type of simulation is able to provide useful information on grain size evolution with density. However, in the MC method, model parameters and time (Monte Carlo steps) may not have a clear physical meaning. In addition, MC models are limited to free sintering [31].

Grain growth at the later stage of sintering has also been simulated with phase field simulations on a relatively large 3D system by Rehn et al. [32], starting with an initial configuration of small isolated pores at triple lines and quadruple junctions. Recently, approaches have been proposed using initial random packings of spherical particles [33], [34], where starting from an initial configuration typically obtained by discrete simulations, the authors perform 3D phase field simulations with the main diffusion mechanisms simulated (surface, grain boundary, and bulk diffusion). The effect of rigid-body motion of individual particles may also be included [34]. In the latter study, the authors were able to run simulations with about 3000 particles and up to a final relative density of around 0.8. Although, the number of particles is already a great improvement, it comes at the cost of massive CPU parallelization (120 CPUs) and may not be sufficient as many grains disappear with coarsening at large relative densities (typically above 0.70 relative density).

Thus, there is still a need for further improvement for numerical simulations that operate at the particle scale to obtain valuable information on the microstructure evolution. The evolution of size distribution, which would necessitate large number of particles for statistics, or the influence of large defects have not been studied for example. Indeed, it would be beneficial to have access to simulations that provide such information with typically 10 times the number of particles and only a fraction of the CPU cost, while retaining the main physical ingredients that govern sintering and grain growth. For example, starting with several tens of thousands of particles would allow for a statistically representative size distribution even at large densities where the number of particles may have decreased down to less than a thousand.

In this context, following the initial work of Parhami and McMeeking [35], Martin et al. [28] have used DEM [36] to model sintering of tens of thousands of particles. Nevertheless, most sintering investigations based on DEM [35], [37]–[42] do not take into account grain growth and coarsening of particles. To our best knowledge, only one DEM study [28] includes a crude model of grain growth that does not consider realistic driving forces at the scale of individual particles. Still, grain growth should be included in large-scale simulations as coarsening and sintering are intimately linked and grain growth affects sintering kinetics [3]. Even in the early stage of sintering, the realism of DEM simulations can benefit from the addition of a physically based grain growth model. Also, DEM provides a natural mean to introduce realistic initial packing with

size distribution [42]–[45]. For packings with size distribution, sintering contact models that handle particles of different sizes are necessary. Whereas most DEM simulations deal with equal size particles [28], [37], [38], [46] or use an equivalent radius by analogy with elastic and plastic contact theories [38], [40], [42], [43], it is necessary to introduce more realistic models for unequal size particles with large size ratios. Pan et al. [14] proposed such a description based on numerical simulations at the scale of individual particles, but to our best knowledge no DEM simulation has yet introduced this type of model.

The aim of this work is thus to propose a discrete model of the sintering of a packing of particles under equilibrated sintering forces coupled with a grain growth model for particles of different sizes. The model, applied at the particle scale, should be sufficiently realistic to agree with state-of-the-art phase field simulations that operate at much smaller length scales, while taking advantage of the fully discontinuous framework of DEM to simulate large packings that can be statistically useful for further analysis. The model is limited to initial and intermediate stage sintering. In the model description section, we first briefly delineate the DEM methodology and the model focusing on the description of the sintering contact laws that include: the normal and tangential contact forces, the evolution of the contact size and equilibrium contact size for two particles unequal in size. The proposed grain growth model is then detailed with the necessary conditions for triggering each mechanism (surface diffusion and GB migration). The model results for two particles are analyzed and validated against phase field simulation for each stage of the sintering process. In the last section, the sintering of 40,000 and 400,000 alumina particle packings are simulated for various GB mobility and initial particle size distribution. The results are compared to experiments and discussed in light of existing laws for grain growth kinetics and mean grain size - density trajectory.

3.2 Model description

The model is developed in the DEM code dp3D, dedicated to materials science and already used for sintering studies over the last 15 years [28], [47]–[49]. Here we briefly describe its general scheme. Each particle is a single crystallographic grain and is considered as a sphere which upon densification can indent its neighbors. Note that unlike in the description proposed by Lange and Kellet [3] there is no distinction between particles and grain and thus GB migration is bound to be an inter-particle/grain mass transport. The main geometrical parameters defining two particles in contact are given in Fig. 3.1, where r_s and r_l are the radius of the *smaller* and *larger* particles, respec-

tively, a is the contact radius and h is their mutual indentation. Unlike the classical DEM approach, the radius of particles can evolve depending on matter diffusion driven by curvature gradient. Particles interact through their contacts that transmit forces. Rotations are not allowed here as they are rapidly opposed by resisting moments when contact size becomes finite. Contact forces are summed for each particle and the total force is used to compute explicitly the acceleration, velocity and the new position of each particle using Newton's second law with a velocity Verlet algorithm.

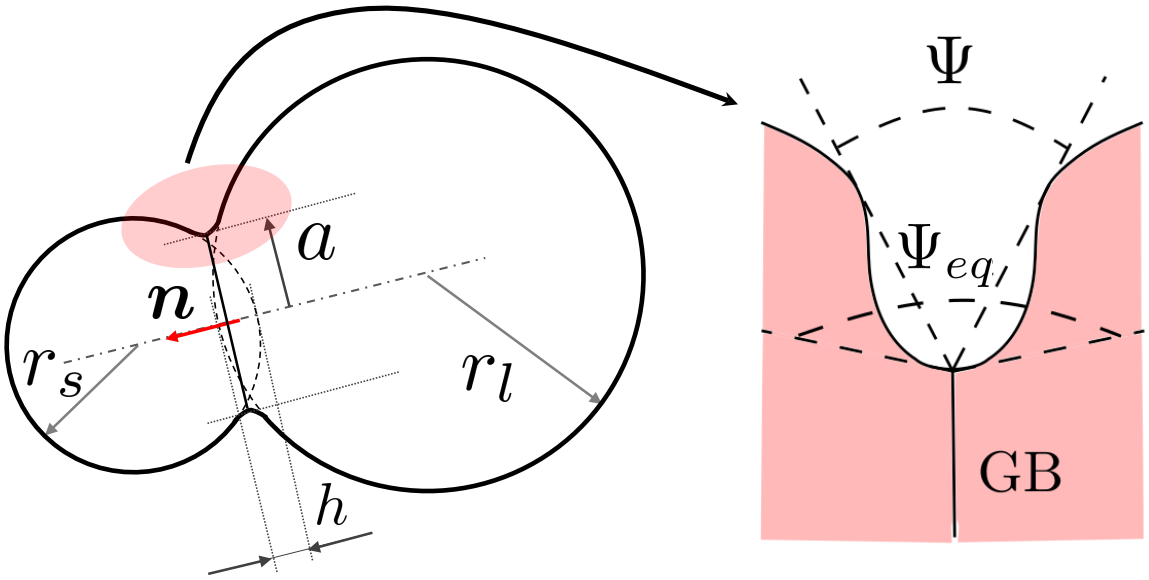

Figure 3.1: Geometrical parameters for a *large* particle (radius r_l) sintering with a *small* one (radius r_s). h, a and $\boldsymbol{n}$ are the geometric indentation, the contact radius and the normal vector, respectively. Ψ is the contact angle and Ψ_{eq} is the equilibrium dihedral angle at the grain boundary GB.

Contact detection is a critical stage for the computational efficiency of large DEM simulations. This is especially true here since grain growth implies the coexistence of particles of very different sizes along the simulation as large particles will grow at the expense of smaller ones. Standard detection schemes for nearly monomodal packings such as Verlet list together with the Linked-Cell method are insufficient in that case. A fast multilevel algorithm as proposed by Ogarko and Luding [50] was implemented to resolve effectively this issue.

Free sintering is modeled here within a periodic box in all three directions. The stress tensor Σ_{pq} is calculated from Love's formulation using the p^{th} component of the total contact force vector $\boldsymbol{F}$ and the q^{th} component of the branch vector that connects the two particle centers [51]:

$$\Sigma_{pq} = \frac{1}{V} \sum_{contacts} F_p \left(r_s + r_l - h\right) n_q \tag{3.1}$$

where the summation is made on all contacts with normal vector $\mathbf{n}$ (Fig. 3.1), and V is the volume of the periodic box. The macroscopic strain-rates are imposed to the simulation box, such that the principal components of the macroscopic stress tensor Σ_{pq} tends to zero at each time-step. Note that the same scheme can be used for stress-assisted sintering.

3.2.1 Contact laws for sintering

The normal force between two sintering particles in contact is derived from the models of Bouvard and McMeeking [46] and of Pan et al. [14]. The Bouvard and McMeeking model applies to pairs of particles of identical size whereas Pan et al. fitted their results for two particles of different sizes with a similar expression as Bouvard and McMeeking. These expressions can be rearranged to derive the normal force N between two particles with radii r_s and r_l:

$$N = \frac{\pi a^4}{\left(1+\frac{r_s}{r_l}\right)\beta\Delta_{GB}}\frac{\mathrm{d}h}{\mathrm{d}t} - \frac{\alpha}{\beta}\pi r_l\gamma_S \tag{3.2}$$

which introduces the surface energy γ_S and a diffusion-related term:

$$\Delta_{GB} = \frac{\Omega}{k_b T} D_{GB}\delta_{GB} \tag{3.3}$$

where $D_{GB} = D_{0GB}\exp\frac{-Q_{GB}}{RT}$ is the diffusion coefficient along the grain boundary with activation energy Q_{GB} at temperature T, δ_{GB} the grain boundary thickness, k_b the Boltzmann constant and Ω the atomic volume. The α and β parameters depend on the ratio of the grain boundary diffusion to surface diffusion $\xi = \delta_{GB}D_{GB}/\delta_S D_S$ [46]. Here, for a given temperature, grain boundary and surface diffusion coefficients D_{GB} and D_S were chosen and $(\alpha;\beta)$ were set in accordance with ξ parameter (Table 3.1 and [28]). Eq. (3.2) introduces a viscous component (repulsive or attractive) that counteracts the relative approach of the two particles while the second term is always attractive and represents the force responsible for shrinkage. Another method for accounting for unequal size particles in Eq. (3.2), in analogy with elasticity, is to use the equivalent radius $\frac{r_s r_l}{r_s+r_l}$ [28], [38], [52]. The two methods depart only markedly for large size ratios, for which Eq. (3.2) better captures the Pan et al. [14] finite difference results, with larger values of both the viscous and tensile components. Eq. (3.2) introduces the contact radius a to the power 4 in the viscous term, thus accounting for the slower kinetics of sintering as a increases. Our DEM model introduces a contact radius evolution equation. The Coble model [53], valid for equal-sized particles writes:

$$a^2 = 2rh \tag{3.4}$$

For two particles of different sizes, Pan et al. [14] fitted their finite difference simulation results to obtain a generalized equation:

$$a^2 = \kappa \left[0.5 \left(1 + \frac{r_s}{r_l}\right)\right]^{\zeta} r_l h \tag{3.5}$$

where $\kappa = 2.4$ and $\zeta = 1.5$ are fitted empirical values. Note that in the original Pan's equations (Eqs. (3.2) and (3.5)), the initial radii are considered whereas in our DEM model, we use the current radii. The proposed model reproduces correctly the original results from Pan et al. [14] (see section A.1 of the Supplementary Information (SI)).

As the contact grows, the sum of the grain boundary and surface energies may reach a local minimum from which any perturbation of the contact shape increases the total energy. This equilibrium state is obtained when the contact angle Ψ reaches the equilibrium dihedral angle Ψ_{eq}. The calculation of the corresponding equilibrium contact radius a_{eq} is based on geometric considerations to obtain a relation between the contact angle Ψ and the contact radius a, whatever mechanism is at play for its growth. This results in a set of nonlinear equations (see section A.2 of the SI) that can be numerically resolved and fitted linearly reasonably well for a wide range of contact angles and particle size ratios leading to:

$$a_{eq} = \frac{\Psi_{eq}}{\hat{\Psi}} \frac{r_s}{1 + \frac{r_s}{r_l}} \tag{3.6}$$

where $\hat{\Psi} = 92.937°$ is a fitted constant. This is a generalization of the work of Lange [3], which assumed a simplest contact geometry strictly defined by the intersection of two spheres. Finally, when $a = a_{eq}$ the equilibrium configuration is reached and the tensile shrinkage term in Eq. (3.2) is set to zero so that any additional growth of the contact requires a compressive force. Additionally to normal interactions (Eq. (3.2)), tangential viscous interactions are also introduced as detailed in [38], with a dimensionless viscous parameter $\mu_v = 0.01$.

3.2.2 Grain growth

The evolution of the radius of a particle is calculated by considering the exchange of volume at each contact, with the volume flux always from the smaller to the larger particle. The sum of volume fluxes for each particle leads to an updated radius. When the volume of a given particle decreases below a critical value ($C \times \frac{4}{3}\pi r_{m,0}^3$) (with $r_{m,0}$ the initial mean radius), the particle is simply removed from the box and its volume is equally distributed to all remaining particles. We checked that results are not affected by the value of C, providing $C \leq 10^{-3}$.

The values of the current contact radius (Eq. (3.5)) and contact equilibrium size (Eq. (3.6)) are used to activate specific grain growth mechanisms. When activated, the equation for the volume variation of a *large* particle l in contact with a *small* one s writes:

$$\frac{\mathrm{d}V_{l,s}}{\mathrm{d}t} = 4\pi r_l^2 \frac{\mathrm{d}r_l}{\mathrm{d}t} = \sum_i J_i A_i \Omega \tag{3.7}$$

where the volume exchanged for a given contact $\mathrm{d}V_{l,s}$ is due to different mechanisms of mass transport (*Surface* diffusion S or *grain boundary Migration* GBM), each one represented by a flux cross-section area A_i and by an atomic flux density J_i ($i = S, GBM$):

$$J_i = -\frac{D_i}{k_b T} \nabla P_i \tag{3.8}$$

GB migration and surface diffusion are considered here as they are recognized as the two mass transport mechanisms contributing to grain growth as discussed in the introduction. Both mass fluxes can be represented by a generic form, where D_i is the diffusion coefficient of the mechanism, and ∇P_i the Laplace pressure gradient that causes mass transfer. The volume variation of the smaller particle s in contact with the larger one l is $\frac{\mathrm{d}V_{s,l}}{\mathrm{d}t} = -\frac{\mathrm{d}V_{l,s}}{\mathrm{d}t}$, thus ensuring volume conservation.

Both grain growth mechanisms are based on the curvature gradient as the driving force. The curvature difference is related with the chemical potential [54], which is proportional to the local Laplace pressure gradient. Denoting γ_S and γ_{GB} the surface and grain boundary energies, for two spherical particles the Kelvin equation leads to a Laplace pressure difference of $2\gamma_S \left(\frac{1}{r_l} - \frac{1}{r_s}\right)$ and $2\gamma_{GB} \left(\frac{1}{r_l} - \frac{1}{r_s}\right)$ for surface diffusion and GB migration, respectively [3], [55]. Although reasonable for surface diffusion, this expression is a simplification of the real configuration for GB migration. First, it is considered that grain boundary interfaces are dominant when grain boundary migration is active and, as proposed in mean field theories of grain growth [5], [56], a mean Laplace pressure difference at particle scale is used.

The activation criteria for these mechanisms are based on equilibrium considerations. For surface diffusion, matter from the smaller particle has to flow to the neck before migrating to the larger particle. Therefore, to allow mass transfer between particles, the local neck curvature cannot be concave. This configuration occurs when two particles in contact reach the equilibrium configuration [3], i.e., the contact angle Ψ reaches the equilibrium dihedral angle Ψ_{eq}. Hence, grain growth by surface diffusion is activated once the condition $a \geq a_{eq}$ is fulfilled. (Fig. 3.2 stage 2). At this stage, as stated above, the shrinkage term in Eq. (3.2) is set to zero (Fig. 3.2 stage 2).

For GB migration, the growth is activated when thermodynamically favorable conditions are met, i.e., when the grain boundary area does not increase during GB mi-

gration [3]. Thus, GB migration is activated in our model when the contact radius is equal or greater than the radius of the smallest particle (Fig. 3.2 stage 3).

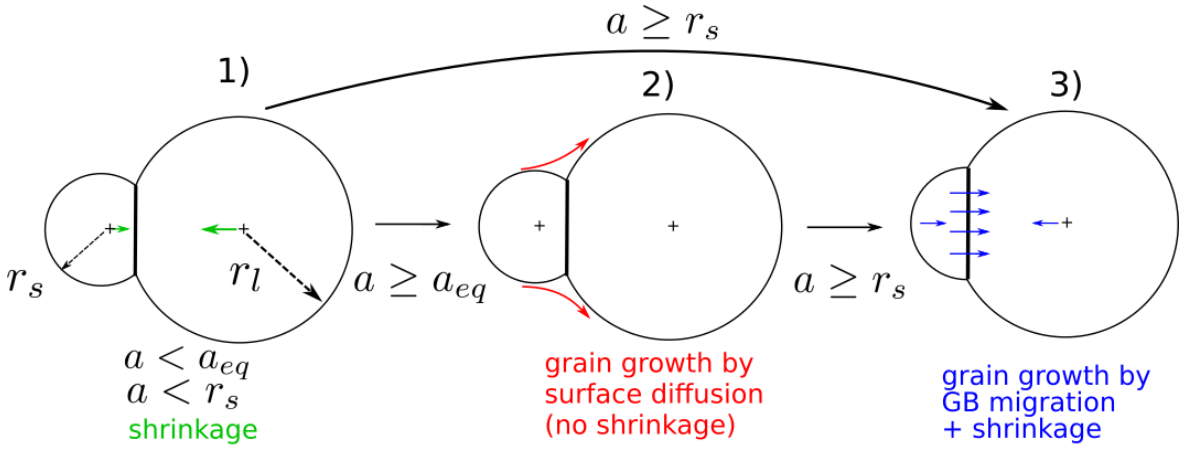

Figure 3.2: Possible mechanisms activated for sintering and grain growth. 1) Standard sintering with shrinkage without grain growth when the neck is sufficiently small. 2) Surface diffusion without shrinkage when the neck radius is larger than or equal to the equilibrium neck radius (Eq. (3.6)). 3) GB migration with shrinkage when the neck radius is larger than or equal to the smallest particle radius. Note that mechanism 1) may lead directly to 3). The GB considered in the model is not flat, the straight line in the figure is only a representation.

The pressure gradient calculation in Eq. (3.8) necessitates the definition of a proper distance to write the local Laplace pressure gradient. For surface diffusion, we choose the center-to-center distance, $(r_s + r_l - h)$, considering that it represents a suitable average distance for the flux of matter. For GB migration, instead of using the transverse grain boundary diffusion coefficient D_{GBM} as the input parameter we introduce the more convenient and often used grain boundary mobility, $M_{GB} = \frac{D_{GBM}\Omega}{k_b T \delta_{GB}}$. Hence, the considered diffusion distance is implicitly the grain boundary thickness δ_{GB}. At the macroscopic scale, the grain boundary mobility depends on the porosity [57], [58] and the grain boundary misorientation [59], [60]. In our model, we consider the intrinsic grain boundary mobility [61], that depends only on temperature via an Arrhenius law [57]. Porosity is indirectly taken into account by the local configuration of contacts. Additionally, the grain boundary and surface energies are considered constant. The exchange area for surface diffusion is a circular ring of radius a and thickness of the surface diffusion layer δ_S. For GB migration, it is the entire area of the neck, that is considered as circular.

The DEM implicit assumption of indented spherical particles is no more fulfilled for the small particle at the later stage of grain growth [14], [23]. The DEM geometrical sphere simplification leads to a very small contact area in the last instants of grain growth which unrealistically slows down mass transport. Thus, we assume this area to

be constant (with a^* the related neck radius) for the computation of matter fluxes and contact forces from the beginning of GB migration. With these simplifying assumptions, the following contributions for the fluxes of matter by *Surface* diffusion ($i = S$) and *grain boundary migration* ($i = GBM$) write:

$$\left(\frac{\mathrm{d}V_{l,s}}{\mathrm{d}t}\right)_S = -2\frac{D_S}{k_b T}\gamma_S \Omega \frac{\frac{1}{r_l} - \frac{1}{r_s}}{r_l + r_s - h}\left[\pi(a+\delta_S)^2 - \pi a^2\right] \tag{3.9}$$

$$\left(\frac{\mathrm{d}V_{l,s}}{\mathrm{d}t}\right)_{GBM} = -2M_{GB}\gamma_{GB}\left(\frac{1}{r_l} - \frac{1}{r_s}\right)\left[\pi a^{*2}\right] \tag{3.10}$$

Both coefficients M_{GB} and D_S introduce temperature dependence through Arrhenius law with pre-exponential factors M_{0GB} and D_{0S}, and activation energies Q_{GBM} and Q_S, respectively.

To sum up, Eqs. (3.9) and (3.10) are applied at each time step for each contact when appropriate conditions are met by a. Three scenarios are possible as sketched in Fig. 3.2 depending on the values of the contact radius. The shrinkage force is reactivated in stage 3. This reactivation is required to avoid unrealistic losses of contacts when particle size ratio becomes too large. In addition, for the sake of simplicity and considering that once GB migration is activated it is the dominant mechanism [10], [11], matter transport by surface diffusion is not active for a contact in stage 3. Note also that stage 3 may arise either from stage 1 or 2. The model thus creates a coupling between grain growth and sintering kinetics, which will be studied in the next sections.

3.3 Results and discussion

The grain growth mechanisms considered above are valid for a wide variety of ceramics and metals. To illustrate the accuracy of the model, we choose to apply it to alumina, as literature provides extensive material data (see Table 3.1). No fitting parameter is used in this comparison. A wide variation of D_S is reported in the literature as discussed by Tsoga and Nikolopoulos [62]. We chose the data of Robertson and Chang [63] (powder from Morganite inc.) as they were obtained for the largest temperature range (1100-1720°C). This leads to a ratio between grain boundary and surface diffusion $\xi = 0.001$. Likewise, M_{GB} has a wide range that depends strongly on porosity [57] and on the presence of dopants [12], [64]. To our knowledge, experimental GB mobility data for porous alumina (relative density < 0.95) is available in literature only for temperatures above 1600°C [12], [13]. We chose the GB mobility from [57] measured for the largest temperature range (1325-2020°C). As this data is for dense alumina and the GB mobility M_{GB} is one of the most relevant parameters affecting grain growth, we

$\delta_{GB}D_{0GB}$ (m^3/s)	1.3x10^{-8} [65]	Q_{GB} (kJ/mol)	475 [66]
D^*_{0S} (m^2/s)	0.09 [63]	Q_S (kJ/mol)	313.8 [63]
M^*_{0GB} (m^3/(N.s))	0.02 [57]	Q_{GBM} (kJ/mol)	443 [57]
Ψ_{eq} (°)	138 [62]	Ω (m^3)	2.11x10^{-29} [63]
γ_S (J/m^2)	0.905 [63]	γ_{GB} (J/m^2)	$2\gamma_S \cos(\Psi_{eq}/2)$
α[1]	2.46 or 2.48 [46][1]	β	4 [46]
$r_{m,0}$ (μm)	0.2 [67]	σ_0	0.23 [67]

[1] $\alpha = 2.46$ for D^*_{0S} ($\xi = 0.001$) and $\alpha = 2.48$ for $0.1D^*_{0S}$ ($\xi = 0.01$), linearly interpolated from [46].

Table 3.1: Parameters used in the simulations for alumina. Diffusion coefficients and mobility are functions of the temperature T with Arrhenius dependence of the form $\exp\left(\frac{-Q}{RT}\right)$. Simulations are conducted at T=1350°C.

will study the influence of lower values of M_{GB}. All parameters used in the simulations are shown in Table 3.1.

3.3.1 Sintering of two particles

First, we compare our results with other approaches on a simple configuration made of two unequally sized particles. Kumar et al. [23] have tackled this problem through numerical simulations by representing thermodynamic quantities in the system by phase fields and minimizing its total free energy (bulk free energy, surface and grain boundary energy). Using a surface mesh and the Surface Evolver program, Wakai et al. [26] also provide numerical solutions with a rather different method. Note that the initial ratio of the two particles is different in the two studies ($\frac{r_{s,0}}{r_{l,0}} = 0.5$ and 0.75) and that Wakai et al. consider sintering by evaporation-condensation instead of coupled GB/surface diffusion as in Kumar's study and the present one. Fig. 3.3 compares the evolution of the contact radius and of the radius of the smaller particle (both normalized by their maximum values) from the present study to those of these prior works. Two simulations with different values of the initial size ratio at 1350°C for alumina were carried out. Three stages corresponding to the three possible mechanisms modeled (Fig. 3.2) are clearly visible on the simulations: initial neck growth without changes in radii followed by a second stage characterized by a slow decrease of the small particle radius at a nearly constant neck size and a third stage with both fast decrease in neck size and small particle radius.

The evolution of the contact size and the small particle size (Fig. 3.3) are in correct qualitative accordance with both Kumar et al. and Wakai et al. albeit an earlier onset of grain growth for their simulations. Also, the transitions between each stage are more gradual in their simulations as in our model different mechanisms cannot

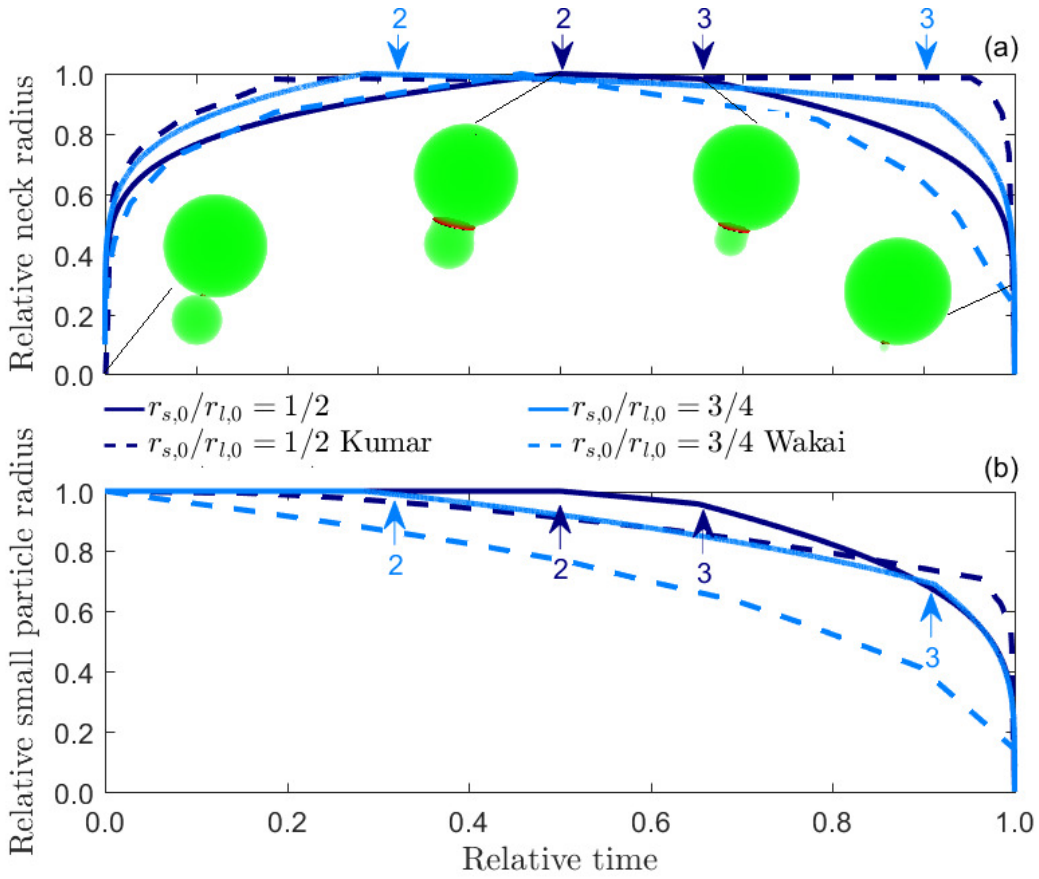

Figure 3.3: Evolution of the normalized contact radius $\frac{a}{\max(a)}$ (a) and of the normalized smaller particle radius $\frac{r_s}{\max(r_s)}$ (b) for two values of the initial size ratio $r_{s,0}/r_{l,0}$. Comparison with results from Kumar et al. [23] and Wakai et al. [26]. The numbers and arrows show the beginning of second (surface diffusion) and third (grain boundary migration) stages (Fig. 3.2). Time is normalized by the total time of disappearance of the smaller particle. Snapshots of the configuration of the pair of particles and the neck are given at various stages: initial, stage 2 and 3 and on the way to the final disappearance of the smallest particle. The images have been generated from particles positions and radii, and the computed neck size (Eq. (3.5)). The geometry used to represent the necks is two inverse tori tangent to each particle, which degenerate to a cylinder having the radius of the small particle in the last stage (see section A.2 of the SI).

occur simultaneously (e.g. grain growth by surface diffusion and GB migration). In addition, in our model an underestimation of the mass transport by surface diffusion is possible due to the distance chosen ($r_s + r_l - h$) for the gradient in Eq. (3.8) as this approximation is reasonable if we assume a linear gradient. In all practical situations where the gradient is not linear, the gradient will be steeper.

In short, it can be concluded that our simplistic two-sphere scheme correctly reproduce the scenario predicted by both the phase field approach of Kumar et al. [23] and the surface evolver approach of Wakai et al. [26], but with significantly less computational effort. This is both mandatory, as we are aiming for several tens of thousands of particles in DEM, and encouraging as it means that DEM simulations will not com-

promise too much on accuracy compared to more elaborate methods.

The influence of the two main material parameters of the grain growth model, namely surface diffusivity and grain boundary mobility is assessed. Fig. 3.4a indicates that, as expected, higher values of both parameters reduce the time for disappearance of the smallest particle. We checked that the values are in the same order of magnitude than that of Pan et al. [14]. Fig. 3.4a also clearly shows the necessity to include both mechanisms in a coarsening model at the length scale of particles. If only surface diffusion (first decay slope) is considered, it would take an unrealistically long time to remove the whole mass. Despite the rapid action of GB migration (second decay slope), surface diffusion is required to reach the geometric starting conditions, i.e., the small particle size reaches the neck size.

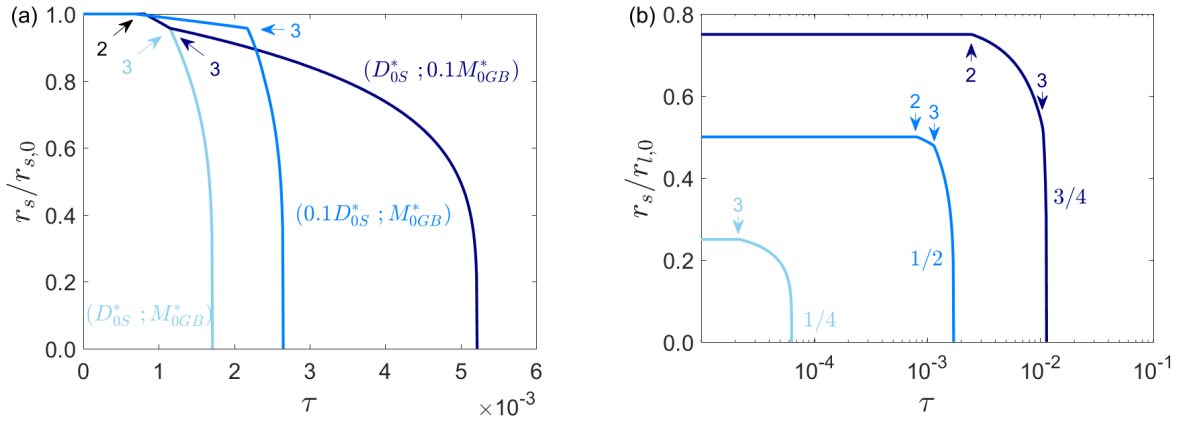

Figure 3.4: Evolution of the smaller particle radius with normalized time $\tau = \frac{r_{l,0}^4 k_b T}{\gamma_S D_{GB} \delta_{GB} \Omega}$ [14]. a) For different pair values of surface diffusivity (D_S) and grain boundary mobility (M_{GB}) defined by the values in Table 3.1. The radius of the smaller particle is normalized by its initial value (r_{s0}). b) For different initial size ratios between the smaller and larger particles. The radius of the smaller particle is normalized by the initial radius of the larger particle (r_{l0}). The numbers show the beginning of stage 2 (surface diffusion) and 3 (GB migration) (see Fig. 3.2).

Realistic initial green packings should feature particles with a wide range of size ratios. Fig. 3.4b displays the disappearance dynamics of the smallest particle for different initial size ratios. As expected from examining the gradient terms in Eqs. (3.9) and (3.10), the vanishing time is considerably shorter for smaller ratios, with two orders of magnitude, between the vanishing times of ratios $\frac{1}{4}$ and $\frac{3}{4}$. Surface diffusion, if activated, is the limiting stage for grain growth due to its duration. Interestingly, for ratio $\frac{1}{4}$ stage 2 is absent. This is because this configuration already exhibits, after sintering (stage 1), the geometrical conditions to immediately start grain growth by GB migration.

3.3.2 Sintering of large packings of particles

Packings made of 40,000 and 400,000 particles were used. The preparation procedure of the initial green packings is detailed in section A.3 of the SI.

3.3.2.1 Comparison to Nettleship experimental data

In order to evaluate the newly formulated model at the scale of a large packing, we chose to focus on the only study on alumina that carefully reports the particle size distribution during sintering (see section A.3 of the SI for a description of the lognormal(μ_0, σ_0^2) size distribution adopted here) [67]. Indeed, we observed that the initial particle size distribution significantly affects the simulation results, hence the need to have access to this information for a proper comparison. The simulation parameters are reasonable values from the literature (Table 3.1) and the initial particle size distribution and green density match the experiments of Nettleship et al. The comparison is carried out in terms of grain size - relative density trajectory (Fig. 3.5a) and evolution of the lognormal law parameter σ (Fig. 3.5b). Three different values of GB mobility were tested. The simulations were stopped either when they reached $D = 0.95$ or when they experienced very rapid grain growth that was incompatible with numerical stability within reasonable computational times. Simulations show that GB mobility strongly affects the results and that the nominal value M^*_{0GB} taken from literature measurements on dense alumina is too high to reproduce the grain growth trajectory of Nettleship sintering experiment. A more appropriate value might lie between $0.25M^*_{0GB}$ and $0.5M^*_{0GB}$, and it is probable that this value evolves with density during the course of sintering [9]. Fig. 3.5b shows that the self-similarity (i.e. $\sigma =$ constant) observed in Nettleship experiments up to $D \approx 0.9$ is not correctly reproduced by simulations but the widening of the size distribution during the whole sintering is in reasonable agreement. At the onset of grain growth, before particles begin to disappear, a strict self-similarity is not expected in the simulations as mass transfer between particles increases the size of large particles and decreases the size of small particles, thus broadening the size distribution. The first part of simulations with a moderate increase of σ can however be interpreted as a normal grain growth, in contrast to the faster increase of σ observed for M^*_{0GB} that is typical of abnormal grain growth i.e., a fast increase in size of only a few particles. Such behavior is also observed for experimental data, but only above $D = 0.95$. It is worth noting that while local variations of GB mobility (due to inhomogeneous distribution of impurities, crystallographic orientations, etc...) are generally claimed to be responsible for abnormal grain growth [9]; here, we observe that these, while surely exacerbating the phenomenon, do not appear to be mandatory. Last, 40k and

400k packings exhibit very similar outputs indicating that 40k particles are sufficient to obtain representative results with periodic boundary conditions in this system.

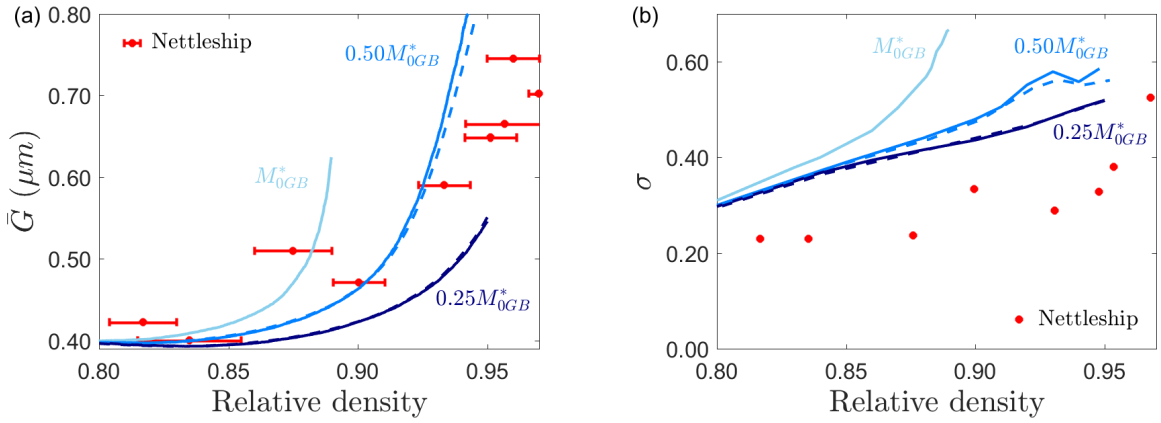

Figure 3.5: Comparison of DEM simulations with alumina experimental data from Nettleship et al. [67]. Simulations results are obtained using three different values of grain boundary mobility (M_{GB}) with M^*_{0GB} given in Table 3.1. Results for packings made of 40k particles (solid lines) and 400k particles packings (dashed lines) are shown. (a) Mean grain size-density trajectories. (b) σ parameter of the lognormal(μ, σ^2) grain size distribution along densification.

Various visual representations of the microstructure evolution during a sintering simulation are provided in Fig. 3.6. It is interesting to note that at $D = 0.85$ grain growth is clearly present visually while it is barely noticeable on the mean grain size value ($\frac{\bar{G}-\bar{G}_0}{\bar{G}_0} \approx 1\%$). In other words, it is not required to observe a significant increase in mean grain size to have significant grain growth that might influence the microstructure and sintering kinetics. Another remarkable point is a global microstructure coarsening. Indeed, even if a quantitative evaluation has not been performed, pore coarsening is clearly observed above $D = 0.85$. On the last two snapshots, some contact impingements are also noticed. These impingements are in conflict with the DEM hypothesis of independent treatment of the contacts but we believe that, at least in the density range 0.85 - 0.9, they are relatively rare events that do not challenge the simulation results. However, above $D = 0.9$ the simulation results should be taken with more caution.

3.3.2.2 Sintering and grain growth kinetics

Although Nettleship et al. do not report grain growth kinetics, it is an important output of the simulation that can be investigated in light of the existing classical power laws. Using simulations described above, both relative density and mean grain size are plotted on Fig. 3.7 as a function of the normalized time $\tau = \frac{r^4_{m,0} k_b T}{\gamma_S D_{GB} \delta_{GB} \Omega}$. A first qualitative observation is that, in these typical sintering conditions, grain growth

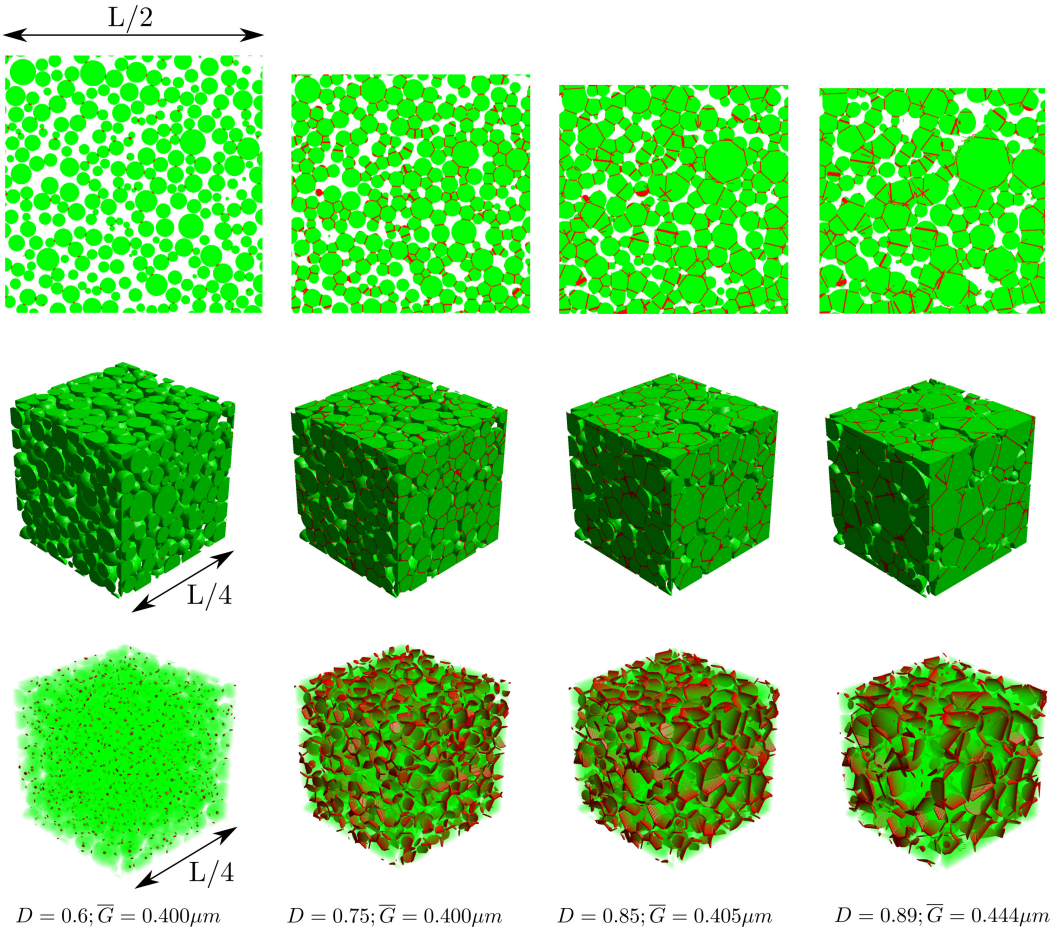

Figure 3.6: Evolution of the microstructure of a 40k particles packing, $0.5M^*_{0GB}$ and $\sigma = 0.23$. The 2D and 3D images have been generated from particles positions and radii, and the computed neck sizes (Eq. (3.5)). The geometry used for the necks is two inverse tori tangent to each particle (see section A.2 of the SI) and GBs are displayed in red. For the sake of clarity only a portion of the total volume (L^3) is shown.

slows down densification kinetics. This is a classically observed phenomenon, which is explained both by a decrease of the driving force for sintering and by an increase of the diffusion distances, with the increase of particle size. In addition, simulations show that this decrease in densification rate is pronounced even for a barely perceptible increase in mean grain size and seems to limit the achievable final density. This last point should be taken with care, however, as the DEM intrinsic hypothesis to treat separately the contacts is not met at high densities. An intriguing and also never or rarely experimentally observed point, but reported in the idealized grain growth simulations of Wakai et al. [68], is the observed slight decrease in mean grain size before the expected increase. The explanation is nonetheless very simple: for a given volume transferred from a smaller particle to a larger one, the decrease of the small particle radii will be proportionally more important than the radius change of the larger particles, thus decreasing the mean radius. The subsequent increase in mean particle

size is a direct consequence of the decrease of the number of particles, a phenomenon only active after some time as observed in Fig. 3.7b. This time represented by dotted lines represents the incubation and transition periods reported by Wakai et al. from which the classical power law ($\bar{G}^n - \bar{G}_0^n \propto t$) starts. We obtain n values in between 2.6 and 3.1, which are consistent with experimentally observed values [4], [7] but slightly larger than the expected value $n = 2$ from theory [5], [9], [11]. This theoretical value has been derived under the assumption of GB migration as the dominant mechanism. The mean field analysis conducted by Hillert [5] or its simplified version proposed by Kang [9] can be applied to Eqs. (3.9) and (3.10) (see section A.4 of the SI). The theoretical exponents obtained are $n = 4$ for grain growth by surface diffusion (Eq. (3.9)) and, as expected, $n = 2$ for grain growth by grain boundary migration (Eq. (3.10)). It is thus consistent with our results which indicate that n tends to 2 as the grain boundary mobility increases. For the highest value of the grain mobility, abnormal grain growth runaway was triggered in the simulation. This simulation has been stopped at this point as it was not possible to handle it correctly and no power-law fit was attempted. The value $n = 4$ predicted by Riedel et al. [69] takes into account the pinning of GB by closed pores which slows down the grain boundary motion. Our model does not take this pinning into account but nevertheless reproduces correctly the experimental data up to quite high densities.

The rate of disappearance of grains is not widely discussed in the solid-phase sintering literature. For dense materials [70] or liquid phase sintering [4] it is accepted that the number of grains N_p scales with the inverse of time ($N_p \propto 1/t$). Fig. 3.7b indicates that simulations lead to $N_p \propto 1/t^m$ with $1.2 < m < 1.5$, where higher GB mobilities result in higher rates of decay. Note that for longer times τ, the rate of decay slows down and m tends towards values closer to unity.

3.3.2.3 Influence of particle size distribution

Our model can be advantageously used to study the impact of the initial particle size distribution, a task that would be tedious experimentally, and that is hardly accessible by other numerical approaches due to the large number of particles required. It is observed in Fig. 3.8 that a slight broadening of the initial size distribution can strongly promote early grain growth. This effect of initial particle size distribution is a common experimental observation [4], [71]–[74]. From our two particle results in Fig. 3.4b, we conclude that a direct grain boundary migration (i.e., without surface diffusion stage) is one of the mechanisms for earlier grain growth of wider distributions that necessarily exhibit larger particle size ratios. In addition, the slight initial decrease of the mean grain size (Fig. 3.8) disappears for larger size distribution. This explains why this

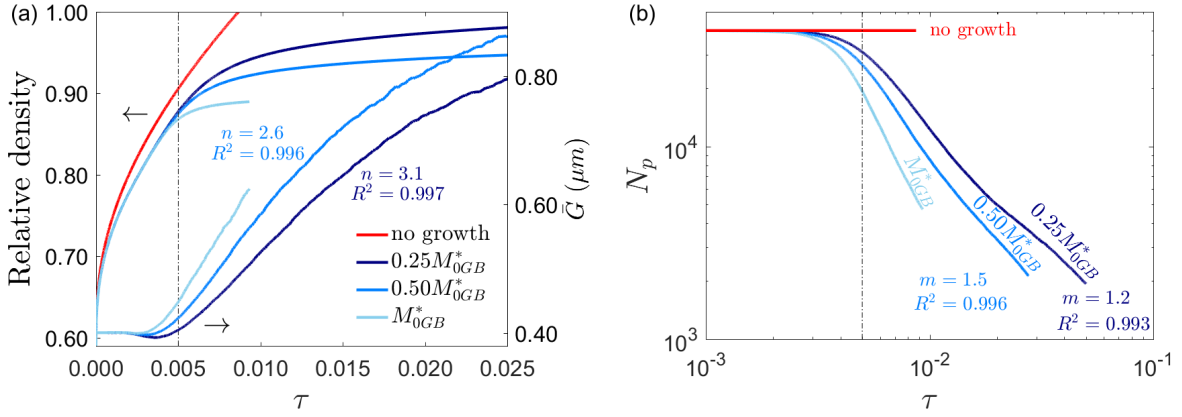

Figure 3.7: Densification and grain growth kinetics for three values of GB mobility with M^*_{0GB} from Table 3.1 together with a simulation without any grain growth. Dashed vertical lines indicate the starting time for the fitting curves. (a) Relative density and mean grain size $\bar{G}$ versus normalized time $\tau = \frac{r^4_{m,0} k_b T}{\gamma_S D_{GB} \delta_{GB} \Omega}$. The power-law exponents n for grain growth ($\bar{G}^n - \bar{G}^n_0 \propto t$) are indicated together with their R-square values. (b) Number of particles N_p (for a 40,000 particles packing) as a function of normalized time τ. The exponent m of the power-law $N_p \propto 1/t^m$ is indicated.

phenomenon, although reported in simulations [68], is not observed experimentally.

3.3.2.4 Normalized grain size - density trajectory and comparison with experimental data

The observed large influence of the initial size distribution confirms that any direct comparison with experimental data not reporting it might be doubtful. Still, after the initial assessment of the model using Nettleship data we sought for a broader simulation-experiment comparison. Available data encompasses very different mean (or median) particle sizes, sintering temperatures, purity and size distributions (mostly unknown). Still, Bernard-Granger et al. have demonstrated that ${\bar{G}_0}^2/\bar{G}^2$ is linear with D [11] under the assumption that the main mechanism for grain growth is GB migration. According to their work, the proportionality coefficient k is a function of $\bar{G}_0$ and the ratio of diffusion coefficients D_{GBM}/D_{GB}. The temperature has only a minor influence on k through the different activation energies of D_{GBM} and D_{GB}, which is consistent with the observation that grain size - density trajectory is not temperature-dependent [11]. Thus, the comparison between our isothermal simulations with experimental data using a heating rate ramp followed by an isothermal dwell is relevant. Section A.6 of the SI confirms that the introduction of a realistic heating rate ramp has no significant impact on the grain size - density trajectory. This relationship between grain size and density has actually long been experimentally observed as reported by German [4], but in the form $\bar{G} = \theta \bar{G}_0/\epsilon^{1/2}$ with $\epsilon = 1 - D$ the porosity. As illustrated in Fig. 3.9, plot-

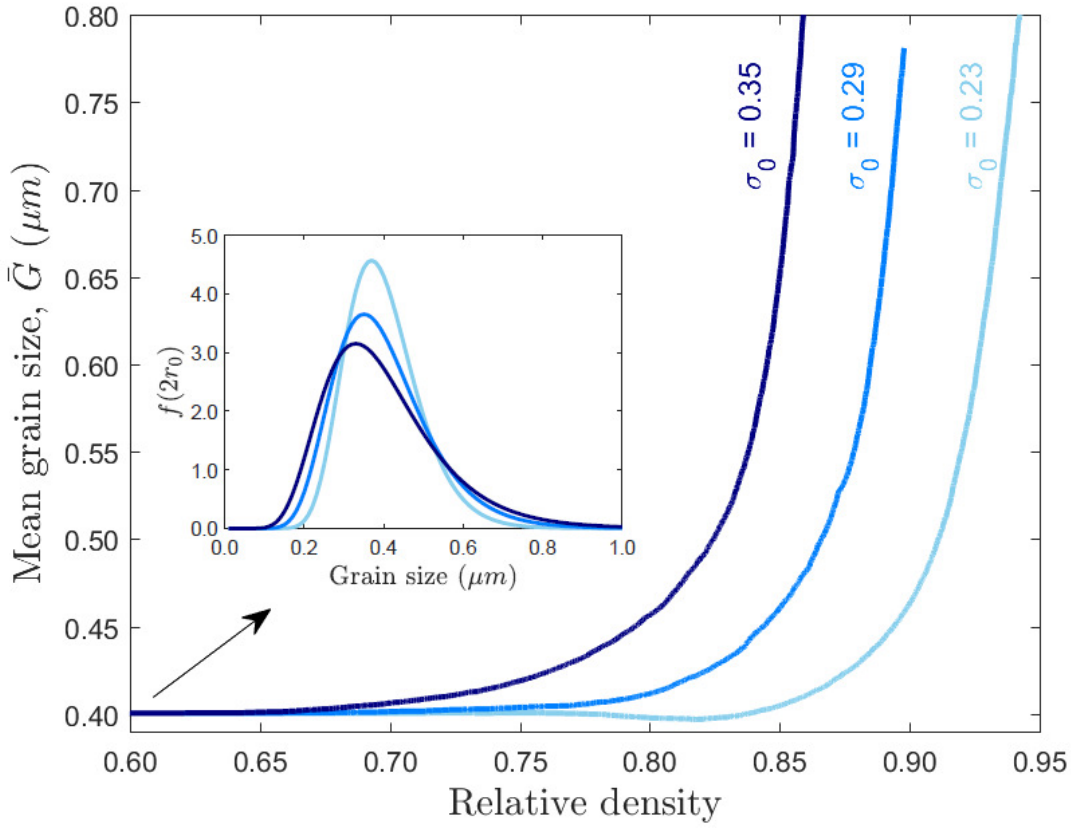

Figure 3.8: Effect of the initial size distribution on grain growth. Mean grain size $\bar{G}$ as a function of density for three initial standard deviations of the lognormal(μ_0, σ_0^2) distribution. A wider distribution results in earlier grain growth. The initial size distribution for each sample is shown in the inset.

ting $\bar{G_0}^2/\bar{G}^2$ versus relative density is an attractive approach to normalize and report very different experimental data on a single plot. The linearity is clearly confirmed for most of the collected data. German proposed that θ has generally a value near 0.6. Given that the slope k in Fig. 3.9 is related to θ by $\theta = 1/|k|^{1/2}$, we obtain a wider range $0.41 < \theta < 0.72$ from the literature (not considering values from Bae and Baik that are not typical due to the very large particle size). The numerical results also show that $|k|$ decreases with grain size and the values obtained are in agreement with those computed from the theoretical formula of Bernard-Granger et al. [11], using the same set of parameters (see section A.5 of the SI). The simulations bring valuable additional information and show that the decrease of $|k|$ with grain size is associated with an earlier and more progressive, non-linear, onset of grain growth. The influence of a narrower size distribution is a delayed onset of grain growth but without considerable change in $|k|$. A decrease of grain boundary mobility logically slows grain growth in favor of densification. The onset of grain growth is also slightly delayed to larger densities and the beginning of the trajectory is non-linear with a moderate rate

which might be related to more important first stage of grain growth dominated by surface diffusion. Indeed, linearity has been established under the assumption of grain growth by GB migration only. Interestingly, the experiment of Berry et al. (Al_2O_3 without MgO doping) also exhibits a non-linear trajectory but with a different shape as compared to the simulations. The same curve behavior of Berry et al. is observed in Greskovich and Lay [75] and in Zhao and Harmer [64]. While the simulation trajectory has a convex shape (increasing grain growth - density rate) the experiment trajectory has a concave shape (decreasing grain growth - density rate). This latter behavior might be explained by a decreasing GB mobility at the onset of pore closure due to an associated increase of pore drag. In addition, pore and grain sizes could also influence the GB mobility through varying amount of drag effects. Introducing a density- or grain-size-dependent grain boundary mobility could thus make some sense and help to model more correctly some experimental cases.

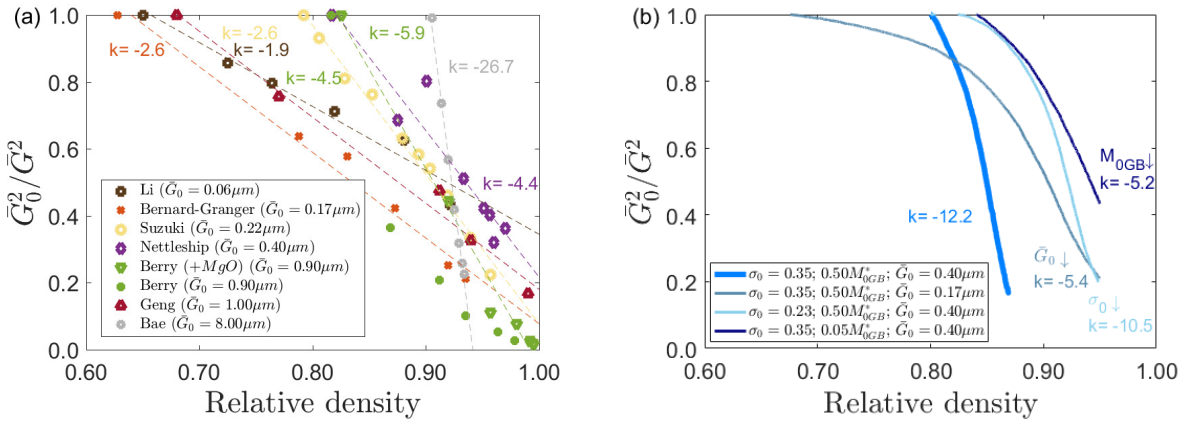

Figure 3.9: Grain size-density trajectories. (a) Experimental data (symbols) from Li and Ye [76], Bernard-Granger and Guizard [10], Geng et al. [77], Nettleship et al. [67], Suzuki et al. [78], Berry and Harmer [12] and Bae and Baik [13]. Dashed lines show linear fits with the corresponding slope k. (b) Simulations results obtained for different initial mean grain size $\bar{G}_0$, initial grain size distribution σ_0 and grain boundary mobility M_{0GB}.

It can be concluded that, by adjusting the particle size distribution and GB mobility, the model has the ability to reproduce the large range of observed grain growth - density trajectories. However, we believe that using these as two fitting parameters might not be relevant since the involved intercorrelated phenomena might be too complex to be caught by a simple variation of grain size with density.

3.4 Conclusion

Sintering and grain growth are a highly coupled phenomena with shrinkage, surface diffusion, grain boundary migration and particle coalescence arising simultaneously, that

poses a challenge to current simulation methods. Until now, these couplings have only been successfully treated by mesoscale phase-field or Monte Carlo methods. By taking full advantage of the 3D discontinuous discrete element framework, simulations presented here provide an alternative that has the ability to treat very large systems. The adopted model treats nonetheless the main fluxes of matter between particles through physically-based interaction laws to provide reasonable accuracy. Its limitation lies mainly on the assumption that interactions between particles are handled as pairs. As densification progresses, contact impingement becomes more likely which restricts the domain of quantitative validity of our DEM simulations to initial and intermediate sintering stages ($D \leq 0.90 - 0.95$). Also, our model considers a grain boundary mobility that only depends on temperature. This is questionable for the final stage of sintering for which the pore drag force on grain boundary mobility can be significant. Still, for initial and intermediate stages, using reasonable material parameters from the literature the model correctly reproduces experimental mean grain size evolution for alumina. For realistic particle size distribution, grain growth can affect the sintering kinetics and the microstructure evolution early in the first stage and in the intermediate stage of sintering. Hence, the realism of DEM simulation of sintering is largely improved by the present model as compared to earlier DEM approaches that do not account for grain growth. Taking advantage of the large systems tractable by DEM, the influence of initial particle size distribution on grain growth has been studied. The DEM simulations show, as reported from experiments [4], that broader particle size distributions exhibit faster grain growth. This points to some potential avenues for retarding grain growth with narrower initial size distributions. However, narrow size distributions are difficult to achieve experimentally and lead to a smaller green density that is detrimental for densification. The present DEM model might help to optimally choose the size distribution for a given system. As large-scale simulations are feasible with DEM (up to 400 000 particles have been treated here), future work will address more complex sintering conditions (sintering on a substrate, composites, presence of defects, stress-assisted sintering, two-step sintering...). Improvements of the model should for example consider the use of a porosity- or impurity-dependent GB mobility. This should provide a better understanding of the conditions, strongly dependent on GB mobility, that lead either to the emergence of a self-similar grain size distribution or, on the contrary, to abnormal grain growth. Further improvements of the model, however, will be hampered by a lack of experimental data for its reliable assessment.

References

[1] B. Paredes-goyes, D. Jauffres, J.-m. Missiaen, and C. L. Martin, "Grain growth in sintering : A discrete element model on large packings," *Acta Materialia*, vol. 218, p. 117 182, 2021, ISSN: 1359-6454. DOI: 10.1016/j.actamat.2021.117182.

[2] R. M. German, *Sintering: from Empirical Observations to Scientific Principles*. Boston: Butterworth-Heinemann, 2014, ISBN: 978-0-12-401682-8.

[3] F. F. Lange and B. J. Kellett, "Thermodynamics of Densification: II, Grain Growth in Porous Compacts and Relation to Densification," *Journal of the American Ceramic Society*, vol. 72, no. 5, pp. 735–741, 1989, ISSN: 15512916. DOI: 10.1111/j.1151-2916.1989.tb06209.x.

[4] R. M. German, "Coarsening in sintering: Grain shape distribution, grain size distribution, and grain growth kinetics in solid-pore systems," *Critical Reviews in Solid State and Materials Sciences*, vol. 35, no. 4, pp. 263–305, 2010, ISSN: 10408436. DOI: 10.1080/10408436.2010.525197.

[5] M. Hillert, "On the theory of normal and abnormal grain growth," *Acta Metallurgica*, vol. 13, no. 3, pp. 227–238, 1965, ISSN: 00016160. DOI: 10.1016/0001-6160(65)90200-2.

[6] M. Rahaman, *Ceramic processing and sintering, second edition*. CRC Press, Jan. 2003, pp. 1–875. DOI: 10.1201/9781315274126.

[7] W. D. Kingery and B. Françis, "Grain Growth in Porous Compacts," *Journal of the American Ceramic Society*, vol. 48, no. 10, pp. 546–547, 1965, ISSN: 15512916. DOI: 10.1111/j.1151-2916.1965.tb14665.x.

[8] R. M. German, "The contiguity of liquid phase sintered microstructures," *Metallurgical Transactions A*, vol. 16, no. 7, pp. 1247–1252, 1985, ISSN: 03602133. DOI: 10.1007/BF02670329.

[9] S.-J. L. Kang, *Sintering Densification, Grain Growth, and Microstructure*. Oxford: Butterworth-Heinemann, 2005, pp. xi –xii, ISBN: 978-0-7506-6385-4. DOI: https://doi.org/10.1016/B978-075066385-4/50000-5.

[10] G. Bernard-Granger and C. Guizard, "New relationships between relative density and grain size during solid-state sintering of ceramic powders," *Acta Materialia*, vol. 56, no. 20, pp. 6273–6282, 2008, ISSN: 13596454. DOI: 10.1016/j.actamat.2008.08.054.

[11] G. Bernard-Granger, N. Monchalin, and C. Guizard, "Sintering of ceramic powders: Determination of the densification and grain growth mechanisms from the "grain size/relative density" trajectory," *Scripta Materialia*, vol. 57, no. 2, pp. 137–140, 2007, ISSN: 13596462. DOI: 10.1016/j.scriptamat.2007.03.030.

[12] K. A. Berry and M. P. Harmer, "Effect of MgO Solute on Microstructure Development in Al2O3," *Journal of the American Ceramic Society*, vol. 69, no. 2, pp. 143–149, 1986, ISSN: 15512916. DOI: 10.1111/j.1151-2916.1986.tb04719.x.

[13] I.-J. Bae and S. Baik, "Abnormal Grain Growth of Alumina," *Journal of the American Ceramic Society*, vol. 80, no. 5, pp. 1149–1156, 1997, ISSN: 0002-7820. DOI: 10.1111/j.1151-2916.1997.tb02957.x.

[14] J. Pan, H. Le, S. Kucherenko, and J. A. Yeomans, "A model for the sintering of spherical particles of different sizes by solid state diffusion," *Acta Materialia*, vol. 46, no. 13, pp. 4671–4690, 1998, ISSN: 13596454. DOI: 10.1016/S1359-6454(98)00144-X.

[15] D. Zhang, A. Weng, S. Gong, and D. Zhou, "Computer simulation of grain growth of intermediate*/ and final-stage sintering and Ostwald ripening of BaTiO 3-based PTCR ceramics," *Materials Science and Engineering: B*, vol. 99, pp. 428–432, 2003. DOI: 10.1016/S0921-5107(02)00449-X.

[16] H. Itahara, T. Tani, H. Nomura, and H. Matsubara, "Computational design for grain-oriented microstructure of functional ceramics prepared by templated grain growth," *Journal of the American Ceramic Society*, vol. 89, no. 5, pp. 1557–1562, 2006, ISSN: 00027820. DOI: 10.1111/j.1551-2916.2006.00954.x.

[17] V. Tikare, M. Braginsky, D. Bouvard, and A. Vagnon, "Numerical simulation of microstructural evolution during sintering at the mesoscale in a 3D powder compact," *Computational Materials Science*, vol. 48, no. 2, pp. 317–325, 2010, ISSN: 09270256. DOI: 10.1016/j.commatsci.2010.01.013.

[18] S. Hara, A. Ohi, and N. Shikazono, "Sintering analysis of sub-micron-sized nickel powders: Kinetic Monte Carlo simulation verified by FIB-SEM reconstruction," *Journal of Power Sources*, vol. 276, pp. 105–112, Feb. 2015, ISSN: 03787753. DOI: 10.1016/j.jpowsour.2014.11.110.

[19] Y. Zhang, X. Xiao, and J. Zhang, "Kinetic Monte Carlo simulation of sintering behavior of additively manufactured stainless steel powder particles using reconstructed microstructures from synchrotron X-ray microtomography," *Results*

in Physics, vol. 13, Jun. 2019, ISSN: 22113797. DOI: 10.1016/j.rinp.2019.102336.

[20] A. Kazaryan, Y. Wang, S. A. Dregia, and B. R. Patton, "Grain growth in systems with anisotropic boundary mobility: Analytical model and computer simulation," *Physical Review B - Condensed Matter and Materials Physics*, vol. 63, no. 18, pp. 1–11, 2001, ISSN: 1550235X. DOI: 10.1103/PhysRevB.63.184102.

[21] K. Asp and J. Ågren, "Phase-field simulation of sintering and related phenomena - A vacancy diffusion approach," *Acta Materialia*, vol. 54, no. 5, pp. 1241–1248, 2006, ISSN: 13596454. DOI: 10.1016/j.actamat.2005.11.005.

[22] Y. U. Wang, "Computer modeling and simulation of solid-state sintering: A phase field approach," *Acta Materialia*, vol. 54, no. 4, pp. 953–961, 2006, ISSN: 13596454. DOI: 10.1016/j.actamat.2005.10.032.

[23] V. Kumar, Z. Z. Fang, and P. C. Fife, "Phase field simulations of grain growth during sintering of two unequal-sized particles," *Materials Science and Engineering A*, vol. 528, no. 1, pp. 254–259, 2010, ISSN: 09215093. DOI: 10.1016/j.msea.2010.08.061.

[24] K. Ahmed, C. A. Yablinsky, A. Schulte, T. Allen, and A. El-Azab, "Phase field modeling of the effect of porosity on grain growth kinetics in polycrystalline ceramics," *Modelling and Simulation in Materials Science and Engineering*, vol. 21, no. 6, 2013, ISSN: 09650393. DOI: 10.1088/0965-0393/21/6/065005.

[25] S. Biswas, D. Schwen, J. Singh, and V. Tomar, "A study of the evolution of microstructure and consolidation kinetics during sintering using a phase field modeling based approach," *Extreme Mechanics Letters*, vol. 7, pp. 78–89, 2016, ISSN: 23524316. DOI: 10.1016/j.eml.2016.02.017.

[26] F. Wakai, M. Yoshida, Y. Shinoda, and T. Akatsu, "Coarsening and grain growth in sintering of two particles of different sizes," *Acta Materialia*, vol. 53, no. 5, pp. 1361–1371, 2005, ISSN: 13596454. DOI: 10.1016/j.actamat.2004.11.029.

[27] J. Bruchon, D. Pino-Muñoz, F. Valdivieso, and S. Drapier, "Finite element simulation of mass transport during sintering of a granular packing. Part I. Surface and lattice diffusions," *Journal of the American Ceramic Society*, vol. 95, no. 8, pp. 2398–2405, 2012, ISSN: 00027820. DOI: 10.1111/j.1551-2916.2012.05073.x.

[28] C. L. Martin, L. C. Schneider, L. Olmos, and D. Bouvard, "Discrete element modeling of metallic powder sintering," *Scripta Materialia*, vol. 55, no. 5, pp. 425–428, 2006, ISSN: 13596462. DOI: 10.1016/j.scriptamat.2006.05.017.

[29] K. Shinagawa, "Simulation of grain growth and sintering process by combined phase-field/discrete-element method," *Acta Materialia*, vol. 66, pp. 360–369, 2014, ISSN: 13596454. DOI: 10.1016/j.actamat.2013.11.023.

[30] T. Matsuda, "Development of a DEM taking account of neck increments caused by surface diffusion for sintering and application to analysis of the initial stage of sintering," *Computational Materials Science*, vol. 196, no. April, p. 110 525, 2021, ISSN: 0927-0256. DOI: 10.1016/j.commatsci.2021.110525.

[31] M. W. Reiterer and K. G. Ewsuk, "An analysis of four different approaches to predict and control sintering," *Journal of the American Ceramic Society*, vol. 92, no. 7, pp. 1419–1427, Jul. 2009, ISSN: 00027820. DOI: 10.1111/j.1551-2916.2009.03009.x.

[32] V. Rehn, J. Hötzer, W. Rheinheimer, M. Seiz, C. Serr, and B. Nestler, "Phase-field study of grain growth in porous polycrystals," *Acta Materialia*, vol. 174, pp. 439–449, Aug. 2019, ISSN: 13596454. DOI: 10.1016/j.actamat.2019.05.059.

[33] J. Hötzer, M. Seiz, M. Kellner, W. Rheinheimer, and B. Nestler, "Phase-field simulation of solid state sintering," *Acta Materialia*, vol. 164, pp. 184–195, 2019, ISSN: 13596454. DOI: 10.1016/j.actamat.2018.10.021.

[34] R. Termuhlen, X. Chatzistavrou, J. D. Nicholas, and H. C. Yu, "Three-dimensional phase field sintering simulations accounting for the rigid-body motion of individual grains," *Computational Materials Science*, vol. 186, no. June 2020, p. 109 963, 2021, ISSN: 09270256. DOI: 10.1016/j.commatsci.2020.109963.

[35] F. Parhami and R. M. McMeeking, "A network model for initial stage sintering," *Mechanics of Materials*, vol. 27, no. 2, pp. 111–124, 1998, ISSN: 01676636. DOI: 10.1016/S0167-6636(97)00034-3.

[36] P. Cundall and O. Strack, "A discrete numerical model for granular assemblies," *Géotechnique*, pp. 47–65, 1979, ISSN: 01489062. DOI: 10.1016/0148-9062(79)91211-7.

[37] B. Henrich, A. Wonisch, T. Kraft, M. Moseler, and H. Riedel, "Simulations of the influence of rearrangement during sintering," *Acta Materialia*, vol. 55, no. 2, pp. 753–762, 2007, ISSN: 13596454. DOI: 10.1016/j.actamat.2006.09.005.

[38] C. L. Martin and R. K. Bordia, "The effect of a substrate on the sintering of constrained films," *Acta Materialia*, vol. 57, no. 2, pp. 549–558, 2009, ISSN: 13596454. DOI: 10.1016/j.actamat.2008.09.041.

[39] C. Wang and S. Chen, "Application of the complex network method in solid-state sintering," *Computational Materials Science*, vol. 69, pp. 14–21, 2013, ISSN: 09270256. DOI: 10.1016/j.commatsci.2012.11.020.

[40] S. Martin, M. Guessasma, J. Léchelle, J. Fortin, K. Saleh, and F. Adenot, "Simulation of sintering using a Non Smooth Discrete Element Method. Application to the study of rearrangement," *Computational Materials Science*, vol. 84, pp. 31–39, 2014, ISSN: 09270256. DOI: 10.1016/j.commatsci.2013.11.050.

[41] R. Besler, M. Rossetti Da Silva, J. J. Do Rosario, M. Dosta, S. Heinrich, and R. Janssen, "Sintering Simulation of Periodic Macro Porous Alumina," *Journal of the American Ceramic Society*, vol. 98, no. 11, pp. 3496–3502, 2015, ISSN: 15512916. DOI: 10.1111/jace.13684.

[42] S. Nosewicz, J. Rojek, and M. Chmielewski, "Discrete Element Framework for Determination of Sintering and Postsintering Residual Stresses of," *Materials*, vol. 13, no. 4015, pp. 1–21, 2020. DOI: 10.3390/ma13184015.

[43] A. Wonisch, T. Kraft, M. Moseler, and H. Riedel, "Effect of different particle size distributions on solid-state sintering: A microscopic simulation approach," *Journal of the American Ceramic Society*, vol. 92, no. 7, pp. 1428–1434, 2009, ISSN: 00027820. DOI: 10.1111/j.1551-2916.2009.03012.x.

[44] S. Martin, S. Navarro, H. Palancher, A. Bonnin, J. Léchelle, M. Guessasma, J. Fortin, and K. Saleh, "Validation of DEM modeling of sintering using an in situ X-ray microtomography analysis of the sintering of NaCl powder," *Computational Particle Mechanics*, vol. 3, no. 4, pp. 525–532, 2016, ISSN: 21964386. DOI: 10.1007/s40571-015-0062-7.

[45] L. Olmos, C. L. Martin, D. Bouvard, D. Bellet, and M. Di Michiel, "Investigation of the sintering of heterogeneous powder systems by synchrotron microtomography and discrete element simulation," *Journal of the American Ceramic Society*, vol. 92, no. 7, pp. 1492–1499, 2009, ISSN: 00027820. DOI: 10.1111/j.1551-2916.2009.03037.x.

[46] D. Bouvard and R. M. McMeeking, *Deformation of Interparticle Necks by Diffusion-Controlled Creep*, 1996. DOI: 10.1111/j.1151-2916.1996.tb07927.x.

[47] C. L. Martin, H. Camacho-Montes, L. Olmos, D. Bouvard, and R. K. Bordia, "Evolution of defects during sintering: Discrete element simulations," *Journal of the American Ceramic Society*, vol. 92, no. 7, pp. 1435–1441, 2009, ISSN: 00027820. DOI: 10.1111/j.1551-2916.2009.03014.x.

[48] Z. Yan, C. L. Martin, O. Guillon, D. Bouvard, and C. S. Lee, "Microstructure evolution during the co-sintering of Ni/BaTiO3 multilayer ceramic capacitors modeled by discrete element simulations," *Journal of the European Ceramic Society*, vol. 34, no. 13, pp. 3167–3179, 2014, ISSN: 09552219. DOI: 10.1016/j.jeurceramsoc.2014.04.013.

[49] J. R. Carazzone, C. L. Martin, and Z. C. Cordero, "Crack initiation, propagation, and arrest in sintering powder aggregates," *Journal of the American Ceramic Society*, vol. 103, no. 9, pp. 4754–4773, 2020, ISSN: 15512916. DOI: 10.1111/jace.17170.

[50] V. Ogarko and S. Luding, "A fast multilevel algorithm for contact detection of arbitrarily polydisperse objects," *Computer Physics Communications*, vol. 183, no. 4, pp. 931–936, 2012, ISSN: 00104655. DOI: 10.1016/j.cpc.2011.12.019.

[51] J. Christoffersen, M. M. Mehrabadi, and S. Nemat-Nasser, "A Micromechanical Description of Granular Material Behavior.," vol. 48, no. June, p. 67, 1981.

[52] F. Parhami, R. M. McMeeking, A. C. Cocks, and Z. Suo, "A model for the sintering and coarsening of rows of spherical particles," *Mechanics of Materials*, vol. 31, no. 1, pp. 43–61, 1999, ISSN: 01676636. DOI: 10.1016/S0167-6636(98)00049-0.

[53] R. L. Coble, "Initial Sintering of Alumina and Hematite," *Journal of the American Ceramic Society*, vol. 41, no. 2, pp. 55–62, 1958.

[54] C. Herring, "Diffusional viscosity of a polycrystalline solid," *Journal of Applied Physics*, vol. 21, no. 5, pp. 437–445, 1950, ISSN: 00218979. DOI: 10.1063/1.1699681.

[55] S. J. L. Kang and Y. I. Jung, "Sintering kinetics at final stage sintering: Model calculation and map construction," *Acta Materialia*, vol. 52, no. 15, pp. 4573–4578, 2004, ISSN: 13596454. DOI: 10.1016/j.actamat.2004.06.015.

[56] F. Humphreys, "A unified theory of recovery, recrystallization and grain growth, based on the stability and growth of cellular microstructures—I. The basic model," *Acta Materialia*, vol. 45, no. 10, pp. 4231–4240, 1997, ISSN: 13596454. DOI: 10.1016/S1359-6454(97)00070-0.

[57] S. J. Dillon and M. P. Harmer, "Intrinsic grain boundary mobility in alumina," *Journal of the American Ceramic Society*, vol. 89, no. 12, pp. 3885–3887, 2006, ISSN: 00027820. DOI: 10.1111/j.1551-2916.2006.01331.x.

[58] R. J. Brook, "Pore-Grain Boundary Interactions and Grain Growth," *Journal of the American Ceramic Society*, vol. 52, no. 1, pp. 56–57, 1969, ISSN: 15512916. DOI: 10.1111/j.1151-2916.1969.tb12664.x.

[59] J. W. Rutter and K. T. Aust, "Migration of 100 tilt grain boundaries in high purity lead," *Acta Metallurgica*, vol. 13, no. 3, pp. 181–186, 1965, ISSN: 00016160. DOI: 10.1016/0001-6160(65)90194-X.

[60] G. Gottstein, D. A. Molodov, and L. S. Shvindlerman, "Grain boundary migration in metals: recent developments," *Interface Science*, vol. 6, no. 1-2, pp. 7–22, 1998, ISSN: 09277056. DOI: 10.1023/a:1008641617937.

[61] J. E. Burke and D. Turnbull, "Recrystallization and grain growth," *Progress in Metal Physics*, vol. 3, no. C, 1952, ISSN: 05028205. DOI: 10.1016/0502-8205(52)90009-9.

[62] A. Tsoga and P. Nikolopoulos, "Groove Angles and Surface Mass Transport in Polycrystalline Alumina," *Journal of the American Ceramic Society*, vol. 77, no. 4, pp. 954–960, 1994, ISSN: 15512916. DOI: 10.1111/j.1151-2916.1994.tb07252.x.

[63] W. M. Robertson and R. Chang, "The Kinetics of Grain-Boundary Groove Growth on Alumina Surfaces," *The Role of Grain Boundaries and Surfaces in Ceramics*, pp. 49–60, 1966. DOI: 10.1007/978-1-4899-6311-6{_}4.

[64] J. Zhao and M. P. Harmer, "Sintering of Ultra-High-Purity Alumina Doped Simultaneously with MgO and FeO," *Journal of the American Ceramic Society*, vol. 70, no. 12, pp. 860–866, 1987, ISSN: 15512916. DOI: 10.1111/j.1151-2916.1987.tb04906.x.

[65] A. Wonisch, O. Guillon, T. Kraft, M. Moseler, H. Riedel, and J. Rödel, "Stress-induced anisotropy of sintering alumina: Discrete element modelling and experiments," *Acta Materialia*, vol. 55, no. 15, pp. 5187–5199, 2007, ISSN: 13596454. DOI: 10.1016/j.actamat.2007.05.038.

[66] O. A. Ruano, J. Wadsworth, and O. D. Sherby, "Deformation of fine-grained alumina by grain boundary sliding accommodated by slip," *Acta Materialia*, vol. 51, no. 12, pp. 3617–3634, 2003, ISSN: 13596454. DOI: 10.1016/S1359-6454(03)00180-0.

[67] I. Nettleship, R. J. McAfee, and W. S. Slaughter, "Evolution of the grain size distribution during the sintering of alumina at 1350°C," *Journal of the American Ceramic Society*, vol. 85, no. 8, pp. 1954–1960, 2002, ISSN: 00027820. DOI: 10.1111/j.1151-2916.2002.tb00387.x.

[68] F. Wakai, N. Enomoto, and H. Ogawa, "Three-dimensional microstructural evolution in ideal grain growth general statistics," *Acta Materialia*, vol. 48, no. 6, pp. 1297–1311, 2000, ISSN: 13596454. DOI: 10.1016/S1359-6454(99)00405-X.

[69] H. Riedel and J. Svoboda, "A theoretical study of grain growth in porous solids during sintering," *Acta Metallurgica Et Materialia*, vol. 41, no. 6, pp. 1929–1936, 1993, ISSN: 09567151. DOI: 10.1016/0956-7151(93)90212-B.

[70] F. N. Rhines, K. R. Craig, and R. T. DeHoff, "Mechanism of steady-state grain growth in aluminum," *Metallurgical Transactions*, vol. 5, no. 2, pp. 413–425, 1974, ISSN: 03602133. DOI: 10.1007/BF02644109.

[71] B. R. Patterson and V. D. Parkhe, "Particle Size Distribution Effects on Sintering of Spherical Tungsten.," *Progress in Powder Metallurgy*, vol. 41, no. August, pp. 347–354, 1986.

[72] Z. Fang and B. R. Patterson, "Experimental investigation of particle size distribution influence on diffusion controlled coarsening," *Acta Metallurgica Et Materialia*, vol. 41, no. 7, pp. 2017–2024, 1993, ISSN: 09567151. DOI: 10.1016/0956-7151(93)90372-Y.

[73] J. M. Ting and R. Y. Lin, "Effect of particle size distribution on sintering - Part II Sintering of alumina," *Journal of Materials Science*, vol. 30, no. 9, pp. 2382–2389, 1995, ISSN: 00222461. DOI: 10.1007/BF01184590.

[74] R. Bjørk, V. Tikare, H. L. Frandsen, and N. Pryds, "The effect of particle size distributions on the microstructural evolution during sintering," *Journal of the American Ceramic Society*, vol. 96, no. 1, pp. 103–110, 2013, ISSN: 00027820. DOI: 10.1111/jace.12100.

[75] C. Greskovich and K. W. LAY, "Grain Growth in Very Porous Al2O3 Compacts," *Journal of the American Ceramic Society*, vol. 55, no. 3, pp. 142–146, 1972, ISSN: 15512916. DOI: 10.1111/j.1151-2916.1972.tb11238.x.

[76] J. Li and Y. Ye, "Densification and grain growth of Al2O3 nanoceramics during pressureless sintering," *Journal of the American Ceramic Society*, vol. 89, no. 1, pp. 139–143, 2006, ISSN: 00027820. DOI: 10.1111/j.1551-2916.2005.00654.x.

[77] X. Geng, Y. Hong, J. Lei, J. Ma, J. Chen, H. Xiao, J. Tong, R. K. Bordia, and F. Peng, "Ultra-fast, selective, non-melting, laser sintering of alumina with anisotropic and size-suppressed grains," *Journal of the American Ceramic Society*, vol. 104, no. 5, pp. 1997–2006, 2021, ISSN: 15512916. DOI: 10.1111/jace.17617.

[78] M. Suzuki and K. Kawazoe, "Effective surface diffusion coefficients of volatile organics on activated carbon during adsorption from aqueous solution," *Journal of Chemical Engineering of Japan*, vol. 8, no. 5, pp. 379–382, 1975, ISSN: 00219592. DOI: 10.1252/jcej.8.379.

Chapter 4

Grain growth in two-step sintering

This chapter describes the application of the grain growth model developed in chapter 3 to non-isothermal sintering. In particular we investigate two-step sintering of nano-powders. This is presented as a scientific article entitled *Two-step sintering of alumina nano-powders: A discrete element study* accepted in *Journal of the European Ceramic Society* in September 2022 [1]. The article is reported as accepted, with its two appendices included in Appendix B.

The previous chapter detailed the model of grain growth implemented in the DEM code. The application focused on the study of grain growth in isothermal conventional sintering. This application was mainly used as a validation of the model as it showed that the grain size evolution predicted by DEM simulations was in reasonable agreement with experimental data. The Supplementary Information (Appendix A) reported some basic simulations involving different heating rates, which showed that the sintering trajectory remains unchanged for micronic alumina powders, as expected. Thus, we can use the possibility to impose heating ramps in the DEM code to push further the application of the grain growth model. This can prove particularly useful for nano-powders since experimental results on alumina nano-powders [2] indicates that the densification trajectory depends on the heating rate value. This chapter will employ the developed model of grain growth in the nonisothermal sintering of alumina nano-powders, specifically during two-step sintering.

Two-step sintering is characterized by the use of a thermal cycle to retard grain growth. However, the underlying mechanisms are still unclear, especially for alumina. Therefore, this study will allow to both test the model ability of reproduce the heating rate dependence of nano-powders and to investigate a possible mechanism of two-step sintering.

During the development of this chapter, the need of an adjustment of the grain growth model emerged. This is related to the considered hypothesis that for a given contact, the smaller particle always transfer mass to the larger one. Results of small-scale simulations, discussed in chapter 2, suggest this is not always the case in nano-powders. In this chapter, this observation is integrated in the DEM model.

This study completes the first axis of the PhD thesis outlined in chapter 1.

Abstract

Avoiding grain growth during sintering of ceramic nano-powders is of great technological interest. Although two-step sintering is an effective technique to achieve this goal, the mechanisms at play are not well understood. This study adapts our previous discrete model to investigate the conventional and two-step sintering of nano-powders. The densification and grain growth results agree qualitatively well with experimental data on α-alumina. Simulations confirm that faster heating rates retard grain growth in conventional sintering of nano-alumina. Our results support the hypothesis that the success of nano-alumina two-step sintering relies on the sharp increase in the activation energy of the grain boundary mobility at low temperatures. Simulations indicate a transition temperature of 1100°C and that at least a 2.5-fold increase in activation energy is required to explain the suppression of grain growth. The relative weights of surface diffusion and of grain boundary motion for grain growth are clarified.

Keywords: nano-powders, two-step sintering, grain growth, alumina, discrete element method

4.1 Introduction

Solid-state sintering produces dense or density-controlled materials from ceramic or metallic powders using thermal energy. The driving force for sintering is the reduction in the total interfacial energy of the system [3], [4]. There are two contributions to the reduction of the product γA, where γ is the average interface energy and A is the total interface area of the system: $A\mathrm{d}\gamma$ and $\gamma \mathrm{d}A$. Thus, during sintering, a coupling between two mechanisms occurs: densification that reduces interfacial energy ($\mathrm{d}\gamma$) by replacing solid-gas interfaces by less energetic solid-solid interfaces, and coarsening that reduces interfacial area ($\mathrm{d}A$) [3], [5]. In general, materials scientists and practitioners favor densification while attempting to limit coarsening.

This is especially true when starting from nano-powders (typically < 100 nm grain size) that have great scientific and technological interest. The short diffusion distances in nano-powders inherently favor both grain growth and densification kinetics. Yang et al. [2] have recently demonstrated that the densification of nano-sized α-alumina powders proceeds through the same dominant mechanism as that involved in the sintering of micron-sized alumina, namely grain boundary diffusion. For nano-powders, keeping submicronic size grains while ensuring a nearly dense material is challenging. A fast-heating rate is an efficient processing method to enhance densification over grain growth. It is based on the usual condition for most materials that activation energies

of grain boundary diffusion along the boundary (densification) are higher than that of grain boundary diffusion perpendicular to the boundary (grain growth) [4]. Fast heating rates may be effectively combined with a modification of the thermal cycle, using a combination of high and low temperatures. This so-called two-step sintering technique may be declined in several variants [6]. Following the two-step approach proposed by Chen and Wang on Y_2O_3 [7], Yang et al. [2], [8] have recently demonstrated the effectiveness of two-step sintering technique to densify Al_2O_3 ceramic nano-powders while keeping small grain size ($\approx$ 40 nm).

The reason for the suppression of grain growth in the two-step sintering of α-alumina is still under study. For Y_2O_3 Chen and Wang have argued that it is possible, at low temperature, to almost eliminate grain boundary motion while keeping grain boundary diffusion active. Their argument is based on the theory proposed by Gottstein et al. that triple junctions can drag grain boundary motion at low temperature [9]. In particular, these authors have been able to confirm experimentally their theoretical predictions by measuring mobility of triple junctions on Zn and Al tricrystals [9], [10]. Accordingly, a transition in grain boundary mobility between grain boundary-controlled motion at high temperature and triple junction-controlled motion at low temperature is expected. Such a mobility transition has indeed been observed in Y_2O_3 polycrystals [11] thus confirming the suggested scenario. For α-alumina, the interplay between surface diffusion, grain boundary diffusion along and perpendicular to the grain boundary is not sufficiently documented to unambiguously propose a clear scenario. This task is made more difficult by the fact that, in conjunction with temperature changes, the microstructure itself undergoes profound alterations. The initial material is granular and begins as an assembly of discrete particles that interact with small contacts. It ends as a set of grains with small isolated pores remaining.

Numerical modeling can provide a better understanding of the grain growth of nano-powders during conventional and two-step sintering. At the atomistic scale using molecular dynamics, Ding et al. [12] provided insights into the mechanisms of neck and grain growth during the sintering of 2 and 3 nanoparticles. Depending on the crystalline orientation of the grains, they observed the disappearance of the grain boundary and the switch of neck growth mechanisms halfway during the sintering process. At the particle scale, Benabou and Wang [13] used the surface evolver approach to simulate the sintering of up to 40 particles. The detailed description of the surfaces allowed them to observe the elimination of pores and the disappearance of small particles by grain growth. Monte Carlo methods can also model efficiently the sintering of a reasonable number of initial particles with realistic interactions [14]. There is a drastic decrease in particle number with coarsening. Thus, a representative packing

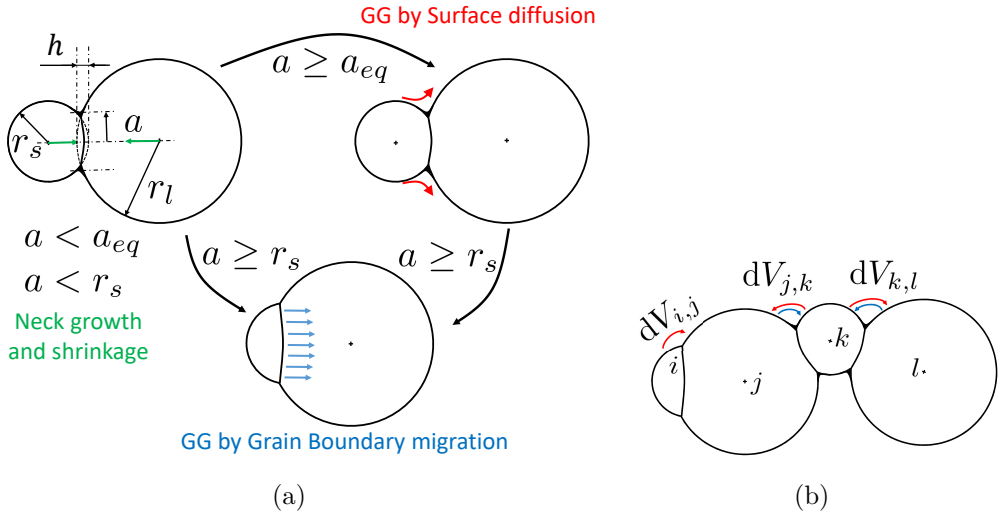

Figure 4.1: Graphical summary of the model. (a) Grain growth (GG) by Surface diffusion is activated after neck growth reaches the equilibrium configuration. Grain growth by Grain Boundary migration can be attained after GG by surface diffusion or directly after neck growth. (b) Volume exchange $\mathrm{d}V$ is always from small to large particle when the small particle has only one contact (i, j). For small particles with more than one contact ((j, k) and (k, l)), a large particle may give volume $\mathrm{d}V$ to a small one with probability $P_{s,l}$.

with a large initial number of particles is needed to properly study the microstructure evolution in simulations. Using discrete element modeling (DEM), we have already successfully investigated grain growth occurring during the sintering of large packings of micronic α-alumina particles (up to 400 000) [15].

The aim of this study is to extend our previous work to analyze grain growth and densification of nano-sized α-alumina during conventional and two-step sintering. Section 2 summarizes our model with some modifications to correctly model nano-powders. The simulations and comparison with experimental data of conventional sintering are presented in Section 3. These simulations are performed for different heating rates. The evolution of density, densification rate and grain size with temperature are reported and critically compared to experimental data from Yang et al. [2]. The volumes transferred by surface diffusion and grain boundary migration are quantified. Section 4 presents two-step sintering simulations, their comparison to experimental data and a discussion on the origin of the absence of grain growth.

4.2 Model description

The details of the model (contact laws, contact size, grain growth model) can be found in [16]. Here we summarize its main ingredients and report the material parameters used in the simulations. In DEM, particles are represented as spheres that are

progressively truncated at contacts with other particles as sintering proceeds. The powder compact is modeled as a 3D random assembly of spherical particles interacting through their contacts. At each time step, all contacts are considered and contact forces are calculated and summed up for all particles. Particle velocities and new positions are updated using a velocity-Verlet algorithm. As proposed in our earlier work [17] and classically adopted by other researchers in DEM simulations of sintering [18]–[23], normal contact forces appear between particles including two components. The viscous component introduces the diffusion coefficient along the grain boundary $D_{GB} = D_{0GB} \exp \frac{-Q_{GB}}{RT}$ with temperature dependence (activation energy Q_{GB}). This component opposes the relative motion between the two particles. The tensile component (also known as the sintering force) introduces the surface energy γ_S. The expression of the normal force is derived from results obtained by Bouvard et al. [24] and Pan et al. [25] and accounts for sintering by coupled grain boundary diffusion and surface diffusion, typical of solid-state sintering of oxide ceramics. The contact radius a is calculated here from the model of Pan et al. [25] for particles of different sizes. The size of the contact plays an important role in the model as it dictates the transition from one mechanism to another. The equilibrium contact radius a_{eq}, at which the sum of the grain boundary and surface energies reaches a local minimum, is given by the equilibrium dihedral angle Ψ_{eq}. When the contact size becomes larger than a_{eq}, grain growth (GG) by surface diffusion becomes active, unless the smallest particle is itself smaller than the contact, in which case GG by grain boundary migration becomes active (Fig. 4.1a).

Grain growth is modelled by simply considering that an exchange of matter $\mathrm{d}V$ results in a radius decrease and a radius increase for the two particles in contact. The flux of matter $\frac{\mathrm{d}V}{dt}$ originates from two contributions: *Surface* (S) diffusion or *Grain Boundary Migration* (GBM). The surface diffusion contribution writes:

$$\left(\frac{\mathrm{d}V}{\mathrm{d}t}\right)_S = -4\pi \frac{\delta_S D_{0S} \exp \frac{-Q_S}{RT}}{k_B T} \gamma_S \Omega \frac{\frac{1}{r_l} - \frac{1}{r_s}}{r_l + r_s - h} a \qquad a \geq a_{eq} \tag{4.1}$$

where h is the geometric indentation between the two spherical discrete elements (Fig. 4.1a), $k_b T$ has the usual meaning, Ω is the atomic volume and δ_S is the thickness of the diffusion layer. The Grain Boundary Migration diffusion contribution writes:

$$\left(\frac{\mathrm{d}V}{\mathrm{d}t}\right)_{GBM} = -2M_{0GB} \exp \frac{-Q_{GBM}}{RT} \gamma_{GB} \left(\frac{1}{r_l} - \frac{1}{r_s}\right) \left[\pi a^{*2}\right] \qquad a \geq r_s \tag{4.2}$$

with a^* the contact radius when Grain Boundary Migration becomes active. Both Eqs. (4.1) and (4.2) have temperature dependence through Arrhenius law with pre-

exponential factors D_{0S} and M_{0GB}, and activation energies Q_S and Q_{GBM}, respectively. Note that as sketched in Fig. 4.1a, the two contributions are mutually exclusive, i.e., only one (or none) is active at a given point for a contact.

When Grain Boundary Mobility is active ($a > r_s$), by default the volume of matter flows from the small to the large particle. We have observed that this simplistic assumption triggers abnormal grain growth in our simulations for nano-sized particles. As compared to our previous work in [16], we have thus added an ingredient to the model that controls the occurrence of abnormal grain growth by introducing some departure from this default condition. This is carried out by stating that a small particle that has two or more contacts (particle k in Fig. 4.1b) has a probability $P_{s,l}$ to have positive matter flux from the larger one. This scenario is supported by finite difference simulations on particles of different sizes for two or three particles in contact [26]. For nanosized particles, these authors reported the intriguing result that a small particle in contact with two larger ones can develop some resistance to invasion. In particular, they showed that, rather than shrinking, the small particle grows at the expense of the two larger ones. Eventually, the small particle always disappears as the boundary migrates. This result was further refined by molecular dynamics simulations of nanoparticles sintering [12] that showed that many different scenarios could exist, depending mainly on the initial crystalline misalignment between particles. These results indicate that local curvature (or grain size for spherical grains) may not always dictate the grain boundary velocity when departing from the simplistic model of two grains. This is consistent with recent experimental results that reveal that there is no observed relationship between grain boundary velocity and curvature in polycrystalline Ni with multiple grain boundaries [27]. These scenarios cannot be realistically included in DEM simulations with several hundreds of thousands of particles. The probability $P_{s,l}$ that a small particle (with more than one contact) can temporarily eat away a larger one accounts for these alternative scenarios in a very simple manner. We set this value in all simulations to $P_{s,l} = 1/4$, and observed that this was sufficient to prevent abnormal grain growth.

4.3 Sintering at constant heating rate

The model described above was applied to simulate the sintering of α-Al_2O_3 nanopowders, which has been thoroughly examined experimentally in [2], [8]. Starting from a powder cold-compacted to a green density of 0.48, sintering was carried out at various heating rates. The initial powder (before compaction) was observed by TEM at approximately 5 nm in size, with a narrow initial grain-size distribution (standard deviation

normalized by the average grain size = 0.23). Numerical specimens were prepared to reproduce this initial green packing. We observed in our simulations that applying a 500 MPa axial stress on this packing already triggered at room temperature some grain coarsening (i.e. $a \geq a_{eq}$ or $a \geq r_s$) due to surface energy effects. This is because adhesive forces induce local elastic strains that are far from negligible for nano-powders. Using the DMT model, which is well adapted for hard and small particles [28], [29], the equilibrium contact radius a of two identical spheres of radius r with Young's modulus E and Poisson's ratio ν writes:

$$\frac{a}{r} = \frac{3}{2}\pi\frac{\gamma_s}{r}\frac{1-\nu^2}{E} \tag{4.3}$$

yielding a value $a/r \approx 0.17$. Eq. (4.3) is derived for two particles without external stress. Adding external stress further increases strain at contacts, which should lead to irreversible grain deformation and coalescence even below 800°C. Thus, we started our sintering simulations with an average grain size of 10 nm, which is in good accordance with SEM observations [2]. Packings made of 400 000 randomly located particles, with an initial relative standard deviation of the grain-size distribution of 0.23 were compacted up to 0.50 relative density in a periodic simulation box to obtain the starting green powder. This large number of initial particles is needed to obtain statistically meaningful results at the end of sintering when a large number of particles have disappeared (see Appendix B.1).

Material parameters used in the simulations are summarized in Table 4.1. Activation energies for grain boundary diffusion, Q_{GB}, surface diffusion, Q_S, and grain boundary mobility, Q_{GBM}, were taken directly from the literature, and are the same as those used for micronic α-alumina powder sintering in [16]. The prefactor of the grain boundary diffusion coefficient was adjusted to fit the experimentally observed relative density at $T_1 = 1150$°C for a 10 °C/min heating rate. The partially sintered packing obtained at this temperature is used for two-step sintering simulations in section 4.4. The prefactor of the surface diffusion coefficient was chosen to keep the same ratio of the grain boundary diffusion to surface diffusion ($\xi = 0.001$) as in our previous work for a temperature of 1350°C. For small values of ξ (associated with the lower temperatures simulated here), the work of Bouvard and McMeeking [24] suggests that the tensile term in the normal force expression depends only weakly on ξ. This ensures that the parameters of the sintering model used for micronic sizes remain valid [16]. Note that the activation energies in Table 4.1 are consistent with the range proposed in [2] for nano-powders.

$\delta_{GB}D_{0GB}$ (m^3/s)	1.04x10^{-11}	Q_{GB} (kJ/mol)	475 [30]
D_{0S} (m^2/s)	7.2x10^{-05}	Q_S (kJ/mol)	313.8 [31]
M_{0GB} (m^3/(N.s))	0.02 [16], [32]	Q_{GBM} (kJ/mol)	443 [32]
Ψ_{eq} (°)	138 [33]	Ω (m^3)	2.11x10^{-29} [31]
γ_S (J/m^2)	0.905 [31]	γ_{GB} (J/m^2)	$2\gamma_S \cos(\Psi_{eq}/2)$

Table 4.1: Material parameters used for α-alumina.

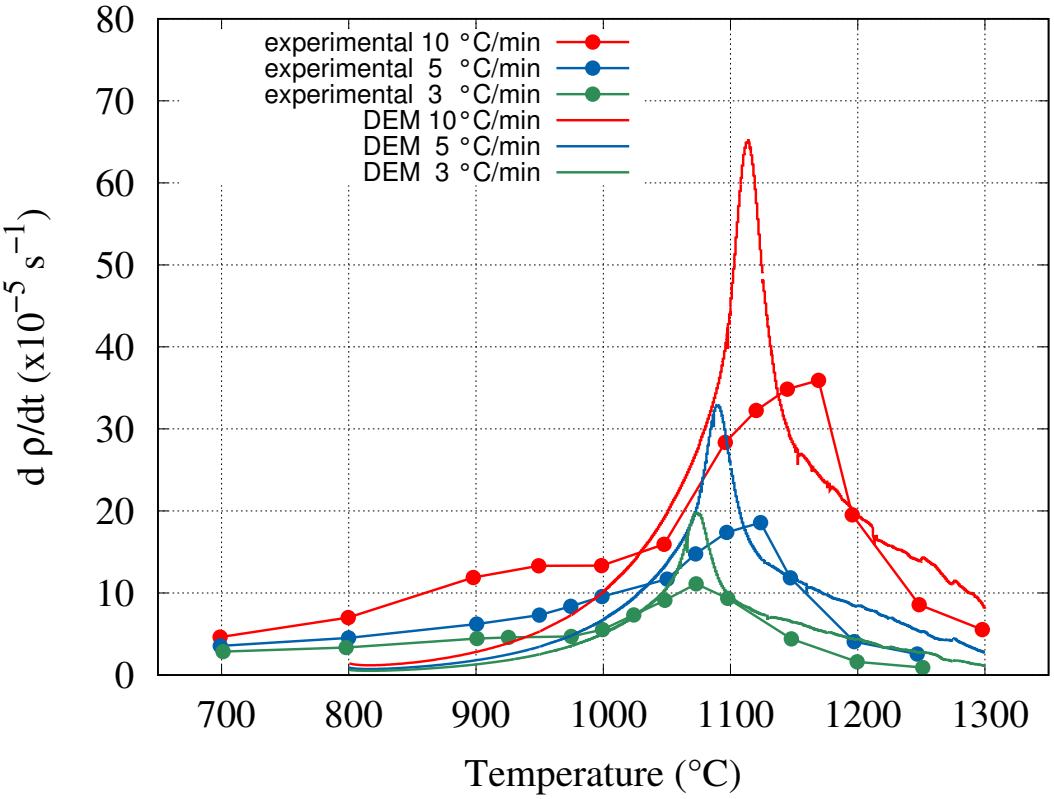

Figure 4.2: Densification rate evolution with temperature for three heating rates: 3, 5 and 10°C/min. Experimental data for α-alumina from [2]

.

Fig. 4.2 shows the evolution of the densification rate $\mathrm{d}\rho/\mathrm{d}t$ for the three simulated heating rates (3, 5 and 10°C/min). Fig. 4.2 indicates that, owing to the very small size of the starting powders, densification is already active at 800°C. This may be understood by recognizing that the sintering force expression in our model leads to a time normalization (before coarsening mechanisms start to play a role) that scales with the mean particle size, G to the power 4: $\tau \propto \langle r \rangle^4$. This is in line with classic analytical models that lead to densification rates scaling with G^4 [34].

While our simulations indicated that the heating rate has a minor influence on the sintering of micro-alumina [16], this is no more the case for nano-alumina. For all three heating rates, the densification rate increases to a maximum and decreases to very small values when full density is approached. The temperature at which this maximum occurs increases with increasing heating rates. A higher heating rate is

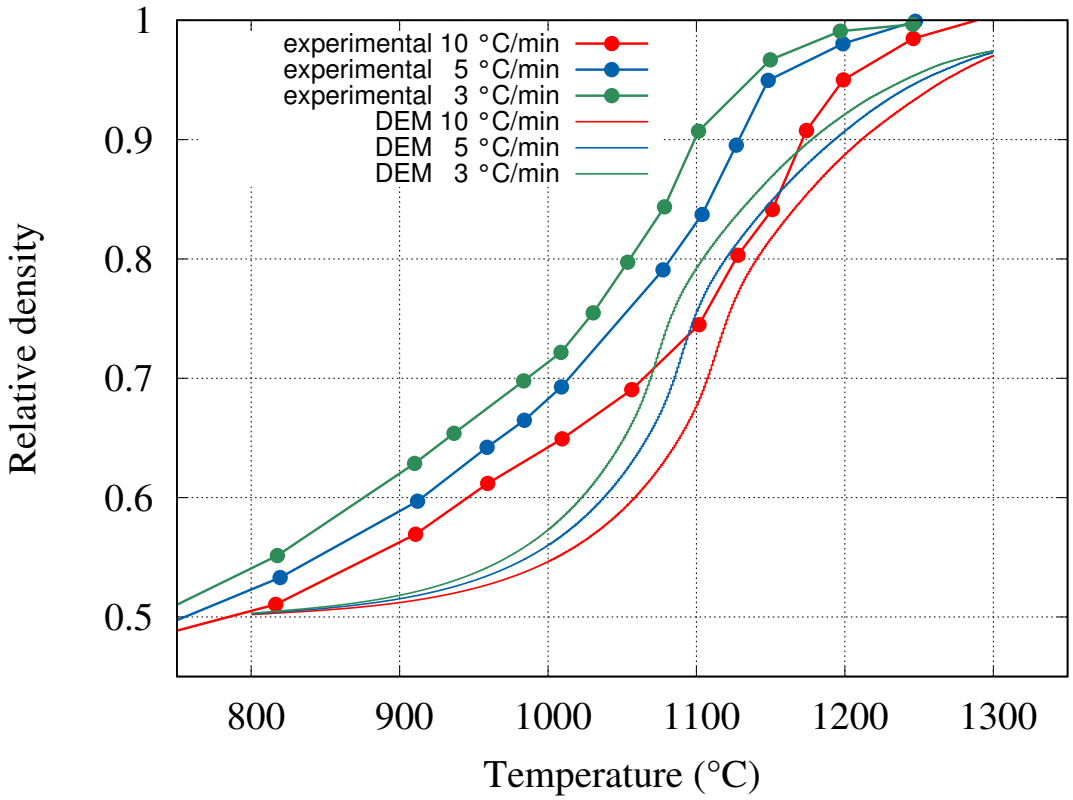

Figure 4.3: Relative density evolution with temperature for three heating rates: 3, 5 and 10°C/min. Experimental data for α-alumina from [2]

.

associated to a higher maximum densification rate: the peak densification rate at 10°C/min is three times as fast as that at 3°C/min. This is the result of two effects. First, Fig. 4.3 shows the evolution of density with temperature. It indicates that at a given temperature, a faster heating rate results in a lower relative density, thus keeping the driving force for densification higher. Second, Fig. 4.4 shows that grain growth arises at higher temperatures as the heating rate increases. The occurrence of the maximum densification rate is well correlated in all three simulations to the initiation of grain growth. Fig. 4.4 indicates that the heating rate has a clear effect on the final grain size.

Figs. 4.2, 4.3 and 4.4 include experimental data from [2] for comparison. Recall that the only material parameter that was adjusted was the prefactor of the grain boundary diffusion coefficient to fit approximately the experimental relative density for 10°C/min at $T_1 = 1150$°C. The comparison demonstrates that the DEM simulations are able to capture qualitatively well all relevant experimental features. In particular, the bell shape of the densification rate with temperature (Fig. 4.2), the S shape of the evolution of the density with temperature (Fig. 4.3), and the concave shape of the grain growth (Fig. 4.4). However, some quantitative differences are clear. In particular,

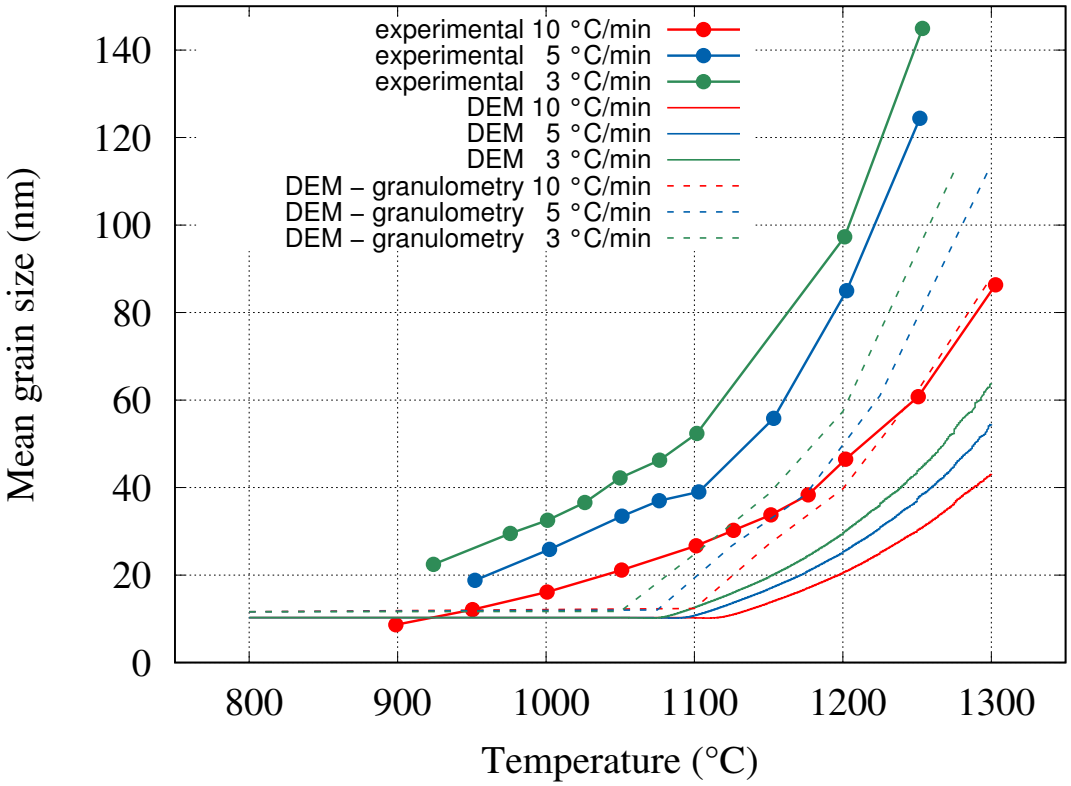

Figure 4.4: Mean grain size evolution with temperature for three heating rates: 3, 5 and 10°C/min. Experimental data for α-alumina from [2]. The dashed lines represent the mean grain size of the DEM packings calculated by image analysis (granulometry algorithm).

the DEM simulations underestimate the initial sintering activity of the powder at low temperature (both densification rate and grain growth). Because of the strong model assumptions, it was not possible to fit the densification curves at both low and high temperatures. In particular the following model assumptions may not be valid: homogeneous packing (nano powders are prone to agglomeration), presence of defects, impurities or irregularly shaped particles (due to high-energy ball milling [2]). The choice was made to fit densities at high temperatures and consequently the densification is underestimated at low temperatures. For grain growth, the delayed initiation is linked to our simplistic assumption that surface diffusion and grain boundary motion are mutually exclusive and abruptly starts only when the contact radius is above a critical radius (Fig. 4.1). This results in DEM relative density curves lagging behind the experimental curves at low temperature. In addition, we observed that the mean grain size of DEM packings calculated using image analysis on 3D images generated from the simulations (dashed lines in Fig. 4.4) results in larger grain size that are in better accordance with experimental data. This methodology, comparable to the one used by [2], is detailed in Appendix B.2.

Keeping in mind these discrepancies with experimental data, the mechanisms that

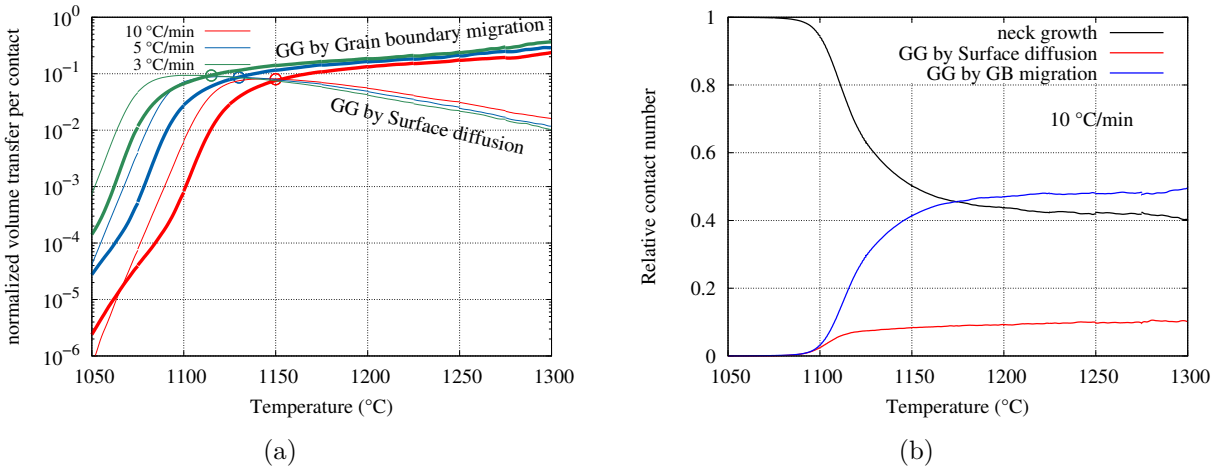

Figure 4.5: DEM simulation results. a) Evolution of the mean volume transferred per contact (normalized by the mean volume of particles) with temperature for three heating rates: 3, 5 and 10°C/min. Two contributions for grain growth (GG) are shown: surface diffusion (Eq. (4.1)) and grain boundary migration (Eq. (4.2)). Circles indicate the temperature at which grain boundary migration contribution exceeds surface diffusion contribution. b) Evolution of the relative contact number (normalized by the total number of contacts) for each possible status: neck growth, GG by surface diffusion and GB migration for 10°C/min.

lead to grain growth in nano-powders can still be analyzed using the detailed results of DEM simulations. Fig. 4.5a shows on a log-scale the mean volume transferred per contact at a given temperature. It is separated into the two contributions given by Eqs. (4.1) and (4.2). Fig. 4.5a indicates that at low temperature, surface diffusion is the main contributor to grain growth, although this contribution becomes significant only above 1070-1100°C, depending on the heating rate. This is in line with the general view that at lower sintering temperatures, surface diffusion dominates matter redistribution during grain growth. Grain boundary migration becomes dominant at higher temperature with large transfer of volumes from one particle to another (compared to the actual volume of particles). Fig. 4.5b confirms this result. It shows the evolution of contact status as temperature increases for the 10°C/min heating rate (it is representative of all 3 heating rates). At low temperatures, all contacts are in the initial neck growth status and gradually shift to grain growth by surface diffusion and by grain boundary migration. Note that below 1100°C, Fig. 4.5b shows that very few contacts contribute to grain growth, thus explaining the very small volume transfer indicated by Fig. 4.5a for these temperatures at 10°C/min.

Because new contacts arise between particles all along sintering due to densification and rearrangement of particles, neck growth and shrinkage are still active leading to the continuation of densification. These results are similar qualitatively to those obtained for micronic powders [16]. It shows that conventional sintering models can be applied to

	ρ_c	G (nm)	T_1 (°C)	T_2 (°C)
10°C/min	0.82	13.6	1150	1025
5°C/min	0.76	10.7	1100	975
3°C/min	0.72	10.2	1075	950

Table 4.2: Main parameters of the second-step sintering. ρ, G : density and mean grain size attained in the first step. T_1: temperature at which this density was obtained, and T_2: temperature of the second isothermal sintering step.

nano-powders and reproduce their very good sinterability and significant grain growth.

Fig. 4.5a also explains the results shown in Fig. 4.4, which indicate the beneficial effect of higher heating rates to retard grain growth. The shift from surface diffusion to grain boundary migration triggers significant grain growth in our model. This shift arises at higher temperature for faster heating rates. We believe that our model underestimates grain growth by surface diffusion at low temperature (as proved by the grain size curves lagging behind the experimental curves at low temperature, Fig. 4.4). Still, Fig. 4.5a points to an interesting lever to retard grain growth: delaying the migration of grain boundaries, which is much more effective than surface diffusion for grain growth.

A practical alternative to retard the migration of grain boundaries is to actually freeze this mechanism by using two-step sintering, which takes advantage of low temperatures in a second prolonged isothermal stage [6]. This is studied in the next section.

4.4 Two-step sintering

Numerical samples originating from constant heating rate simulations were retrieved for a second sintering step at a lower constant temperature. In line with the experimental procedure adopted in [2], table 4.2 lists the main parameters of these simulations. The densities obtained in simulation at the end of the first step (ρ_c) are lower than the experimental densities (Fig. 4.3). As input for the second step, we opted to use the microstructure obtained at the experimental temperature T_1 instead of the microstructure obtained at the same density of experiments.

First, we ran the simulations of the second step (lower temperature) with the same activation energies as in the first step (higher temperature). In that case, considerable grain growth is observed. However, Gottstein et al. [9] observed that at low temperatures the motion of the grain boundary is controlled by the 3-grains junction lines that have a higher mobility activation energy. This was the principle employed by Chen

and Wang [7] to propose for the first time the variant of two-step sintering used in the present study. The effect of the junction mobility results in a higher apparent activation energy of the grain boundary motion below a transition temperature. This has been measured experimentally for aluminum crystals [10], tungsten [35] and yttria-stabilized zirconia [11]. The multiplicative factor of the observed increase in activation energy is between 1.9 and 2.6. Yang et al. [2] suggested that this activation energy increase could also occur in the case of α-alumina. Thus, we have tested a higher activation energy of grain boundary migration Q_{GBM} for low temperatures in our simulations.

Fig. 4.6 shows the grain boundary mobility as a function of temperature, where the slope represents the value of the activation energy Q_{GBM}. Data points are collected from the literature [32], [36]–[40]. For the first step, we choose Q_{GBM}=443kJ/mol according to α-alumina experimental data at high temperatures (red line). To the best of our knowledge, no activation energies for junction mobility or for grain boundary mobility at temperatures below 1325°C are reported in the literature. Based on the data for other materials commented above, we choose an activation energy $2.5 \times Q_{GBM}$ (blue line) for the second step. Regarding the transition temperature, there is also no experimental data for alumina. Based on our simulation results of grain size (Fig. 4.4), we choose $T = 1100$°C as below this temperature grain growth is negligible. Simulations indicate that using lower transition temperatures, very high nonphysical values of activation energy ($> 3 \times Q_{GBM}$) would be needed to suppress grain growth. We corroborated that using the selected activation energy and transition temperature in the second step has negligible effects in the results of the first step.

Simulations of the second step were carried out for the three heating rates studied in the previous section, using $2.5 \times Q_{GBM}$ at low temperatures. Fig. 4.7 illustrates the 3D microstructural evolution from DEM simulations for conventional and two-step sintering for the heating rate 5°C/min. From 0.50 to 0.76 relative density ($T = 800$°C $\rightarrow T_1 = 1100$°C), the number of particles decreases (from 400 000 to 263 000) due to some volume transfer but without significant increase of the mean grain size. Conventional sintering ($T_1 = 1100$°C $\rightarrow T = 1175$°C) leads to grain growth as already indicated in Fig. 4.4 with a further decrease in particle number (from 263 000 to 36 000). In contrast, two-step sintering ($T_2 = 975$°C) keeps the same number of particles and mean grain size.

Fig. 4.8 shows the grain size-density trajectories obtained by simulations for both conventional sintering and in two steps. The simulations of two-step sintering were able to reproduce the experimental results, i.e., annihilating the grain growth while continuing densification. During the second step, a slight grain growth is observed at 10°C/min, while no grain growth occurs for the two slower heating rates. This is due

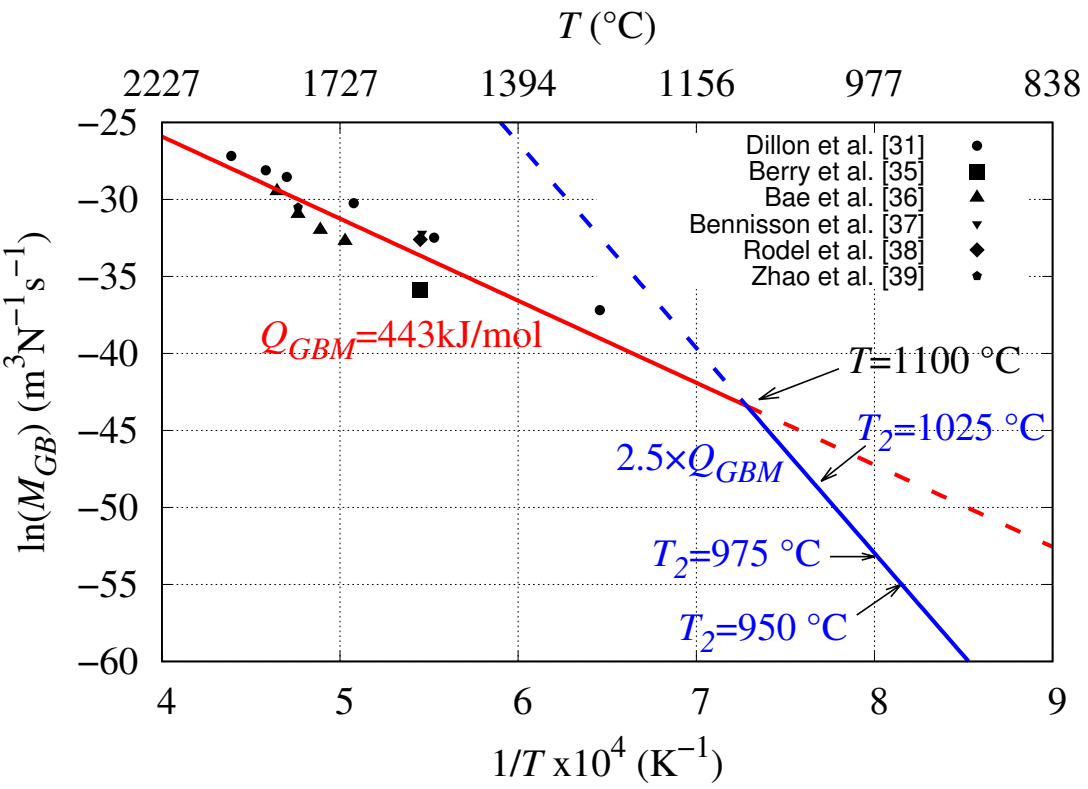

Figure 4.6: Grain boundary mobility of α-alumina with data points from the literature [32], [36]–[39], [41]. Q_{GBM}=443kJ/mol (red line) is the standard value used for the first step. An increase of $2.5 \times Q_{GBM}$ (blue line) is considered for the second step with a transition temperature at T =1100°C. T_2 is the temperature of the second step according to table 4.2.

to a combined effect of much higher grain boundary mobility for 10°C/min (higher T_2, table 4.2 and Fig. 4.6) and a more advanced state of the microstructure on the sintering trajectory at the beginning of the second step in our simulations, which favors grain growth.

In order to inspect the alterations produced by two-step sintering on grain growth, Fig. 4.9 shows the volume transferred by surface diffusion and grain boundary motion for one and two-step sintering. In accordance with Fig. 4.8, the grain growth from both mechanisms is lower in two-step than in conventional sintering. The decrease of the volume transferred by surface diffusion is essentially due to the lower temperature employed in two-step sintering. One way to further decrease it is to use a powder with a narrow initial size distribution as indicated for nanopowders by Fang et al. [42] and verified by simulations in micro-alumina in our previous work [16]. The decrease of volume transmitted by grain boundary migration is much more substantial (Fig. 4.9) and caused both by the reduction of process temperature and, mainly, by the increase of the associated activation energy (Fig. 4.6). Therefore, our simulations suggest the validity of the hypothesis proposed by Yang et al. [2] on the grain boundary

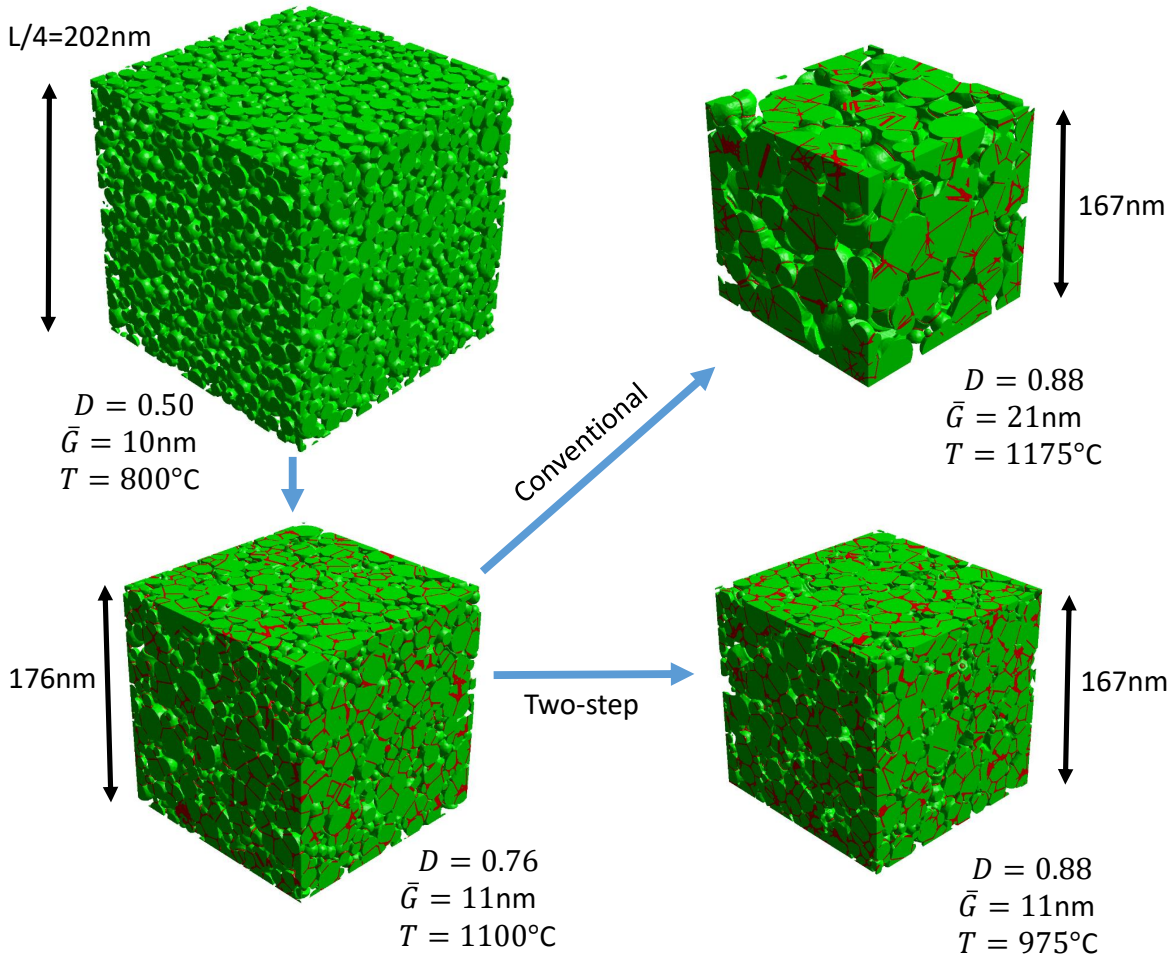

Figure 4.7: Evolution of DEM microstructures at 5°C/min heating rate. The sintered necks are represented by two inverted tori tangent to each particle [16]. Grain boundaries are shown in red. Only a portion of the total simulation cube (L^3) is shown for clarity.

mobility transition as a cause for the effectiveness of the α-alumina two-step sintering. This applies since the activation energy of the alumina grain boundary diffusion, that governs densification, is assumed constant and is lower than the activation energy of GB mobility. We studied the effect of different values of the activation energy of the GB mobility (Fig. 4.10). Simulations confirm that an increase of at least $2.5 \times Q_{GBM}$ is necessary to suppress grain growth. We also observed that keeping the same value for the activation energy ($1.0 \times Q_{GBM}$, pink curve), the two-step trajectory actually accelerates grain growth as compared to conventional sintering for 10°C/min (dashed red line). This is again because the activation energy of the grain boundary mobility is lower than that of the grain boundary diffusion. The sintering temperature being low ($T_2 = 1025$°C), a significant grain growth is obtained after a long sintering time (170h), which is contradictory to experimental data for two-step sintering. The densification kinetics is very slow in this case, due to the significant growth of grains. For two-step

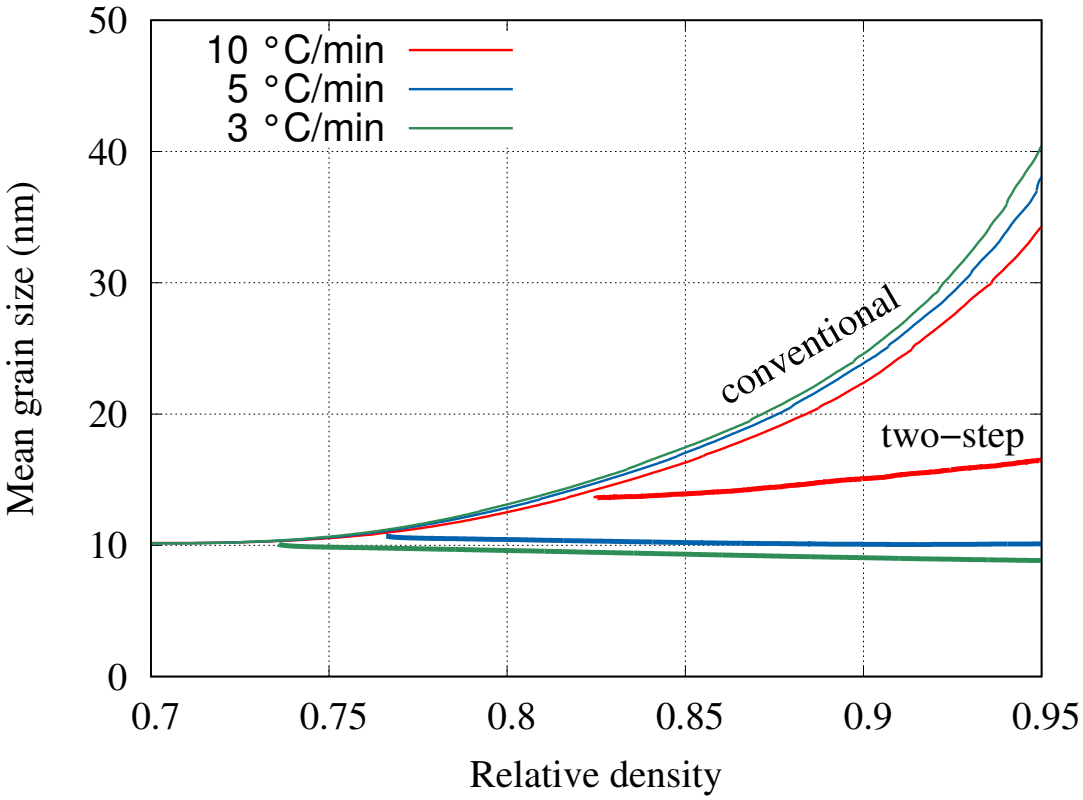

Figure 4.8: DEM simulation results. Grain size - density trajectories for three heating rates: 3, 5 and 10°C/min obtained by DEM simulations. Two-step sintering curves are represented by thicker lines, while thinner lines represent conventional sintering. The second step is performed at constant temperature after a first heating ramp stage. Sintering temperatures are given in Table 4.2. A high activation energy for grain boundary mobility ($2.5 \times Q_{GBM}$) is used in the second step as sketched in Fig. 4.6.

sintering and $2.5 \times Q_{GBM}$, the times indicated (in hour) in Fig. 4.10 are in line with experimental data, which report full densification after 40 hours of sintering in the second step [2].

4.5 Conclusion and outlook

The sintering behavior, even for only two nanoparticles, can be complex and strongly dependent on the crystalline orientation as shown in [12]. Our discrete model at the particle scale cannot reproduce all the subtleties that can be simulated at the atomic scales. Still, our simulations show good agreement with experimental data in terms of the evolution of the densification rate, density and grain size. However, the very early densification and grain growth of nano-powders reported by Yang et al. [2] are not correctly reproduced by the model.

A limitation in our discrete modeling is the assumption of spherical particles that indent during sintering. This hypothesis is particularly challenged in the last stage of

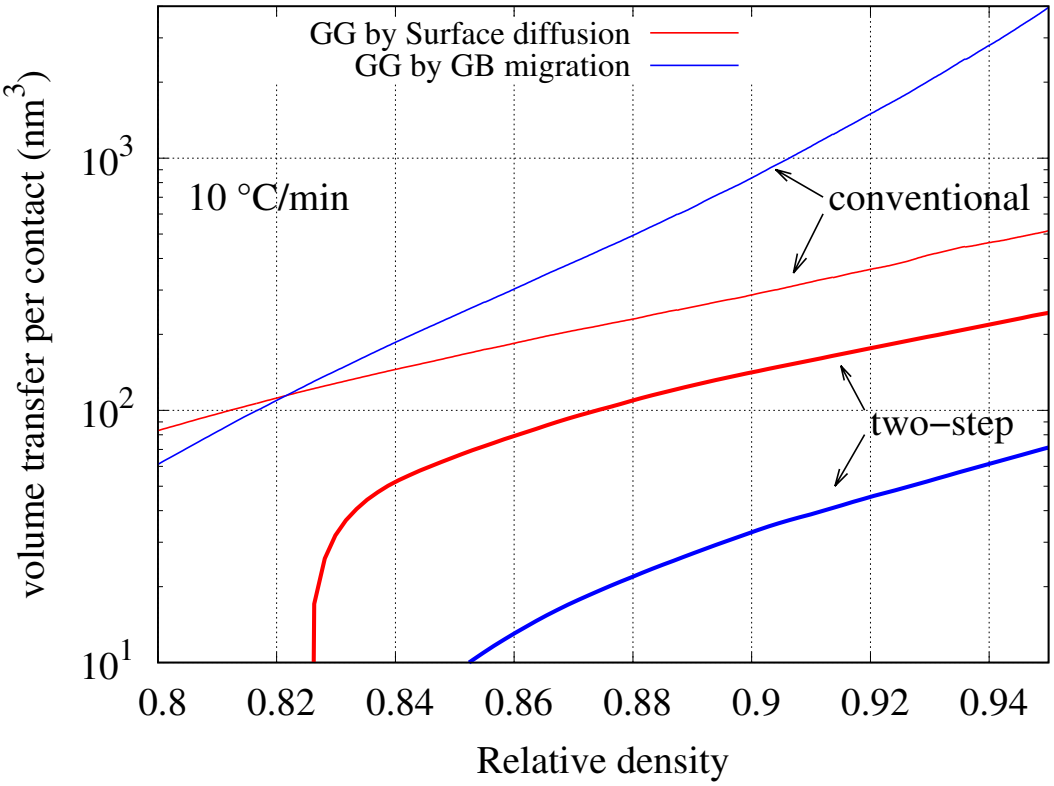

Figure 4.9: DEM simulation results. Transferred volume per contact for the two grain growth mechanisms considered in the DEM simulations. Comparison between conventional and two-step sintering.

grain growth where a typical pear shape has been suggested by two-particles modeling [25], [43]. Freeing from this assumption, while keeping the discrete framework, can only be achieved by introducing a new paradigm such as using level-set representation of particles [44].

We observed that for nanoparticles, abnormal grain growth is triggered in our simulations if we enforce the simplistic rule that small particles are always eaten away by larger ones. This phenomenon needs further investigation to clarify the conditions that lead to abnormal grain growth. In particular, molecular dynamics simulations could help (if they are able to model several tens of nanoparticles for large physical times) to detect the conditions that lead to abnormal versus normal grain growth. The transfer of matter from one grain to another is dictated by the local curvature. For spherical grains, as used here, the local curvature is uniquely related to particle sizes. This is clearly simplistic and simulating non-spherical geometries would certainly provide more realistic information about abnormal grain growth.

With the ability to study thermal cycles during sintering, the model confirms the effectiveness of using fast heating rates to retard grain growth in conventional sintering of nano-powders. The mechanisms underlying the efficiency of two-step sintering of α-

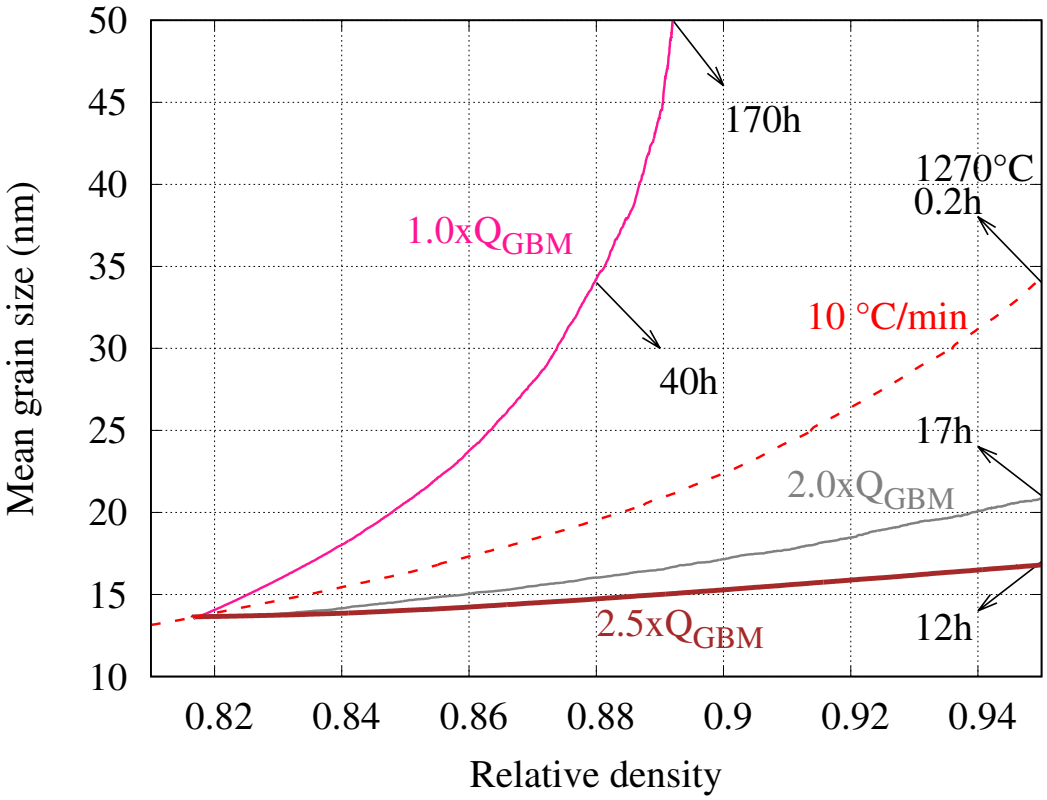

Figure 4.10: DEM simulation results. Grain size-density trajectories for different Q_{GBM} in the second step at $T_2 = 1025$°C (solid lines) and in conventional sintering for 10°C/min (dashed line). Times in hour are indicated to illustrate the associated sintering kinetics.

alumina and more generally of ceramic oxides still need some further investigation, both from experiments and modelling. Still, this study plausibly supports the hypothesis of [2] that a transition of the apparent activation energy of the grain boundary mobility is the main reason. Our results suggest that the halting of grain growth in the second step is explained by a large increase (≥ 2.5) of the activation energy of grain boundary mobility for a transition temperature of 1100° C. Further experimental and numerical studies are needed to confirm these values and to clarify whether the cause of the mobility activation energy is the junction drag or some other property of the alumina grain boundary.

References

[1] B. Paredes-Goyes, A. M. Venkatesh, D. Jauffres, and C. L. Martin, "Two-step sintering of alumina nano-powders: A discrete element study," *Journal of the European Ceramic Society*, 2023, ISSN: 0955-2219. DOI: https://doi.org/10.1016/j.jeurceramsoc.2022.10.001.

[2] H. Yang, L. Li, Y. Li, B. Shen, Y. Kang, L. Zhao, J. Li, Y. Dong, and J. Li, "Unveiling exceptional sinterability of ultrafine α-Al2O3 nanopowders," *Journal of Materiomics*, vol. 7, no. 4, pp. 837–844, 2021, ISSN: 23528486. DOI: 10.1016/j.jmat.2020.12.011.

[3] S.-J. L. Kang, *Sintering Densification, Grain Growth, and Microstructure*. Oxford: Butterworth-Heinemann, 2005, pp. xi –xii, ISBN: 978-0-7506-6385-4. DOI: https://doi.org/10.1016/B978-075066385-4/50000-5.

[4] R. K. Bordia, S. J. L. Kang, and E. A. Olevsky, "Current understanding and future research directions at the onset of the next century of sintering science and technology," *Journal of the American Ceramic Society*, vol. 100, no. 6, pp. 2314–2352, 2017, ISSN: 15512916. DOI: 10.1111/jace.14919.

[5] G. Bernard-Granger and C. Guizard, "New relationships between relative density and grain size during solid-state sintering of ceramic powders," *Acta Materialia*, vol. 56, no. 20, pp. 6273–6282, 2008, ISSN: 13596454. DOI: 10.1016/j.actamat.2008.08.054.

[6] N. J. Lóh, L. Simão, C. A. Faller, A. De Noni, and O. R. Montedo, "A review of two-step sintering for ceramics," *Ceramics International*, vol. 42, no. 11, pp. 12 556–12 572, 2016, ISSN: 02728842. DOI: 10.1016/j.ceramint.2016.05.065.

[7] X.-H. Wang and I.-W. Chen, "Sintering dense nanocrystalline ceramics without final-stage grain growth," *Nature*, vol. 404, no. 9 March, pp. 168–171, 2000.

[8] Y. Dong, H. Yang, L. Zhang, X. Li, D. Ding, X. Wang, J. Li, J. Li, and I. W. Chen, "Ultra-Uniform Nanocrystalline Materials via Two-Step Sintering," *Advanced Functional Materials*, vol. 31, no. 1, pp. 1–9, 2021, ISSN: 16163028. DOI: 10.1002/adfm.202007750.

[9] G. Gottstein, V. Sursaeva, and L. S. Shvindlerman, "Effect of triple junctions on grain boundary motion and grain microstructure evolution," *Interface Science*, vol. 7, no. 3, pp. 273–283, 1999, ISSN: 09277056. DOI: 10.1023/a:1008721426104.

[10] S. G. Protasova, G Gottstein, D. A. Molodov, V. G. Sursaeva, and S Shvindlerman, "Triple junction motion in aluminum tricrystals," *Acta Materialia*, vol. 49, pp. 2519–2525, 2001.

[11] Y. Dong and I. W. Chen, "Mobility transition at grain boundaries in two-step sintered 8 mol yttria-stabilized zirconia," *Journal of the American Ceramic Society*, vol. 101, no. 5, pp. 1857–1869, 2018, ISSN: 15512916. DOI: 10.1111/jace.15362.

[12] L. Ding, R. L. Davidchack, and J. Pan, "A molecular dynamics study of sintering between nanoparticles," *Computational Materials Science*, vol. 45, no. 2, pp. 247–256, 2009, ISSN: 09270256. DOI: 10.1016/j.commatsci.2008.09.021.

[13] L Benabou and X Wang, "International Journal for Computational Methods in Simulation of silver nanoparticles sintering at high temperatures based on theoretical evaluations of surface and grain boundary mobilities," *International Journal for Computational Methods in Engineering Science and Mechanics*, vol. 0, no. 0, pp. 1–12, 2020. DOI: 10.1080/15502287.2020.1841334.

[14] F. Raether, G. Seifert, and H. Ziebold, "Simulation of Sintering across Scales," *Adv. Theory Simulations*, vol. 2, no. 7, pp. 1–19, 2019, ISSN: 25130390. DOI: 10.1002/adts.201900048.

[15] B. Paredes-goyes, D. Jauffres, J.-m. Missiaen, and C. L. Martin, "Grain growth in sintering : A discrete element model on large packings," *Acta Materialia*, vol. 218, p. 117 182, 2021, ISSN: 1359-6454. DOI: 10.1016/j.actamat.2021.117182.

[16] B. Paredes-Goyes, D. Jauffres, J.-M. Missiaen, and C. L. Martin, "Grain growth in sintering: a discrete element model on large packings," *Acta Materialia*, vol. 218, p. 117 182, 2021, ISSN: 13596454. DOI: 10.1016/j.actamat.2021.117182.

[17] C. L. Martin, L. C. Schneider, L. Olmos, and D. Bouvard, "Discrete element modeling of metallic powder sintering," *Scripta Materialia*, vol. 55, no. 5, pp. 425–428, 2006, ISSN: 13596462. DOI: 10.1016/j.scriptamat.2006.05.017.

[18] B. Henrich, A. Wonisch, T. Kraft, M. Moseler, and H. Riedel, "Simulations of the influence of rearrangement during sintering," *Acta Materialia*, vol. 55, no. 2, pp. 753–762, 2007, ISSN: 13596454. DOI: 10.1016/j.actamat.2006.09.005.

[19] C. Wang and S. H. Chen, "The influence of agglomerates on the densification and microstructural evolution in sintering of a multi-particle system," *Science China: Physics, Mechanics and Astronomy*, vol. 55, no. 6, pp. 1051–1058, 2012, ISSN: 16747348. DOI: 10.1007/s11433-012-4743-4.

[20] S. Nosewicz, J. Rojek, K. Pietrzak, and M. Chmielewski, "Viscoelastic discrete element model of powder sintering," *Powder Technology*, vol. 246, pp. 157–168, 2013, ISSN: 00325910. DOI: 10.1016/j.powtec.2013.05.020.

[21] R. Besler, M. Rossetti Da Silva, J. J. Do Rosario, M. Dosta, S. Heinrich, and R. Janssen, "Sintering Simulation of Periodic Macro Porous Alumina," *Journal of the American Ceramic Society*, vol. 98, no. 11, pp. 3496–3502, 2015, ISSN: 15512916. DOI: 10.1111/jace.13684.

[22] H. Xin, W. C. Sun, and J. Fish, "Discrete element simulations of powder-bed sintering-based additive manufacturing," *Int. J. Mech. Sci.*, vol. 149, no. November 2017, pp. 373–392, 2018, ISSN: 00207403. DOI: 10.1016/j.ijmecsci.2017.11.028.

[23] T. Matsuda, "Development of a DEM taking account of neck increments caused by surface diffusion for sintering and application to analysis of the initial stage of sintering," *Computational Materials Science*, vol. 196, no. April, p. 110 525, 2021, ISSN: 0927-0256. DOI: 10.1016/j.commatsci.2021.110525.

[24] D. Bouvard and R. M. McMeeking, *Deformation of Interparticle Necks by Diffusion-Controlled Creep*, 1996. DOI: 10.1111/j.1151-2916.1996.tb07927.x.

[25] J. Pan, H. Le, S. Kucherenko, and J. A. Yeomans, "A model for the sintering of spherical particles of different sizes by solid state diffusion," *Acta Materialia*, vol. 46, no. 13, pp. 4671–4690, 1998, ISSN: 13596454. DOI: 10.1016/S1359-6454(98)00144-X.

[26] H. Ch'ng and J. Pan, "Sintering of particles of different sizes," *Acta Materialia*, vol. 55, no. 3, pp. 813–824, 2007, ISSN: 13596454. DOI: 10.1016/j.actamat.2006.07.015.

[27] D. Bhattacharya, R. Kawamoto, K. Karapiperis, J. E. Andrade, and A. Prashant, "Mechanical behaviour of granular media in flexible boundary plane strain conditions: experiment and level-set discrete element modelling," *Acta Geotechnica*, vol. 16, no. 1, pp. 113–132, 2021, ISSN: 18611133. DOI: 10.1007/s11440-020-00996-8.

[28] B. V. Derjaguin, V. M. Muller, and Y. P. Toporov, "Effect of contact deformations on adhesion of particles," *J. Colloid Interface Sci.*, vol. 53, pp. 314–326, 1975.

[29] C. L. Martin and R. K. Bordia, "Influence of adhesion and friction on the geometry of packings of spherical particles," *Phys. Rev. E*, vol. 77, p. 31 307, 2008.

[30] O. A. Ruano, J. Wadsworth, and O. D. Sherby, "Deformation of fine-grained alumina by grain boundary sliding accommodated by slip," *Acta Materialia*, vol. 51, no. 12, pp. 3617–3634, 2003, ISSN: 13596454. DOI: 10.1016/S1359-6454(03)00180-0.

[31] W. M. Robertson and R. Chang, "The Kinetics of Grain-Boundary Groove Growth on Alumina Surfaces," *The Role of Grain Boundaries and Surfaces in Ceramics*, pp. 49–60, 1966. DOI: 10.1007/978-1-4899-6311-6{_}4.

[32] S. J. Dillon and M. P. Harmer, "Intrinsic grain boundary mobility in alumina," *Journal of the American Ceramic Society*, vol. 89, no. 12, pp. 3885–3887, 2006, ISSN: 00027820. DOI: 10.1111/j.1551-2916.2006.01331.x.

[33] A. Tsoga and P. Nikolopoulos, "Groove Angles and Surface Mass Transport in Polycrystalline Alumina," *Journal of the American Ceramic Society*, vol. 77, no. 4, pp. 954–960, 1994, ISSN: 15512916. DOI: 10.1111/j.1151-2916.1994.tb07252.x.

[34] J. D. Hansen, R. P. Rusin, M. Teng, and D. L. Johnson, "Combined-Stage Sintering Model," *Journal of the American Ceramic Society*, vol. 75, no. 5, pp. 1129–1135, 1992, ISSN: 15512916. DOI: 10.1111/j.1151-2916.1992.tb05549.x.

[35] Z. J. Liu, Q. Cheng, Y. Wang, Y. Li, and J. Zhang, "Sintering neck growth mechanism of Fe nanoparticles: A molecular dynamics simulation," *Chemical Engineering Science*, vol. 218, p. 115 583, 2020, ISSN: 00092509. DOI: 10.1016/j.ces.2020.115583.

[36] K. A. Berry and M. P. Harmer, "Effect of MgO Solute on Microstructure Development in Al2O3," *Journal of the American Ceramic Society*, vol. 69, no. 2, pp. 143–149, 1986, ISSN: 15512916. DOI: 10.1111/j.1151-2916.1986.tb04719.x.

[37] S. I. Bae and S. Baik, "Sintering and grain growth of ultrapure alumina," *Journal of Materials Science*, vol. 28, no. 15, pp. 4197–4204, 1993, ISSN: 00222461. DOI: 10.1007/BF00351254.

[38] S. J. Bennison and M. P. Harmer, "Effect of Magnesia Solute on Surface Diffusion in Sapphire and the Role-of Magnesia in the Sintering of Alumina," *Journal of the American Ceramic Society*, vol. 73, no. 4, pp. 833–837, 1990, ISSN: 15512916. DOI: 10.1111/j.1151-2916.1990.tb05122.x.

[39] J. Rödel and A. M. Glaeser, "Anisotropy of Grain Growth in Alumina," *Journal of the American Ceramic Society*, vol. 73, no. 11, pp. 3292–3301, 1990, ISSN: 15512916. DOI: 10.1111/j.1151-2916.1990.tb06452.x.

[40] J. Zhao and M. P. Harmer, "Effect of Pore Distribution on Microstructure Development: III, Model Experiments," *Journal of the American Ceramic Society*, vol. 75, no. 4, pp. 830–843, 1992, ISSN: 15512916. DOI: 10.1111/j.1151-2916.1992.tb04148.x.

[41] J. Zhao and M. P. Harmer, "Effect of Pore Distribution on Microstructure Development: III, Model Experiments," *Journal of the American Ceramic Society*, vol. 75, no. 4, pp. 830–843, 1992, ISSN: 15512916. DOI: 10.1111/j.1151-2916.1992.tb04148.x.

[42] Z. Z. Fang, H. Wang, and V. Kumar, "Coarsening, densification, and grain growth during sintering of nano-sized powders—A perspective," *International Journal of Refractory Metals and Hard Materials*, vol. 62, pp. 110–117, 2017, ISSN: 22133917. DOI: 10.1016/j.ijrmhm.2016.09.004.

[43] V. Kumar, Z. Z. Fang, and P. C. Fife, "Phase field simulations of grain growth during sintering of two unequal-sized particles," *Materials Science and Engineering A*, vol. 528, no. 1, pp. 254–259, 2010, ISSN: 09215093. DOI: 10.1016/j.msea.2010.08.061.

[44] R. Kawamoto, E. Andò, G. Viggiani, and J. E. Andrade, "Level set discrete element method for three-dimensional computations with triaxial case study," *Journal of the Mechanics and Physics of Solids*, vol. 91, pp. 1–13, 2016, ISSN: 00225096. DOI: 10.1016/j.jmps.2016.02.021.

Chapter 5

LS-DEM model of sintering

This chapter introduces a proof of concept of a LS-DEM framework for studying the sintering of non-spherical particles. This is presented as a scientific article entitled *A level set Discrete Element Model (LS-DEM) for sintering with an optimization-based contact detection* that will be submitted to one of the following journals: *Computational Particle Mechanics*, *Computational Materials Science* or *Modelling and Simulation in Materials Science and Engineering* at the end of 2022.

Previous chapters have described the development and application of a coupled grain growth and densification model for studying sintering from a discrete perspective. This allowed us to investigate the microstructural evolution of large packings of spherical particles. Chapter 2 showed that sintering is a curvature-driven process and that there are no DEM sintering methods for non-spherical particles in the literature. The fact that many sintering powders are composed of non-spherical particles, motivates the second axis of this PhD thesis, dedicated to the development of a DEM framework for non-spherical particles. The reader's attention is attracted to the fact that this chapter focuses more on computational methods than on materials science, unlike the previous chapters. This is because, as stated above, the proposed LS-DEM framework is essentially a proof of concept with applications following later on.

The fundamentals of the LS-DEM method, capable of describing arbitrary shape particles from a DEM perspective, were presented in chapter 2. In this chapter the main ingredients of the proposed LS-DEM sintering model are explained. Emphasis is on the proposed algorithm of contact detection for non-spherical particles, which is a critical change from the straightforward contact detection for spherical particles discussed in chapters 1 and 2. The developed sintering framework is valid for modeling arbitrary shape particles. Here, as a proof of concept, the simulations are performed for ellipsoidal particles and without considering grain growth.

The incorporation of non-spherical particles into DEM simulations of sintering, as with the introduction of grain growth (chapter 3), calls for new expressions for the normal force and for the neck size. Simple approximations are employed in this chapter, nevertheless their validation or the proposition of new expressions should be the object of future work. This chapter completes the modeling proposed in this PhD.

Abstract

Sintering is a well-known high temperature process for the consolidation of ceramic, metal and polymer powders. The Discrete Element Method (DEM) has been effectively used to model the sintering process at the particle scale considering spherical particles. However, manufacturing processes result very often in non-spherical particles. Since sintering is a curvature-driven process, it is important to take deviation from sphericity into account. This study presents for the first time a DEM sintering model for non-spherical particles. The description and dynamic evolution of arbitrary shape particles is achieved by using the level set discrete element method (LS-DEM). The original LS-DEM approach used boundary nodes on the particles to detect contacts. We use an optimization-based contact detection approach. This improves the capture of small contacts, which are important for a correct description of sintering evolution with a reasonable CPU consumption. A Newton-Raphson scheme is employed for the optimization algorithm. The normal force and neck size evolution expressions of spherical particles are adapted for arbitrary shape particles by using the local curvature at the contact. The developed model is validated for elastic contacts on superquadric ellipsoids. It is validated for sintering contacts by comparing with standard DEM on spheres. This work is a proof of concept of a LS-DEM sintering model. It is applied to investigate the densification and consolidation kinetics of a packing of ellipsoidal particles.

Keywords: discrete element method, level set, sintering, non-spherical particles, contact detection, optimization.

5.1 Introduction

Sintering is a prominent high-temperature process to manufacture ceramic, metallic and polymeric materials by consolidating powders. The driving force to transform an initial particulate material into a bulk material is the reduction of the interfacial energy of the system. The seminal experimental work of Petzow and Exner showed that particle rearrangement is an important feature of solid-state sintering for crystalline and amorphous powders [1]. More recent studies using X-ray tomography confirmed that translational, rolling and intrinsic rotation movements of particles play an important role [2]. These works substantiated the argument that during sintering, powders cannot be considered as a continuum and that the discrete nature of the initial material is maintained at a late stage of the process. This motivated the use of discrete simulations to take explicitly into account the particulate nature of the processed material.

The Discrete Element Method (DEM), is well adapted to this task as it can handle the interactions of a large number of discrete particles. It has been used extensively to model sintering over the past 20 years [3]–[13]. For simplicity and to limit CPU time, all these studies represent particles as spheres. The main reason is that contact detection between two spheres is fast and can be fairly easily optimized. Nevertheless, actual particles are not spherical. For example, SEM images of common alumina powders show that the particle shape is far from being spherical (Figure 5.1a). Even particles in advanced alumina manufacturing process, where the size, size distribution and shape are controlled, are not perfect spheres (Figure 5.1b). The shape can influence the microstructural evolution as sintering is a curvature-driven process. For instance, kinetic Monte-Carlo simulations have found that packings with higher aspect ratio particles reach higher densities [14], [15].

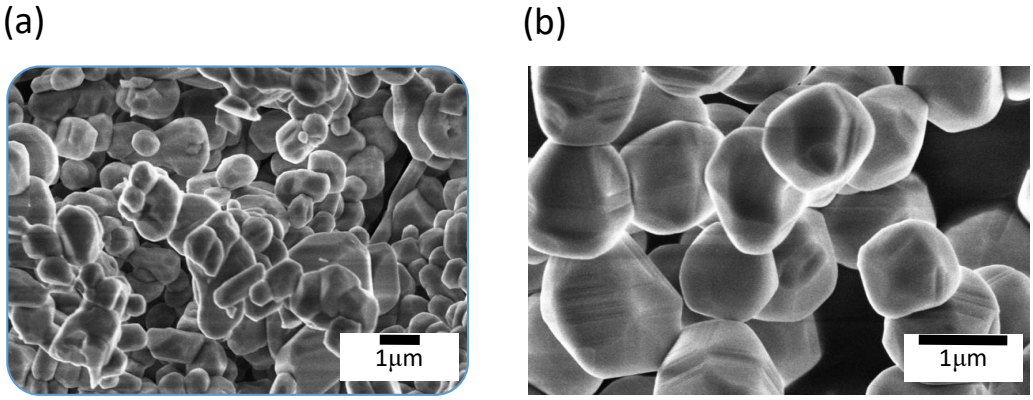

Figure 5.1: SEM images of powders of a) alumina from general manufacturing process (Bayer process), b) alumina from advanced manufacturing process (hydrolysis of aluminum alkoxide) (Courtesy of Aatreya Manjulagiri Venkatesh)

In the DEM framework, the most common representations of non-spherical particles, as summarized by Lu et al. [16], are multi-spheres, ellipsoids, polyhedral, superquadrics, the combination of geometric elements, and potential particles. Multi-spheres is a widely used method for representing arbitrary shape particles, however for sintering applications is not convenient since the local curvature may not be correctly captured. More recently new representations have been proposed in terms of level sets [17], surface meshes [18] and Fourier series [19].

The level-set method was pioneered by Dervieux and Thomasset [20] and by Osher and Sethian [21]. It uses a scalar function to represent a close surface in 3D. The level-set function is zero for any point on the particle surface, negative inside and positive outside. Coupling DEM and level-sets (LS-DEM) [17] is an interesting approach that captures arbitrary shapes using level sets, while keeping the discontinuous framework of DEM. The method allows to obtain the real shapes of particle directly

from 3D tomography images. Although LS-DEM computational cost is higher than DEM, the method is tractable for tens or hundreds of thousands of particles [17]. A detailed comparison between LS-DEM and DEM on accuracy and computational cost has been recently proposed [22]. LS-DEM has already been applied for triaxial compaction tests [17], breakage mechanics [23], [24], electrostatic cohesion [25], prediction of shear banding [26], the investigation of incremental behavior of granular materials [27] and particle bonding [28]. The above studies have in common that they focus on geomaterials, which feature elasto-plastic interactions between particles. For engineering materials, the sintering at high temperature of specific contact laws have been provided for DEM [3], [4], [12] with spherical particles. They introduce material parameters such as diffusion coefficients and surface energies. So far, and to the best of our knowledge, LS-DEM has not been applied to the sintering process. The aim of this work is to present a LS-DEM framework that is compatible both with elasto-plastic interactions and sintering interactions.

Contact detection is the most challenging stage of simulating non-spherical particles. LS-DEM, as proposed originally by Kawamoto et al. [17] performs this task by creating boundary nodes on the particle surface and evaluating if they are inside another particle (see Fig. 2.17 in chapter 2). As part of our initial test, we have applied this technique to a packing of relative density 0.59 with non-uniform size particles, generated by classic DEM. The packing is composed of 400 spherical particles, which allows a direct comparison with DEM results on one LS-DEM timestep. Fig. 5.2 shows the percentage of contacts detected by LS-DEM as a function of the number of boundary nodes per particle. Fig. 5.2 indicates that even 40 000 nodes only detect around 70% of the existing contacts. For denser packings (0.64 and 0.69), we observed that 4 000 nodes lead to 99% of the contacts detected. This indicates that the contact detection algorithm mainly misses small contacts. These results are coherent with those of Duriez et al. [22] who have shown that 10 000 nodes lead to a 15% underestimation of the macroscopic pressure (the number of missed contacts is not indicated). In a packing where interactions are elastic, missing small contacts (30% for 40 000 nodes) has only a limited impact on the macroscopic pressure since the pressure is linearly related to contact forces (Love equation [29]). However, for sintering, small contacts are associated with large tensile forces driven by surface energy minimization (as detailed in section 5.2.4). Thus, small contact detection is critical for a correct description of the packing macroscopic behavior, and in particular of the densification rate, and of the rearrangement of particles.

Increasing the number of boundary nodes is not a viable option as it becomes CPU prohibitive above 10 000 nodes. A recent LS-DEM study [30] applied an optimization-

based contact detection in order to decrease the computational cost and eliminate the dependence of the force on the number of boundary nodes. While they used a derivative-free optimization algorithm, we opt to use the Newton-Raphson method because of its fast local convergence and the ease of calculating derivatives from the discrete level set function, which will also be used for curvature calculation. This approach is based on the two-contact points search proposed by Houlsby [31] in the context of what he is defining as 2D potential particles (and what we define shape function). The author developed it for convex particles, however, we add here a multi-start strategy for contact detection among convex particles, that could also be used to find multiple contact points in non-convex particles.

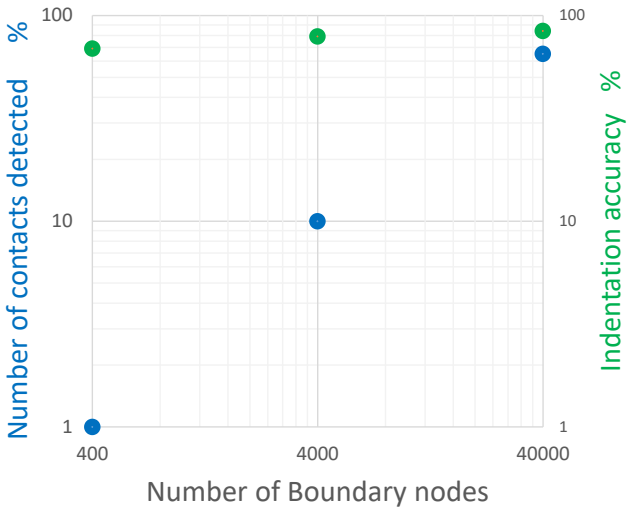

Figure 5.2: Contact detection accuracy for an initial sintering packing as a function of the number of boundary nodes in original LS-DEM for a packing density of 0.59.

Our work presents a LS-DEM model of sintering with an optimization-based contact detection. Section 5.2 describes the model detailing the contact detection scheme. Section 5.3 validates the developed model for elastic and sintering interactions. Section 5.4 models the sintering of a two-particle system and of a packing of particles. As the aim is to provide a proof of concept of our scheme, we have limited applications to ellipsoid shapes.

5.2 Model description

5.2.1 Equations of motion

The evolution of the center of mass position, $\vec{x_i}$, for each particle i follows Newton's second law:

$$m_i \ddot{\vec{x}_i} = \sum \vec{F_{ij}} \tag{5.1}$$

where m_i is the particle mass and $\vec{F_{ij}}$ the total force (with normal and tangential components in the local framework) exerted by a particle j in contact. The particle position is updated by imposing first an affine displacement which follows the macroscopic imposed strain-rate and integrating Eq. (5.1) using a Velocity Verlet algorithm as detailed in [32].

For non-spherical particles, even in the absence of frictional forces, rotations need to be considered. We approximate sintering as a quasi-static process, in this case the nonlinear term of the general equation of rotational motion can be neglected obtaining the following expression for the angular position $\vec{\theta_i}$ [33]:

$$I_i \ddot{\vec{\theta}_i} = \sum \vec{M_{ij}} \tag{5.2}$$

with the particle moment inertia I_i and the torque $\vec{M_{ij}}$. In addition, the quasi-static assumption also allows the non-diagonal terms of the moment of inertia tensor to be neglected [33], [34]. The particle mass and moment of inertia are estimated as proposed in the original LS-DEM methodology [17].

Quaternions are used to track rotations of particles. The advantage (as compared to Euler angles) is to avoid singularities at small angles [35]. A quaternion $\mathbf{q}$, defined by an orientation vector $\vec{u}$ and an angle θ, is attached to each particle:

$$\mathbf{q} = (q_0, q_1, q_2, q_3,)^T = cos(\theta(t)/2) + sin(\theta(t)/2)\,[u_x\vec{x} + u_y\vec{y} + u_z\vec{z}] \tag{5.3}$$

At each time step, its variation is calculated depending on the rotational velocity at full time step $\vec{\theta}_{t+\Delta t}$:

$$\mathbf{q}_{\Delta t} = \cos\left(\frac{|\vec{\theta}_{t+\Delta t}|\Delta t}{2}\right) + \sin\left(\frac{|\vec{\theta}_{t+\Delta t}|\Delta t}{2}\right)\frac{\vec{\theta}_{t+\Delta t}}{|\vec{\theta}_{t+\Delta t}|} \tag{5.4}$$

The updated orientation is computed by the quaternion product: $\mathbf{q}_{t+\Delta t} = \mathbf{q}_t\mathbf{q}_{\Delta t}$ [36].

5.2.2 Discrete level set function and derivatives

The particle shape is described by the signed distance to the particle surface (level set) stored at grid points [17]. The level set can be computed analytically from the distance equation to a 3D shape or obtained from tomography images of the packing of particles [37].

The bounding sphere of the particle is used to build a local uniform Cartesian grid with $ncell_{int}$ number of cells in each direction (Figure 5.3). $ncell_{ext}$ extra cells of the same size are added in all directions for contact detection purposes (see section 5.2.3). The level set values are stored on all these grid points (green dots in Figure 5.3).

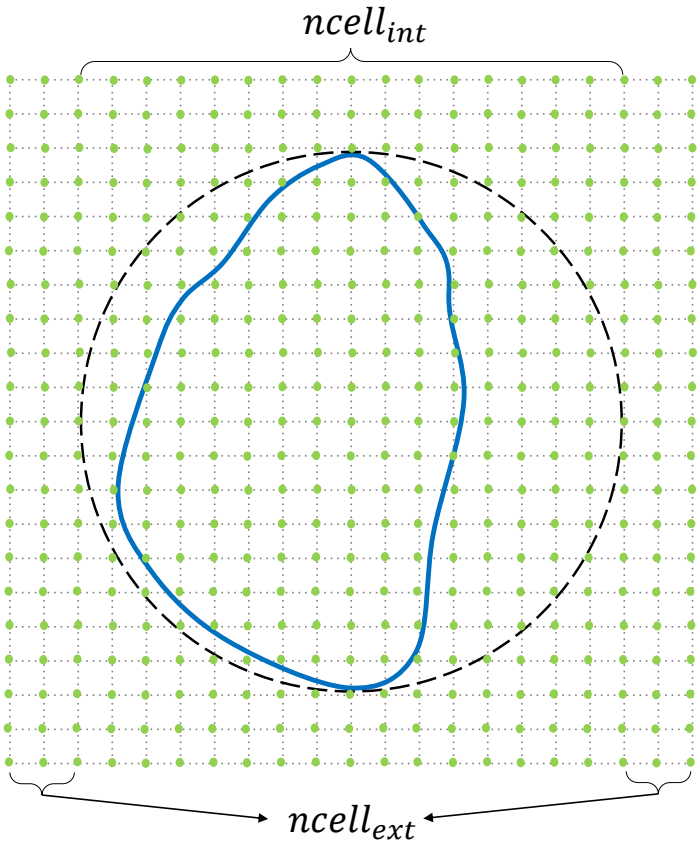

Figure 5.3: 2D schematic of a local grid of a particle with grid points in green. The grid is composed by $ncell_{int}$+$ncell_{ext}$ cells in each direction. The bounding sphere of the particle is represented by the dashed circle.

During the contact detection and calculation stages, the level set values and their derivatives are required at points among the grid points. Linear interpolation is used to calculate the level set value ϕ at any point p from the surrounding abc grid points

with level set values ϕ_{abc} [17]:

$$\phi(p) = \sum_{a=0}^{1}\sum_{b=0}^{1}\sum_{c=0}^{1}\phi_{abc}\left[(1-a)(1-x)+ax\right] \\ \left[(1-b)(1-y)+by\right]\left[(1-c)(1-z)+cz\right] \quad (5.5)$$

Here for simplicity, the first and second derivatives of the level set are computed by central finite differences (FD). To prevent the second derivative from vanishing due to the first-degree polynomial $\phi(p)$, a FD step size greater than the grid cell size is adopted. We verified that these approximations do not have any noticeable impact on the final results.

In contrast with other LS-DEM works, our contact law needs the input of the local curvature (see section 5.2.4). We use the mean curvature instead of the Gaussian curvature to avoid singularities of the curvature radius as pointed out by Podlozhnyuk et al. [38] for superquadric particles. The mean curvature κ of level sets is used by adopting the formula proposed in [39] for implicit surfaces. Writing κ in terms of first and second derivatives of a particle i gives:

$$\kappa = \frac{\begin{array}{r}\phi_{ix}^2\phi_{iyy} - 2\phi_{ix}\phi_{iy}\phi_{ixy} + \phi_{iy}^2\phi_{ixx} + \phi_{ix}^2\phi_{izz} - 2\phi_{ix}\phi_{iz}\phi_{ixz} \\ + \phi_{iz}^2\phi_{ixx} + \phi_{iy}^2\phi_{izz} - 2\phi_{iy}\phi_{iz}\phi_{iyz} + \phi_{iz}^2\phi_{iyy}\end{array}}{2|\nabla\phi_i|^3} \quad (5.6)$$

where $\phi_{ik} = \frac{\partial\phi_i}{\partial k}$ and $\phi_{ikl} = \frac{\partial^2\phi_i}{\partial k\partial l}$.

5.2.3 Contact detection

5.2.3.1 Particle-particle contact

The search algorithm for contacts is based on an optimization approach. We extend to 3D the method developed by Houlsby [31] for 2D particles. These particles had an analytical expression describing their shape. In our case, we adapt the method to the level set discretized on the grid.

Recall that for a given particle, its level set is negative inside the particle, zero on the surface, and positive outside as shown in Figure 5.4. Let i and j be two particles in potential contact, in a first step, the objective is to find, if it exists, the innermost point in j while imposing that it belongs to the surface of i ($\vec{x}_{op,\phi i}$ in Figure 5.4). This point can be found by solving the following constrained optimization problem:

$$\begin{array}{ll}\min\limits_{x,y,z} & \phi_j(x,y,z) \\ \text{s.t.} & \phi_i(x,y,z) = 0\end{array} \quad (5.7)$$

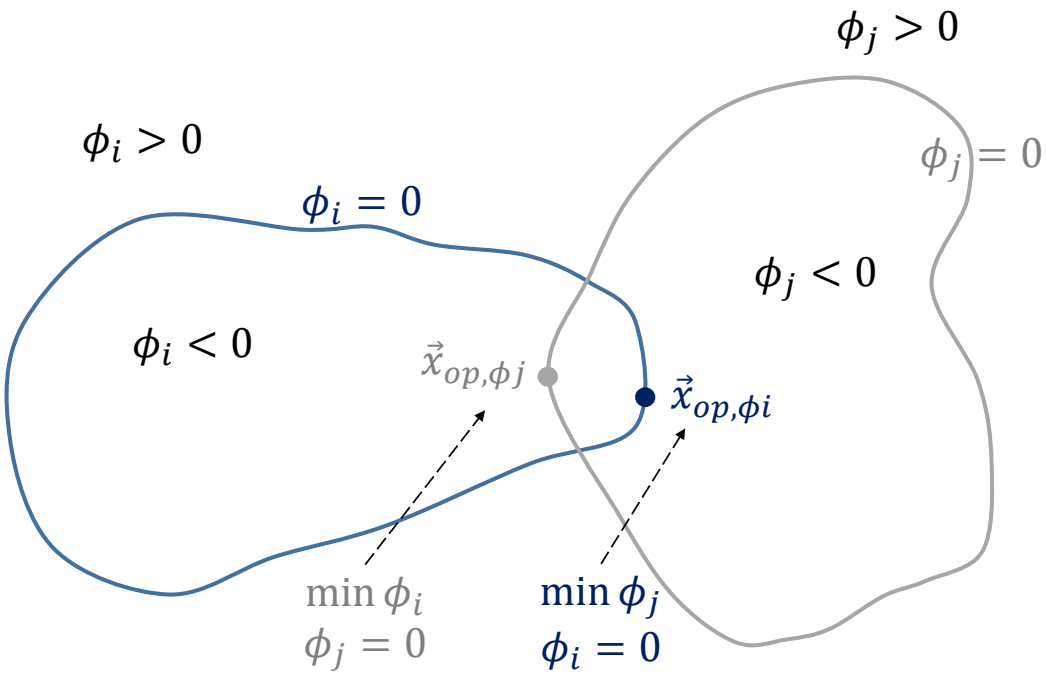

Figure 5.4: Optimization-based contact detection for two particles i and j described by level sets ϕ. $\vec{x}_{op,\phi i}$ is the innermost point in j on the surface of i (first step). $\vec{x}_{op,\phi j}$ is the innermost point in i on the surface of j (second step).

where s.t. stands for subject to. If the point found is inside the particle j, i.e., $\phi_j\left(\vec{x}_{op,\phi i}\right) < 0$, the two particles are in contact. In that case, a similar optimization problem is solved to find the point $\vec{x}_{op,\phi j}$ (Figure 5.4):

$$\begin{aligned} \min_{x,y,z} \quad & \phi_i\left(x,y,z\right) \\ \text{s.t.} \quad & \phi_j\left(x,y,z\right) = 0 \end{aligned} \tag{5.8}$$

This second optimization step is needed to compute the required contact parameters [31] (section 5.2.4). It is also used as a back-up to ensure that the contact actually exists. This is because in a few cases, inaccuracies can arise due to the discretized character of the level set function on the grid.

Solving the optimization problems in Eqs. (5.7) and (5.8) separately, Houlsby [31] applied in 2D the method of Lagrangian multipliers to obtain a set of nonlinear equations, which he solved with the Newton-Raphson (N-R) method. Here, the same approach is adopted. The linear system of one N-R iteration that we have obtained for the optimization problem (5.7) is in 3D:

$$\begin{pmatrix} \phi_{ix} & \phi_{iy} & \phi_{iz} \\ \phi_{ixx}\phi_{jy} + \phi_{ix}\phi_{jxy} - \phi_{jxx}\phi_{iy} - \phi_{jx}\phi_{ixy} & \phi_{ixy}\phi_{jy} + \phi_{ix}\phi_{jyy} - \phi_{jxy}\phi_{iy} - \phi_{jx}\phi_{iyy} & \phi_{ixz}\phi_{jy} + \phi_{ix}\phi_{jyz} - \phi_{jxz}\phi_{iy} - \phi_{jx}\phi_{iyz} \\ \phi_{ixx}\phi_{jz} + \phi_{ix}\phi_{jxz} - \phi_{jxx}\phi_{iz} - \phi_{jx}\phi_{ixz} & \phi_{ixy}\phi_{jz} + \phi_{ix}\phi_{jyz} - \phi_{jxy}\phi_{iz} - \phi_{jx}\phi_{iyz} & \phi_{ixz}\phi_{jz} + \phi_{ix}\phi_{jzz} - \phi_{jxz}\phi_{iz} - \phi_{jx}\phi_{izz} \end{pmatrix} \begin{pmatrix} \Delta x \\ \Delta y \\ \Delta z \end{pmatrix} = \begin{pmatrix} -\phi_i \\ -\phi_{ix}\phi_{jy} + \phi_{jx}\phi_{iy} \\ -\phi_{ix}\phi_{jz} + \phi_{jx}\phi_{iz} \end{pmatrix} \tag{5.9}$$

or in compact form:

$$\mathbf{J}\vec{\Delta_x} = -\Phi \tag{5.10}$$

where $\mathbf{J}$ is the Jacobian matrix. At iterations nr, the new point is $\vec{x}_{nr+1} = \vec{x}_{nr} + \alpha_{nr}\vec{\Delta_x}$ with α_{nr} a scalar ($\alpha_{nr} \leq 1$). The optimal point $\vec{x}_{op,\phi i}$ is obtained after a few N-R iterations. The scalar parameter α_{nr} ensures stability and is calculated as in [38]. The initial point $\vec{x}_{0sph}$ is chosen as the barycenter of the two spheres that circumscribe the particles. The barycenter initial point for N-R is kept as long as no contact is found. Once a contact is detected, the last value of $\vec{x}_{op,\phi i}$ is kept for the next time step as the initial point for N-R.

In very few instances, we have observed that the above procedure does not detect existing contacts. This issue is due to the local convergence of Newton-Raphson. To make contact detection more robust, we implement a simple multi-start strategy. If the $\vec{x}_{0sph}$ initial point does not lead to a contact, N_{ms} random points on the surface of a sphere with origin in $\vec{x}_{0sph}$ and with radius $r_{ms} = 0.5\ \min(r_i, r_j)$ are tested as initial points for the N-R search. There is a compromise between the effectiveness of the method and the computational cost. Our simulations have shown that $N_{ms} = 5$ gives a good balance for ellipsoids. The number of grid cells N_{cell} also affects this choice.

5.2.3.2 Particle-plane contact

Similarly, the contact detection of a particle-plane pair is based on optimization. From the general equation of the plane, a level set function can be deduced. This allows to formulate the optimization problem in the form of Eq. (5.7), where i is the particle and j the plane. We consider only planes perpendicular to the main axes. For illustration, considering a plane perpendicular to the z axis, the following system of equations is obtained:

$$\begin{pmatrix} \phi_{ix} & \phi_{iy} & \phi_{iz} \\ \phi_{ixx} & \phi_{ixy} & \phi_{ixz} \\ \phi_{ixy} & \phi_{iyy} & \phi_{iyz} \end{pmatrix} \begin{pmatrix} \Delta x \\ \Delta y \\ \Delta z \end{pmatrix} = \begin{pmatrix} -\phi_i \\ -\phi_{ix} \\ -\phi_{iy} \end{pmatrix} \tag{5.11}$$

The simplicity of the level set of a plane makes Eq. (5.11) simpler than particle-particle Eq. (5.9). Eq. (5.11) is solved in the same way with a multi-start procedure. The only difference is that for particle-plane it is not necessary to solve the second optimization problem (Eq. (5.8)).

5.2.4 Sintering contact law

Once a contact between two particles i and j is detected, the contact force is calculated in the next stage. Like other forces, the sintering force needs the values of the overlap or indentation h_{ij} and of the unit normal vector at the contact. Unlike the original LS-DEM method, we have two points at each contact ($\vec{x}_{op,\phi i}$ and $\vec{x}_{op,\phi j}$) instead of one. Therefore, the contact variables are calculated based on the two points. We follow the procedure of potential particles proposed in [31] that suggests to average the values. The indentation then between two particles is given by:

$$h_{ij} = \frac{-\phi_i\left(\vec{x}_{op,\phi j}\right) - \phi_j\left(\vec{x}_{op,\phi i}\right)}{2} \tag{5.12}$$

while the unit normal vector is calculated from:

$$\vec{n}_{ij} = \frac{\nabla\phi_i\left(\vec{x}_{op,\phi i}\right) - \nabla\phi_j\left(\vec{x}_{op,\phi j}\right)}{\left|\nabla\phi_i\left(\vec{x}_{op,\phi i}\right) - \nabla\phi_j\left(\vec{x}_{op,\phi j}\right)\right|} \tag{5.13}$$

Our force calculation depends on the maximum indentation, which makes it mesh independent, unlike some of the others LS-DEM approaches [40].

For two spherical particles, the normal force N_{ij} [32], [41] is:

$$N_{ij} = \frac{\pi a_{ij}^4}{8\Delta_{GB}} \frac{\mathrm{d}h_{ij}}{\mathrm{d}t} - \frac{\alpha}{2}\pi R_{eq,ij}\gamma_S \tag{5.14}$$

where α is a parameter of the model, γ_S is the surface energy and $\Delta_{GB} = \frac{\Omega}{k_b T} D_{GB}\delta_{GB}$, with the atomic volume Ω, the Boltzmann constant k_b, the temperature T, the grain boundary diffusivity D_{GB}, the grain boundary thickness δ_{GB} and $R_{eq,ij}$ the equivalent radius. The first term is a viscous component that counteracts the relative motion of the two particles and the second term is the sintering attractive force. Eq. (5.14) introduces the rate of approach of the two particles ($\frac{\mathrm{d}h_{ij}}{\mathrm{d}t}$). This value is computed using the relative velocity of the two particles (at the last time step) and the unit

normal vector $\vec{n}_{ij}$.

A simple analytical equation of the mean normalized indentation as a function of time can be derived from Eq. (5.14) by assuming that the packing equilibrium is attained if contacts fulfill $N_{ij} = 0$. This simplistic assumption, together with assuming that all particles have the same radius $R = 2R_{eq}$, and that the initial indentation is zero leads to:

$$\left(\frac{h}{R}\right)^3 = \frac{3}{2}\frac{\alpha\Delta_{GB}}{R^4}t \tag{5.15}$$

Eq. (5.15) exhibits the classic dependence to time ($h \propto t^{1/3}$) proposed by [42]. It will be used for comparison with LS-DEM simulations.

Eq. (5.14) has been developed for two spherical particles (radii r_i and r_j), with $R_{eq,ij} = r_i r_j/(r_i + r_j)$, denominated as the equivalent radius. Sintering is a process driven by the local curvature gradient. Thus, we propose to generalize Eq. (5.14) for non-spherical particles by ascribing the mean local curvature radii to r_i and r_j. A similar approach was employed for the elastic Hertzian law in [38] with good results when compared with FEM simulations. The mean local curvatures κ_i and κ_j are calculated from Eq. (5.6) on the contact points $\vec{x}_{op,\phi i}$ and $\vec{x}_{op,\phi j}$. The curvature radii are given by $r_i = 1/\kappa_i$ and $r_j = 1/\kappa_j$ in Eq. (5.14). The sintering neck size a is related to the indentation by Coble's geometric model [32], [43]:

$$a_{ij}^2 = 4R_{eq,ij}h_{ij} \tag{5.16}$$

Tangential forces are neglected. Thus, the force between two sintering particles is given by: $\vec{F_{ij}} = N_{ij}\vec{n}_{ij}$. Unlike spheres, a normal force applied on a non-spherical particle creates a torque. Grain growth is not considered here.

5.3 Validation

In this and the following section, analyses are performed with ellipsoidal particles defined by semi-axes a, b, c. In particular, we work with different types of spheroids (ellipsoid of revolution with $a = b$) shown in Figure 5.5. Spheroid A is a prolate spheroid ($a < c$) without any rotation, while B has a rotation of 90°with respect to axis x and C is an oblate spheroid $a > c$.

A level-set for these spheroids must be provided to fill the grid points as described by Eq. (5.5). There is no simple analytical equation for the level-set of a spheroid. An exact method, which rests on the numerical resolution to find the roots of polynomial equations, has been proposed by Eberly [44]. An alternative consists of approximating the level-set value by using a second ellipsoid that passes through the point p at which

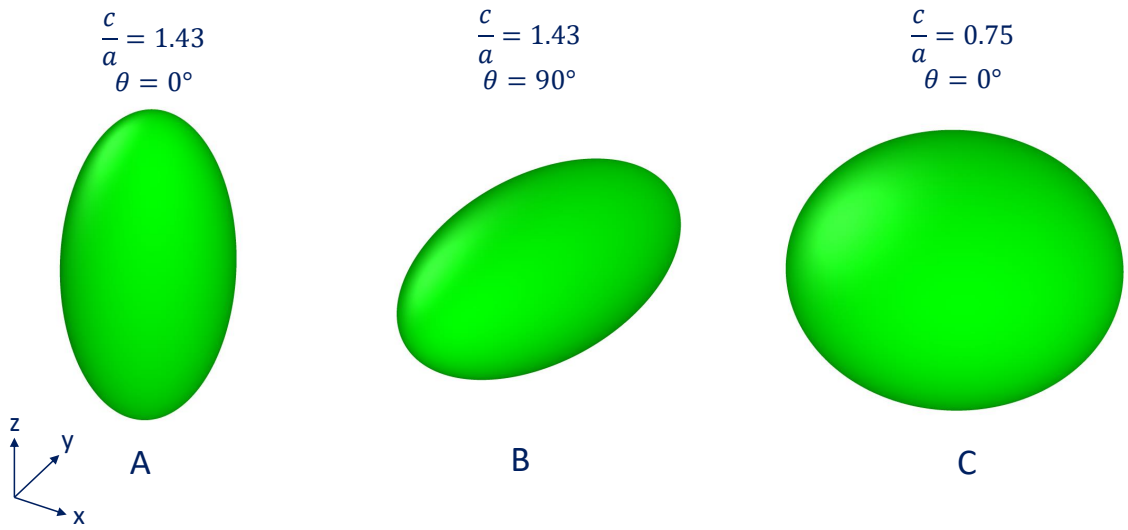

Figure 5.5: Mean indentation of ellipsoids as a function of time during jamming.

the level-set value must be determined. The level-set is approximated by the distance between point p and p_0. Fig. 5.6 shows schematically that the value is exact on the apex of the ellipsoid (and on the surface of the ellipsoid) and overestimates $\phi(p)$ otherwise. For a ellipsoid with semi-axes $a = 0.5, b = 0.5, c = 1$, we checked that the maximum error is of the order of 10% of the larger semi-axis for $\phi(p) > 0$ with the standard grid used around the particle (see Fig. 5.3).

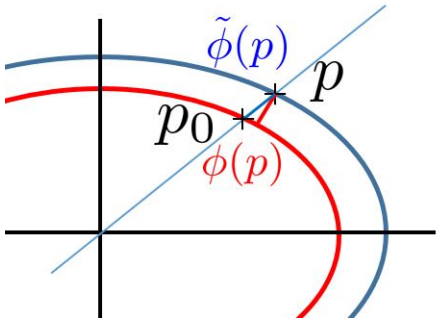

Figure 5.6: Exact level-set $\phi(p)$ and approximate level-set $\tilde{\phi}(p)$ and for an ellipsoid.

5.3.1 Elastic contact between two ellipsoidal particles

The first test aims at validating the basic calculations of our model. For this, a simple system of two equal-size ellipsoids B (Figure 5.5) aligned on the z axis with elastic contact is chosen. The contact force is calculated as a function of the mutual indentation using the Hertz equation:

$$N_{Hertz} = \frac{2}{3}\frac{E}{1-\nu^2}R_{eq}^{1/2}h^{3/2} \tag{5.17}$$

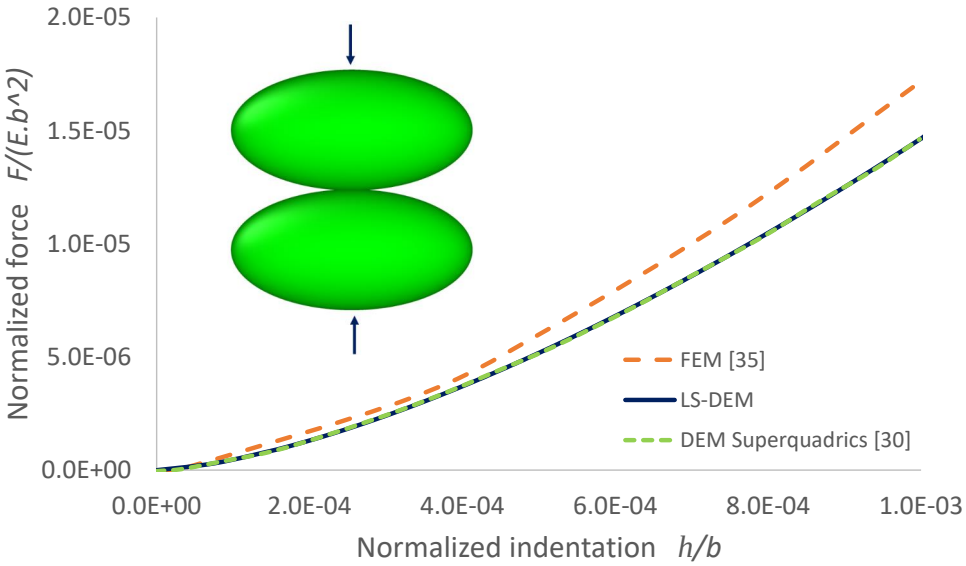

Figure 5.7: Resulting normalized elastic force versus the indentation between two aligned ellipsoids for LS-DEM, DEM superquadrics [38] and FEM [45]. The force is normalized by Eb^2, where E is the Young's modulus and b is the short axis.

A complete description of the problem is found in [38]. Figure 5.7 shows the results of our LS-DEM calculation compared with DEM superquadrics [38] and FEM calculation [45]. The overlay of the DEM superquadrics and our curve demonstrates that the calculation of the local curvature and the first and second derivatives of our level set function is correct. The close results to FEM values support the previously discussed hypothesis of using the local curvature radii in the Hertzian law. Additionally, it is possible to confirm the ability of detecting very small contacts, which will be discussed further in the next sections.

5.3.2 *Jamming* of a packing of ellipsoidal particles

The relative density of packings prior to sintering is usually between 0.50-0.65. This is close to the density of a random close packing or a maximally random jammed state [46]. Such a packing can be obtained numerically by the jamming of an initial random gas of particles. The procedure consists of randomly locating particles into the simulation box with the only constraint that there is no contact between them. The jamming itself is a stress-controlled simulation with a very small control pressure P as compared to the Young's modulus of the particles ($P/E = 10^{-6}$). This ensures that mutual indentation between particles is kept very small and does not contribute to densification (only particle rearrangement contributes to densification). With such a scheme, a maximum packing fraction is asymptotically approached while the pressure tends toward the control pressure. Details on this process for spherical particles can

be found in [47].

The jamming process is a relevant test of the proposed algorithm for contact detection as it tests its ability to detect small contacts. The packing procedure is performed for two packings of 1 000 non-uniform size particles composed by prolate ellipsoids with aspect ratio $c/a = 1.43$ and oblate ellipsoids with aspect ratio $c/a = 0.75$. The simulation box is delimited by stiff planes that interact with particles with the Hertzian equation (Eq.5.17). Figure 5.8 shows the jamming of prolate ellipsoids and oblate ellipsoids from a relative density of 0.22 and 0.33, respectively, to a final density of 0.52. The normalized mean indentation is kept in low values around 10^{-3}, which is consistent with the applied pressure.

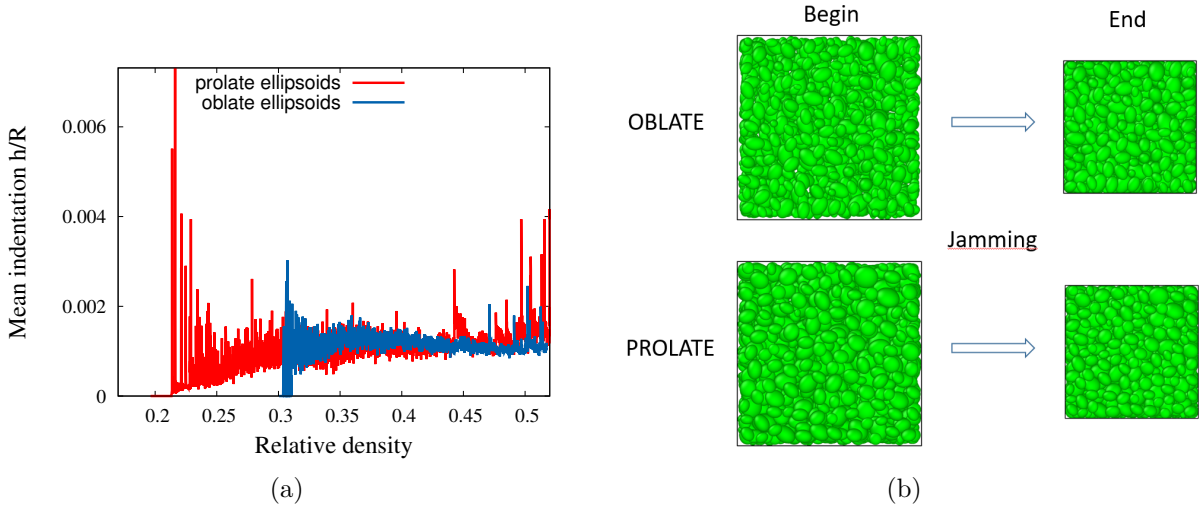

Figure 5.8: (a) Mean indentation of ellipsoids as a function of relative density during jamming. (b) Initial and final microstructures obtained.

5.3.3 Sintering of a packing of spherical particles

The tests with elastic contacts in the preceding sections have validated the main components of the model (see appendix C.1, for a test that validates the rotations using quaternions). The objective of this section is to check and validate the simulations that implement sintering contacts. A packing of LS spherical particles is chosen to compare with the analytical solution and DEM results. The initial packing contains 100 particles and exhibits a relative density D =0.52, i.e., a packing with very small indentations (h=0.001). The simulation is carried out until h/R=0.1, which is the most critical stage for contact detection and calculation. We use here a mesh with $ncell_{int} = 50$ and $ncell_{ext} = 20$.

The left axis of Figure 5.9 shows the evolution of the mean indentation with time for LS-DEM and DEM simulations. All the curves are noisy due to the small number of

particles (and non-periodic conditions). Both curves display almost the same evolution. For completeness, the results are compared with the analytical solution given by eq. (5.15). The right axis of Figure 5.9 plots $(h/R)^3$ vs time. Both LS-DEM and DEM simulations agree reasonably well with the linear analytical solution.

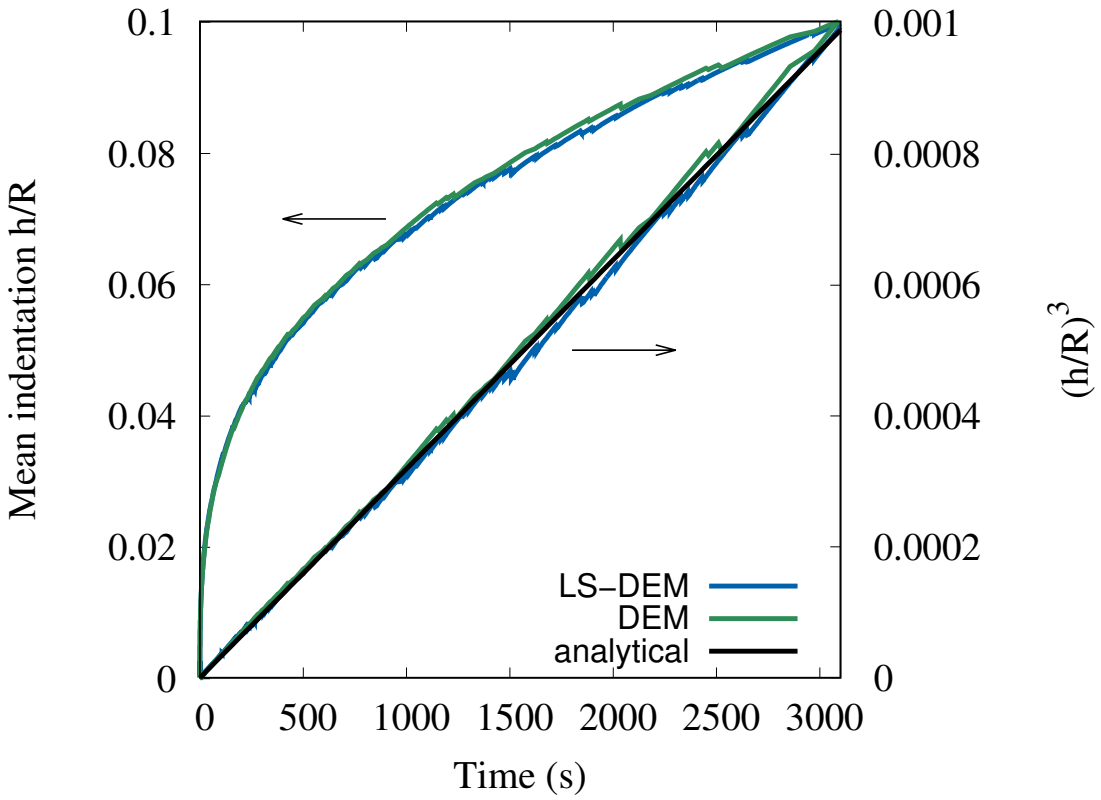

Figure 5.9: Comparison of the evolution of densification: mean normalized indentation (left) and mean normalized indentation to the cube (right) for comparison with the analytical solution (Eq. 5.15). Simulations are carried out with spheres.

Figure 5.10 presents the evolution of the mean coordination number z_c with time for LS-DEM and DEM. In contrast with the indentation, the LS-DEM coordination number differ markedly from the DEM results. Inspection of the results revealed that at the first time step the number of contacts detected by LS-DEM is smaller than for DEM. This makes each simulation follows a different dynamic hereafter. This particularly affects sintering since very small contacts will trigger the attraction term in Eq. (5.14) with very small viscous counteraction (the viscous term scales with h^2). Fig. 5.10 shows that later in the simulation, due to the different integrated history of the compacts, LS-DEM and DEM differ, and the number of contacts in LS-DEM overreaches that of DEM. Still, an agreement on the mean indentation is achieved (Figure 5.9) because contacts, that exist in LS-DEM and not in DEM, quickly increase to the mean value due to the term a^4 in Eq. (5.14). The same agreement was observed for the neck size a. Therefore, a good correlation between LS-DEM and DEM simulations of spheres

was found for the densification kinetics (h) and the consolidation kinetics (a).

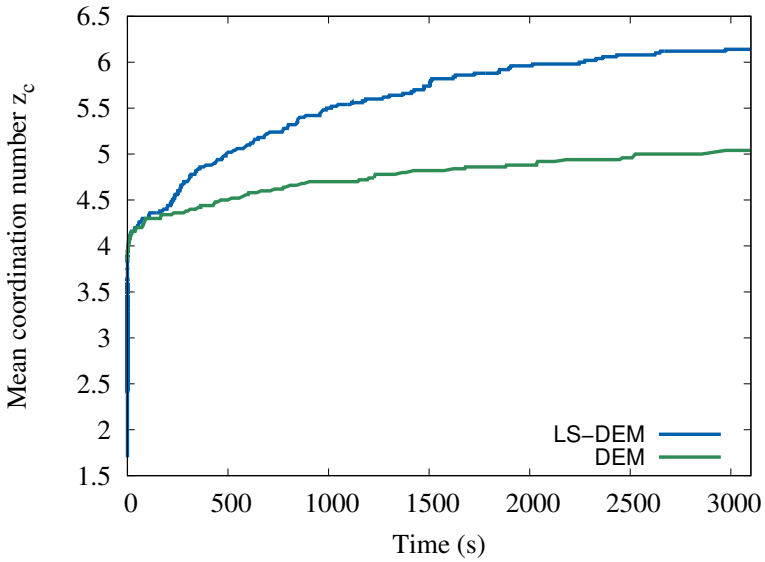

Figure 5.10: Comparison of the evolution of the mean coordination number for spherical particles.

5.4 Applications

5.4.1 Sintering between two ellipsoidal particles

So far, the DEM models have been applied to the sintering of spherical particles. In order to gain a better understanding of the behavior of ellipsoidal particles sintering, first, a system of two prolate particles of equal size is investigated. Two ellipsoids A and two ellipsoids B (Figure 5.5) aligned on the z axis are studied to evaluate the influence of curvature on sintering rates. Simulations with LS spheres ($a = b = c$) of radius c are also performed to assess the influence of the particle aspect ratio.

Figure 5.11a shows the evolution of the normalized mean indentation, i.e., densification, with time. The analytical solution provides an insight about the observed behavior: (Eq. (5.15)) shows that the normalized indentation (h/R_{eq}) scales with ($1/R_{eq}^4$). Given that at each contact point $R_{eq,sp} > R_{eq,B} > R_{eq,A}$, the expected mean indentation follows $h_A > h_B > h_{sp}$, as observed in the simulations.

DEM simulations on spherical particles show that two packings can be compared simply by inspecting their normalized indentation h/R: a larger h/R for a given packing is associated to a larger normalized neck size a/R. This does not apply anymore for particles with different aspect ratios, as indicated by comparing Figure 5.11a and b. Ellipsoids A exhibit the highest normalized indentation (where R is the radius of the bounding sphere, i.e., $R = c$ for ellipsoids A and B), while spheres have the largest

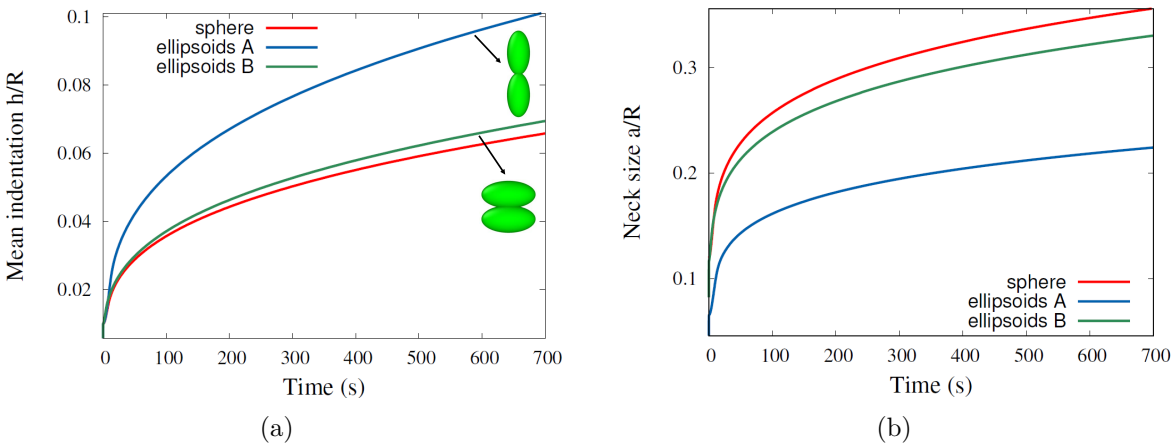

Figure 5.11: (a) Densification and (b) consolidation kinetics of two particles for different particle aspect ratios. R is the mean radius of the bounding spheres.

neck. This is a consequence of our choice of keeping the same Coble's geometric model for ellipsoids and simply replacing radii by curvature radii (Eq. (5.16)).

5.4.2 Sintering of a packing of ellipsoidal particles

The previous section, limited to two particles, showed a decoupling between densification (indentation) and consolidation (contact size) when departing from spherical particles. Simulations of a packing of particles can provide more realistic information. Packings of 1 000 prolate and oblate ellipsoidal particles with aspect ratio $c/a = 1.43$ and $c/a = 0.75$ respectively are used. These packings are non-monomodal. Particles are generated from bounding spheres following a lognormal distribution with lognormal standard deviation 0.20. The initial packings for sintering were generated in section 5.3.2. The stiff planes that were used to jam the packings are translated away from the surface of the packing. This ensures that they do not interact during sintering. The results are compared with simulations of spherical particles of mean radius $0.5\mu m$. We ensure that oblate, prolate and spherical particles have the same volume. We use here a mesh with $ncell_{int} = 100$ and $ncell_{ext} = 20$.

Figure 5.12a shows the evolution of the densification with time. The packings with ellipsoids have a faster densification than spheres. This would indicate that particles with larger aspect ratios promote faster densification. Also, Figure 5.12b shows that the mean coordination number is higher for ellipsoids highlighting a stronger rearrangement. These results have been also observed by kinetic Monte-Carlo (kMC) simulations [14], [15], which also worked with spheres and ellipsoids of same volume.

Together, Figure 5.12a and b provide some evidence that local curvature variations promote faster densification (Figure 5.12a) and that non-sphericity promote particle

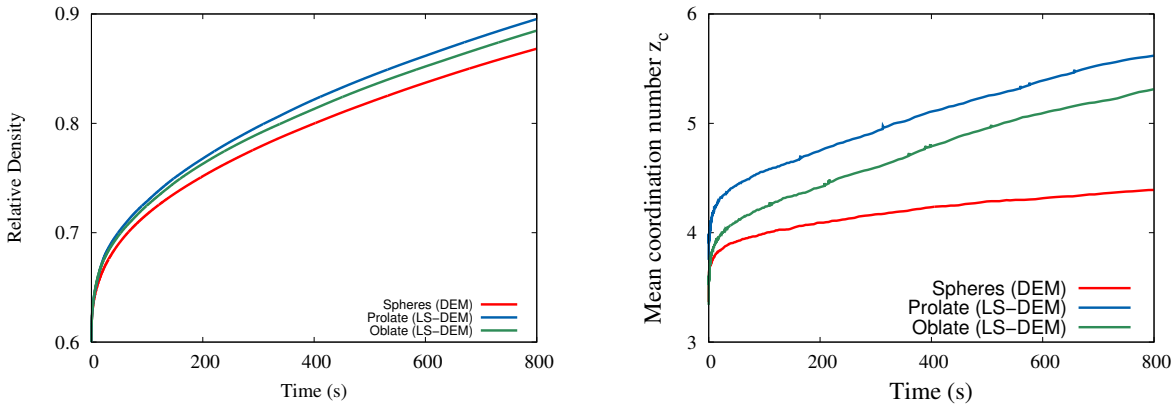

(a) (b)

Figure 5.12: Evolution of (a) the densification and (b) the mean coordination number during sintering of a packing for different particle aspect ratios.

rearrangement (Figure 5.12b). The results presented in this section are preliminary. More realistic results will be obtained with inclusion of periodic boundary conditions, tangential forces and resisting moments.

5.5 Conclusions and Perspectives

The modeling of sintering of non-spherical particles is challenging. The sintering LS-DEM developed in this work looks promising to study the densification of realistic packings composed of non-spherical particles. The framework developed can be applied to sintering of arbitrary shaped particles. Here, the sintering of ellipsoidal particles has been simulated as a proof of concept. Our future work will focus on the use of arbitrary shape particles extracted from tomography images. Still, many aspects should be improved to reach fast and accurate simulations.

Contact detection is one of the most critical stages when modeling non-spherical particles. The presented optimization-based contact detection is effective for detecting small contacts, that are important for sintering due to the high attractive force produced. The use of a multi-start optimization algorithm was proposed in order to decrease the number of missed contacts. This technique can also be used in future work to detect multiple contact points in non-convex particles.

The optimization-based contact detection has a lower CPU consumption than the boundary nodes technique since the number of level-set function evaluations is lower. However, our simulations show that the number of grid cells and thus RAM consumption is higher in the former. A detailed comparison of the overall computational cost between both methods is needed. If the RAM consumption is limiting, one solution can be to employ more effective grid structures like octree as proposed in [22]. Another

possible approach can be to use a density-based grid cell size, as a fine grid is mainly needed at low densities when contacts are very small.

The LS-DEM model described here was fully integrated into the `dp3D` code. Thus, all the contact laws that exist in `dp3D` should *a priori* be available for use with LS-DEM. The `dp3D` code is parallelized with a fine-grained method (at the loop level) with `openMP` directives. The LS-DEM contact detection scheme is within the main loop over contacts that is parallelized. However, it is clear that an optimization is needed. In particular, the access to the memory is an important bottleneck when parallelizing a code and it is an added issue for the current version of the LS-DEM, which uses many very large arrays to access grid points.

Moreover, here we extend the normal force and neck size expressions of spherical to non-spherical particles by simply using the local curvature radii instead of the sphere radii. A validation of this assumption is needed. Alternatively, a new formulation of an expression of the sintering force for non-spherical particles should be proposed. This was already proposed for elasticity with ellipsoidal particles [45] or arbitrary shaped particles [48], [49].

All the simulations carried out in this chapter have used stiff walls (jamming) or free surfaces (sintering) as boundary conditions. Periodic boundary conditions are handy to study packing behavior by minimizing the effect of boundary conditions. A generalization of our LS-DEM formulation is thus needed for periodic conditions.

References

[1] G. Petzow and H. E. Exner, *Particle Rearrangement in Solid State Sintering.* 1976. DOI: 10.1515/ijmr-1976-670906.

[2] R Grupp, M Nothe, B Kieback, and J Banhart, "Cooperative material transport during the early stage of sintering," *Nat. Commun.*, vol. 2, p. 298, 2011. DOI: 10.1038.

[3] C. L. Martin, L. C. Schneider, L. Olmos, and D. Bouvard, "Discrete element modeling of metallic powder sintering," *Scripta Materialia*, vol. 55, no. 5, pp. 425–428, 2006, ISSN: 13596462. DOI: 10.1016/j.scriptamat.2006.05.017.

[4] B. Henrich, A. Wonisch, T. Kraft, M. Moseler, and H. Riedel, "Simulations of the influence of rearrangement during sintering," *Acta Materialia*, vol. 55, no. 2, pp. 753–762, 2007, ISSN: 13596454. DOI: 10.1016/j.actamat.2006.09.005.

[5] C. Wang and S. Chen, "Application of the complex network method in solid-state sintering," *Computational Materials Science*, vol. 69, pp. 14–21, 2013, ISSN: 09270256. DOI: 10.1016/j.commatsci.2012.11.020.

[6] S. Martin, M. Guessasma, J. Léchelle, J. Fortin, K. Saleh, and F. Adenot, "Simulation of sintering using a Non Smooth Discrete Element Method. Application to the study of rearrangement," *Computational Materials Science*, vol. 84, pp. 31–39, 2014, ISSN: 09270256. DOI: 10.1016/j.commatsci.2013.11.050.

[7] S. Nosewicz, J. Rojek, K. Pietrzak, and M. Chmielewski, "Viscoelastic discrete element model of powder sintering," *Powder Technology*, vol. 246, pp. 157–168, 2013, ISSN: 00325910. DOI: 10.1016/j.powtec.2013.05.020.

[8] R. Besler, M. Rossetti Da Silva, J. J. Do Rosario, M. Dosta, S. Heinrich, and R. Janssen, "Sintering Simulation of Periodic Macro Porous Alumina," *Journal of the American Ceramic Society*, vol. 98, no. 11, pp. 3496–3502, 2015, ISSN: 15512916. DOI: 10.1111/jace.13684.

[9] S. Martin, S. Navarro, H. Palancher, A. Bonnin, J. Léchelle, M. Guessasma, J. Fortin, and K. Saleh, "Validation of DEM modeling of sintering using an in situ X-ray microtomography analysis of the sintering of NaCl powder," *Computational Particle Mechanics*, vol. 3, no. 4, pp. 525–532, 2016, ISSN: 21964386. DOI: 10.1007/s40571-015-0062-7.

[10] T. Rasp, C. Jamin, O. Guillon, and T. Kraft, "Cracking and shape deformation of cylindrical cavities during constrained sintering," *Journal of the European Ceramic Society*, vol. 37, no. 8, pp. 2907–2917, 2017, ISSN: 1873619X. DOI: 10.1016/j.jeurceramsoc.2017.03.013.

[11] S. Nosewicz, J. Rojek, and M. Chmielewski, "Discrete Element Framework for Determination of Sintering and Postsintering Residual Stresses of," *Materials*, vol. 13, no. 4015, pp. 1–21, 2020. DOI: 10.3390/ma13184015.

[12] B. Paredes-goyes, D. Jauffres, J.-m. Missiaen, and C. L. Martin, "Grain growth in sintering : A discrete element model on large packings," *Acta Materialia*, vol. 218, p. 117 182, 2021, ISSN: 1359-6454. DOI: 10.1016/j.actamat.2021.117182.

[13] M. H. P. Teixeira, V. Skorych, R. Janssen, S. Y. G. González, A. De Noni, J. B. Rodrigues Neto, D. Hotza, and M. Dosta, "High heating rate sintering and microstructural evolution assessment using the discrete element method," *Open Ceramics*, vol. 8, no. September, 2021, ISSN: 26665395. DOI: 10.1016/j.oceram.2021.100182.

[14] Z. Yan, S. Hara, and N. Shikazono, "Effect of powder morphology on the microstructural characteristics of La0.6Sr0.4Co0.2Fe0.8O3 cathode: A Kinetic Monte Carlo investigation," *International Journal of Hydrogen Energy*, vol. 42, no. 17, pp. 12 601–12 614, 2017, ISSN: 03603199. DOI: 10.1016/j.ijhydene.2017.03.136.

[15] R. Bjørk, "The sintering behavior of ellipsoidal particles," *Journal of the American Ceramic Society*, no. May, pp. 1–10, 2022, ISSN: 0002-7820. DOI: 10.1111/jace.18580.

[16] G. Lu, J. R. Third, and C. R. Müller, "Discrete element models for non-spherical particle systems: From theoretical developments to applications," *Chemical Engineering Science*, vol. 127, pp. 425–465, 2015, ISSN: 00092509. DOI: 10.1016/j.ces.2014.11.050.

[17] R. Kawamoto, E. Andò, G. Viggiani, and J. E. Andrade, "Level set discrete element method for three-dimensional computations with triaxial case study," *Journal of the Mechanics and Physics of Solids*, vol. 91, pp. 1–13, 2016, ISSN: 00225096. DOI: 10.1016/j.jmps.2016.02.021.

[18] L. Zhan, C. Peng, B. Zhang, and W. Wu, "A surface mesh represented discrete element method (SMR-DEM) for particles of arbitrary shape," *Powder Technology*, vol. 377, pp. 760–779, 2020, ISSN: 00325910. DOI: 10.1016/j.powtec.2020.09.046.

[19] Z. Lai, Q. Chen, and L. Huang, "Fourier series-based discrete element method for computational mechanics of irregular-shaped particles," *Computer Methods in Applied Mechanics and Engineering*, vol. 362, p. 112 873, 2020, ISSN: 00457825. DOI: 10.1016/j.cma.2020.112873.

[20] A. Dervieux and F. Thomasset, "A finite element method for the simulation of a rayleigh-taylor instability," in *Approximation methods for Navier-Stokes problems*, Springer, 1980, pp. 145–158.

[21] S. Osher and J. A. Sethian, "Fronts propagating with curvature-dependent speed: Algorithms based on Hamilton-Jacobi formulations," *Journal of Computational Physics*, vol. 79, no. 1, pp. 12–49, 1988, ISSN: 10902716. DOI: 10.1016/0021-9991(88)90002-2.

[22] J. Duriez and S. Bonelli, "Precision and computational costs of Level Set-Discrete Element Method (LS-DEM) with respect to DEM," *Computers and Geotechnics*, vol. 134, no. January, p. 104 033, 2021, ISSN: 18737633. DOI: 10.1016/j.compgeo.2021.104033.

[23] J. M. Harmon, D. Arthur, and J. E. Andrade, "Level set splitting in DEM for modeling breakage mechanics," *Computer Methods in Applied Mechanics and Engineering*, vol. 365, p. 112 961, 2020, ISSN: 00457825. DOI: 10.1016/j.cma.2020.112961.

[24] S. A. Pazmiño, A. X. Jerves, J. Dijkstra, D. A. Medina, and H. P. Jostad, "A generalized 3DLS-DEM scheme for grain breakage," *Computer Methods in Applied Mechanics and Engineering*, vol. 399, p. 115 383, 2022, ISSN: 00457825. DOI: 10.1016/j.cma.2022.115383.

[25] D. Bustamante, A. X. Jerves, and S. A. Pazmiño, "A generalized three-dimensional discrete element method with electrostatic induced cohesion," *Granular Matter*, vol. 22, no. 4, pp. 1–13, 2020, ISSN: 14347636. DOI: 10.1007/s10035-020-01048-4.

[26] R. Kawamoto, E. Andò, G. Viggiani, and J. E. Andrade, "All you need is shape: Predicting shear banding in sand with LS-DEM," *Journal of the Mechanics and Physics of Solids*, vol. 111, pp. 375–392, 2018, ISSN: 00225096. DOI: 10.1016/j.jmps.2017.10.003.

[27] K. Karapiperis, J. Harmon, E. Andò, G. Viggiani, and J. E. Andrade, "Investigating the incremental behavior of granular materials with the level-set discrete element method," *Journal of the Mechanics and Physics of Solids*, vol. 144, p. 104 103, 2020, ISSN: 00225096. DOI: 10.1016/j.jmps.2020.104103.

[28] J. M. Harmon, K. Karapiperis, L. Li, and S. Moreland, "Particle bonding within the level set discrete element method," *Computer Methods in Applied Mechanics and Engineering*, vol. 373, p. 113 486, 2021, ISSN: 0045-7825. DOI: 10.1016/j.cma.2020.113486.

[29] J. Christoffersen, M. M. Mehrabadi, and S. Nemat-Nasser, "A Micromechanical Description of Granular Material Behavior.," vol. 48, no. June, p. 67, 1981.

[30] A. Davis, B. West, N. Frisch, D. O'Connor, and M. Parno, "ParticLS: Object-oriented software for discrete element methods and peridynamics," *Computational Particle Mechanics*, 2021, ISSN: 2196-4386. DOI: 10.1007/s40571-021-00392-3.

[31] G. T. Houlsby, "Potential particles: a method for modelling non-circular particles in DEM," *Computers and Geotechnics*, vol. 36, no. 6, pp. 953–959, 2009, ISSN: 0266352X. DOI: 10.1016/j.compgeo.2009.03.001.

[32] C. L. Martin and R. K. Bordia, "The effect of a substrate on the sintering of constrained films," *Acta Materialia*, vol. 57, no. 2, pp. 549–558, 2009, ISSN: 13596454. DOI: 10.1016/j.actamat.2008.09.041.

[33] R. Hart, P. A. Cundall, and J. Lemos, "Formulation of a three-dimensional distinct element model-Part II. Mechanical calculations for motion and interaction of a system composed of many polyhedral blocks," *International Journal of Rock Mechanics and Mining Sciences and*, vol. 25, no. 3, pp. 117–125, 1988, ISSN: 01489062. DOI: 10.1016/0148-9062(88)92294-2.

[34] B. Salque, "Caractérisation mécanique de la respiration des hydrures pour uneconception optimisée des réservoirs de stockage de l'hydrogène par voie solide," Theses, Université Grenoble Alpes, Jun. 2017.

[35] A. Džiugys and B. Peters, "An approach to simulate the motion of spherical and non-spherical fuel particles in combustion chambers," *Granular Matter*, vol. 3, no. 4, pp. 231–265, 2001, ISSN: 14345021. DOI: 10.1007/pl00010918.

[36] A. Wachs, L. Girolami, G. Vinay, and G. Ferrer, "Grains3D, a flexible DEM approach for particles of arbitrary convex shape - Part I: Numerical model and validations," *Powder Technology*, vol. 224, pp. 374–389, 2012, ISSN: 00325910. DOI: 10.1016/j.powtec.2012.03.023.

[37] I. Vlahinić, E. Andò, G. Viggiani, and J. E. Andrade, "Towards a more accurate characterization of granular media: Extracting quantitative descriptors from tomographic images," *Granular Matter*, vol. 16, no. 1, pp. 9–21, 2014, ISSN: 14345021. DOI: 10.1007/s10035-013-0460-6.

[38] A. Podlozhnyuk, S. Pirker, and C. Kloss, "Efficient implementation of superquadric particles in Discrete Element Method within an open-source framework," *Computational Particle Mechanics*, vol. 4, no. 1, pp. 101–118, 2017, ISSN: 21964386. DOI: 10.1007/s40571-016-0131-6.

[39] R. Goldman, "Curvature formulas for implicit curves and surfaces," *Computer Aided Geometric Design*, vol. 22, no. 7 SPEC. ISS. Pp. 632–658, 2005, ISSN: 01678396. DOI: 10.1016/j.cagd.2005.06.005.

[40] L. Li, E. Marteau, and J. E. Andrade, "Capturing the inter-particle force distribution in granular material using LS-DEM," *Granular Matter*, vol. 21, no. 3, pp. 1–16, 2019, ISSN: 14347636. DOI: 10.1007/s10035-019-0893-7.

[41] D. Bouvard and R. M. McMeeking, *Deformation of Interparticle Necks by Diffusion-Controlled Creep*, 1996. DOI: 10.1111/j.1151-2916.1996.tb07927.x.

[42] R. Coblenz William; Coble, "Iniitial stage solid state sintering models. A critical analysis and assesment," *Sintering Processes*, vol. 13, no. January 1980, pp. 141–157, 1980. DOI: 10.1007/978-1-4899-5301-8.

[43] R. L. Coble, "Initial Sintering of Alumina and Hematite," *Journal of the American Ceramic Society*, vol. 41, no. 2, pp. 55–62, 1958.

[44] David Eberly, *Distance from a Point to an Ellipse, an Ellipsoid, or a Hyperellipsoid*.

[45] Q. J. Zheng, Z. Y. Zhou, and A. B. Yu, "Contact forces between viscoelastic ellipsoidal particles," *Powder Technology*, vol. 248, pp. 25–33, 2013, ISSN: 00325910. DOI: 10.1016/j.powtec.2013.03.020.

[46] S. Torquato, T. M. Truskett, and P. G. Debenedetti, "Is random close packing of spheres well defined?" *Physical Review Letters*, vol. 84, no. 10, pp. 2064–2067, 2000, ISSN: 10797114. DOI: 10.1103/PhysRevLett.84.2064.

[47] C. L. Martin and R. K. Bordia, "Influence of adhesion and friction on the geometry of packings of spherical particles," *Physical Review E - Statistical, Nonlinear, and Soft Matter Physics*, vol. 77, no. 3, pp. 1–8, 2008, ISSN: 15393755. DOI: 10.1103/PhysRevE.77.031307.

[48] Y. T. Feng, K. Han, and D. R. Owen, "Energy-conserving contact interaction models for arbitrarily shaped discrete elements," *Computer Methods in Applied Mechanics and Engineering*, vol. 205-208, no. 1, pp. 169–177, 2012, ISSN: 00457825. DOI: 10.1016/j.cma.2011.02.010.

[49] Y. T. Feng, "An energy-conserving contact theory for discrete element modelling of arbitrarily shaped particles: Basic framework and general contact model," *Computer Methods in Applied Mechanics and Engineering*, vol. 373, p. 113 454, 2021, ISSN: 00457825. DOI: 10.1016/j.cma.2020.113454.

Chapter 6

General conclusion and perspectives

6.1 Conclusions

In the last 20 years, DEM has been successfully used to model densification during sintering at the particle length scale. The simplicity of the approach has allowed the simulation of the microstructural evolution of packings with many thousands of particles, with ever-increasing refinements to get closer to realistic conditions. In addition to study the influence of the initial microstructure and process parameters, the method provides the ability of analyzing more complex sintering scenarios such as: anisotropy, defect evolution, influence of second phases, constrained sintering, among others. The coupling in this work with a grain growth model should improve the realism of these analyses, but more importantly allows other applications in sintering, where grain growth is important, to be explored.

The proposed grain growth model has as a basic assumption that smaller particles transfer mass to larger particles by surface diffusion and grain boundary motion. Each mechanism has a different condition for being activated, resulting in three possible states for each contact: shrinkage, grain growth by surface diffusion, or grain growth by grain boundary migration with shrinkage. The DEM model is in good agreement with more sophisticated models for a two-particle system and with experimental grain growth data from micron alumina sintering. One of the challenges for the application of the model is the choice of diffusivity and mobility values, which are lacking in the literature for many materials or present very large variations. In particular, the model is sensitive to the grain boundary mobility, whose values can trigger abnormal grain growth, with a higher broadening of the distribution size, in cases not observed in experiments. However, this work shows the need of further numerical and experimental analysys of the condition to have self-similarity in nano and micropowders. Despite this, the coupled model is able to provide the densification and grain growth kinetics, the sintering trajectory and even more specific data, as the evolution of the particle size distribution. The ability of taking particle initial size distributions from experiments allowed to observe that wider distributions favor grain growth to the detriment of densification. Improvements can be made in the direction of the grain boundary mobility description, which here only depends on the sintering temperature and is the

same for all grains. It is interesting to note that our observation that a narrow particle size distribution may retard grain growth is central to the strategy employed by Yang et al. [1] for nano-powders.

Therefore, it seemed appropriate to use the model to investigate a current practical challenge, that is to limit grain growth during the sintering of nano-powders. The mechanisms and stages already validated for micronic powders were kept. Nevertheless, a probability that small particles that have more than one contact can receive mass from large particles was introduced to avoid artificial abnormal grain growth. Although this idea is supported by some nano-powders simulations, more investigations are needed to verify the very existence of this phenomenon, its probability, and its underlying mechanisms. Similarly, the next section discusses other possible model improvements, which may be appropriate to avoid the observed abnormal grain growth, since the origin of this phenomenon may not be the hypothesis that matter always goes from small to large particles. Nevertheless, the model was able to predict qualitatively experimental data of nonisothermal conventional sintering and of two-step sintering. The simulations confirm that faster heating rates retard grain growth in conventional sintering of alumina. Furthermore, these simulations demonstrated one of the qualities of numerical modeling, that is the ability to test new ideas that are difficult to measure experimentally. In this sense, DEM simulations support the hypothesis that the effectiveness of two-step sintering is linked to the increase of the activation energy of the grain boundary mobility for alumina at low temperatures.

Regarding the second axis of the thesis, a proof of concept of a LS-DEM model for capturing arbitrary shape particles in sintering was developed. In this study, it was possible to perform jamming and sintering simulations of ellipsoidal particles. Although the implemented optimization approach for contact detection needs adjustments, it shows more effectiveness when compared with the boundary nodes approach for the detection of small contacts in sintering. Still, a detailed comparison of the overall computational cost of both methods is needed. Some future improvements are proposed in the next section. Despite the higher computational cost compared to the classical DEM, the model is still feasible to run simulations of packings with thousands of particles. The results shown for this preliminary LS-DEM sintering model are only a first glimpse of the possible applications of the modeling of arbitrary shape particles in sintering within the DEM framework.

6.2 Perspectives

6.2.1 DEM grain growth model

The model could be used in a wider variety of sintering applications if the predicted grain growth is smoother and less likely to produce artificial abnormal grain growth. To this end, two central hypotheses must be addressed, and critically assessed. First, the question of whether the flux of mass is always from the small to the large particle during grain growth. At the nanoscale, molecular dynamics simulations could investigate this phenomenon. For micronic particles, the good resolution of in-situ nano-tomography could be used to follow the behavior of two or three particles in contact, specifically the evolution of the particle volume and the center-to-center approach.

The second assumption that can be questioned relates to the mechanisms in each status and the conditions for moving from one status to another. Currently, the shift is made on the basis of the neck size and the two particle radii only. This information is a simplistic approximation mainly because the particles are spheres and no information about the surrounding porosity is taken into account. More information at the length scale of the contact in addition to theoretical models should guide us to make a more realistic choice of the mechanisms and conditions at each state. A possibility is to estimate the pore size and the pore coordination number (z_p) based on the Voronoi tessellation method available in `dp3D`.

Also, the grain growth model assumes that once grain boundary mobility is active, grain growth by surface diffusion is not. In other words, the two grain growth mechanisms are mutually exclusive (Fig. 3.2 in chapter 2). This simplistic assumption may have to be modified to account for the geometry of the neighboring pores (concave versus convex pores). Similarly, in future work, efforts should be directed at improving the accuracy of the model, for example by including the dependence of grain boundary mobility M_{GB} on mean porosity (or relative density D). If Voronoi tessellation is used, one may go even further by using a more local information (local density, local geometry to decide whether the grain boundary may be pinned) to modify the grain boundary mobility at the scale of a given contact. These perspectives are sketched in Fig. 6.1. In addition, a better approximation of the local curvature used in the grain growth volume balance can be achieved by using realistically shaped particles with LS-DEM.

Finally, future experimental work is needed for measuring the effective diffusivities of powders in nano and micronic particles. This will allow to check the validity of the very different prefactor values used here at the two scales. Moreover, a better

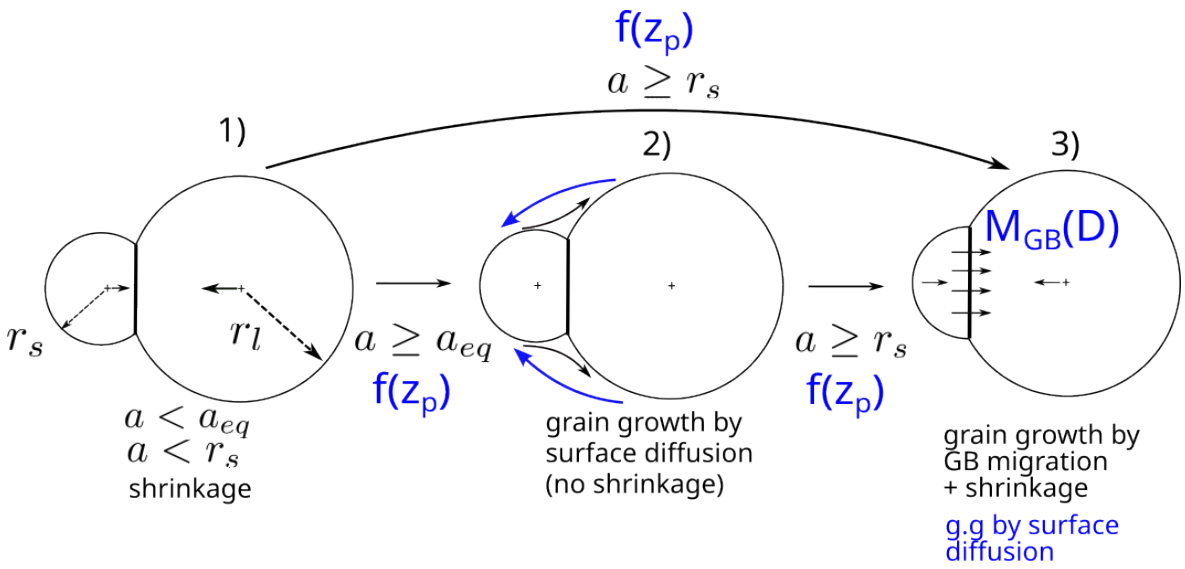

Figure 6.1: Future work (blue) on the mechanisms and conditions of grain growth modeling informed by the pore coordination number z_p, or the relative density D.

understanding of the influence of the diffusivities on the grain growth in the simulations can be reached using the ratio of diffusivities along and transverse to the grain boundary. This is similar to the already employed ratio between grain boundary and surface diffusion. These data on diffusivities are central to the quantitative quality of DEM simulations for sintering. They may also originate from numerical simulations at lower scales (molecular dynamics in particular).

6.2.2 LS-DEM sintering model

Being a proof of concept, the developed LS-DEM sintering model requires even more immediate improvements. The inclusion of periodicity is the most pressing perspective in order to eliminate the influence of boundaries in current simulations. Another main step in reaching the full capacity of LS-DEM is the ability to capture the real shapes of particles from tomographic images. Thus, an efficient preprocessing tool is needed to transfer effectively the information from X-tomography images to level-sets on a grid.

Additional future work may be the simulation of large packing during sintering. In this case the RAM consumption can be a limiting factor, mainly due to the use of the optimization-based contact detection. A solution is the use of more efficient level set data structures. An example is the octree method as suggested for LS-DEM by Duriez and Galusinsky [2].

Regarding sintering, although rotations are already implemented, this should be improved by implementing tangential forces and resisting moments. This is because, large necks grow quite rapidly during sintering and may block entirely rotations. Once

these steps have been completed, it will be possible to move on to LS-DEM modeling of grain growth and coalescence. At this point, level-sets present a great advantage allowing quite naturally the merging of two particles of arbitrary shape. This is achieved by doing the following union Boolean operation between particles i and j to obtain a new particle k:

$$\phi_k(x,y,z) = min\left(\phi_i(x,y,z), \phi_j(x,y,z)\right) \tag{6.1}$$

This is similar to the approach employed by of Harmon et al. [3] for modeling breakage mechanics, where intersection and difference operations were performed (Fig. 6.2). However, there is a subtlety in sintering, as there is no conservation of mass when two indented particles are simply merged together. A simple approach may be to first perform an intersection operation between i and j to obtain a new particle, whose volume can be calculated to obtain the intersection volume of i and j. Now the merging operation (eq. 6.1) is performed and the intersection volume is homogeneously added to the new particle k.

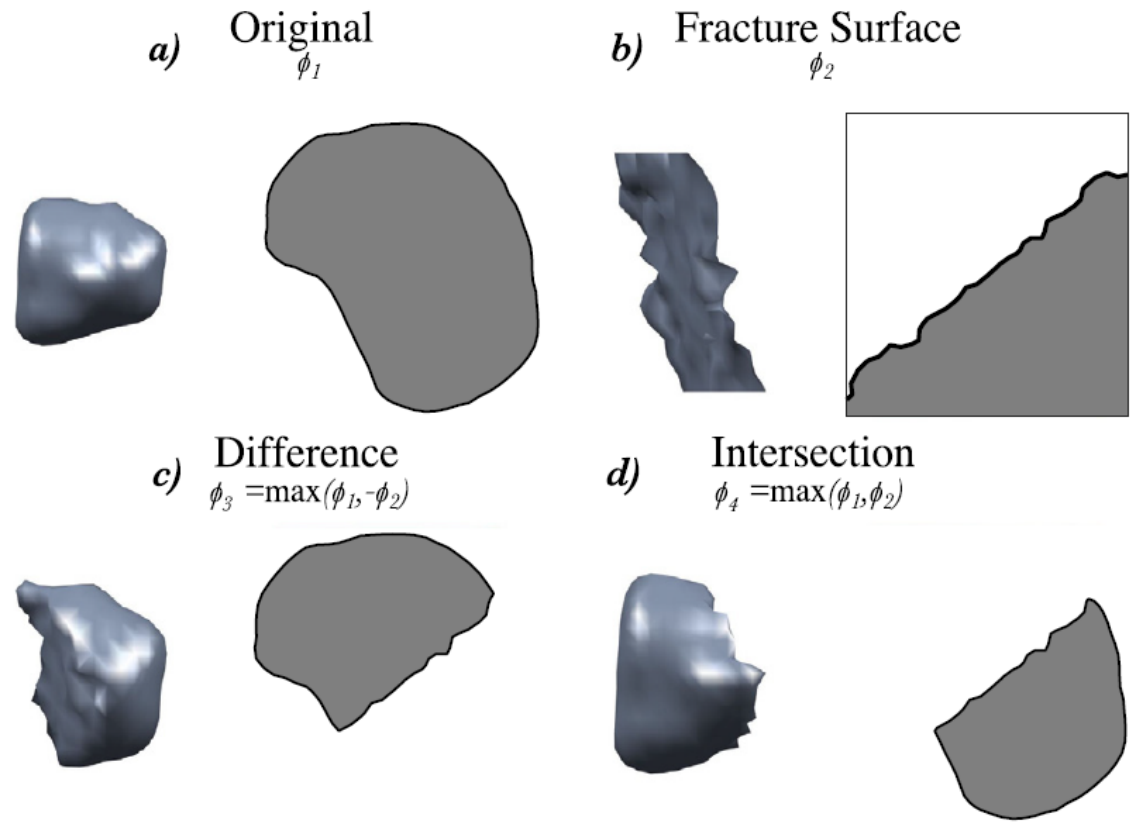

Figure 6.2: Breakage of particles in LS-DEM as proposed by Harmon et al. [3]

In the same direction, but with a paradigm shift, a future work could be to migrate from the DEM perspective to a framework allowing the motion of particle surfaces using the level set method. It has been used extensively in many different applications for

describing interface motion and, to the best of our knowledge, only once for sintering in [4]. This choice will depend on the type of sintering applications envisaged. Fig. 6.3 [5] shows an example of the evolution and merging of interfaces that the level set method can handle.

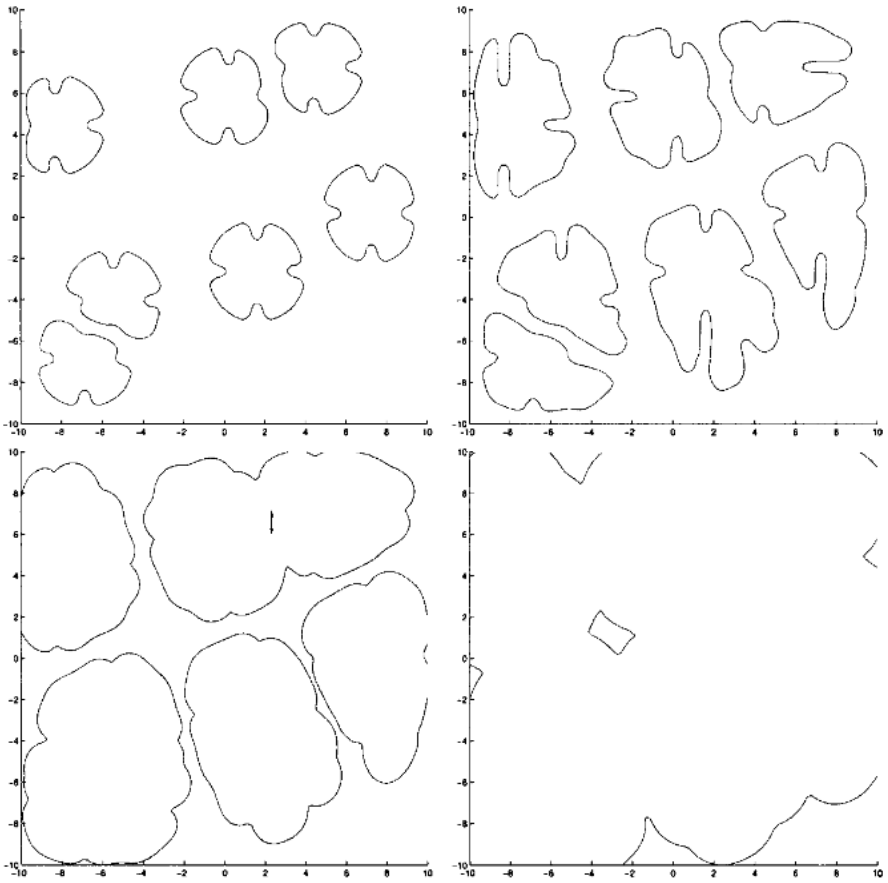

Figure 6.3: Growth and merging of arbitrary shape surfaces described by the level set method [5]

All these perspectives have for objective to make DEM simulations more realistic. The downside is that they make also DEM simulations much more complex from a numerical point of view. This is somewhat in contradiction with the original philosophy of DEM, which central numerical scheme is very simple (see Fig. 2.13). Thus, a good balance must be found between going towards more realistic simulations and keeping a simple and robust numerical method.

References

[1] H. Yang, L. Li, Y. Li, B. Shen, Y. Kang, L. Zhao, J. Li, Y. Dong, and J. Li, "Unveiling exceptional sinterability of ultrafine α-Al2O3 nanopowders," *Journal*

of Materiomics, vol. 7, no. 4, pp. 837–844, 2021, ISSN: 23528486. DOI: 10.1016/j.jmat.2020.12.011.

[2] J. Duriez and C. Galusinsky, "Level Set Representation on Octree for Granular Material with Arbitrary Grain Shape," pp. 64–71, 2020. DOI: 10.14311/tpfm.2020.009.

[3] J. M. Harmon, D. Arthur, and J. E. Andrade, "Level set splitting in DEM for modeling breakage mechanics," *Computer Methods in Applied Mechanics and Engineering*, vol. 365, p. 112 961, 2020, ISSN: 00457825. DOI: 10.1016/j.cma.2020.112961.

[4] J. Bruchon, D. Pino-Muñoz, F. Valdivieso, and S. Drapier, "Finite element simulation of mass transport during sintering of a granular packing. Part I. Surface and lattice diffusions," *Journal of the American Ceramic Society*, vol. 95, no. 8, pp. 2398–2405, 2012, ISSN: 00027820. DOI: 10.1111/j.1551-2916.2012.05073.x.

[5] F. Gibou, R. Fedkiw, R. Caflisch, and S. Osher, "A Level Set Approach for the Numerical Simulation of Dendritic Growth," vol. 19, no. December, pp. 183–199, 2003.

Appendix A

Supplementary Information of Chapter 3

A.1 Shrinkage and shrinkage rate: comparison with Pan et al. results

The Eq. (3.5) from the main text shows the dependence of the contact radius a on the indentation h from Pan et al. [1]. The only difference is we opted for convenience to take the current radii and not the initial radii.

In order to check the validity of the new equation, we compare in Fig. A.1 the obtained shrinkage $\tilde{h}$ and shrinkage rate $\frac{d\tilde{h}}{dt}$ for a given contact radius. Our simulation results reproduced the original results from Pan et al.

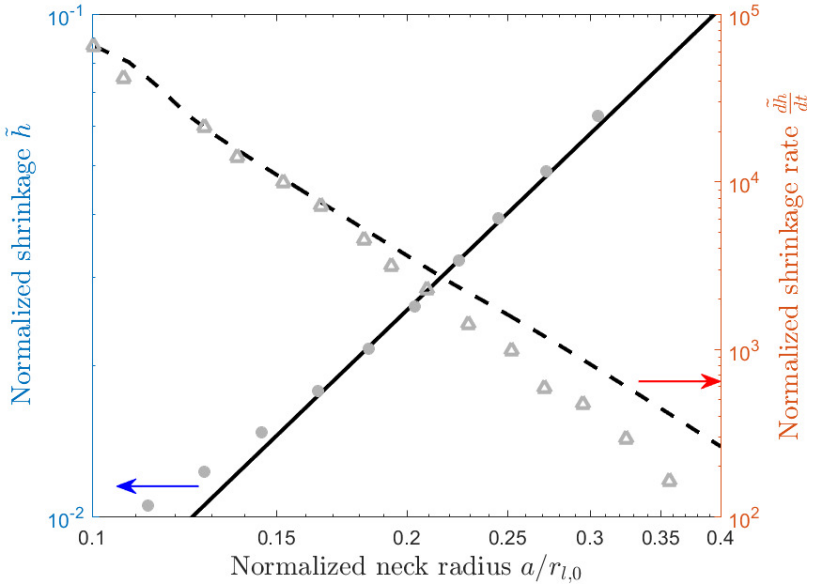

Figure A.1: Normalized shrinkage and shrinkage rate versus neck radius. Comparison between DEM simulations (—— ; - - -) and Pan et al. [1] (• ; △). Shrinkage is normalized by the initial large particle radius $r_{l,0}$, while the shrinkage rate is normalized by $\Delta_{GB}\gamma_S/r_{l,0}^3$.

A.2 Equilibrium neck size

In our study the relation between the contact size a and the contact angle Ψ are based on geometric considerations. The basic representation and parameters for two spherical particles are shown in Fig. A.2.

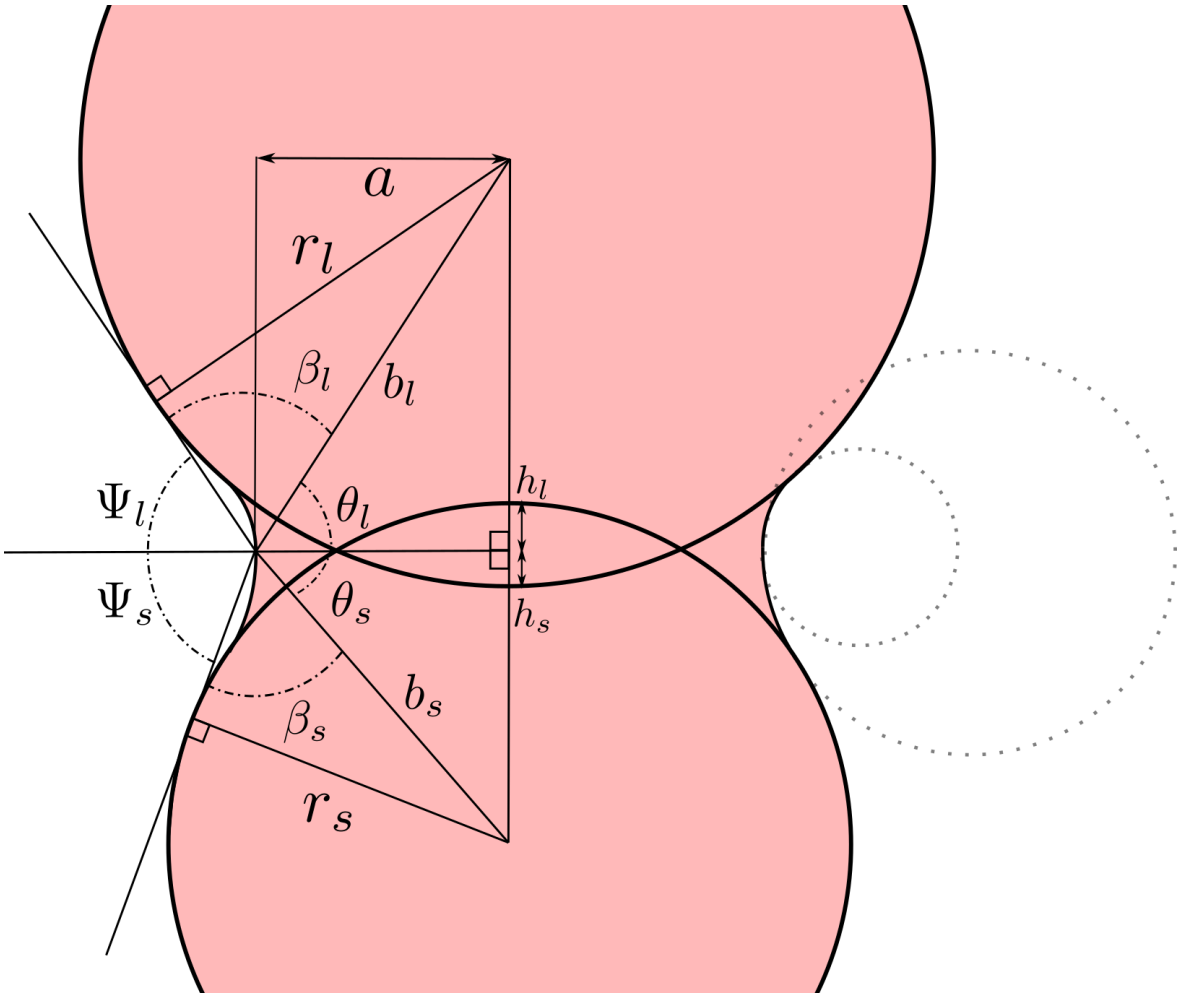

Figure A.2: Geometrical parameters for a contact between two unequal in size spherical particles.

From this scheme the following trigonometric and geometrical expressions can be written:

$$b_l = \sqrt{a^2 + (r_l - h_s)^2} \qquad b_s = \sqrt{a^2 + (r_s - h_l)^2} \tag{A.1}$$

$$\beta_l = \arcsin \frac{r_l}{b_l} \qquad \beta_s = \arcsin \frac{r_s}{b_s} \tag{A.2}$$

$$\theta_l = \arccos \frac{a}{b_l} \qquad \theta_s = \arccos \frac{a}{b_s} \tag{A.3}$$

$$\Psi_l = \pi - \beta_l - \theta_l \qquad \Psi_s = \pi - \beta_s - \theta_s \tag{A.4}$$

$$\Psi = \Psi_l + \Psi_s \tag{A.5}$$

$$h = h_l + h_s \tag{A.6}$$

Dropping the square terms for simplicity leads to the following relation between h_l and h_s:

$$\frac{h_l}{r_l} = \frac{h_s}{r_s} \tag{A.7}$$

Our approach allows to choose any contact size. The expression of Pan et al. [1] is used to define the relation between the indentation h and the contact size a due to its accuracy to describe contact size in sintering and taking into account particles of different sizes:

$$a^2 = \kappa \left[0.5\left(1 + \frac{r_s}{r_l}\right)\right]^{\zeta} r_l h \tag{A.8}$$

The above equations form a nonlinear set of equations that relates Ψ to a and that can be solved numerically or analytically. Fig. A.3 shows the numerical solution (points) for different initial size ratios.

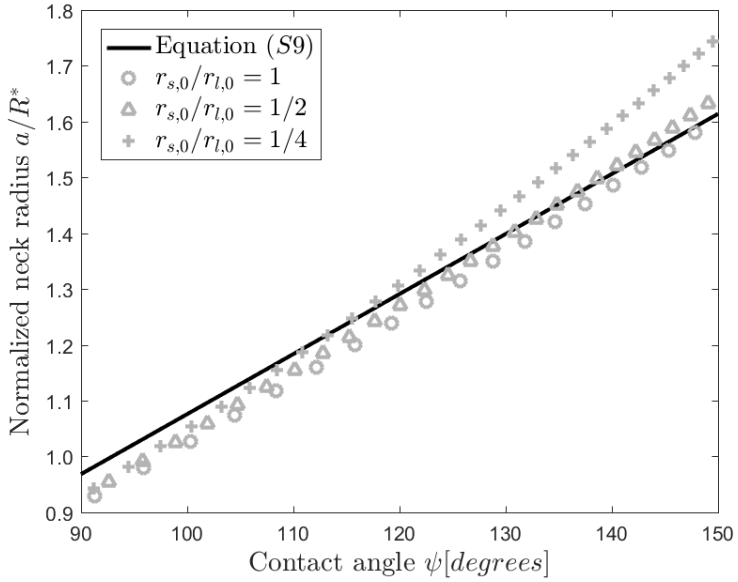

Figure A.3: Geometrical relationship between neck size and contact angle for different initial size ratios between the smaller and larger particles with $R^* = \frac{r_s r_l}{r_s + r_l}$.

We propose a simple linear fit to relate both variables in order to save on computational time:

$$a = \frac{\Psi}{\hat{\Psi}} \frac{r_s}{1 + \frac{r_s}{r_l}} \tag{A.9}$$

This solution is plotted as a straight line in Fig. A.3 with $\hat{\Psi} = 92.937°$. We observe that the linear equation fits the numerical results well for any value of the size ratio greater than $\frac{1}{4}$. When the contact angle of equilibrium (dihedral angle Ψ_{eq}) is used, the contact size of equilibrium a_{eq} is obtained. This value is important in the model

as it is the condition to start grain growth by surface diffusion and to stop sintering.

A.3 Sample preparation

Initial packings of particles are generated by random sequential addition of non-contacting particles followed by isostatic densification. Periodic boundary conditions are applied on all three directions. Here, since large particle size distributions are used and coarsening drastically decreases the number of particles, a large initial number of particles is required to obtain statistically significant bulk properties. 40,000 particles have turned out to be sufficient while resulting in reasonable computation times with our parallelized DEM dp3D code. Much larger packings (400,000 particles) have been tested without noticeable differences (Fig. 5).

Any particle size distribution can be accommodated and a lognormal size distribution, often used to describe experimental powders, is chosen here. During the initial isostatic densification, only Hertzian elastic forces are considered. At the end of this jamming process, before sintering, the packing relative density is 0.59, to allow comparison of our results with the experiments of Nettleship et al. [2]. The initial radius r_0 of the particles is given by a lognormal distribution (μ_0, σ_0^2), with parameters μ_0 and σ_0. The probability density function f is:

$$f(r_0) = \frac{1}{r_0 \sigma_0 \sqrt{2\pi}} \exp\left(-\frac{(\ln r_0 - \mu_0)^2}{2\sigma_0^2}\right) \tag{A.10}$$

The mean particle radius is $r_{m,0} = \exp\left(\mu_0 + \frac{\sigma_0^2}{2}\right)$ and the relative standard deviation $\sqrt{\exp(\sigma_0^2) - 1}$. Note that mean grain sizes $\bar{G}$, i.e., twice the particle radii, are reported in the following in order to be consistent with experimental data.

A.4 Mean field analysis of grain growth kinetics

Scaling laws of the form $\bar{G}^n - \bar{G}_0^n \propto t$ may be derived from the mass transfer equations used in the DEM model, i.e., Eqs. (7), (8) and (9) of the main text. From these equations, the scaling of the growth rate $\frac{dr}{dt}$ of a particle of radius r immersed in a matrix of particles of mean radius $\bar{r}$ can be obtained for each specific mechanism of grain growth. Let us first consider grain growth by surface diffusion:

$$\frac{dr}{dt} \propto \frac{1}{r^2} \frac{\frac{1}{\bar{r}} - \frac{1}{r}}{r + \bar{r}} A_S \tag{A.11}$$

$A_S \approx Z 2\pi a_{eq} \delta_S$ with the coordination number $Z \propto \frac{4\pi r^2}{\pi a_{eq}^2}$ i.e. the surface of the particle considered divided by the surface of one contact at equilibrium. Then, from Eq. (6) of the main text $a_{eq} \propto \frac{\bar{r}r}{\bar{r}+r}$ hence:

$$\frac{dr}{dt} \propto \frac{1}{r\bar{r}} \left(\frac{1}{\bar{r}} - \frac{1}{r} \right) \tag{A.12}$$

From Eq. (A.12) the mean grain growth rate $\frac{d\bar{r}}{dt}$ can be obtained following the mathematically complex approach of Hillert [3]. Here, for the sake of simplicity we opt for the simplified approach proposed by Kang [4] in the context of Ostwald ripening. It uses the approximate relation $\frac{d\bar{r}}{dt} \approx \left(\frac{dr}{dt}\right)_{max}$. Derivation of Eq. (A.12) gives $\left(\frac{dr}{dt}\right)_{max}$ for $r = 2\bar{r}$ leading to :

$$\frac{d\bar{r}}{dt} \propto \frac{1}{\bar{r}^3} \tag{A.13}$$

and finally after replacing $\bar{r}$ by $\bar{G}$ and integration $\bar{G}^4 - \bar{G}_0^4 \propto t$ for grain growth by surface diffusion.

Following a similar analysis, from Eq. (7) and (9) of the main text and assuming $A_{GBM} \propto r^2$ we obtain for grain growth by GB migration:

$$\frac{dr}{dt} \propto \left(\frac{1}{\bar{r}} - \frac{1}{r} \right) \tag{A.14}$$

$$\frac{d\bar{r}}{dt} \propto \left(\frac{1}{\bar{r}} \right) \tag{A.15}$$

which lead, in accordance with Hillert [3] and Bernard-Granger et al. [5] to $\bar{G}^2 - \bar{G}_0^2 \propto t$ for grain growth by GB migration.

A.5 Theoretical versus simulation sintering trajectory slope k

As commented in the main text, Bernard-Granger et al. determined that $\bar{G_0}^2/\bar{G}^2$ is linear with D [5] if the main mechanism for grain growth is GB migration. The slope of this curve k is given by:

$$k = \bar{G_0}^2 \frac{\gamma_{GB} D_{GBM}}{100 \gamma_S \delta_{GB}^2 D_{GB}} \tag{A.16}$$

The slope k is obtained by our simulations and compared with the theoretical k from Eq. (A.16). We study in Fig. A.4 the influence of the initial mean grain size $\bar{G}_0$ and of the grain boundary mobility M_{0GB} (i.e. D_{GBM}). The other parameters of the simulation are kept fixed following the values in Table 1 of the main text.

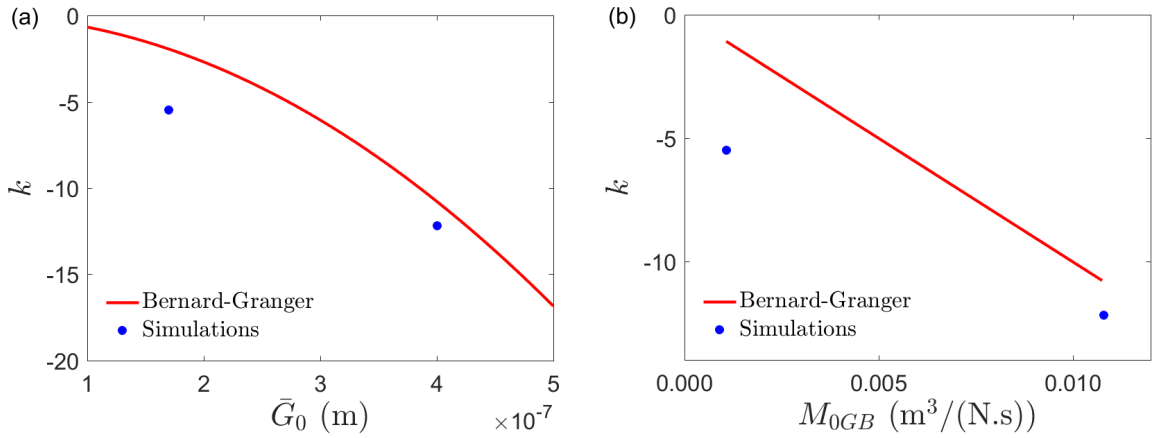

Figure A.4: Dependence of the sintering trajectory slope k on the (a) Initial mean grain size and on the (b) Grain boundary mobility. Theoretical calculations from Bernard-Granger et al. [5].

In Fig. A.4 we can observe simulation results are relatively closer to the theoretical values. The main reason for obtaining faster slopes in the simulation can be the initial size distribution, this information is not taken into account on the theoretical analysis. For instance, as showed in Fig. 9b of the main text, a narrower size distribution decreased $|k|$ from 12.2 to 10.5. In addition, our model includes surface diffusion on top of grain boundary migration.

A.6 Heating rate influence

All the simulations in our study were performed in isothermal conditions. Here we show the influence of a heating rate ramp followed by an isothermal dwell. Three different ramps are used: 2°C/min, 10°C/min, 100°C/min (Fig. A.5a) and compared with the isothermal simulation, i.e., infinite heating rate. Fig. A.5b shows different densification kinetics for various heating rates. The figure indicates that the densification rate is similar when the temperature reaches the plateau.

Fig. A.6 shows the grain growth kinetics. As expected, grain growth arises sooner when a higher heating rate is used. After the start of the grain growth, its rate is almost the same regardless of the heating rate. This is confirmed by the dashed lines representing the curves translated by the time necessary to reach the start of the grain growth. These translated curves almost match the isothermal case.

We wish to verify the relevance of comparing the experimental grain size - density trajectories obtained with a realistic heating ramp with our simulation results in isothermal conditions (Fig.9 of the main text). Fig. A.7 confirms that the trajectories for different heating rates are nearly identical. Thus, this makes relevant the analysis

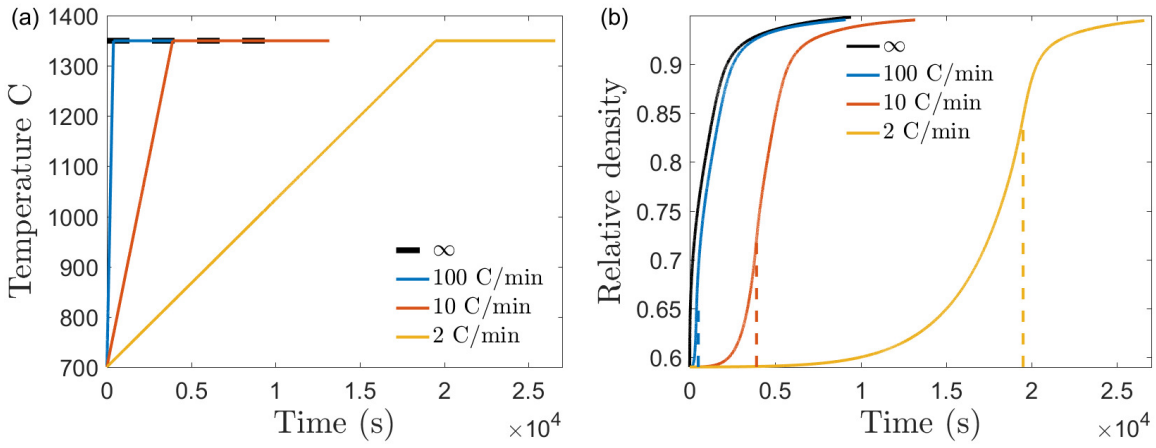

Figure A.5: Simulations with different heating rates. (a) Sintering temperature profiles. (b)Evolution of density with time. The dash lines indicate the time at which the temperature reaches the plateau.

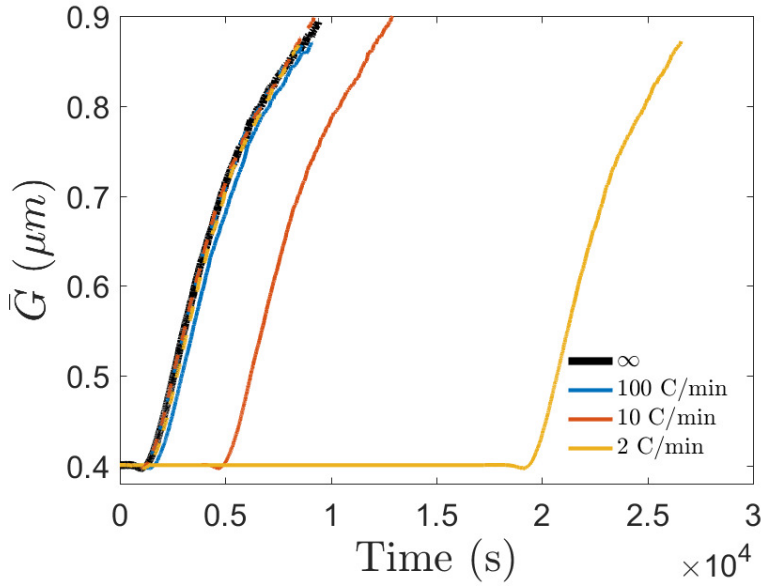

Figure A.6: Grain size - density trajectory for different heating rate ramps. Dashed lines show the curves displaced in order to compare their evolution with the isothermal sample.

performed in Section 3.2.4 of the main text.

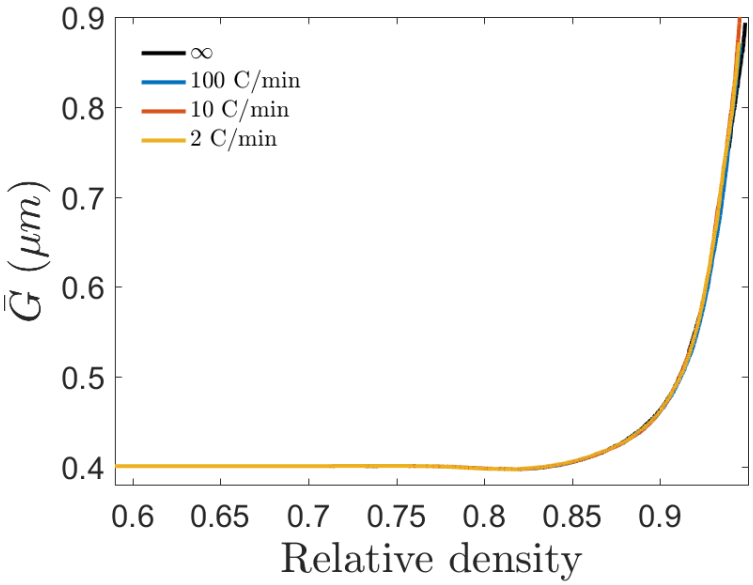

Figure A.7: Grain size - density trajectories for different heating rates.

Appendix B
Appendices of Chapter 4

B.1 Influence of the initial packing particle number

DEM has the ability to handle packings with a large number of particles in a feasible time. Nevertheless, even if millions of particles are considered, this value is much lower than the number of particles used in experiments. It is thus necessary to choose a number of particles that lead to a representative behavior of the real experimental packing. The simulation results should converge when increasing the number of particles. This is more critical in simulations of grain growth as the number of particles decreases significantly during sintering. Fig. B.1 shows the evolution of the mean grain size with temperature for packings with initially: 4 000, 40 000 and 400 000 particles. Below 1200°C, all three packings have the same behavior. As the number of particles continues to decrease, some discrepancies appear for the two smaller packings. This is critical at the end of sintering for the 4 000 packing, as very few particles remain (only 12 at 1300°C). We note that results converge to the 400 000 packing curve, thus this initial packing is used for all simulations. For a parallel simulation on four CPU cores, the computational time is approximately five days.

B.2 Calculation of the mean grain size

The simplest method to compute the mean grain size in our DEM simulations is to perform the average of the diameter over all particles, which are considered as perfect spheres (with the indented volume kept in the calculation to account for material deposition at the neck). In experiments, starting from microstructural observations, significantly different approaches are used to deal with real non-spherical shapes. To illustrate this, the DEM packings (indented spheres inverted with torus necks shape [6]) are rendered in 3D and exported in the form of RAW image stacks (see Fig. 4.7). To estimate the mean grain size, we use the granulometric analysis method [7], a widely used approach in image processing to estimate the size of structural features. This image analysis is computationally feasible if the number of particles in the images is around a few thousands. For this purpose, we use packings with initially 4 000 and

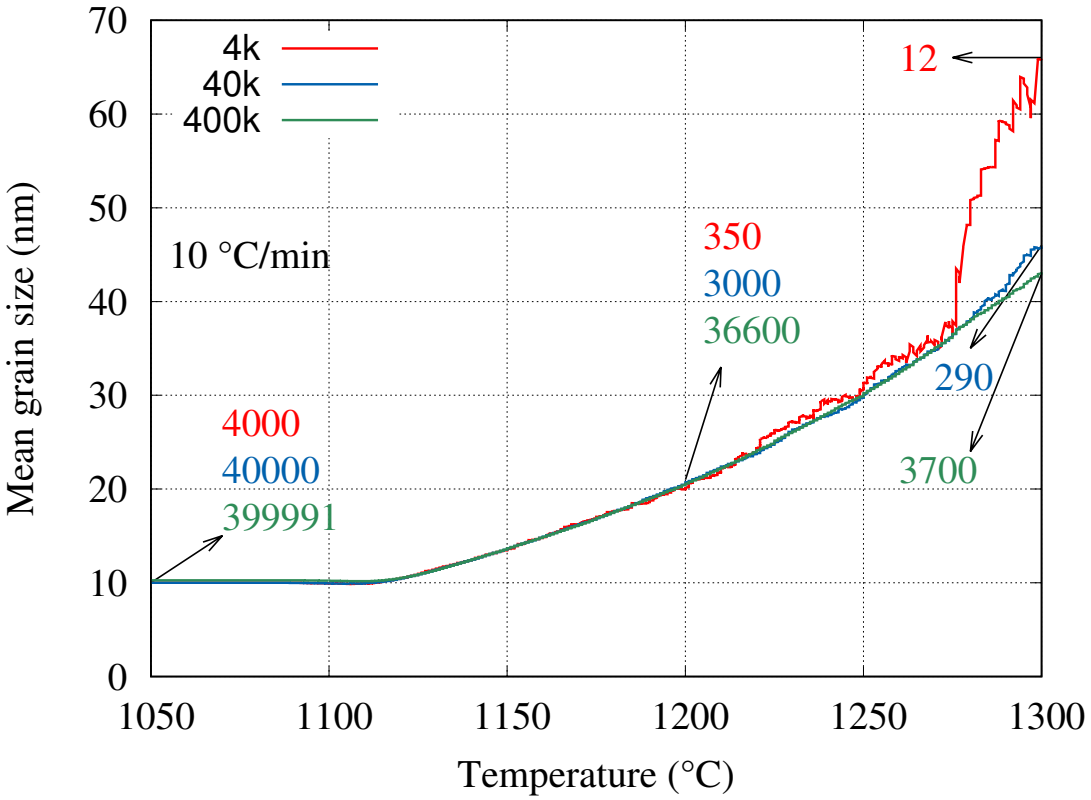

Figure B.1: Evolution of the mean grain size with temperature for increasing number of particles in the initial packing (4 000, 40 000 and 400 000). The number of particles remaining for each packing is indicated at 1050, 1200 and 1300°C.

40 000 particles for the initial and intermediate stage of sintering respectively. In Appendix A, we have shown that the results are similar to the 400 000 packing at those stages. The granulometry algorithm in the GrainFind module of GeoDict [8] is then capable of evaluating the size of grains, first by converting the image stacks into a distance map by Euclidean distance transform (EDT) and then by fitting pre-defined spheres into the structure. The spheres are successively fitted into the grain volume in a descending order, thus giving an estimation of their diameters. In that sense, it is a purely geometrical measurement as it does not require knowledge of the characteristics of individual grains and non-spherical complex grains can be assigned the diameters of the largest spheres that can be inscribed.

Appendix C

Appendices of Chapter 5

C.1 Validation of rotations

The implementation of the LS-DEM model (chapter 5) makes it necessary to include rotations in `dp3D` even if no friction is considered. Quaternions are used to implement rotations. The quaternions are used several times in each time step to rotate points in the contact detection stage to obtain their level set value. Likewise, the rotation of the particle moment of inertia is achieved by using the associated quaternion. The update of each particle quaternion following eq. 5.4 is also implemented in `dp3D`.

In order to test all the rotation elements above, a simple validation test of three ellipsoids is created. Figure C.1 shows the schematic of the test. All the ellipsoid rotations and translations are locked, except for the rotation of particle 3. The initial configuration features an indentation only between particles 1 and 3. Therefore particle 3 will rotate until it reaches an equilibrium configuration. The simulation is carried out with a Hertzian contact (5.17), no adhesion, no friction and in a quasi-static analysis.

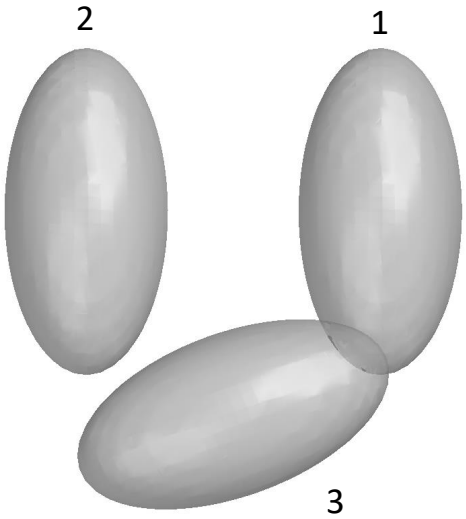

Figure C.1: Initial configuration of the three ellipsoids test

Figure C.2 shows the evolution of the normal force for the two existing contacts with time. Initially, a large compressive force is generated between particles 1 and 3 due to their initial overlap while no force exists for contact $2-3$. Particle 3 begins to

rotate clockwise and then in the opposite direction until the equilibrium configuration is reached after approximately 600 time steps. Figure C.3 shows the final configuration. Note that damping is used with the standard damping scheme (global and contact) of the `dp3D` code (see https://www.overleaf.com/read/xvtqjkgrppvd).

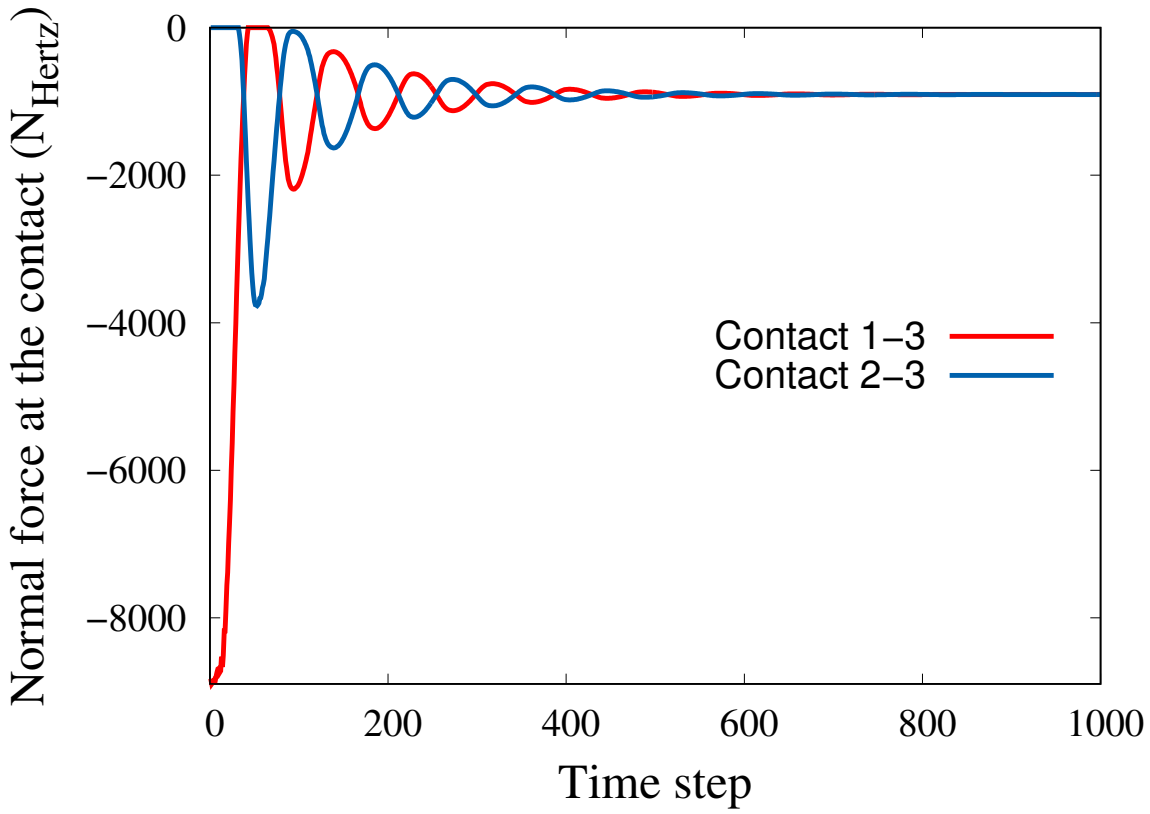

Figure C.2: Evolution of the normal force at each contact until equilibrium is reached

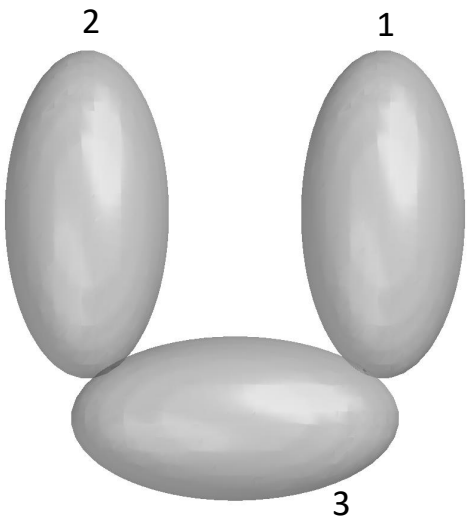

Figure C.3: Final configuration of the three ellipsoids test

References

[1] J. Pan, H. Le, S. Kucherenko, and J. A. Yeomans, "A model for the sintering of spherical particles of different sizes by solid state diffusion," *Acta Materialia*, vol. 46, no. 13, pp. 4671–4690, 1998, ISSN: 13596454. DOI: 10.1016/S1359-6454(98)00144-X.

[2] I. Nettleship, R. J. McAfee, and W. S. Slaughter, "Evolution of the grain size distribution during the sintering of alumina at 1350°C," *Journal of the American Ceramic Society*, vol. 85, no. 8, pp. 1954–1960, 2002, ISSN: 00027820. DOI: 10.1111/j.1151-2916.2002.tb00387.x.

[3] M. Hillert, "On the theory of normal and abnormal grain growth," *Acta Metallurgica*, vol. 13, no. 3, pp. 227–238, 1965, ISSN: 00016160. DOI: 10.1016/0001-6160(65)90200-2.

[4] S.-J. L. Kang, *Sintering Densification, Grain Growth, and Microstructure*. Oxford: Butterworth-Heinemann, 2005, pp. xi –xii, ISBN: 978-0-7506-6385-4. DOI: https://doi.org/10.1016/B978-075066385-4/50000-5.

[5] G. Bernard-Granger, N. Monchalin, and C. Guizard, "Sintering of ceramic powders: Determination of the densification and grain growth mechanisms from the "grain size/relative density" trajectory," *Scripta Materialia*, vol. 57, no. 2, pp. 137–140, 2007, ISSN: 13596462. DOI: 10.1016/j.scriptamat.2007.03.030.

[6] Z. Yan, C. L. Martin, O. Guillon, D. Bouvard, and C. S. Lee, "Microstructure evolution during the co-sintering of Ni/BaTiO3 multilayer ceramic capacitors modeled by discrete element simulations," *Journal of the European Ceramic Society*, vol. 34, no. 13, pp. 3167–3179, 2014, ISSN: 09552219. DOI: 10.1016/j.jeurceramsoc.2014.04.013.

[7] J. Chermant and M. Coster, "Granulometry and Granulomorphy by Image Analysis," *Acta Stereologica*, vol. 10, pp. 7–23, 1991.

[8] Becker, J., Biebl, F., Glatt, E., Cheng, L., Grießer, A., Groß, M., Linden, S., Mosbach, D., Wagner, C., Weber, A., Westerteiger, R., *Geodict image processing platform*, GeoDict (Release 2022) [Simulation software] Math2Market GmbH, doi.org/10.30423/release.geodict2022, 2021.